Multipolar magnon modes of the skyrmion lattice probed by magneto-optic and magneto-elastic coupling

Zur Erlangung des akademischen Grades eines

DOKTORS DER NATURWISSENSCHAFTEN (Dr. rer. nat.)

von der KIT-Fakultät für Physik des
Karlsruher Instituts für Technologie (KIT)
angenommene

DISSERTATION

von

Riccardo Ciola

Tag der mündlichen Prüfung:	19.12.2025
1. Referent:	Prof. Dr. Markus Garst (TFP)
2. Korreferenten:	Prof. Dr. Jörg Schmalian (TKM)

Multipolar magnon modes of the skyrmion lattice probed by magneto-optic and magneto-elastic coupling

To obtain the academic degree of

DOCTOR OF NATURAL SCIENCES (Dr. rer. nat.)

from the Department of Phyics at the
Karlsruhe Institute of Technology (KIT) accepted

DISSERTATION

by

Riccardo Ciola

Date of oral examination:	19.12.2025
1st examiner:	Prof. Dr. Markus Garst (TFP)
2nd examiner:	Prof. Dr. Jörg Schmalian (TKM)

Acknowledgments

This thesis marks an important step in a journey that began many years ago, when I used to take apart my brother's toys to understand how they worked, though I was never able to put them back together. That same curiosity has stayed with me ever since, driving me to seek not only new answers but, above all, new questions to explore. Along the way, this journey has been enriched by the many people I have met, whose guidance, friendship, and support have made it truly special, and to whom I now wish to extend my heartfelt thanks.

First and foremost, I would like to express my sincere gratitude to Prof. Markus Garst for his continuous support, enthusiasm, and guidance throughout these years. Our discussions have always been a source of reflection and inspiration. You have taught me never to take anything for granted and to approach research with both rigour and genuine curiosity. Your passion has inspired me to become a better scientist and a more thoughtful person.

I am deeply thankful to all my collaborators who have made these years so enriching. In particular, I wish to thank Dr. Volodymyr Kravchuk for his invaluable help and support, especially during the early stages of my PhD, and Dr. Ping Che for the stimulating and enjoyable work we shared. Your dedication and curiosity have been truly inspiring, and I will treasure both the scientific and personal lessons I learned from you.

I would also like to thank my colleagues for the many discussions, shared lunches, and moments of mutual support that made daily life in the office so enjoyable. A special thanks goes to Daniel, Lars, and Konrad for your patience, kindness, and constant willingness to help. My gratitude extends to all members of the Graduate School of Quantum Matter, with whom I shared stimulating discussions and countless evenings of fun, including many games of Werewolf. Karlsruhe has truly become a second home thanks to all of you.

I am especially grateful to my friends, near and far, for their constant encouragement and understanding. These years abroad have made me appreciate even more the strength of our friendships, which have never wavered despite the distance. You were always just a phone call or a few hours of FlixBus away. This achievement belongs to you as much as it does to me. In particular, my heartfelt thanks go to Aurora, for standing by my side through every challenge and adventure. You know better than anyone what this achievement means to me, and I am deeply grateful for your support and friendship.

I owe my gratitude to my parents and my brother, for their unconditional support and for helping me become the person I aspired to be. Your trust, encouragement, and love have been a constant source of strength throughout my life, and I could not have reached this point without you.

Finally, my deepest gratitude goes to Beatrice, to whom I dedicate this achievement. You have supported, encouraged, and loved me every single day, and none of this would have been possible without you. Thank you for every phone call, every weekend trip, and every little moment we spent together. I feel incredibly lucky to have you by my side, and your presence gives me the strength to face any challenge with a smile.

Abstract

Magnetic skyrmion lattices in noncentrosymmetric chiral magnets form regular hexagonal arrangements with lattice constants on the order of tens of nanometers. These topological periodic spin textures act as natural magnonic crystals, eliminating the need for challenging nano-fabrication and enabling bottom-up engineering of magnon band structures in the exchange-dominated spinwave regime. Such systems host a rich manifold of topological magnon bands with multipolar character and non-reciprocal dispersions. While low-energy excitations at small wavevector have been extensively investigated using microwave and optical spectroscopies, and excitations at large wavevector have been accessed through neutron scattering, the intermediate momentum regime, where the spinwave wavelength matches the lattice periodicity, remains largely unexplored. This regime is essential for understanding magnon propagation, hybridization, and interference in periodic magnetic textures, and is highly relevant for future magnonic applications. In this thesis, we investigate the spinwave dynamics at intermediate wavevectors in the chiral magnet Cu_2OSeO_3, focusing on the system's response to magneto-optic and magneto-elastic coupling within the skyrmion lattice phase. Two complementary experimental techniques are employed: micro-focused Brillouin light scattering (BLS) and ultrasonic pulse-echo spectroscopy. In the first study, we develop a general theoretical framework for analysing BLS spectra, which allows for the unambiguous identification of the magnon bands observed experimentally. Beyond the well-known dipolar counterclockwise, breathing, and clockwise modes, we identify two additional multipolar modes with quadrupole and sextupole character, respectively. By incorporating magneto-elastic coupling into our theoretical model, we further describe the collective hybrid excitations that emerge from the interplay between magnetic and elastic degrees of freedom. In particular, we analyse the hybridization between low-energy magnon modes and acoustic phonons induced by the noncentrosymmetric cubic crystal lattice. The comparison with the experimental data reveal an additional low-energy excitation with quadrupolar character. Furthermore, we study the opening of a phason gap governed by the strength of the magneto-elastic coupling. Together, these results advance the experimental and theoretical understanding of skyrmion lattice dynamics into previously inaccessible regimes and establish a foundation for future studies and applications of hybrid magnonic systems based on topological spin textures.

Contents

1 Introduction **1**

2 Theory of Chiral Magnets **5**

2.1 Chiral Magnets 5

2.1.1 Magnetic phase diagram 7

2.1.2 Magnetic skyrmions 10

2.1.3 Topological charge of magnetic skyrmions 12

2.2 Theoretical description 13

2.2.1 Ginzburg-Landau theory 14

2.2.2 Free energy of chiral magnets 16

2.2.3 Mean-field analysis 20

2.3 Linear σ model 24

2.3.1 Theoretical formulation in momentum space 26

2.3.2 Numerical implementation 28

3 Linear Spinwave Theory **33**

3.1 Landau-Lifshitz equation 33

3.2 Linear spinwave theory in chiral magnets 35

3.2.1 Magnon excitations in the field-polarised phase 36

3.2.2 Magnon excitations in the conical phase 38

3.3 Magnon excitations in the SkL phase 41

3.3.1 Momentum space formulation 42

3.3.2 Mode characterisation 46

3.3.3 Spectrum 50

3.3.4 Experimental observations 51

4 Theoretical description of Brillouin light scattering **55**

4.1 Magneto-optic coupling 55

4.1.1 Differential scattering cross section 56

4.1.2 Fluctuation-dissipation theorem 58

4.1.3 Spectral weights . . . 60
4.2 Theory of micro-focused BLS . . . 61
4.2.1 Experimental setup . . . 61
4.2.2 Electric field distribution . . . 63
4.2.3 Micro-focused BLS cross section . . . 66
4.2.4 Micro-focused BLS spectra . . . 69

5 Cryogenic micro-focused BLS in Cu_2OSeO_3 71
5.1 Experimental setup . . . 71
5.1.1 Magnon wavevectors domain . . . 73
5.1.2 Cooling procedure . . . 75
5.2 Zero-field cooling . . . 76
5.2.1 Field polarised phase . . . 76
5.2.2 Conical phase . . . 78
5.3 Field cooling . . . 79
5.3.1 Magnon bands structure . . . 81
5.3.2 Mode identification . . . 82
5.3.3 Conclusions . . . 85

6 Theory of magneto-elastic coupling 87
6.1 Linear elasticity theory . . . 88
6.1.1 Strain tensor . . . 88
6.1.2 Free energy functional . . . 89
6.2 Magneto-elastic coupling . . . 91
6.2.1 Coupling tensor . . . 92
6.2.2 Free energy analysis . . . 94
6.3 Skyrmion lattice phase . . . 95
6.3.1 Formulation in reciprocal space . . . 95
6.3.2 Equilibrium configurations . . . 100

7 Collective magneto-elastic dynamics in the skyrmion lattice phase 105
7.1 Phonon dynamics . . . 105
7.2 Unified magneto-elastic dynamics . . . 107
7.2.1 Linearisation . . . 108
7.2.2 Excitations in the SkL phase . . . 109
7.3 Spectrum . . . 111
7.3.1 Zero magneto-elastic coupling . . . 112
7.3.2 Hybridisation with dipole modes . . . 114

7.3.3 Hybridisation with quadrupole mode 116

8 Non-reciprocal phonon propagation along skyrmion strings 119

8.1 Ultrasonic pulse-echo measurements 119

8.1.1 Experimental setup 120

8.1.2 Results 121

8.1.3 Discussion 123

8.2 Phason mode in the skyrmion lattice phase 127

8.2.1 Phason gap 128

9 Conclusions and Outlook 131

A Appendix: Spinwave time evolution 135

B Bibliography 141

C List of Figures 155

1 Introduction

Motivation

Spin waves describe the collective precession of localized magnetic moments in magnetically ordered materials and can be viewed as the magnetic counterparts of sound or light waves in their respective media. This classical concept was first introduced by F. Bloch [1, 2] and later refined by Holstein & Primakoff [3] and Dyson [4], who established the theoretical foundations of spinwave theory. Magnons are the quanta of spin waves and act as bosonic quasiparticles that carry spin and angular momentum without implying electric charge transport. Their dual nature enables, for example, the excitation and propagation [5], reflection and refraction [6–8], interference and diffraction [9–11] of spinwaves and even Bose–Einstein condensation of magnons [12].

The field of magnonics has developed from this foundation into a rapidly growing research area that seeks to harness spin waves for the transmission and manipulation of information [13–15]. Unlike charge-based electronics, where resistive losses and Joule heating limit efficiency and speed, magnonics offers a route toward low-power and high-frequency signal processing. Spinwave amplitudes and phases can encode information, and their mutual interference can implement logic operations, all without the motion of charge carriers. Recent experimental and technological progress has considerably advanced the capabilities of magnonics. Reliable and efficient excitation and detection schemes, including spin-torque oscillators [16], spin-Hall effect-based antennas [17, 18], and magneto-optical probes [14, 15], now enable the generation and manipulation of magnons with wavelengths as short as a few tens of nanometers and frequencies extending into the gigahertz and terahertz regimes. The continuous improvement of magnetic materials with low Gilbert damping, such as yttrium iron garnet and certain chiral magnets, has allowed coherent spinwave propagation over macroscopic distances. At the same time, advances in nanofabrication and patterning have enabled the realization of complex magnonic circuits integrating multiple elements for wave-based computation, frequency multiplexing, and even neuromorphic or reservoir computing [19–22]. These developments are motivated by the search for efficient and sustainable alternatives to CMOS technology, particularly in view of the growing energy demands associated with

artificial intelligence and data processing.

Spin waves in periodic magnetic structures, often referred to as magnonic crystals, exhibit band structures similar to those found in photonic or phononic systems, with frequency gaps and dispersions determined by the underlying periodicity [23]. By engineering such periodic modulations, one can design magnon band structures with tailored group velocities, bandgaps, and even nontrivial topological properties. This capability enables the realization of chiral edge modes that propagate without backscattering, offering a pathway to robust magnonic transport and topological spinwave devices. Traditionally, magnonic crystals have been fabricated through lithographic patterning that imposes artificial periodic variations in material parameters such as magnetization, anisotropy, or exchange stiffness. While highly versatile, these top-down approaches are limited by fabrication complexity and spatial resolution, motivating the exploration of self-organized or emergent magnetic superstructures as naturally periodic platforms for magnonic phenomena.

An especially promising example of such emergent periodic systems is provided by magnetic skyrmion lattices. Skyrmions are topologically nontrivial, nanoscale spin configurations stabilized by the competition between symmetric exchange interactions and antisymmetric Dzyaloshinskii–Moriya interactions (DMI) in noncentrosymmetric magnets. Each skyrmion corresponds to a swirling spin texture in which the magnetization wraps the unit sphere exactly once, endowing it with a quantized topological charge (*see Section 2.1.2*). Under suitable magnetic field and temperature conditions, these skyrmions condense into a regular hexagonal lattice with lattice constants typically between 50 and 100 nanometers. The existence of skyrmions was first predicted theoretically by Bogdanov and collaborators in the early 1990s [24–26] and later confirmed experimentally in the chiral magnet MnSi through small-angle neutron scattering [27]. Soon after, similar skyrmion phases were discovered in materials such as FeGe and Cu_2OSeO_3, as well as in ultrathin films with interfacial DMI [28–36]. These discoveries gave rise to the field of skyrmionics, which investigates the creation, manipulation, and dynamics of skyrmions for both fundamental studies and potential technological applications [37].

The skyrmion lattice can thus be understood as a self-organized, reconfigurable magnonic crystal which provides a unique environment for studying spinwave dynamics in the exchange-dominated regime [38]. Its periodic, noncollinear magnetisation acts as a naturally modulated potential for magnons, resulting in a complex magnonic band structure characterised by nonreciprocal dispersion induced by the lack of inversion symmetry [39]. Moreover, its topological nature is reflected in a non-trivial reciprocal-space topology of the magnon bands, which generates magnonic edge states exhibiting unique transport phenomena, such as the magnon Hall effect [40–44]. The intricate nature of the skyrmion lattice configuration leads to a rich magnonic band structure, characterised by a plethora of multipolar excitation

modes [39, 45].

Experimentally, the spinwave dynamics of skyrmion lattices have been investigated through a range of spectroscopic techniques. Wave-guide microwave spectroscopy provides access to zero-wavevector excitations, revealing the characteristic triplet of counterclockwise, breathing, and clockwise modes [46–51]. Complementary methods such as resonant elastic x-ray scattering [52] and time-resolved magneto-optical measurements [53, 54] have confirmed these resonances in the close vicinity of the Γ-point. More recently, inelastic neutron scattering was employed to observe the corresponding finite-wavevector dynamics, extending the accessible region of the magnon dispersion [43].

Despite this progress, our understanding of the full magnonic spectrum in skyrmion lattices remains incomplete. Experimental access is constrained by selection rules and by the limitations of conventional probes. Microwave spectroscopy is restricted to dipole-active excitations at vanishing wavevector, while neutron scattering, though capable of reaching large momentum transfers, typically averages over many modes and cannot resolve individual bands. The intermediate regime, where the magnon wavelength is comparable to the lattice constant, is particularly challenging. Yet this regime is of crucial importance for magnonic applications, as it governs the propagation and interference of magnons in naturally periodic textures and determines how information could be processed or transmitted within such systems.

In this Thesis, we aim to narrow this gap by presenting two complementary studies that advance beyond the current state of the art. The first study employs magneto-optic coupling to investigate spinwave dynamics at wavelengths comparable to the inter-skyrmion distance. Using micro-focused Brillouin light scattering, we identify different multipolar excitation modes over a broad range of magnetic fields. The second study explores the influence of magneto-elastic coupling within the skyrmion lattice phase. In this regime, spin waves interact with acoustic phonons at finite wavevectors, leading to the emergence of magnon–phonon hybrid modes. Ultrasonic velocity measurements reveal clear evidence of this interaction, providing indirect access to a low-energy multipolar magnon mode. Together, these investigations extend the understanding of skyrmion lattice dynamics into new regimes, effectively linking conventional experimental techniques with prospective magnonic applications.

Thesis outline

The Thesis is organised as follow: **Chapter 2** introduces the magnetic phase diagram of chiral magnets and develops the mean-field description of isotropic chiral magnets within the Ginzburg–Landau framework. Special emphasis is placed on the stabilization and properties of the skyrmion lattice configuration, which forms the central focus of this work. **Chapter 3** examines the spinwave dynamics within the magnetically ordered phases of chiral magnets. The analysis is based on the lossless Lan-

dau–Lifshitz equation, which describes the dynamical response of the local magnetization to external perturbations and provides the theoretical foundation for the subsequent studies of magnon excitations. **Chapter 4** presents the theoretical formulation of micro-focused Brillouin light scattering (BLS) spectroscopy mediated by magneto-optic coupling. The model developed here offers a general description applicable to various experimental configurations and fills a gap in the existing literature by providing a systematic approach to interpret micro-focused BLS data. **Chapter 5** reports experimental results of finite-wavevector spinwave spectroscopy across multiple magnetic phases of Cu_2OSeO_3, obtained using micro-focused BLS. These measurements reveal two previously unobserved multipolar magnon bands in the skyrmion lattice phase, extending the understanding of the complex magnonic spectrum of this system. **Chapter 6** introduces magneto-elastic coupling in chiral magnets and investigates its impact on the equilibrium properties of the skyrmion lattice. Mean-field solutions of the coupled magneto-elastic system are derived by minimizing the Ginzburg–Landau free energy functional, exploring the interplay between magnetic and elastic degrees of freedom. **Chapter 7** examines how magneto-elastic coupling modifies the collective excitations of the skyrmion lattice. In particular, it demonstrates how this coupling gives rise to hybridization between spinwave and acoustic phonon modes, leading to the formation of magnon–phonon hybrid excitations. **Chapter 8** presents an experimental study of the phonon magneto-chiral effect in the skyrmion lattice phase, investigated through ultrasonic pulse-echo measurements. The observed modifications in the phonon velocity provide indirect evidence of a low-energy multipolar magnon mode. Furthermore, the chapter discusses the behaviour of the phason mode and the emergence of a phason gap in the presence of magneto-elastic coupling. Finally, **Chapter 9** summarizes the main findings of this work and outlines potential directions for future research, particularly in the context of understanding the spinwave dynamics in topological magnetic textures for future applications in the field of magnonics.

2 Theory of Chiral Magnets

In this Chapter, we review the rich magnetic phase diagram of chiral magnets. We begin by introducing the variety of ordered magnetic phases that emerge below the critical temperature T_c, highlighting the energetic mechanisms that stabilise their characteristic non-collinear spin textures. Subsequently, we develop the mean-field description of isotropic chiral magnets within the Ginzburg–Landau formalism, including the effects of dipolar interactions. This approach provides a unified framework to capture the essential features of the different magnetic states and to analyse their relative stability. Finally, we focus on the magnetic skyrmion lattice phase, where we describe the numerical procedure employed to minimise the Ginzburg–Landau free energy functional and obtain the equilibrium spin configuration. The results presented here serve as a foundation for the theoretical analysis presented in the subsequent Chapters.

2.1 Chiral Magnets

Magnetism in solid-state systems is a macroscopic manifestation of the quantum mechanical interactions between electron spins. One of the most fundamental models used to describe magnetic ordering in insulating systems is the Heisenberg model [55, 56], which captures the exchange interaction between localized spins on a lattice. In its simplest form, the Hamiltonian for a Heisenberg (anti-)ferromagnet is given by [57]

$$\mathscr{H}_{\text{Heisenberg}} = -J \sum_{\langle i,j \rangle} \mathbf{S}_i \cdot \mathbf{S}_j \,, \tag{2.1}$$

where $\mathbf{S}_i$ and $\mathbf{S}_j$ are classical or quantum spin vectors located at sites i and j, respectively, and the sum runs over nearest-neighbour pairs. The exchange constant J determines the nature of the spin alignment: $J > 0$ favours ferromagnetic order, i.e., parallel alignment, while $J < 0$ leads to antiferromagnetic order, i.e., antiparallel alignment. This isotropic exchange interaction respects both time-reversal and spatial inversion symmetries and thus favours collinear spin arrangements. However, in materials lacking inversion symmetry, either due to their bulk crystal structure or at interfaces, an additional antisymmetric exchange interaction can arise [58–61]. An important example of this is represented by the Dzyaloshin-

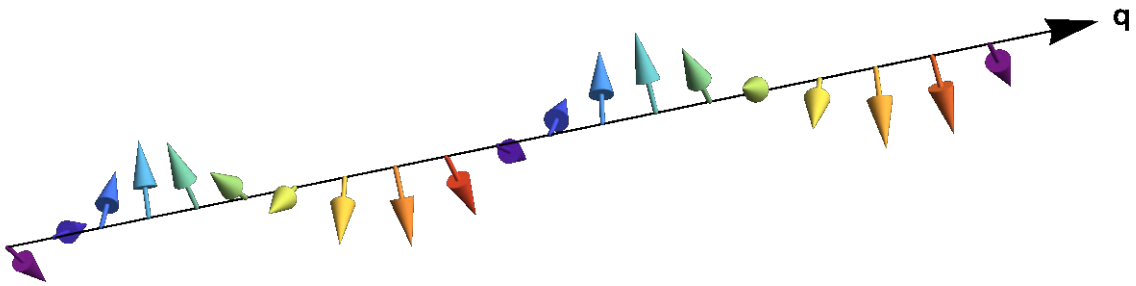

Figure 2.1.: **Helix configuration.** The competition between Heisenberg and Dzyaloshinskii–Moriya interaction stabilises noncollinear spin textures. In the helical phase, the magnetization winds around **q**, the propagation vector denoted by the black arrow in the Figure, and is perpendicular to it.

skii–Moriya interaction (DMI), which plays a fundamental role throughout the rest of this dissertation. First proposed by Dzyaloshinskii (1958) [62] and microscopically justified by Moriya (1960) [63] using spin–orbit coupling considerations, the DMI takes the form

$$\mathscr{H}_{\mathrm{DMI}} = \sum_{\langle i,j \rangle} \mathbf{D}_{ij} \cdot (\mathbf{S}_i \times \mathbf{S}_j) \,, \tag{2.2}$$

where $\mathbf{D}_{ij}$ is the Dzyaloshinskii–Moriya vector, whose direction and magnitude are determined by the details of the crystal symmetry and spin–orbit coupling. Unlike the Heisenberg term, the DMI explicitly breaks inversion symmetry and favours noncollinear, twisted spin textures with a well-defined sense of rotation.

This intrinsic asymmetry gives rise to chirality in the magnetic configuration. In a chiral magnet, spin structures such as helices, cycloids, and skyrmions exhibit a fixed handedness, left- or right-handed, dictated by the orientation of $\mathbf{D}_{ij}$ [64–66]. To understand the effect of the DMI more intuitively, consider a simple one-dimensional spin chain shown in Fig. 2.1. The Heisenberg term tries to align neighboring spins, while the DMI prefers them to be perpendicular with a particular handedness. The competition between these two interactions leads to helical configurations, in which the direction of the spin vector rotates along the chain. The resulting ground state is a noncollinear and chiral magnetic structure. Here, the term chirality refers to the geometrical property that the spin configuration cannot be superimposed on its mirror image by any combination of rotations and translations. In the case of a helical spin texture, this manifests as a handedness of the rotation: spins may rotate in a right-handed or left-handed fashion as one moves along the helix axis. The sign of the DMI determines which chirality is energetically favoured.

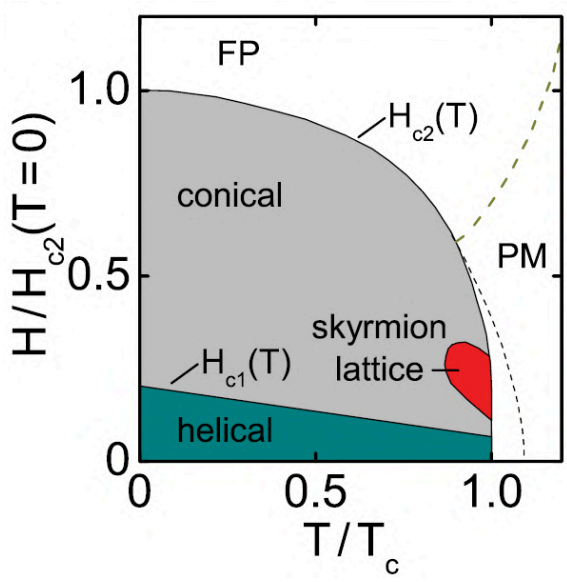

Figure 2.2.: **Qualitative magnetic phase diagram of the cubic chiral helimagnets.** Magnetic phase diagram as a function dimensionless temperature and applied magnetic field. T_c indicates the transition temperature between the disordered paramagnetic phase and the helical configuration in the absence of external fields. The critical field H_{c2} denotes the phase transition between the conical and the field-polarised states. The phase diagram is taken from Ref. [39].

2.1.1 Magnetic phase diagram

Chiral magnets present a rich platform for exploring the interplay of symmetry, topology, and spin dynamics [13, 15, 67–69]. The competition between the Heisenberg exchange, DMI, external fields and anisotropies can stabilize a wide variety of nontrivial spin textures, many of which are of significant interest for both fundamental physics and technological applications such as magnonics and novel computing [15, 22, 23, 37]. Examples of such materials include the metallic compound MnSi [70] and the insulating oxide Cu_2OSeO_3 [71] . Both crystallise in a cubic lattice structure known as the B20 structure [72], with symmetry transformations described by the space group $P2_13$. The point symmetry group at the component sites is C_3, the cyclic group of 3-fold $2\pi/3$ rotations about an appropriate [111]-axis. The nonsymmorphic group $P2_13$ contains in addition 3 screw rotations which involve 2-fold rotations about one of the three [100]-axis followed by an appropriate non-primitive translation $(0, 1/2, 1/2)$. It is worth noticing that the list of symmetry transformations does not include inversion, which makes the B20 compounds a suitable candidate for exploring noncollinear spin textures in the bulk. In this Thesis, we focus primarily on the insulating material Cu_2OSeO_3, presenting a series of experiments investigating its dynamical properties. In fact, due to its relatively low magnetic damping [49], this material represents the ideal platform for the study of magnon dynamics [39, 48, 50, 51, 73–76].

Fig. 2.2 shows the typical phase diagram corresponding to noncentrosymmetric cubic helimagnets as a function of temperature and applied magnetic field [27, 30, 77]. At high temperatures, the system is in a

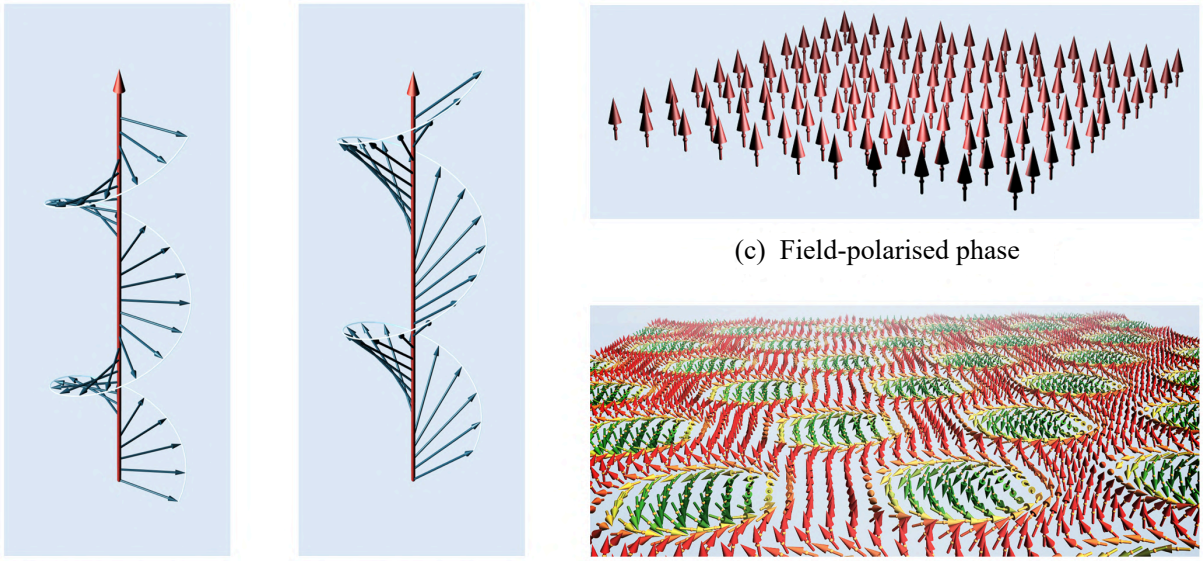

(a) Helical phase (b) Conical phase (c) Field-polarised phase (c) Skyrmion lattice phase

Figure 2.3.: **Magnetically ordered phases in chiral magnets.** Picture taken from Ref. [78]

paramagnetic state, where local magnetization points in arbitrary directions, and the net-magnetization is zero. Below its magnetic ordering temperature T_c , the material exhibits several distinct magnetic phases, whose stability is governed by different competing energy terms: symmetric Heisenberg exchange, anti-symmetric Dzyaloshinskii–Moriya interaction, Zeeman energy due to applied magnetic fields, and crystalline anisotropies.

Helical phase

At low applied magnetic fields and temperatures below T_c, cubic helimagnets enter a helical phase [59, 60, 79]. In this regime, the dominant ferromagnetic exchange interaction favours collinear spin alignment, while the DMI promotes canting of neighboring spins with a fixed handedness. The competition between these two interactions results in a long-wavelength spin spiral, or helix, where the magnetization rotates in a plane perpendicular to the propagation vector $\mathbf{q}$ (Fig. 2.3**a**). In the continuos approximation, the helix pitch is fixed by the ratio between the DMI and the exchange strength. This quantity plays a fundamental role in describing the different configurations of standard bulk chiral magnets. In fact, it determines the typical length scale of the spatial modulation of all the non-collinear spin textures arising in the ordered magnetic phases. In Cu_2OSeO_3, the helix pitch is approximately $2\pi/Q \approx 62$nm [48, 75], where we introduced the characteristic wavevector $Q = D/J$. The direction of $\mathbf{q}$ is determined by the weak cubic crystalline anisotropy, which selects the $[100]$ axes as easy propagation directions [80]. In this phase, the system spontaneously breaks rotational symmetry, and multiple helical domains with different $\mathbf{q}$ orientations may coexist.

Conical phase

When the applied magnetic field reaches the critical value H_{c1}, the system transitions from the helical phase into the conical phase. In this configuration, the magnetization spirals around the field direction, forming a cone with its axis aligned along $\mathbf{H}^{\text{ext}}$, as shown in Fig. 2.3**b**. The cone angle decreases with increasing field strength, reflecting the increasing influence of the Zeeman energy, which favours alignment of spins with the external field. This angle θ is determined according to

$$M_s \cos\theta = \chi_{\text{con}} H\,, \tag{2.3}$$

where M_s indicates the saturation magnetisation and χ_{con} is the magnetic susceptibility in the conical phase. χ_{con} can be determined from the internal magnetic field $\mathbf{H}^{\text{int}}$, which depends on the macroscopic sample shape via the demagnetisation field $\mathbf{H}^{\text{dem}} = \mathbf{H}^{\text{int}} - \mathbf{H}^{\text{ext}}$. Therefore, a shape independent magnetic susceptibility can be defined via

$$\chi_{\text{con}}^{\text{int}} = \frac{1}{\chi_{\text{con}}^{-1} - N_z}\,, \tag{2.4}$$

where N_z is the demagnetisation factor corresponding to a principal axis along the applied field direction. In Cu_2OSeO_3, the internal magnetic susceptibility is $\chi_{\text{con}}^{\text{int}} = 1.76$ [48]. The conical phase preserves the chiral twisting favoured by DMI while partially accommodating the field-induced polarization, representing a compromise between DMI, exchange, and Zeeman energy contributions.

Field-polarised (FP) phase

At high magnetic fields, the Zeeman energy dominates all other interactions, leading to a transition into the field-polarised (FP) phase, in which all spins are aligned parallel to the external field (Fig. 2.3**c**). This configuration is reached for the critical field $H_{c2} = M_s/\chi_{\text{con}}$, which corresponds to a degenerate cone angle according to Eq. (2.3). We can express the internal critical field value in terms of the magnetic susceptibility and saturation magnetisation as $\mu_0 H_{c2}^{\text{int}} = \mu_0 M_s/\chi_{\text{con}}^{\text{int}}$, with μ_0 being the vacuum magnetic permeability. The value of this critical field in Cu_2OSeO_3 depends on the temperature and the direction of the applied field, and it is on the order of 50 mT for low temperatures $T \ll T_c$, with $T_c \simeq 57$ K [30]. Despite being dominated by Zeeman interaction, the system does not behave as a standard ferromagnet. In particular, its low-energy excitation frequency is influenced by the chirality of the crystal lattice.

High-temperature skyrmion lattice (HT-SkL) phase

In a narrow region of the phase diagram, just below T_c and for intermediate magnetic fields, cubic chiral magnets can stabilise a skyrmion lattice phase, also referred to in the literature as the A-phase. This configuration was originally predicted by A. N. Bogdanov and collaborators in the late 1980s and early 1990s [24–26], and later experimentally found in the metallic compound MnSi by Mühlbauer *et al.* [27]. Since then, this phase has been observed in different noncentrosymmetric cubic magnets [28–36], establishing a new field of research at the intersection of magnetism, topology, and spintronics. Here, the

system forms a periodic array of magnetic skyrmions: topologically nontrivial spin configurations with quasi-particle character in which the magnetization whirls forming a vortex-like structure, as illustrated in Fig. 2.3**d** (*see next Section for more details*). In the lattice phase, these skyrmions organise into a hexagonal arrangement in the plane perpendicular to the applied magnetic field. The lattice constant weakly depends on the applied magnetic field, and it is of the same order of magnitude as the inverse of the helix pitch Q. The stability of the skyrmion lattice arises from the interplay between exchange, DM, Zeeman interactions, and thermal fluctuations. In fact, near the ordering temperature, thermal fluctuations become relevant and can entropically stabilise the skyrmion phase over the competing conical or helical states [27]. Additionally, in Cu_2OSeO_3 weak magnetocrystalline anisotropy and dipolar interactions play a role in locking the orientation and symmetry of the skyrmion lattice [81, 82].

The resulting magnetic phase diagram is highly sensitive to temperature, magnetic field orientation, and sample history, reflecting the finely tuned energetic balance describing the system. Moreover, Cu_2OSeO_3 showed evidence of two additional phases that can be stabilised under specific conditions: the **low-temperature skyrmion lattice (LT-SkL) phase** and the **tilted conical phase** [80, 83–87]. Both of these noncollinear spin texture configurations arise in the low-temperature regime due to the relatively strong magnetocrystalline anisotropies in this material [84]. The LT-SkL phase represents an additional SkL phase with similar properties, but it is distinguished by a different stabilisation mechanism: rather than being entropically driven, its stability arises from competing energy contributions at the mean-field level. The tilted conical phase emerges when the magnetic field is applied along a low-symmetry direction, i.e., not along the crystal principal axes [100]. Here, the propagation vector $\mathbf{q}$ of the spin spiral is not perfectly aligned with the applied field, and it is tilted towards the crystal easy axes in order to lower the magnetocrystalline anisotropy contribution.

In addition to the stable configurations presented in the phase diagram, the topological nature of the skyrmion lattice phase enables the realisation of robust, topologically protected meta-stable phases characterised by a long lifetime [76, 87–89]. For example, for low magnetic fields applied along specific directions, the system can realise an **elongated skyrmion lattice (eSkL) phase** [51]. Here, the triangular magnetic lattice and the circular shape of the skyrmions are distorted to lower the energetic contribution coming from the magnetocrystalline anisotropy, in analogy with the tilted conical phase.

2.1.2 Magnetic skyrmions

The concept of skyrmion originates from high-energy physics and dates back to the pioneering work of Tony Skyrme in the early 1960s [90, 91]. In these papers, Skyrme introduced a nonlinear field theory in which baryons emerge as topological solitons of a continuous pion field. His model, now known as the Skyrme model, was constructed to describe baryons as stable field configurations within a relativistic Lagrangian that includes both quadratic and quartic gradient terms to prevent collapse of the soliton

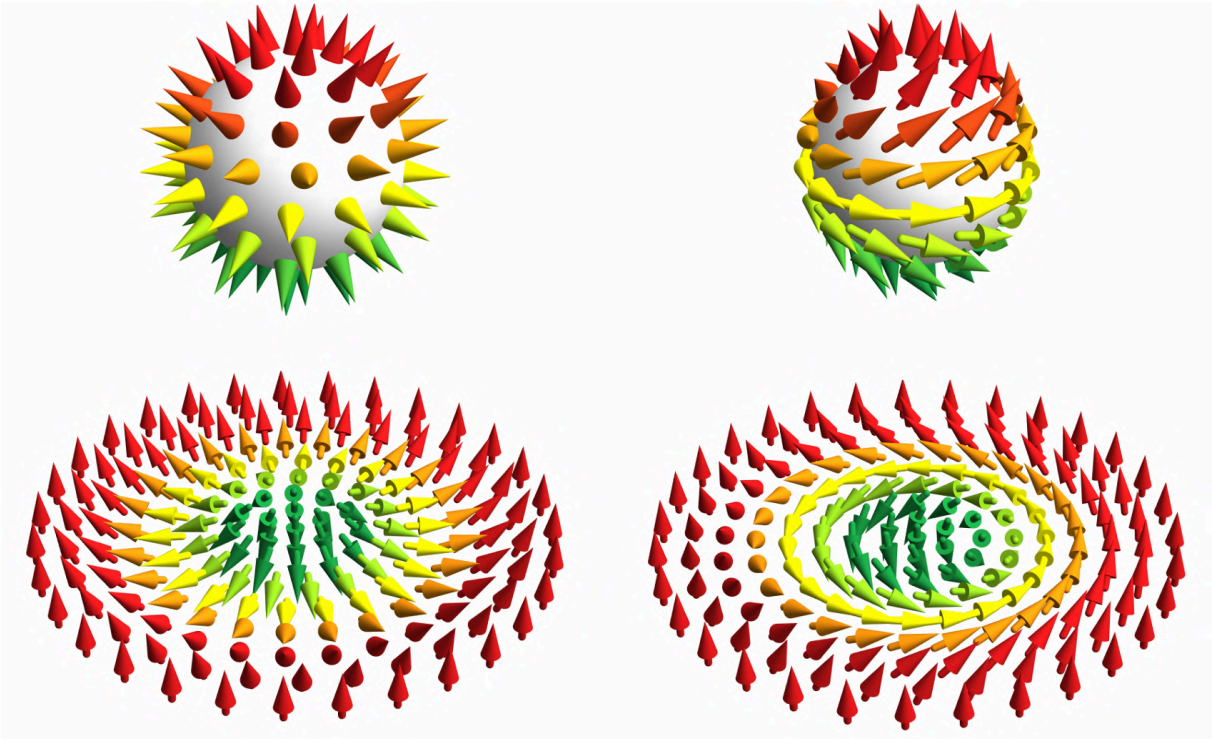

Néel-type skyrmion Bloch-type skyrmion

Figure 2.4.: **Stereographic projection of (baby) skyrmions.** The south pole of the sphere is mapped onto the origin of $\mathbb{R}^2$, while the north pole corresponds to infinity. By introducing the transformation $\rho \mapsto \tan^{-1}(\rho)$, the infinite plane $\mathbb{R}^2$ can be compactly represented on a finite disk, where ρ denotes the radial distance from the origin. The configurations shown on the left and right correspond to Néel-type and Bloch-type skyrmions, respectively. The figure is adapted from Ref. [78].

solutions. The resulting configurations, dubbed skyrmions, are characterized by a nontrivial winding number, corresponding to the conserved baryon number in the model. Mathematically, the Skyrme field is a mapping from three-dimensional space into a target manifold, typically $SU(2) \cong S^3$. The topological stability of the soliton is guaranteed by the nontrivial third homotopy group $\pi_3(S^3) = \mathbb{Z}$, which classifies field configurations by an integer-valued topological charge, interpreted as the baryon number.

Though originally proposed in the context of particle physics, the skyrmion concept gradually found relevance in other areas of physics, including condensed matter, due to its universal topological properties [92–94]. A particularly important development came with the so-called baby skyrmion: a simplified two-dimensional analog of the original three-dimensional skyrmion, which emerges in nonlinear sigma models defined on a two-dimensional plane. In this case, the order parameter field $\mathbf{n}(\mathbf{r})$ maps points in the plane $\mathbb{R}^2$ to a unit sphere S^2, and the solitonic solutions are classified by the second homotopy group $\pi_2(S^2) = \mathbb{Z}$, which again ensures topological protection [95]. The baby skyrmion model serves as a particularly useful theoretical playground for studying the general properties of topological soli-

tons, such as their energetics, interactions, and dynamics [39, 68, 69]. This theoretical framework laid the groundwork for understanding magnetic skyrmions in chiral magnets, where the local magnetization vector $\mathbf{M}(\mathbf{r})$ plays the role of the order parameter field. In these systems, a magnetic skyrmion can be viewed as a smooth, topologically nontrivial spin configuration in which the magnetization vector wraps the unit sphere exactly once over space, thus realizing a baby skyrmion in a real magnetic material. Fig. 2.4 illustrates the stereographic projection of such vector field from the unit sphere to the target plane, namely $S^2 \to \mathbb{R}^2$. This is shown for two magnetic skyrmion configurations: Néel type (left) and Bloch type (right) respectively, which are obtained from different Dzyaloshinskii–Moriya vectors.

2.1.3 Topological charge of magnetic skyrmions

One of the most fundamental features of magnetic skyrmions is their topological nature, which imparts a form of robustness to their structure. This topological protection arises from the fact that skyrmions are characterized by a nontrivial topological invariant, i.e., a quantity that remains unchanged under continuous deformations of the magnetization field [69].

The continuous classical magnetisation $\mathbf{M}(\mathbf{r})$ can be used to define the vector field

$$\hat{n}(\mathbf{r}) = \frac{\mathbf{M}(\mathbf{r})}{|\mathbf{M}(\mathbf{r})|}, \qquad \hat{n} : \mathbb{R}^2 \to S^2 \tag{2.5}$$

where $\hat{n}(\mathbf{r}) \in S^2$ is a unit vector indicating the local direction of the magnetization. For isolated skyrmions or skyrmion lattices embedded in a uniform magnetic background, the boundary condition is typically

$$\lim_{|\mathbf{r}|\to\infty} \hat{n}(\mathbf{r}) = \hat{n}_0, \tag{2.6}$$

where $\hat{n}_0$ is a constant unit vector usually aligned with the external magnetic field. It is worth noticing that here $\mathbf{r} = (x, y)^T$ is a 2-dimensional vector since we defined the baby skyrmion through the stereographic projection onto the plane $\mathbb{R}^2$.

This effectively compactifies the spatial plane $\mathbb{R}^2$ into a two-sphere S^2, allowing the field configuration to be interpreted as a mapping $\hat{n} : S^2_{\text{space}} \to S^2_{\text{spin}}$. Such maps are classified by the second homotopy group $\pi_2(S^2) = \mathbb{Z}$, meaning each configuration is labelled by an integer topological charge, or skyrmion number Q_{top}, defined as [96]

$$Q_{\text{top}} = \frac{1}{4\pi} \int_{\mathbb{R}^2} \hat{n} \cdot (\partial_x \hat{n} \times \partial_y \hat{n})\, dx\, dy. \tag{2.7}$$

This quantity counts the number of times the magnetization vector wraps the unit sphere as one traverses the spatial plane. This can be used to derive a classification of spin structures based on their topology [95]. The integrand of the topological charge, sometimes referred to as the topological density,

$$q(\mathbf{r}) = \frac{1}{4\pi}\hat{n}\cdot(\partial_x\hat{n}\times\partial_y\hat{n})\,, \tag{2.8}$$

can be used to visualize the spatial distribution of the topological charge in a given configuration. It is often sharply peaked at the center of a skyrmion and decays rapidly away from it.

This topological classification has profound physical implications. First, it leads to quantized and emergent electromagnetic phenomena, such as the topological Hall effect, which arises due to the real-space Berry curvature induced by the non-coplanar spin texture [39–43, 69]. Second, it implies that skyrmions cannot be continuously transformed into the trivial vacuum state without passing through a singular configuration, thus endowing them with a form of topological protection. This mechanism enables to explore a wide range of meta-stable configurations in the magnetic phase diagram presented in Fig. 2.2. For example, the high-temperature skyrmion lattice phase in Cu_2OSeO_3 can be quenched by applying a constant magnetic field while rapidly decreasing the temperature. This results in a meta-stable skyrmion lattice configuration with the same properties as the original phase, and which is made robust due to its topological nature [50, 88]. Moreover, the topological charge plays a central role in the dynamics of skyrmions. For example, in the Thiele equation that describes the collective motion of a skyrmion, the gyrotropic force is directly proportional to Q_{top}. This causes skyrmions to exhibit a transverse deflection, the so-called skyrmion Hall effect, when subjected to external currents or gradients [97].

2.2 Theoretical description

The magnetic phase diagram discussed in the previous Section arise from the interaction between electron spins localised on the atomic crystal lattice. Nevertheless, the noncollinear spin textures that are stabilised in this context posses a characteristic length scale $2\pi/Q$ that governs the spatial variation of the magnetisation. In bulk chiral magnets, this quantity is typically on the order of tens to hundreds of nanometers, that is much larger than the atomic lattice spacing. This pronounced separation of length scales justifies a coarse-grained, continuum description of the magnetisation. Instead of treating individual spins, we describe the system in terms of a continuous classical field $\mathbf{M}(\mathbf{r},t)$, which represents the local magnetisation vector at position $\mathbf{r}$ and time t. This approach allows us to capture the long-wavelength behaviour of the magnetic textures and is especially well-suited for describing their energetics, dynamics, and topological properties. In particular, we describe the system via a Ginzburg–Landau model, which provides the theoretical framework for most of the calculations presented in this dissertation.

2.2.1 Ginzburg-Landau theory

The Ginzburg-Landau theory is a powerful phenomenological framework originally developed to provide a continuum description of phase transitions in the context of superconductivity. Its generality, however, has made it a foundational tool across many branches of condensed matter physics, including magnetism [98]. The model is based on the existence of a critical temperature, T_c, and an order parameter that is non-zero in the ordered phase, i.e. for $T < T_c$, and which becomes zero when increasing the temperature above its critical value. Moreover, the continuous character of the phase transition ensures that the order parameter must be small in the vicinity of the critical temperature. The thermodynamic equilibrium of the system is reached for the configuration that minimises the dimensionless free energy of the system G. This quantity can be calculated from the standard partition function via

$$Z = e^{-G} = \int \mathscr{D}\mathbf{M}\, e^{-F[\mathbf{M}]}, \tag{2.9}$$

with $F[\mathbf{M}]$ being the free energy functional depending on the order parameter $\mathbf{M}(\mathbf{r})$. The free energy can be computed in the mean-field approximation with respect to the local magnetisation

$$G \simeq \min_{\mathbf{M}(\mathbf{r})} \mathrm{F}[\mathbf{M}] = \mathrm{F}[\mathbf{M}^{\mathrm{mf}}], \tag{2.10}$$

where the stationary solution $\mathbf{M}^{\mathrm{mf}}(\mathbf{r})$ satisfies the mean-field equation

$$\left.\frac{\delta F[\mathbf{M}]}{\delta \mathbf{M}}\right|_{\mathbf{M}^{\mathrm{mf}}} = 0. \tag{2.11}$$

In this Chapter, we present the free energy functional corresponding to the standard chiral magnet, and derive the corresponding mean-field solutions. As mentioned in the previous Section, these correspond to the helical/conical configurations, which minimise the free energy in the entire region of the phase diagram where a spatially modulated spin texture is favoured. In the absence of magnetocrystalline anisotropies, a mean-field solution for the SkL phase is found only as a local minima of the system. However, corrections beyond the mean-field approximation can be obtained by including thermal Gaussian fluctuations around the mean-field minimum

$$G \simeq F[\mathbf{M}^{\mathrm{mf}}] + \frac{1}{2} \ln \det \left(\frac{\delta^2 F}{\delta \mathbf{M}\, \delta \mathbf{M}} \right) \Bigg|_{\mathbf{M}^{\mathrm{mf}}}. \tag{2.12}$$

Mühlbauer *et al.* [27] showed that this first order correction term is sufficient to find a region where the topologically non-trivial SkL phase is favoured even for isotropic chiral magnets.

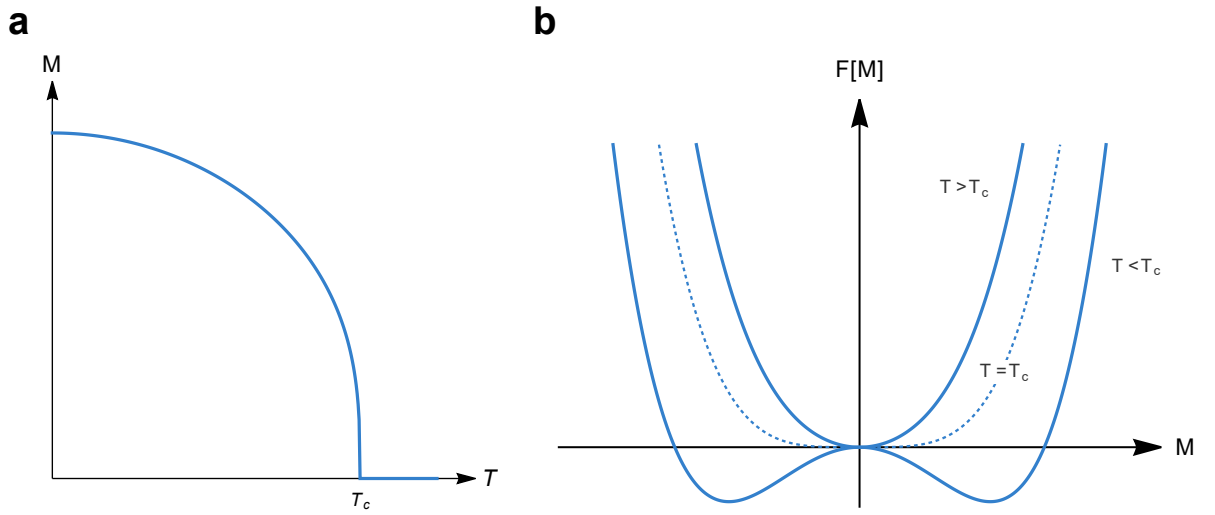

Figure 2.5.: **Mean-field description of a ferromagnetic phase transition.** (**a**) Schematic temperature dependence of the homogeneous magnetisation **M**. (**b**) Sketch of the mean-field free energy functional around the second order phase transition.

Example : standard ferromagnet

Here, we start by analysing an introductory example represented by the standard ferromagnet, which can be found in many textbooks, such as in Refs. [55, 56, 98]. Fig. 2.5**a** illustrates the typical temperature versus applied magnetic field phase diagram. Below the critical temperature T_c, the system is in its ordered phase and is characterised by the uniform magnetisation **M**, which is given by thermal average of the microscopic spins. This quantity changes continuously across the critical temperature and vanishes in the paramagnetic phase, i.e., for $T > T_c$. This second order phase transition can be described using Ginzburg-Landau theory and identifying **M** as the order parameter. Consequently, there must exist a free energy functional $F[\mathbf{M}]$ which satisfies the fundamental symmetries of the system. Moreover, in the low-energy limit, fast fluctuations of the magnetic moments are suppressed, and therefore one additionally expands F in derivatives of the local magnetization $\mathbf{M}(\mathbf{r})$. In the absence of an applied magnetic field and magnetocrystalline anisotropy, the system is invariant under time-reversal symmetry and under rotation of all spins. Therefore, the Ginzburg-Landau free energy functional for a conventional, inversion-symmetric ferromagnet is given by

$$F[\mathbf{M}] = \int d\mathbf{r} \left(r_0 \mathbf{M}^2 + J(\nabla \mathbf{M})^2 + U\mathbf{M}^4 - \mu_0 \mathbf{H} \cdot \mathbf{M} \right). \tag{2.13}$$

Here, r_0, J, and U are phenomenological parameters determined by the microscopic theory of the system. For a ferromagnet, J is positive and favours the alignment of all microscopic spins. The quartic term is responsible for the stability of the system, therefore the prefactor U must be positive. Lastly, r_0 is free to change its sign as a function of temperature, thus we consider the linear expansion $r_0(T) = a(T - T_c^{\mathrm{mf}}) + \mathscr{O}\left((T - T_c^{\mathrm{mf}})^2\right)$ with a prefactor $a > 0$. T_c^{mf} indicates the mean-field critical tem-

perature, i.e., without considering thermal fluctuations and non-linear contributions.

For zero applied magnetic field, the Ginzburg-Landau free energy functional in Eq. (2.13) is minimised by a homogeneous magnetisation configuration, i.e., for $\partial_i \mathbf{M} = 0$, with $i = x, y, z$. The amplitude of the magnetisation is given by

$$\frac{\delta F}{\delta M} = 2MV\left(r_0 + 2UM^2\right) = 0 \quad \Rightarrow \quad M = 0 \vee M = \pm\sqrt{-\frac{r_0}{2U}}\,. \tag{2.14}$$

Above the critical temperature, the parameter r_0 is positive and thus the free energy is minimal for zero magnetisation. In the ordered phase, the magnetisation grows smoothly and two degenerate solutions exists for no applied magnetic field. Fig. 2.5**b** shows the mean-field free energy functional for a homogeneous magnetisation in the paramagnetic, i.e., for $r_0 < 0$, and the ferromagnetic phase, i.e., for $r_0 > 0$. When applying a magnetic field, the last term in Eq. (2.13) breaks the invariance symmetry and the magnetic spins align with the external field. The system is still invariant under the combined transformation $\mathbf{M} \to -\mathbf{M}$ and $\mathbf{H} \to -\mathbf{H}$.

2.2.2 Free energy of chiral magnets

The free energy functional of a standard ferromagnet is presented in Eq. (2.13), which reflects the spatial inversion symmetry of the system. In chiral magnets, the weak spin-orbit coupling leads to the formation of long-ranged noncollinear spin textures, thus breaking inversion symmetry in the system. This can be described by an odd power contribution of the spatial derivatives in the expansion of the energy functional. In linear order, this corresponds to the aforementioned Dzyaloshinskii-Moriya interaction (DMI) [62, 63]

$$\int d\mathbf{r}\, 2D\mathbf{M}\cdot(\nabla\times\mathbf{M})\,, \tag{2.15}$$

where the sign of D determines the left- or right-handed chirality of the system. Eq. (2.15) is known as the Bloch type DMI, which is typically found in bulk chiral magnets. The Ginzburg-Landau free energy functional is then given by

$$F_0[\mathbf{M}] = \int d\mathbf{r}\left(r_0\mathbf{M}^2 + J(\nabla\mathbf{M})^2 + 2D\mathbf{M}\cdot(\nabla\times\mathbf{M}) + U\mathbf{M}^4 - \mu_0\mathbf{H}\cdot\mathbf{M}\right), \tag{2.16}$$

which includes exchange, Dzyaloshinskii-Moriya and Zeeman interactions. The relative strength of the DM and the exchange interaction can be used to introduce a natural length scale, given by the inverse of the wavelength $Q = D/J$, as well as an energy scale, D^2/J. This is used to reduce the number of parameters entering the system via a rescaling of length $\tilde{\mathbf{r}} = Q\mathbf{r}$ and magnetisation $\tilde{\mathbf{M}} = \sqrt{UJ/D^2}\mathbf{M}$, thus leading to

$$F_0[\tilde{\mathbf{M}}] = \kappa\int d\tilde{\mathbf{r}}\left((t+1)\tilde{\mathbf{M}}^2 + (\tilde{\nabla}\tilde{\mathbf{M}})^2 + 2\tilde{\mathbf{M}}\cdot(\tilde{\nabla}\times\tilde{\mathbf{M}}) + \tilde{\mathbf{M}}^4 - \mu_0\tilde{\mathbf{H}}\cdot\tilde{\mathbf{M}}\right). \tag{2.17}$$

Here, $\tilde{\mathbf{H}} = \sqrt{UJ^3/D^3}\mathbf{H}$ is the rescaled magnetic field, while $\kappa = JD/U$ is a dimensionless prefactor that determines the relative weight between the mean-field and fluctuation contribution in the free energy expansion entering Eq. (2.12). The new parameter $t = r_0/(JQ^2) - 1 \propto \tilde{T} - \tilde{T}_c^{\mathrm{mf}}$ indicates the distance to the mean-field phase transition at $t = 0$, with $t > 0$ denoting the paramagnetic phase.

In the Ginzburg–Landau formulation of chiral magnetism, additional energy contributions can be incorporated into the free energy functional as long as they are consistent with the symmetries of the system. Two particularly important terms in this context are the magnetocrystalline anisotropy and the dipolar interaction. The latter is a long-ranged interaction which contributes significantly to both the magnetic structure and the spinwave dynamics of the noncollinear phases. This contribution to the chiral magnet free energy functional is presented in the next Section.

The magnetocrystalline anisotropy arises from higher order spin–orbit coupling, and reflects the influence of the underlying crystal lattice on the preferred orientation of the local magnetization. Although its energy scale is typically small compared to the exchange and Dzyaloshinskii–Moriya interactions, particularly in materials with weak spin–orbit coupling, it nonetheless plays a crucial role in determining various phenomenological properties. For example, it governs the in-plane orientation of the skyrmion lattice domains [81, 82] and is responsible for the stabilisation of the low-temperature skyrmion lattice phase observed in Cu_2OSeO_3 [83–85]. In this Thesis, we restrict our analysis to the limit of weak spin–orbit coupling and therefore neglect magnetocrystalline anisotropies. This choice is motivated by the aim of comparing our theoretical results directly with experimental observations. As will be shown in the following Chapters, our findings already capture the key experimental features with quantitative accuracy. Therefore, introducing anisotropy terms would require additional, largely unknown parameters, which in turn would risk over-fitting and obscuring the essential comparison between theory and experiments.

Dipolar interaction

In addition to the short-range Heisenberg exchange and Dzyaloshinskii–Moriya interactions, the spins also experience long-range interactions. These arise from the fact that each atomic spin carries a magnetic moment $\mathbf{m}_1$, which generates a microscopic magnetic field

$$\mathbf{B}_{\mathrm{dip}}(\mathbf{r}) = \frac{\mu_0}{4\pi}\frac{3\hat{r}(\mathbf{m}_1 \cdot \hat{r}) - \mathbf{m}_1}{r^3} \tag{2.18}$$

at position $\mathbf{r}$ relative to itself. A second magnetic moment $\mathbf{m}_2$ located at position $\mathbf{r}$ would therefore experience a Zeeman-like energy $E_{\mathrm{dip}} = -\mathbf{m}_2 \cdot \mathbf{B}_{\mathrm{dip}}(\mathbf{r})$. The characteristic energy scale of the dipolar, or magnetostatic, interaction is determined by the electron magnetic moment μ_B and the atomic lattice size, which is typically of the order of 10^{-10} m. Usually, this effect is at least three orders of magnitude smaller than the exchange coupling. Nonetheless, the long-range nature of dipolar coupling, decaying

only as the inverse cube of the distance, means that its cumulative effect can become relevant in bulk systems. An example of its macroscopic consequence is the formation of magnetic domains in conventional ferromagnets, where dipolar interactions favour flux-closure configurations that minimize stray fields [99].

In macroscopic solids, the total magnetic field generated by the ensemble of atomic or electronic magnetic moments is a collective effect of a vast number of individual dipoles. Each of these contributes to the overall dipole–dipole interaction energy. Therefore, calculating the exact microscopic magnetic field produced by all these dipoles is often an unsuitable task due to the long-range and nonlocal nature of the dipolar interaction. However, considerable simplifications arise for certain geometries, such as ellipsoidal samples. In this case, when an ellipsoidal sample is placed in a uniform external field $\mathbf{H}^{\text{ext}}$ directed along one of its (semi-)principal axes, the spins tend to align uniformly with the field, resulting in a collective magnetization $\mathbf{M}$. This uniform magnetization generates a so-called demagnetizing field $\mathbf{H}^{\text{dem}}$, which opposes the externally applied field and acts to reduce the internal magnetic field within the material. The net internal magnetic field experienced by the sample is then given by:

$$\mathbf{H}^{\text{int}} = \mathbf{H}^{\text{ext}} + \mathbf{H}^{\text{dem}}. \tag{2.19}$$

The demagnetizing field can be expressed using the demagnetization tensor $\overline{N}$, a symmetric rank-2 tensor whose components depend solely on the sample's shape and orientation with respect to the external field. For ellipsoidal bodies aligned with Cartesian axes $\hat{x}$, $\hat{y}$, and $\hat{z}$, the demagnetizing field simplifies to

$$\mathbf{H}^{\text{dem}} = -\overline{N}\cdot\mathbf{M} = -\begin{pmatrix} N_x & 0 & 0 \\ 0 & N_y & 0 \\ 0 & 0 & N_z \end{pmatrix}\cdot\mathbf{M}, \tag{2.20}$$

where N_x, N_y, and N_z are the demagnetization factors along the respective axes. Importantly, they satisfy the constraint: $N_x + N_y + N_z = 1$.

The demagnetising field contributes to the total energy of the system via the magnetostatic interaction. Within the Ginzburg–Landau framework, and in the limit of long-wavelength magnetisation variations, i.e., for $|\mathbf{k}| \ll 1/L$ where L is the sample size, the homogeneous dipolar energy contribution takes the form [99]

$$F_{\text{dip},\,|\mathbf{k}|\ll 1/\text{L}}[\mathbf{M}] = \frac{1}{2}\mu_0 \int d\mathbf{r}\,\mathbf{M}\cdot\overline{N}\cdot\mathbf{M}. \tag{2.21}$$

This term can be understood as an effective energy penalty associated with maintaining a uniform magnetisation against the internal field generated by the sample's own dipolar interactions. Here, the assumption of spatial homogeneity implies that the magnetization varies slowly on the scale of the sample

dimensions. It is worth noticing that this derivation is strictly correct only for ellipsoidal samples with one of their (semi-)principal axes oriented along the external magnetic field. Nevertheless, in this Thesis we do not consider more complicated cases, and we always approximate the sample geometry by an ellipsoidal body.

For local excitations, characterized by wavevectors $|\mathbf{k}| \gg 1/L$, it becomes necessary to consider the explicit form of the magnetic field generated by the magnetisation itself. In this regime, the microscopic dipole–dipole interaction must be taken into account directly. Because of its long-range nature and nonlocal coupling, evaluating the dipolar contribution in real space is computationally demanding, even for small, discretized systems. An efficient approach is offered by working in reciprocal space, where the convolution form of the dipolar interaction simplifies to a product. Therefore, the dipolar contribution to the free energy in the large-wavevector limit can be expressed as [99]

$$F_{\mathrm{dip},\,|\mathbf{k}|\gg 1/\mathrm{L}}[\mathbf{M}] = \frac{1}{2}\frac{\mu_0}{\nu}\sum_{\mathbf{k}}\frac{(\mathbf{m}_{\mathbf{k}}\cdot\mathbf{k})(\mathbf{m}_{-\mathbf{k}}\cdot\mathbf{k})}{|\mathbf{k}|^2}, \tag{2.22}$$

where ν is the volume of the unit cell, and $\mathbf{m}_{\mathbf{k}}$ denotes the Fourier components of the magnetization field $\mathbf{M}(\mathbf{r})$. These components are defined by the standard Fourier transform

$$\mathbf{M}(\mathbf{r}) = \sum_{\mathbf{k}}\mathbf{m}_{\mathbf{k}}\mathrm{e}^{\mathrm{i}\mathbf{k}\cdot\mathbf{r}} \qquad \text{and} \qquad \mathbf{m}_{\mathbf{k}} = \frac{1}{\nu}\int \mathrm{d}\mathbf{r}\,\mathbf{M}(\mathbf{r})\mathrm{e}^{-\mathrm{i}\mathbf{k}\cdot\mathbf{r}}. \tag{2.23}$$

The reciprocal-space expression (2.22) highlights the anisotropic character of the dipolar interaction, which favours magnetisation components perpendicular to the wavevector $\mathbf{k}$, and penalizes those aligned along it.

The contribution to the free energy functional due to the long-ranged dipolar interaction can be expressed combining the homogeneous and local contributions as

$$F_{\mathrm{dip}}[\mathbf{M}] = \frac{1}{2}\frac{\mu_0}{\nu}\sum_{\mathbf{k}}\mathbf{m}^i_{\mathbf{k}}\,\chi^{-1}_{\mathrm{dip,ij}}(\mathbf{k})\,\mathbf{m}^j_{-\mathbf{k}} \tag{2.24}$$

with

$$\chi^{-1}_{\mathrm{dip,ij}}(\mathbf{k}) = \mu_0\begin{cases}\frac{\mathbf{k}_i\mathbf{k}_j}{|\mathbf{k}|^2} & \text{for} \quad |\mathbf{k}| \gg 1/\mathrm{L} \\ N_{ij} & \text{for} \quad |\mathbf{k}| \ll 1/\mathrm{L}\end{cases}. \tag{2.25}$$

The intermediate regime is more difficult to address because then explicit surface terms enter the calculation. In this Thesis, we restrict the discussion to the asymptotic limits presented here.

2.2.3 Mean-field analysis

Here we analyse the mean-field solution corresponding to the chiral magnet free energy functional presented in Eq. (2.17). This was originally done by A. N. Bogdanov *et al.* [24, 25], and later revised by S. Mühlbauer *et al.* [27] where they showed the skyrmion lattice can be found as a stable mean-field solution upon including Gaussian thermal fluctuations. In this Section we will follow these works and summarise the most important results. In particular, we are interested in the helical and the skyrmion lattice configurations, which we show here that they are both solutions of the differential equation $\frac{\delta F}{\delta \mathbf{M}} = 0$. These noncollinear textures are periodic in space; therefore, it is convenient to express the corresponding magnetisation using the Fourier series presented in Eq. (2.23). Remembering the identity

$$\frac{1}{V}\int d\mathbf{r} e^{i\mathbf{r}\cdot(\mathbf{k}-\mathbf{k}')} = \delta_{\mathbf{k},\mathbf{k}'}\,, \tag{2.26}$$

we can express the rescaled free energy as

$$F[\mathbf{M}] = \sum_{\mathbf{k}} \Bigg[(1+t)\mathbf{m}_{\mathbf{k}}\cdot\mathbf{m}_{-\mathbf{k}} + (\mathbf{k}\cdot\mathbf{k})(\mathbf{m}_{\mathbf{k}}\cdot\mathbf{m}_{-\mathbf{k}}) - 2i\mathbf{m}_{\mathbf{k}}\cdot(\mathbf{k}\times\mathbf{m}_{-\mathbf{k}}) - \mu_0\mathbf{H}\cdot\mathbf{m}_{\mathbf{k}}\delta_{\mathbf{k},\mathbf{0}} + \sum_{\mathbf{k}',\mathbf{k}''}(\mathbf{m}_{\mathbf{k}}\cdot\mathbf{m}_{\mathbf{k}'})(\mathbf{m}_{\mathbf{k}''}\cdot\mathbf{m}_{-\mathbf{k}-\mathbf{k}'-\mathbf{k}''}) \Bigg], \tag{2.27}$$

where the "$\sim$"-notation was dropped for the sake of readability. It is worth noticing that here $\mathbf{k}$ indicates the dimensionless wavevector $\tilde{\mathbf{k}} = \mathbf{k}/Q$, consistent with Eq. (2.17).

In order to show that the helical state is the mean-field solution of the chiral free energy, it is more convenient to rewrite the functional in the following way

$$F[\mathbf{M}] = -V\frac{t^2-\mu_0^2\mathbf{H}^2}{4} + V\sum_{\mathbf{k}\neq\mathbf{0}}\mathbf{m}^{\alpha}_{-\mathbf{k}}[r_{\alpha\beta}(\mathbf{k}) - t\delta_{\alpha\beta}]\mathbf{m}^{\beta}_{\mathbf{k}} + \int d\mathbf{r}\left(\mathbf{M}^2+\frac{t}{2}\right)^2 + V\left(\mathbf{M}_f - \frac{\mu_0\mathbf{H}}{2}\right)^2, \tag{2.28}$$

where $r_{\alpha\beta}(\mathbf{k}) = (1+t+\mathbf{k}^2)\delta_{\alpha\beta} - 2i\varepsilon_{\alpha\beta\gamma}k^{\gamma}$. This formulation is equivalent to Eq. (2.17) and Eq. (2.27). The matrix $[r_{\alpha\beta}(\mathbf{k}) - t\delta_{\alpha\beta}]$ has eigenvalues $\{(|\mathbf{k}-1|)^2, 1+|\mathbf{k}|^2, (|\mathbf{k}+1|)^2\}$. Therefore, this term, as well as the last two terms on the right-hand side of Eq. (2.28), are positive semi-definite. Then, if one constructs a magnetic configuration that sets all these terms individually to zero, it is proven to be the mean-field ground state with free energy $-V(t^2-\mu_0\mathbf{H}^2)/4$.

The first term becomes zero for $|\mathbf{k}| = 1$ in rescaled units, i.e., the solution only possesses a single Fourier component with wavelength $Q = D/J$ on top of the homogeneous contribution. Consequently, we can

make an ansatz for the mean-field solution in the ordered, noncollinear phase, which corresponds to $t < 0$ and $\mu_0 H < \sqrt{-2t}$, that is

$$\mathbf{M}(\mathbf{r}) = \begin{pmatrix} A\cos z \\ A\sin z \\ 0 \end{pmatrix} + \begin{pmatrix} 0 \\ 0 \\ M_f \end{pmatrix} \tag{2.29}$$

describing the conical phase with homogeneous component $\mathbf{M}_f = \frac{1}{V}\int d\mathbf{r}\,\mathbf{M}(\mathbf{r}) = \mathbf{m}_{\mathbf{k}=\mathbf{0}}$. The free energy functional in Eq. (2.16) is rotational invariant; therefore, we assumed without loss of generality that the magnetic field is applied along the $\hat{z}$-direction, which fixes the dimensionless wavevector $\mathbf{k} = (0,0,1)^T \parallel \mathbf{H}$. The quadratic terms in Eq. (2.28) become zero for $\mathbf{M}_f = \mu_0\mathbf{H}/2$ and $2A = \sqrt{-2t - \mu_0^2 H^2}$. This proves that the helix ansatz is the mean-field ground state for the isotropic chiral magnet in the Ginzburg-Landau formalism. Moreover, since $M_f \sim \mu_0 H$, the conical phase changes smoothly into the helical phase for $\mu_0 H \to 0$. In other words, the mean-field formulation does not predict a finite critical field $\mu_0 H_{c1}$.

Effects of the dipolar interaction

The helical ground state might undergo two distinct phase transitions. For large temperatures, i.e., $t \propto T - T_c > 0$, the magnetic order parameter becomes null and the system enters the disordered paramagnetic phase. On the other hand, for $t < 0$ there is a critical field value $\mu_0 H_{c2}$ such that the conical state transitions to the spatially uniform field-polarised phase. This occurs when the in-plane component of the conical state in Eq. (2.29) vanishes uniformly, i.e., for $A = \frac{1}{2}\sqrt{-2t - \mu_0^2 H^2} = 0$. Therefore, the mean-field critical magnetic field is determined by

$$\mu_0 H_{c2} = \sqrt{-2t}\,. \tag{2.30}$$

Upon including the magnetostatic contribution in the free energy functional, we get an additional prefactor in the critical field behaviour, namely

$$\mu_0 H_{c2} = \sqrt{-2t}\left(1 + \frac{\mu_0 N_z}{2JQ^2}\right). \tag{2.31}$$

Therefore, the homogeneous component of the magnetisation takes the form

$$M_f = \frac{\mu_0 H_z}{2 + \frac{\mu_0 N_z}{JQ^2}}\,, \tag{2.32}$$

thus leading to the dimensionless magnetic susceptibility of the conical phase, $\tilde{\chi}_{\mathrm{con}} = M_f/H_z$, being

$$\tilde{\chi}_{\mathrm{con}} = \frac{\mu_0}{2 + \frac{\mu_0 N_z}{JQ^2}}\,. \tag{2.33}$$

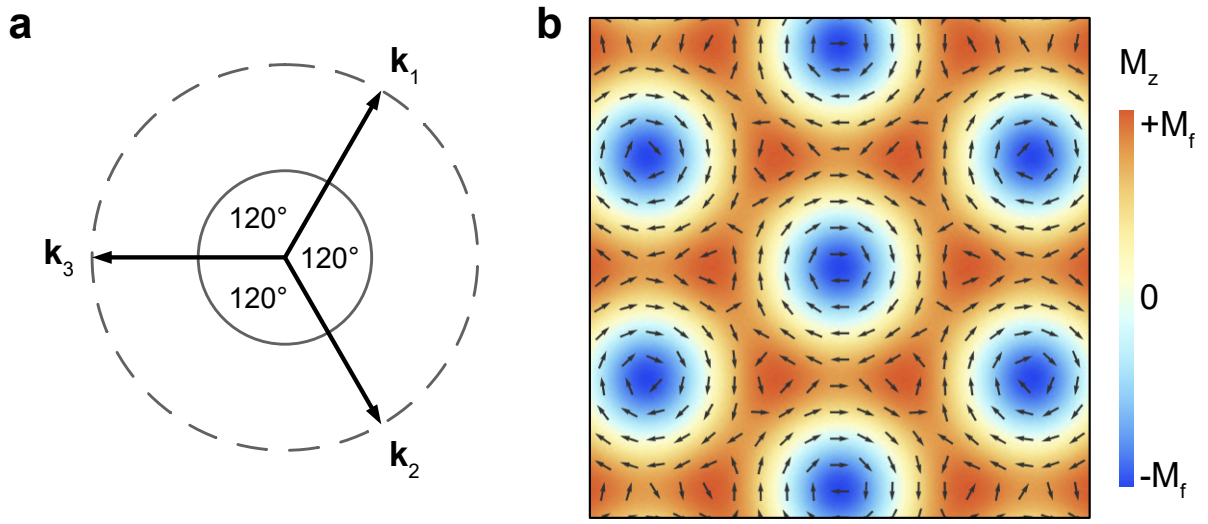

Figure 2.6.: **Triple helix configuration.** (**a**) Basis vectors of the spin order in the skyrmion lattice phase. (**b**) Skyrmion lattice configuration obtained using the triple-**Q** ansatz. The arrows depict the in-plane magnetisation and the colour coding represents its out-of-plane component.

Compared to the dominating temperature dependence of H_{c2}, the conical susceptibility can be seen as a constant. The translation to physical units of the magnetic susceptibility reads

$$\chi_{\mathrm{con}} = \frac{\mu_0 M_s^2}{JQ^2 + \mu_0 M_s^2 N_z} \,. \tag{2.34}$$

According to Eq. (2.4), the magnetic susceptibility in the conical phase can be expressed using its shape independent counterpart $\chi_{\mathrm{con}}^{\mathrm{int}}$, i.e.,

$$\chi_{\mathrm{con}} = \frac{\chi_{\mathrm{con}}^{\mathrm{int}}}{1 + N_z \chi_{\mathrm{con}}^{\mathrm{int}}} \,, \tag{2.35}$$

which then leads to

$$\chi_{\mathrm{con}}^{\mathrm{int}} = \frac{\mu_0 M_s^2}{JQ^2} \,. \tag{2.36}$$

This represents an important quantity that can be directly determined by experimental measurements, hence setting the ratio between the saturation magnetisation and the energy density D^2/J.

Mean-field skyrmion lattice phase : triple-Q ansatz

It is possible to derive a minimal ansatz of the skyrmion lattice configuration from its characteristic signal observed in neutron scattering experiments [27, 30, 77]. For the high-temperature skyrmion pocket, this shows six Bragg spots on a regular hexagon in the plane perpendicular to the applied magnetic field. Consequently, we can identify a minimal basis of three Fourier modes contributing in the skyrmion lattice

phase. In the presence of a sufficiently large external magnetic field, a finite uniform magnetic component $\mathbf{M}_f \parallel \mathbf{H}$ arises. Therefore, the quartic term in Eq. (2.27) contains cubic terms with wavevectors $\mathbf{k}_i \neq \mathbf{0}$,

$$\sum_{\mathbf{k}_1,\mathbf{k}_2,\mathbf{k}_3} (\mathbf{M}_f \cdot \mathbf{m}_{\mathbf{k}_1})(\mathbf{m}_{\mathbf{k}_2} \cdot \mathbf{m}_{\mathbf{k}_3})\delta(\mathbf{k}_1 + \mathbf{k}_2 + \mathbf{k}_3)\,. \tag{2.37}$$

A similar term appears in the theory for crystal formation out of the liquid phase, which shows analogies with the skyrmion lattice nucleation [98]. Here, the three wavevectors are fixed by the inverse length scale of the system, i.e., by $|\mathbf{k}_i| = Q$ for $i = 1,2,3$. Therefore, since these three wavevectors lay in the same plane, their relative angles result of 120°. This arrangement forms the triangular basis shown in Fig. 2.6**a**.

The DMI promotes canting of the magnetization, favouring configurations where $\mathbf{m}_{\mathbf{k}_i} \perp \mathbf{k}_i$ for $i = 1,2,3$. Furthermore, maximizing the energy gain from the term in Eq. (2.37) requires a significant overlap between the modulated magnetization components $\mathbf{m}_{\mathbf{k}_i}$ and the uniform magnetic component $\mathbf{M}_f$, which aligns with the external magnetic field. Consequently, the three wavevectors $\mathbf{k}_i$ must lie perpendicular to the direction of the applied magnetic field, assuming anisotropy effects are negligible. This explains the second key experimental observation: the Bragg spots consistently appear within the plane normal to the applied field, irrespective of the atomic lattice orientation. To a very good approximation, the skyrmion lattice can thus be described as a simple superposition of three helices and a uniform magnetization component

$$\mathbf{M}^{\mathrm{SkL}}(\mathbf{r}) \simeq \mathbf{M}_f + \sum_{i=1}^{3} \mathbf{M}_i^{\mathrm{helix}}(\mathbf{r})\,, \tag{2.38}$$

where

$$\mathbf{M}_i^{\mathrm{helix}}(\mathbf{r}) = A\left(\hat{n}_i^I \cos(\mathbf{k}_i \cdot \mathbf{r}) - \hat{n}_i^{II} \sin(\mathbf{k}_i \cdot \mathbf{r})\right) \tag{2.39}$$

is the magnetization of a single chiral helix with amplitude A, and $\{\mathbf{k}_i, \hat{n}_i^I, \hat{n}_i^{II}\}$ forms an orthonormal basis. All three helices are left-handed since $\mathbf{k}_i = \hat{n}_i^I \times \hat{n}_i^{II}$ for $i = 1,2,3$, and their helical wavevectors $\mathbf{k}_i$ are perpendicular to the magnetic field, $\mathbf{k}_i \perp \mathbf{H}$ for $i = 1,2,3$. The skyrmion lattice configuration in Eq. (2.38) is known as the triple-**Q** ansatz, and it is shown in Fig. 2.6**b**.

Using the triple-**Q** ansatz from Eq. (2.38) within the Ginzburg–Landau free energy framework presented in Eq. (2.16) reveals that the skyrmion lattice forms a locally stable configuration under certain values of the reduced temperature t and external magnetic field $\mu_0 H$. Nevertheless, the conical phase continues to represent the global free energy minimum across the full range of low temperatures and weak magnetic fields when evaluated at the mean-field level.

As depicted in the inset of Fig. 2.7, the free energy difference between the skyrmion and conical phases diminishes significantly near intermediate field strengths, around $H \approx 0.4 H_{\mathrm{c2}}$. This near-degeneracy suggests that contributions beyond the mean-field approximation, particularly thermal fluctuations, may be

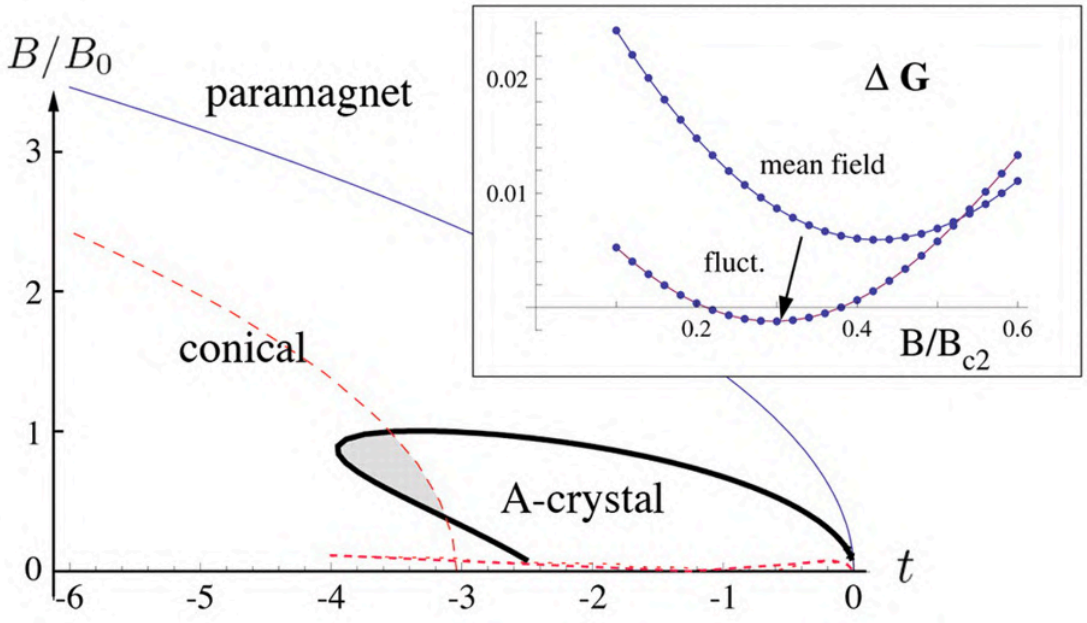

Figure 2.7.: **Mean-field phase diagram with thermal fluctuations.** Theoretical phase diagram as a function of the dimensionless magnetic field and the reduced parameter $t = r_0 J/D^2 - 1$. Inset: Energy difference between the skyrmion and conical phases as a function of the applied magnetic field for $t = -3.5$. The mean-field curve remains positive over the entire field range, indicating that the conical phase is the global minimum within mean-field theory. When thermal fluctuation corrections are included, the energy balance is reversed in a narrow region near the critical temperature T_c, stabilising the skyrmion lattice phase. The figure is taken from Ref. [27].

essential for stabilizing the skyrmion phase. When Gaussian fluctuations around the mean-field solutions are included, as formulated in Eq. (2.12), the skyrmion lattice gains additional stability within a limited field interval [27]. This effect is reflected in the lower curve of the inset in Fig. 2.7, where the skyrmion free energy drops below that of the conical phase. These results indicate that the skyrmion lattice becomes the thermodynamic ground state in a confined region of the temperature–field parameter space due to fluctuation effects. The resulting phase diagram, incorporating both mean-field and fluctuation corrections, is presented in Fig. 2.7.

2.3 Linear σ model

So far in this Chapter we have assumed that the magnitude of the local magnetisation is constant for a given temperature and external field, i.e., $|\mathbf{M}(\mathbf{r})| = \mathbf{M}_0$ with constant $\mathbf{M}_0$. However, in the semi-classical approximation we adopt here, the local magnetisation arises from thermal averaging a large number of atomic spins, hence spatial fluctuations of its magnitude are in principle allowed. Nevertheless, assuming a constant magnitude reduces the degrees of freedom of the corresponding energy density functional, thus enabling an analytical description of the problem. This approach is known as non-linear σ model.

The σ model, first introduced by Gell-Mann and Lévy in 1960 in the context of pion-nucleon interactions in nuclear physics [100], has since become a central tool in various areas of theoretical physics, including condensed matter. The original linear σ model describes scalar fields with both radial and angular degrees of freedom and includes a potential that spontaneously breaks a global symmetry. In the context of condensed matter, σ models arise naturally when describing systems with continuous spin symmetries, such as bulk chiral magnets. A linear sigma model for magnetism starts from a field $\boldsymbol{\phi}(\mathbf{r}) \in \mathbb{R}^N$, with $N = 3$ for spin systems, and includes both the magnitude and direction of the order parameter [101]

$$\mathscr{L}_{\mathrm{L}\sigma\mathrm{M}} = \frac{1}{2}(\partial_\mu \boldsymbol{\phi})^2 + \frac{\lambda}{4}\left(\boldsymbol{\phi}^2 - v^2\right)^2, \tag{2.40}$$

where v sets the scale of spontaneous symmetry breaking. Fluctuations in both amplitude and direction are allowed, making this model useful near phase transitions where the order parameter modulus is not fixed.

In contrast, the non-linear σ model emerges in the low-energy, long-wavelength limit, where amplitude fluctuations of the order parameter are suppressed. The field $\mathbf{n}(\mathbf{r})$ is constrained to lie on the surface of a sphere

$$\mathbf{n}(\mathbf{r}) \in S^{N-1}, \quad \text{with } \mathbf{n}^2 = 1, \tag{2.41}$$

and the Lagrangian reduces to

$$\mathscr{L}_{\mathrm{NL}\sigma\mathrm{M}} = \frac{\rho_s}{2}(\nabla \mathbf{n})^2, \tag{2.42}$$

where ρ_s is the spin stiffness. In this model, the only degrees of freedom are the angular fluctuations, which is often appropriate for describing magnetic textures in ordered magnets deep within the broken symmetry phase. In this context, the non-linear σ model provides a natural language to describe slowly varying, continuous spin textures. In particular, this method effectively captures the low-energy excitations and topological nature of the different magnetic phases. In fact, the vector field in Eq. (2.5) that defines the topological charge Q_{top} arises naturally from the non-linear Lagrangian in Eq. (2.42).

The non-linear σ model provides an appropriate framework to derive mean-field solutions for the helical and conical phases, as well as for the topologically non-trivial skyrmion lattice described by the triple-Q ansatz. In the present work, however, our goal is to obtain numerical solutions of the skyrmion lattice in the presence of dipolar interactions and to compute the corresponding low-energy excitation spectra. For this purpose, it is more convenient to adopt a different approach and describe the local magnetisation using the linear σ model instead. This approach allows for a more efficient numerical minimization of the free-energy functional, as it enables a broader exploration of the energy landscape and reduces the likelihood of becoming trapped in metastable configurations.

Within the linear σ model framework, it is natural to rewrite the free energy density of the chiral magnet $\mathscr{F} = \mathscr{F}_0 + \mathscr{F}_{\text{dip}}$ with respect to the dimensionless field $\mathbf{m}(\mathbf{r})$, with magnetisation $\mathbf{M}(\mathbf{r}) = M_s\mathbf{m}(\mathbf{r})$. The first contribution reads

$$\mathscr{F}_0[\mathbf{m}] = \frac{1}{V}\int d\mathbf{r}\left(J(\nabla\mathbf{m})^2 + 2D\mathbf{m}\cdot(\nabla\times\mathbf{m}) - \mu_0 M_s\mathbf{H}\cdot\mathbf{m} + \lambda\left(1-\mathbf{m}^2\right)^2\right), \tag{2.43}$$

where the last term comes from a simple reformulation of the quadratic and quartic contributions in the Ginzburg-Landau functional. Here, the phenomenological parameter λ measures the stiffness of the magnetic system towards modulations of the local magnetisation length, which relates to the distance from the phase transition in analogy with r_0 before. In fact, in the language of linear σ models, magnitude modulations of the order parameter are associated with a reconfiguration of the ground state. The magnetic dipolar contribution to the free energy density reads

$$\mathscr{F}_{\text{dip}} = \frac{1}{V}\int d\mathbf{r}d\mathbf{r}'\,\frac{\mu_0 M_s^2}{2}\,m_i(\mathbf{r})\chi^{-1}_{\text{dip},ij}(\mathbf{r}-\mathbf{r}')m_j(\mathbf{r}')\,, \tag{2.44}$$

with Fourier transform of the dipolar susceptibility given in Eq. (2.25).

In the absence of magnetocrystalline anisotropies, we can assume the skyrmion lattice configuration lays in the plane perpendicular to the external magnetic field. We further assume that the spin configuration is uniform along this direction, i.e. $\partial_z\mathbf{M}^{\text{SkL}}(\mathbf{r}) = 0$ with field applied along the z-direction. Therefore, we are able to express the local magnetisation as $\mathbf{M}(\boldsymbol{\rho}) = M_s\mathbf{m}(\boldsymbol{\rho})$, with $\boldsymbol{\rho} = (x,y)^T$ indicating the in-plane coordinates. For a boundless magnetic sample in the SkL phase, we are interested in the energy density per unit cell, namely $\varepsilon^{\text{puc}} = E/A^{\text{puc}}L$, where L indicates the sample dimension along the applied field direction. The unit cell area for a 2-dimensional hexagonal lattice is given by $A^{\text{puc}} = \frac{\sqrt{3}}{2}a_{\text{SkL}}^2$, with a_{SkL} denoting the skyrmion lattice constant. Therefore, the volume integral expressed in Eq. (2.43) and Eq. (2.44) reduces to

$$\frac{1}{V}\int d\mathbf{r} \to \frac{1}{A^{\text{puc}}}\int d\boldsymbol{\rho}\,. \tag{2.45}$$

2.3.1 Theoretical formulation in momentum space

In order to numerically minimize the skyrmion lattice energy density it is convenient to reformulate the problem in reciprocal space. The main reason is that the skyrmion lattice is a periodic structure, and this allows us to replace the minimization of a continuous real-space field by a discrete problem involving a finite set of Fourier amplitudes. This discretization reduces the complexity of the calculation, while still capturing the essential physics of the lattice configuration.

We denote by $\mathbf{R_n}$ the Bravais lattice vectors of the magnetic unit cell. The periodicity of the skyrmion lattice implies that the magnetization satisfies

$$\mathbf{M}(\boldsymbol{\rho}+\mathbf{R_n}) = \mathbf{M}(\boldsymbol{\rho})\,. \tag{2.46}$$

Thanks to this property, the local field $\mathbf{m} = \mathbf{M}/M_s$ can be expanded in a discrete Fourier series:

$$\mathbf{m}(\boldsymbol{\rho}) = \sum_{\mathbf{G_\nu}} \mathbf{m}(\mathbf{G_\nu}) \mathrm{e}^{\mathrm{i}\boldsymbol{\rho}\cdot\mathbf{G_\nu}}\,, \tag{2.47}$$

where $\mathbf{G_\nu}$ are the reciprocal lattice vectors of the skyrmion lattice. The Fourier coefficients are obtained by integrating over the unit cell with area A^{puc}:

$$\mathbf{m}(\mathbf{G_\nu}) = \frac{1}{A^{\mathrm{puc}}} \int_{\mathrm{uc}} \mathbf{m}(\boldsymbol{\rho}) \mathrm{e}^{-\mathrm{i}\boldsymbol{\rho}\cdot\mathbf{G_\nu}}\, \mathrm{d}\boldsymbol{\rho}\,. \tag{2.48}$$

In this representation, the problem of finding the equilibrium skyrmion lattice reduces to optimizing the Fourier amplitudes $\mathbf{m}(\mathbf{G_\nu})$ rather than the full continuous field $\mathbf{m}(\boldsymbol{\rho})$.

Lattice geometry and reciprocal basis

For the hexagonal skyrmion configuration, the Bravais lattice vectors can be expressed as

$$\mathbf{R_n} = a_{\mathrm{SkL}}(n_1\mathbf{g}_1 + n_2\mathbf{g}_2)\,, \quad \mathbf{n} = (n_1, n_2) \in \mathscr{Z} \times \mathscr{Z} \tag{2.49}$$

where a_{SkL} denotes the magnetic lattice size, and $\mathbf{g}_1$, $\mathbf{g}_2$ form a covariant basis together with $\mathbf{g}_3$ for the out-of-plane direction, namely

$$\mathbf{g}_1 = \begin{pmatrix} \cos(\pi/6) \\ -\sin(\pi/6) \\ 0 \end{pmatrix}, \quad \mathbf{g}_2 = \begin{pmatrix} \cos(\pi/6) \\ \sin(\pi/6) \\ 0 \end{pmatrix}, \quad \mathbf{g}_3 = \begin{pmatrix} 0 \\ 0 \\ 1 \end{pmatrix}. \tag{2.50}$$

The corresponding reciprocal lattice retains the same hexagonal symmetry. Its vectors can be written as

$$\mathbf{G_\nu} = \frac{2\pi}{a_{\mathrm{SkL}}}(\nu_1\mathbf{g}^1 + \nu_2\mathbf{g}^2)\,, \quad \text{with } \boldsymbol{\nu} = (\nu_1, \nu_2) \in \mathscr{Z} \times \mathscr{Z}\,, \tag{2.51}$$

with respect to the dual contravariant basis $\mathbf{g}^i$. The relation between covariant and contravariant basis vectors is encoded in the metric tensors

$$[g_{ij}] = \begin{bmatrix} 1 & 1/2 & 0 \\ 1/2 & 1 & 0 \\ 0 & 0 & 1 \end{bmatrix}, \quad [g^{ij}] = [g_{ij}]^{-1} = \begin{bmatrix} 4/3 & -2/3 & 0 \\ -2/3 & 4/3 & 0 \\ 0 & 0 & 1 \end{bmatrix}, \tag{2.52}$$

which ensure that $\mathbf{g}^i \cdot \mathbf{g}_j = \delta^i_j$. Explicitly, the contravariant basis vectors are

$$\mathbf{g}^1 = \frac{2}{\sqrt{3}} \begin{pmatrix} \sin(\pi/6) \\ -\cos(\pi/6) \\ 0 \end{pmatrix}, \quad \mathbf{g}^2 = \frac{2}{\sqrt{3}} \begin{pmatrix} \sin(\pi/6) \\ \cos(\pi/6) \\ 0 \end{pmatrix}, \quad \mathbf{g}^3 = \begin{pmatrix} 0 \\ 0 \\ 1 \end{pmatrix}. \tag{2.53}$$

Energy density in reciprocal space

Before proceeding with the Fourier transformation of the free energy functional, it is convenient to express it in dimensionless units. This can be obtained by using the inverse length scale $Q = D/J$, which gives the transformations

$$\mathbf{r} \to \frac{\tilde{\mathbf{r}}}{Q}, \quad V \to \frac{\tilde{V}}{Q^3}, \quad \nabla \to Q\tilde{\nabla}, \tag{2.54}$$

with dimensionless quantities $\tilde{\mathbf{r}}$, $\tilde{V}$ and $\tilde{\nabla}$. We now insert the Fourier expansion (2.47) into the real-space energy density. The orthogonality of the Fourier modes,

$$\frac{1}{A^{\text{puc}}} \int_{\text{uc}} \mathrm{e}^{\mathrm{i}\boldsymbol{\rho}\cdot(\mathbf{G}_{\boldsymbol{\nu}} - \mathbf{G}_{\boldsymbol{\nu}'})} = \delta^{\nu_1'}_{\nu_1} \delta^{\nu_2'}_{\nu_2}, \tag{2.55}$$

simplifies the integrals. After collecting all contributions, the energy density per unit cell can be expressed as

$$\begin{aligned} \frac{\varepsilon^{\text{puc}}}{D^2/J} =& \sum_{\mathbf{G}_{\boldsymbol{\nu}}} \Big[|\mathbf{G}_{\boldsymbol{\nu}}|^2 \mathbf{m}(\mathbf{G}_{\boldsymbol{\nu}}) \cdot \mathbf{m}(-\mathbf{G}_{\boldsymbol{\nu}}) + i\mathbf{G}_{\boldsymbol{\nu}} \cdot \Big[\mathbf{m}(\mathbf{G}_{\boldsymbol{\nu}}) \times \mathbf{m}(-\mathbf{G}_{\boldsymbol{\nu}}) \Big] - \mathbf{m}(\mathbf{G}_{\mathbf{0}}) \cdot \mathbf{h} \Big] \\ &+ \lambda \left[1 - 2 \sum_{\mathbf{G}_{\boldsymbol{\nu}}} \mathbf{m}(\mathbf{G}_{\boldsymbol{\nu}}) \cdot \mathbf{m}(-\mathbf{G}_{\boldsymbol{\nu}}) + \sum_{\mathbf{G}_{\boldsymbol{\nu}_1}, \mathbf{G}_{\boldsymbol{\nu}_2}, \mathbf{G}_{\boldsymbol{\nu}_3}} \Big(\mathbf{m}(\mathbf{G}_{\boldsymbol{\nu}_1}) \cdot \mathbf{m}(\mathbf{G}_{\boldsymbol{\nu}_2}) \Big) \Big(\mathbf{m}(\mathbf{G}_{\boldsymbol{\nu}_3}) \cdot \mathbf{m}(-\mathbf{G}_{\boldsymbol{\nu}_1} - \mathbf{G}_{\boldsymbol{\nu}_2} - \mathbf{G}_{\boldsymbol{\nu}_3}) \Big) \right] \\ &+ \xi_{\text{ms}} \left[\sum_{\mathbf{G}_{\boldsymbol{\nu}} \neq \mathbf{0}} \frac{\Big(\mathbf{m}(-\mathbf{G}_{\boldsymbol{\nu}}) \cdot \mathbf{G}_{\boldsymbol{\nu}} \Big) \Big(\mathbf{m}(\mathbf{G}_{\boldsymbol{\nu}}) \cdot \mathbf{G}_{\boldsymbol{\nu}} \Big)}{|\mathbf{G}_{\boldsymbol{\nu}}|^2} + N_{ij} m^i(\mathbf{G}_{\mathbf{0}}) m^j(\mathbf{G}_{\mathbf{0}}) \right], \end{aligned} \tag{2.56}$$

where $\mathbf{h} = \frac{\mu_0 M_s}{D^2/J}\mathbf{H}$, and λ is now expressed in units of energy density D^2/J. Moreover, $\xi_{\text{ms}} = \frac{\mu_0 M_s^2}{2JQ^2}$ indicates the dimensionless magnetostatic parameter. It is worth noticing that, using the internal magnetic susceptibility in Eq. (2.36), we get $\xi_{\text{ms}} = \frac{\chi^{\text{int}}_{\text{con}}}{2}$.

2.3.2 Numerical implementation

The reciprocal-space energy density in Eq. (2.56) can be minimised with respect to the Fourier components $\mathbf{m}(\mathbf{G}_{\boldsymbol{\nu}})$. This procedure is conceptually similar to the analytical minimisation carried out for the triple-Q ansatz in the previous Section, where only three Fourier modes were retained. Here, however, the summations extend over the full reciprocal space, i.e., infinitely many Fourier components. To make

the problem numerically tractable, we must introduce a cutoff Λ such that only reciprocal vectors with $|\mathbf{G}_{\boldsymbol{\nu}}| \leq \Lambda$ are included. The use of such a cutoff is physically well-motivated. Experimentally, neutron scattering measurements of the skyrmion lattice reveal contributions from only a finite number of Fourier components, whose intensity decreases with increasing wavevector magnitude [27]. Theoretically, the real-space free energy functional is finite for any smooth spin configuration, which guarantees convergence of its Fourier representation in the limit $\Lambda \to \infty$.

Independent degrees of freedom

The reciprocal lattice can be organised in concentric hexagonal "rings" around the origin. The n-th shell contains all reciprocal vectors $\mathbf{G}_{\boldsymbol{\nu}}$ lying within the n-th hexagon. Figure 2.8**a** illustrates the reciprocal space up to three rings, with the dashed circle marking a cutoff between the second and third rings. To preserve the sixfold rotational symmetry of the skyrmion lattice, the cutoff must be chosen such that it falls exactly between two rings. If this condition is not met, the minimisation would artificially break the hexagonal symmetry. For sufficiently large Λ the symmetry emerges naturally, but in practice we enforce this constraint for any finite cutoff used in the calculations.

The computational cost of the minimisation depends directly on the number of degrees of freedom, which is set by the lattice spacing a_{SkL} and the set of Fourier components $\mathbf{m}(\mathbf{G}_{\boldsymbol{\nu}})$ included within the cutoff. Since the n-th ring contains $6n$ points, the total number of reciprocal lattice nodes up to the n-th ring is $1+\sum_{j=1}^{n} 6j$. Each node corresponds to a complex three-dimensional Fourier component

$$\mathbf{m}(\mathbf{G}_{\boldsymbol{\nu}}) = \left(m'_x(\mathbf{G}_{\boldsymbol{\nu}}) + i m''_x(\mathbf{G}_{\boldsymbol{\nu}}), m'_y(\mathbf{G}_{\boldsymbol{\nu}}) + i m''_y(\mathbf{G}_{\boldsymbol{\nu}}), m'_z(\mathbf{G}_{\boldsymbol{\nu}}) + i m''_z(\mathbf{G}_{\boldsymbol{\nu}}) \right)^T , \tag{2.57}$$

which amounts to six real parameters.

Additional constraints can be used to reduce the number of independent contributions.

1. **Reality of the magnetisation**
   Since $\mathbf{M}(\boldsymbol{\rho})$ must be real, the Fourier components satisfy

   $$\mathbf{m}(-\mathbf{G}_{\boldsymbol{\nu}}) = \mathbf{m}(\mathbf{G}_{\boldsymbol{\nu}})^* , \tag{2.58}$$

   which implies that only half of the reciprocal lattice nodes need to be considered explicitly. In Fig. 2.8**a**, orange dots denote independent nodes, while blue dots follow from complex conjugation.

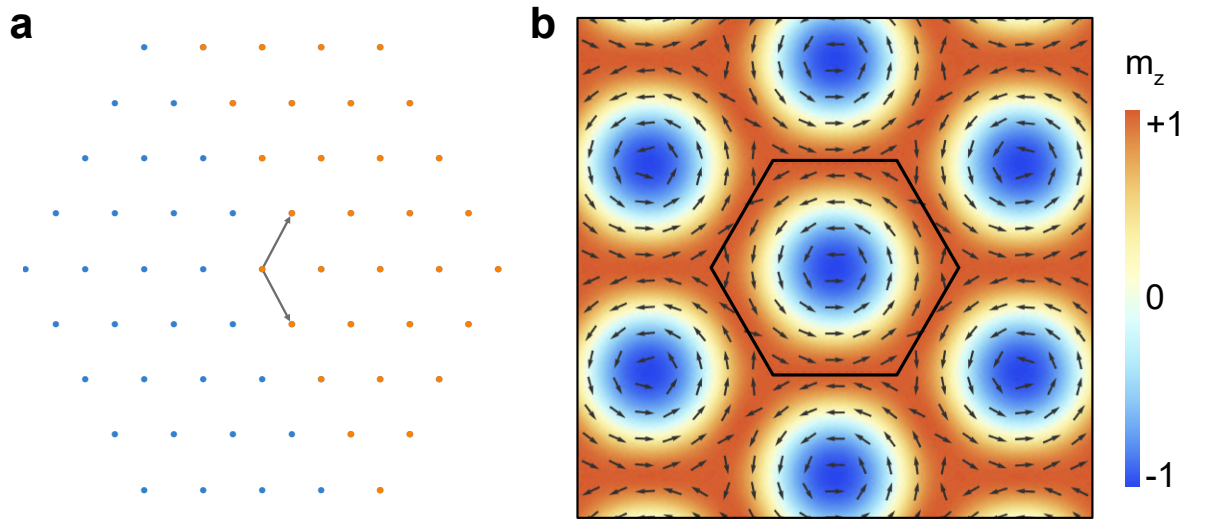

Figure 2.8.: **Skyrmion lattice configuration.** (**a**) Fourier components forming the reciprocal lattice up to the fourth shell. The gray arrows indicate the fundamental reciprocal lattice vectors $\mathbf{G}_{1,0}$ and $\mathbf{G}_{0,1}$, while the orange dots mark the independent Fourier components that remain after accounting for the system's symmetries. (**b**) Real-space skyrmion lattice configuration obtained by numerically minimizing the free energy density using the Fourier components shown in panel (a). The black hexagon denotes the Wigner–Seitz cell, whose size is given by the skyrmion lattice constant a_{SkL}.

2. **Spatial symmetry**

   The regular skyrmion lattice respects inversion-like constraints: $M_{x,y}(-\boldsymbol{\rho}) = -M_{x,y}(\boldsymbol{\rho})$ and $M_z(-\boldsymbol{\rho}) = M_z(\boldsymbol{\rho})$. Consequently, the Fourier components obey

$$\mathbf{m}_{x,y}(-\mathbf{G}_{\boldsymbol{\nu}}) = -\mathbf{m}_{x,y}(\mathbf{G}_{\boldsymbol{\nu}}), \quad \mathbf{m}_z(-\mathbf{G}_{\boldsymbol{\nu}}) = \mathbf{m}_z(\mathbf{G}_{\boldsymbol{\nu}}). \tag{2.59}$$

   This condition can be violated in the presence of additional energy contributions, such as magnetocrystalline anisotropy. In particular, we will relax this condition when including magneto-elastic coupling in the second part of this Thesis.

Combining these two conditions, each independent Fourier mode reduces to only three real parameters:

$$\mathbf{m}(\mathbf{G}_{\boldsymbol{\nu}}) = \left(im''_x(\mathbf{G}_{\boldsymbol{\nu}}), im''_y(\mathbf{G}_{\boldsymbol{\nu}}), m'_z(\mathbf{G}_{\boldsymbol{\nu}}) \right)^T. \tag{2.60}$$

Moreover, for the homogeneous component $\mathbf{G}_{\boldsymbol{\nu}} = \mathbf{0}$, only the longitudinal part $m'_z(\mathbf{G}_{\boldsymbol{\nu}} = \mathbf{0})$ survives. Altogether, the number of degrees of freedom reduces to

$$1 + 6 + 6 \times \left(\sum_{j=1}^{n} 6 \times j \right) \quad \longrightarrow \quad 1 + 1 + 3 \times \left(\sum_{j=1}^{n} 3 \times j \right). \tag{2.61}$$

For example, for $n = 4$ rings this number reduces significantly from 547 to only 137 independent parameters, thus improving the computational time required to find equilibrium configurations.

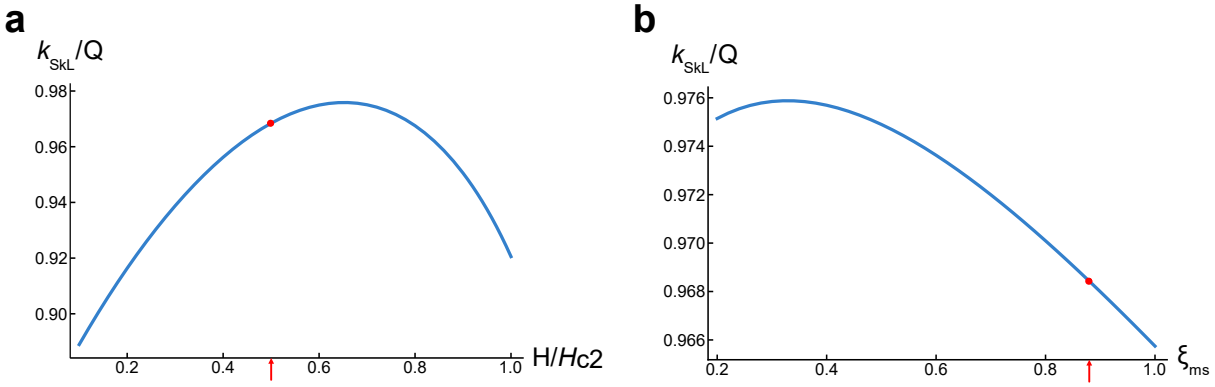

Figure 2.9.: **Reciprocal lattice vector.** Dependence of the skyrmion lattice reciprocal vector on (**a**) the applied magnetic field and (**b**) the magnetostatic parameter. The variation is relatively weak, and in general $k_{\mathrm{SkL}} \simeq Q$ within small deviations. The red arrows indicate the specific values of magnetic field and magnetostatic interaction used for the calculations shown in the opposite figure. In particular, $\xi_{\mathrm{ms}} = 0.88$ corresponds to the experimentally determined value for Cu_2OSeO_3.

Control parameters

The energy density per unit cell in Eq. (2.56) is normalised by introducing the natural length scale J/D and energy scale D^2/J. As a result, only three dimensionless parameters remain:

- the rescaled magnetic field $h = \frac{\mu_0 M_s J}{D^2} H$,
- the magnetostatic parameter $\xi_{\mathrm{ms}} = \frac{\mu_0 M_s^2 J}{2D^2}$,
- the stiffness $\lambda = -\frac{2r_0 J}{D^2}$.

Figure 2.8**b** shows an example of the resulting skyrmion lattice for Bloch-type DMI, calculated at $h = 0.5$ and $\xi_{\mathrm{ms}} = 0.88$, corresponding to the magnetostatic properties of Cu_2OSeO_3. The stiffness $\lambda = 500$ ensures the system is deep inside the ordered phase, so that the ground state configuration is robust against variations of this parameter. The minimisation is performed using Wolfram Mathematica's built-in Newton minimisation method.

The real-space lattice constant a_{SkL} is related to the reciprocal lattice vector k_{SkL}. In particular, for a regular hexagonal lattice we get

$$k_{SkL} = \frac{\sqrt{3}}{2} \frac{2\pi}{a_{\mathrm{SkL}}}. \tag{2.62}$$

Unlike the triple-Q ansatz, where k_{SkL} was fixed by the helix wavevector Q, the numerical minimisation allows for this parameter to take any value. Figure 2.9 illustrates the weak dependence of k_{SkL} on the magnetic field h and the magnetostatic parameter ξ_{ms}. In practice, the energy is minimised at values close to $k_{\mathrm{SkL}} \approx Q$ across a broad parameter range. In Cu_2OSeO_3, this corresponds to a skyrmion lattice constant of $a_{\mathrm{SkL}} \simeq 72$ nm.

3 Linear Spinwave Theory

In this Chapter, we investigate the spinwave dynamics within the ordered magnetic phases of chiral magnets introduced in the previous Chapter. Our analysis is based on the lossless Landau–Lifshitz equation, which governs the dynamical response of the local magnetisation to external perturbations. By linearising this equation around the equilibrium configurations, we focus on small-amplitude, low-energy excitations with respect to the mean-field magnetic texture.

We begin by examining the field-polarised and conical phases, where the problem can be treated semi-analytically, allowing for an intuitive understanding of the magnon modes. We then extend the analysis to the skyrmion lattice phase, deriving its magnon band structure and characterising the corresponding low-energy excitations. Finally, we present numerical results for the magnon dispersion both within the magnetic lattice plane and along the skyrmion tubes.

3.1 Landau-Lifshitz equation

The dynamics of a magnetic system can be understood by first considering the simplest possible case: the response of a single magnetic moment to an external magnetic field. A magnetic moment $\boldsymbol{\mu}$ placed in a field $\mathbf{B}$ experiences the Zeeman interaction, which tends to align the moment along the field direction. The corresponding torque is

$$\boldsymbol{\tau} = \boldsymbol{\mu} \times \mathbf{B}\,, \tag{3.1}$$

which does not force the moment into alignment immediately. Instead, it causes the moment to precess around the field direction, much like a spinning top subject to gravity. Just as the axis of a gyroscope traces out a circular trajectory under the influence of the gravitational torque, a magnetic moment executes a continuous precessional motion around $\mathbf{B}$. The origin of this behavior lies in the relation between the magnetic moment and the underlying angular momentum,

$$\boldsymbol{\mu} = \gamma \mathbf{J}\,, \tag{3.2}$$

with γ the gyromagnetic ratio. The total angular momentum is defined as the sum of orbital and spin contributions, $\mathbf{J} = \mathbf{L} + \mathbf{S}$. The respective gyromagnetic ratios can be derived systematically, and they read $\gamma_L = \frac{q}{2m_q}$ for the orbital part and $\gamma_S = \frac{q}{m_q}$ for the spin part, where q and m_q denote the charge and mass of the particle. Consequently, the magnetic moment takes the form $\boldsymbol{\mu} = \gamma_L \mathbf{L} + \gamma_S \mathbf{S} = \gamma_L(\mathbf{L} + 2\mathbf{S})$, which in general violates Eq. (3.2). To resolve this discrepancy, one considers only the projection of the magnetic moment onto the total angular momentum $\mathbf{J}$, since this quantity is both well-defined and experimentally observable. This motivates the introduction of an effective gyromagnetic ratio,

$$\gamma = g\frac{q}{2m_q}, \tag{3.3}$$

where g is the Landé factor. The value of g can be measured experimentally and reflects the relative weights of the orbital and spin contributions to the total angular momentum. Substituting this into the torque equation gives the fundamental law of motion,

$$\frac{d\mathbf{J}}{dt} = \gamma \mathbf{J} \times \mathbf{B}. \tag{3.4}$$

This equation captures the pure precessional dynamics of a moment in a field, analogous to the gyroscope precessing around the vertical axis under gravity.

If the system contains N magnetic moments per unit volume, we introduce the magnetisation as $\mathbf{M} = \gamma N \mathbf{J}$, and its time evolution is governed by

$$\frac{d\mathbf{M}}{dt} = -\gamma\mu_0 \mathbf{M} \times \mathbf{H}^{\text{eff}}. \tag{3.5}$$

The effective magnetic field can possess several contributions with different physical origins. In general, we express it as the functional derivative of the free energy,

$$\mu_0 \mathbf{H}^{\text{eff}} = -\frac{\delta F}{\delta \mathbf{M}}, \tag{3.6}$$

which might include both internal and external contributions. Eq. (3.5) is known as the lossless form of the Landau-Lifshitz equation, and it describes the conservative precessional motion [102–104]. Real magnetic systems also dissipate energy and eventually relax toward equilibrium. To incorporate this effect phenomenologically, Landau and Lifshitz extended the equation of motion by introducing a damping torque. This leads to the so-called Landau–Lifshitz-Gilbert equation [105]

$$\frac{d\mathbf{M}}{dt} = -\gamma\mu_0 \mathbf{M} \times \mathbf{H}^{\text{eff}} + \frac{\alpha}{M}\mathbf{M} \times \frac{d\mathbf{M}}{dt}, \tag{3.7}$$

where α denotes the damping parameter. The second term on the right-hand side introduces a damping mechanism that reduces the component of $\mathbf{M}$ perpendicular to the field, eventually aligning the

magnetization with its equilibrium direction. Importantly, the damping term is constructed such that the magnitude of **M** remains constant during motion, reflecting the conservation of spin length in the system.

3.2 Linear spinwave theory in chiral magnets

Here we are interested in the low energy excitation modes of the ordered phases of a chiral magnet. This can be achieved by considering small fluctuations with respect to the different equilibrium configurations presented in the previous Chapter, therefore, solving the Landau-Lifshitz equation in the linear approximation [3, 4]. We first assume that the equilibrium configuration is described by the spatially dependent unit vector $\hat{m}_{\rm eq}(\mathbf{r})$. A complete basis is then given by two unit vectors $\hat{e}_1(\mathbf{r})$ and $\hat{e}_2(\mathbf{r})$, spanning the locally orthogonal plane with respect to the equilibrium magnetisation, i.e., $\hat{e}_i(\mathbf{r})\cdot\hat{e}_j(\mathbf{r})=\delta_{ij}$ and $\hat{e}_1(\mathbf{r})\times\hat{e}_2(\mathbf{r})=\hat{m}_{\rm eq}(\mathbf{r})$. The time-dependent magnetisation is expressed via the Holstein–Primakoff transformation [3]

$$\hat{m}(\mathbf{r},t)=\hat{m}_{eq}(\mathbf{r})\sqrt{1-2\frac{g\mu_B}{M_s}\left|\psi(\mathbf{r},t)\right|^2}+\sqrt{\frac{g\mu_B}{M_s}}\left(\psi(\mathbf{r},t)\hat{e}_+(\mathbf{r})+\psi^*(\mathbf{r},t)\hat{e}_-(\mathbf{r})\right), \tag{3.8}$$

where $\hat{e}_\pm=\frac{1}{\sqrt{2}}(\hat{e}_1\pm i\hat{e}_2)$. Eq. (3.8) represents the natural framework to describe the spin excitations precessional motion with amplitudes $\psi(\mathbf{r},t)$ and $\psi^*(\mathbf{r},t)$ in the clockwise and counter-clockwise direction, respectively. Here, $|\psi(\mathbf{r},t)|^2$ indicates the probability density of magnons. In general, the U(1) symmetry associated with the phase of the complex wavefunction ψ is broken. This reflects the fact that the spin angular momentum associated with magnons is not strictly conserved, owing to the effects of spin–orbit coupling, dipolar interactions, and the presence of a non-uniform magnetization. Consequently, the Schrödinger equation does not provide a correct description of the system, and off-diagonal terms arise proportionally to $\psi\psi$ and $\psi^*\psi^*$. This is analogous to the standard BCS theory for superconductors [106]. Therefore, the correct dynamics is given by the Bogoliubov-de Gennes (BdG) wave equation for the spinor $\mathbf{\Psi}^{\rm T}=(\psi,\psi^*)$, that is,

$$i\hbar\tau_z\partial_t\mathbf{\Psi}(\mathbf{r},t)=\mathscr{H}\mathbf{\Psi}(\mathbf{r},t)\,, \tag{3.9}$$

where τ_z is a Pauli matrix and $\mathscr{H}$ indicates the BdG Hamiltonian. It is important to notice that the Hamiltonian exhibits a particle–hole symmetry of the form

$$\tau_x\mathscr{K}\,\mathscr{H}\,\tau_x\mathscr{K}=\mathscr{H}\,, \tag{3.10}$$

where $\mathscr{K}$ denotes complex conjugation. This property stems from the fact that the magnetization is a real-valued quantity. As a result, the spectrum of $\mathscr{H}$ consists of eigenvalue pairs $\pm\omega$. Specifically, if $\mathbf{\Psi}$ is an eigenstate with eigenvalue ω, then $\tau_x\mathscr{K}\mathbf{\Psi}$ is an eigenstate with eigenvalue $-\omega$. This can be understood from the bosonic BdG formalism used to describe spin waves, where the Hamiltonian con-

tains both magnon creation and annihilation operators. This doubling of degrees of freedom ensures that the equations of motion capture the correct bosonic commutation relations. Because of this structure, every magnon excitation with positive frequency ω is accompanied by a partner at frequency $-\omega$. These negative-frequency solutions are not physical excitations themselves but rather reflect the redundancy introduced by the BdG formalism. The true physical spectrum is therefore given by the positive frequencies, while the negative ones can be interpreted as their particle–hole counterparts.

3.2.1 Magnon excitations in the field-polarised phase

We start analysing the simplest spin configuration found in chiral magnets, i.e., the spatially uniform field polarised state. We assume that the external field $\mu_0 H > \mu_0 H_{c2}$ is applied along the $\hat{z}$-direction, hence we define an orthogonal basis by $\hat{e}_1 = \hat{x}$ and $\hat{e}_2 = \hat{y}$. The Hamiltonian governing spinwave excitations in the field-polarized state can be derived directly from the chiral magnet free energy functional [Eq. (2.16)]. In the absence of dipolar interaction, the result is [39]

$$\mathscr{H} = \mathscr{D}\Big(-\mathbb{I}\nabla^2 - 2iQ\tau_z\hat{z}\nabla \Big) + g\mu_B\mu_0 H\mathbb{I} \tag{3.11}$$

where we have introduced the stiffness constant $\mathscr{D} = Jg\mu_B/M_s$.

To account for dipolar effects, it is convenient to switch to momentum space, where the Fourier transform of the bosonic BdG equation takes the form

$$\Big[\hbar\omega\tau_z - \mathscr{H}(\mathbf{k})\Big]\boldsymbol{\Psi}(\mathbf{k},\omega) = 0\,. \tag{3.12}$$

In the long-wavelength limit, i.e., for $|\mathbf{k}| \ll 1/L$, the uniform Hamiltonian reduces to [39]

$$\mathscr{H}_{|\mathbf{k}|\ll 1/L} = g\mu_B\mu_0 H\mathbb{I} + g\mu_B\mu_0 M_s\left(-N_z\mathbb{I} + \frac{N_x+N_y}{2}\mathbb{I} + \frac{N_x-N_y}{2}\tau_x\right), \tag{3.13}$$

where we also included the contribution of magnetostatic interactions. Plugging this into Eq. (3.12) and solving the eigenvalue problem, we find the corresponding magnon dispersion

$$\hbar\omega = g\mu_B\mu_0\sqrt{\left(H + (N_x - N_z)M_s\right)\left(H + (N_y - N_z)M_s\right)}\,. \tag{3.14}$$

This coincides with the standard Kittel formula, which describes the ferromagnetic resonance [107]. Importantly, the uniform excitation mode within a large sample in the field-polarised phase is not affected by the broken inversion symmetry induced by DMI.

When considering local excitations of the field polarised configuration, i.e., for $|\mathbf{k}| \gg 1/L$, the BdG Hamiltonian acquires additional contributions originating from the exchange and DM interactions. This reads [39]

$$\mathscr{H}_{|\mathbf{k}|\gg 1/L} = \mathscr{D}\left(|\mathbf{k}|^2\mathbb{I} + 2Qk_z\tau_z\right) + g\mu_B\mu_0 H_{\text{int}}\mathbb{I} + \frac{g\mu_B\mu_0 M_s}{2|\mathbf{k}|^2}\begin{pmatrix} k_+k_- & k_-^2 \\ k_+^2 & k_+k_- \end{pmatrix}, \tag{3.15}$$

where $H_{\text{int}} = H - N_z M_s$ is the internal field, and $k_\pm = k_x \pm ik_y$. Solving Eq. (3.12) gives the magnon eigenfrequency $\omega(\mathbf{k})$ with

$$\hbar\omega(\mathbf{q}) = 2\mathscr{D}Qk_z + \sqrt{(\mathscr{D}|\mathbf{k}|^2 + g\mu_B\mu_0 H_{int})\left(\mathscr{D}|\mathbf{k}|^2 + g\mu_B\mu_0 H_{int} + \frac{g\mu_B\mu_0 M_s}{|\mathbf{k}|^2}|\mathbf{k}_\perp|^2\right)}, \tag{3.16}$$

where $\mathbf{k}_\perp = (k_x, k_y, 0)$. The square-root contribution in Eq. (3.16) reproduces the well-known Herring–Kittel result for conventional ferromagnets [108]. In addition, the Dzyaloshinskii–Moriya interaction generates the linear term $2\mathscr{D}Qk_z$, which effectively shifts the magnon spectrum along the field direction in momentum space. As a consequence, the dispersion becomes asymmetric with respect to inversion of k_z: for finite longitudinal momentum one finds $\omega(-\mathbf{k}) \neq \omega(\mathbf{k})$. This broken reciprocity, which directly stems from the lack of inversion symmetry inside the system, results in a finite group velocity even at small wavevectors. Its sign depends on the handedness of the crystal, being positive or negative for right- or left-handed sample, respectively. This feature represents one of the most interesting aspects of spinwaves propagation in a chiral magnet, and it will be further explored throughout the rest of the Thesis.

The dispersion relation reaches its minimum at $\mathbf{k} = Q\hat{z}$, where the magnon energy gap takes the value $\Delta = g\mu_B\mu_0 H^{\text{int}} - \mathscr{D}Q^2$. This gap closes at the critical field H_{c2}^{int}, marking the energetic transition between the field polarised and the conical phase.

Characteristic frequency

The resonance frequencies of spinwaves in a chiral magnet can be expressed in dimensionless units $\tilde{\omega}$ by introducing a universal frequency scale for the system, defined as $\tilde{\omega} = \omega/\omega_{\text{c2}}$. This scale naturally arises by rescaling Eq. (3.12), which yields

$$\omega_{\text{c2}} = \frac{\mathscr{D}Q^2}{\hbar} = \frac{\gamma_0 JQ^2}{M_s}, \tag{3.17}$$

where ω_{c2} is commonly referred to as the critical frequency. The term "critical" originates from its connection to the critical internal magnetic field $H_{\text{c2}}^{\text{int}}$. Indeed, substituting Eq. (2.36) into the definition $H_{\text{c2}}^{\text{int}} = M_s/\chi_{\text{con}}^{\text{int}}$ gives

$$H_{\text{c2}}^{\text{int}} = \frac{JQ^2}{\mu_0 M_s}. \tag{3.18}$$

The critical frequency can then be directly related to this field via

$$\hbar\omega_{c2} = g\mu_B\mu_0 H_{c2}^{\text{int}}\,. \tag{3.19}$$

This relation provides a fundamental link between the intrinsic frequency scale of the system and an experimentally accessible parameter, namely the critical magnetic field.

3.2.2 Magnon excitations in the conical phase

The magnetic configuration in the conical phase is given by Eq. (2.29), i.e., $\mathbf{M}(\mathbf{r}) = M_s\hat{m}_{\text{eq}}(\mathbf{r})$ where

$$\hat{m}_{\text{eq}}(\mathbf{r}) = \begin{pmatrix} \sin\theta\cos(Qz) \\ \sin\theta\sin(Qz) \\ \cos\theta \end{pmatrix} \tag{3.20}$$

for $\mathbf{H} = H\hat{z}$. Therefore, we define the local orthogonal frame

$$\hat{e}_1 = \begin{pmatrix} -\sin(Qz) \\ \cos(Qz) \\ 0 \end{pmatrix}, \quad \hat{e}_2 = \begin{pmatrix} -\cos\theta\cos(Qz) \\ -\cos\theta\sin(Qz) \\ \sin\theta \end{pmatrix}. \tag{3.21}$$

The magnon Hamiltonian in the absence of dipolar interaction reads [39]

$$\mathscr{H} = \mathscr{D}\left(-\mathbb{I}\nabla^2 - 2iQ\tau_z\hat{e}_\perp(z)\nabla + \frac{Q^2\sin^2\theta}{1}(\mathbb{I}-\tau_x)\right), \tag{3.22}$$

with $\hat{e}_\perp(z) = (\sin\theta\cos Qz, \sin\theta\sin Qz, 0)^T$. This periodic potential leads to Bragg scattering that opens gaps in the spinwave energy spectrum, thus resulting in the formation of a magnon band structure. According to Bloch's theorem [109], the spinwave spectrum is periodic $\omega_n(\mathbf{k}+mQ\hat{z}) = \omega_n(\mathbf{k})$ for any $m \in Z$, where n indicates the band index. Moreover, as a consequence of this periodicity, the BdG equation in not diagonal in momentum space any more, and it can be expressed as

$$\hbar\omega\tau_z\mathbf{\Psi}(\mathbf{k}+mQ\hat{z},\omega) = \mathscr{H}_{mm'}(\mathbf{k}+m'Q\hat{z})\mathbf{\Psi}(\mathbf{k}+m'Q\hat{z},\omega)\,. \tag{3.23}$$

The Fourier transform of Eq. (3.22) becomes

$$\mathscr{H}^{\text{ex}}_{mm'}(\mathbf{k}) = \delta_{m,m'}\mathscr{D}\left[|\mathbf{k}|^2\mathbb{I} + \frac{Q^2\sin^2\theta}{2}(\mathbb{I}-\tau_x)\right] + \delta_{m-1,m'}\mathscr{D}Q\sin\theta k_-\tau_z + \delta_{m+1,m'}\mathscr{D}Q\sin\theta k_+\tau_z \tag{3.24}$$

where $k_\pm = k_x \pm ik_y$. The contribution of the dipolar interaction was calculated explicitly in Refs. [39, 73], and is given by

$$\mathscr{H}^{\text{dip}}_{mm'}(\mathbf{k}) = \sum_{\alpha,\beta=-1,0,1} H^{\alpha\beta}_{\text{dip}}(\mathbf{k}-\beta Q\hat{z})\delta_{m+\beta-\alpha,m'}\,. \tag{3.25}$$

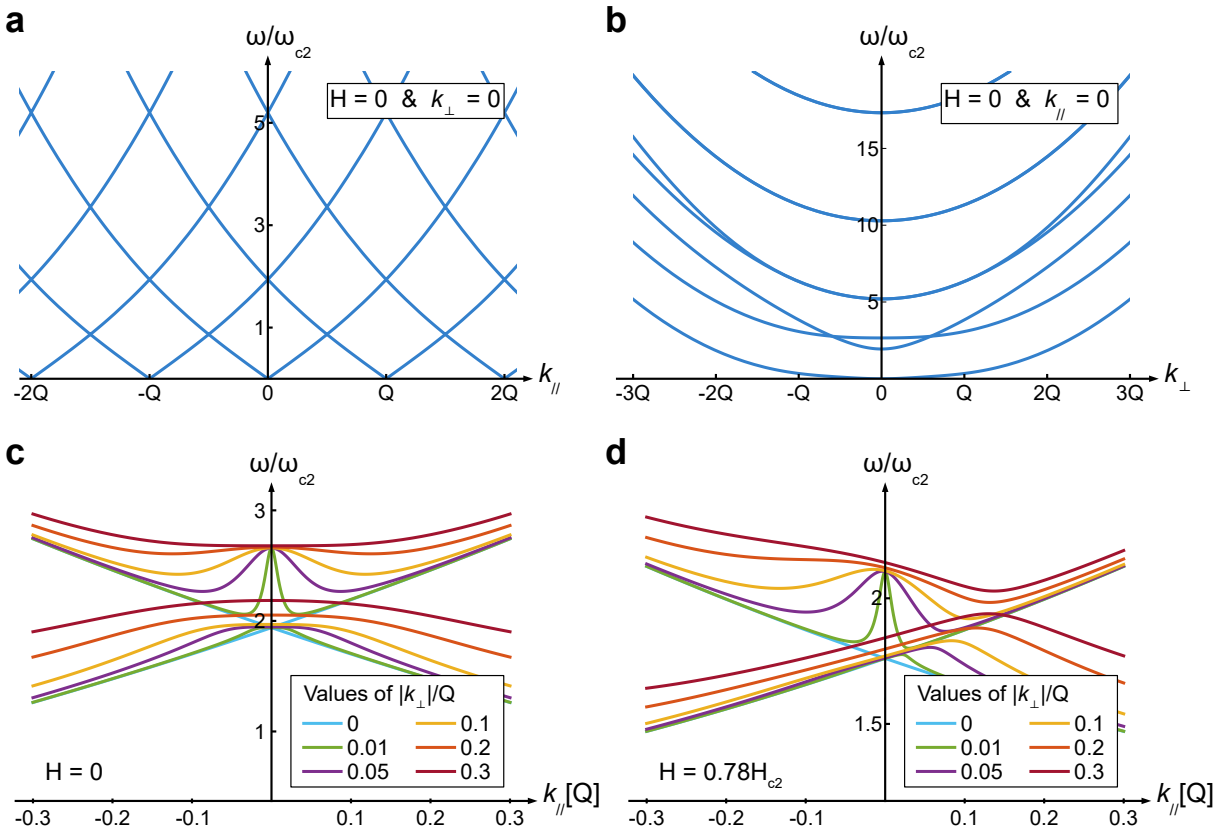

Figure 3.1.: **Magnon band structure of the helical phase.** Spinwave spectrum calculated for (**a**) longitudinal momenta $\mathbf{k}_{\parallel} \parallel \mathbf{Q}$ and (**b**) transverse momenta $\mathbf{k}_{\perp}$ in the absence of a applied magnetic field. (**c**-**d**) Non-analytical behaviour of the magnon dispersion of the bulk $\pm Q$ resonances for small wavevectors $|\mathbf{k}| \ll Q$. In zero field, the dispersion is reciprocal (**c**), whereas a finite magnetic field induces non-reciprocal propagation (**d**).

The tensor components are expressed as

$$H^{\alpha\beta}_{\mathrm{dip}}(\mathbf{k}) = \begin{pmatrix} H^{11}_{\mathrm{dip}}(\mathbf{k}) & H^{10}_{\mathrm{dip}}(\mathbf{k}) & H^{1-1}_{\mathrm{dip}}(\mathbf{k}) \\ H^{01}_{\mathrm{dip}}(\mathbf{k}) & H^{00}_{\mathrm{dip}}(\mathbf{k}) & H^{0-1}_{\mathrm{dip}}(\mathbf{k}) \\ H^{-11}_{\mathrm{dip}}(\mathbf{k}) & H^{-10}_{\mathrm{dip}}(\mathbf{k}) & H^{-1-1}_{\mathrm{dip}}(\mathbf{k}) \end{pmatrix} = \frac{\mathscr{D}Q^2\chi^{\mathrm{int}}_{\mathrm{con}}}{2|\mathbf{k}|^2} \begin{pmatrix} M_+(\mathbf{k}) & L_-(\mathbf{k}) & N_-(\mathbf{k}) \\ L_+(\mathbf{k}) & M_0(\mathbf{k}) & K_-(\mathbf{k}) \\ N_+(\mathbf{k}) & K_+(\mathbf{k}) & M_-(\mathbf{k}) \end{pmatrix} \tag{3.26}$$

with matrix elements

$$\begin{aligned} M_{\pm}(\mathbf{k}) &= |\mathbf{k}_{\perp}|^2 \left[\frac{1}{4} \left((1+\cos^2\theta)\mathbb{I} \pm 2\cos\theta\tau_z \right) + \frac{\sin^2\theta}{4}\tau_x \right], \\ M_0(\mathbf{k}) &= k_z^2 \sin^2\theta(\mathbb{I}-\tau_x), \\ L_{\pm}(\mathbf{k}) &= \frac{k_z k_{\pm}}{2}\sin\theta \left[(-\tau_z \mp i\tau_y) + (-\mathbb{I}+\tau_x)\cos\theta \right], \\ N_{\pm}(\mathbf{k}) &= k_{\pm}^2 \left[-\frac{\sin^2\theta}{4}\mathbb{I} + \frac{1}{4}\left(-(1+\cos^2\theta)\tau_x \pm 2i\cos\theta\tau_y \right) \right], \\ K_{\pm}(\mathbf{k}) &= \frac{k_z k_{\pm}}{2}\sin\theta \left[(\tau_z \mp i\tau_y) + (-\mathbb{I}+\tau_x)\cos\theta \right]. \end{aligned} \tag{3.27}$$

Due to the intricate form of the BdG Hamiltonian, $\mathscr{H}_{mm'}(\mathbf{k}) = \mathscr{H}^{\mathrm{ex}}_{mm'}(\mathbf{k}) + \mathscr{H}^{\mathrm{dip}}_{mm'}(\mathbf{k})$, obtaining closed-form analytical solutions is generally not feasible. However, the problem simplifies considerably for wavevector aligned with the external field, i.e., $\mathbf{k}_\perp = \mathbf{0}$. In this particular case, the spinwave equation becomes diagonal again, and the Hamiltonian reduces to

$$\mathscr{H}_{mm'}(k_z + m'Q) = \delta_{m,m'}\left[\mathscr{D}(k_z + m'Q)^2\mathbb{I} + \frac{\mathscr{D}Q^2(1+\chi^{\mathrm{int}}_{\mathrm{con}})\sin^2\theta}{2}(\mathbb{I} - \tau_x)\right]. \tag{3.28}$$

The eigenfrequency solution corresponding to the purely longitudinal magnon dispersion results

$$\hbar\omega(k_z) = \mathscr{D}k_z\sqrt{k_z^2 + (1+\chi^{\mathrm{int}}_{\mathrm{con}})Q^2\left(1 - \frac{H}{H^{\mathrm{int}}_{c2}}\right)}, \tag{3.29}$$

where we used the cone angle definition [Eq. (2.3)], which reads $\sin^2\theta = 1 - H/H^{\mathrm{int}}_{c2}$.

The full spinwave spectrum can be obtained numerically by solving the eigenvalue problem defined in Eq. (3.23). Fig. 3.1**a** and **b** show the low energy magnon dispersion for $\mathbf{k}_\perp = \mathbf{0}$ and $k_z = 0$, respectively. At the Brillouin-zone center, the system hosts a single gapless excitation. This Goldstone mode arises from the spontaneous breaking of continuous translational symmetry in the helical ground state and is characterized, at low momenta, by the soft dispersion [110–112]

$$\omega^2 \sim \alpha k_z^2 + \beta|\mathbf{k}_\perp|^4. \tag{3.30}$$

The next set of excitations corresponds to the so-called ±Q modes. At zero wavevector, these modes represent spatially uniform precessions of the magnetization, where the total magnetic moment integrated over the sample volume oscillates in opposite directions: the +Q branch rotates counterclockwise, while the -Q branch rotates clockwise around the applied magnetic field. Consequently, they can be probed by magnetic resonance experiments [46]. Because of this helicity matching, the +Q mode evolves continuously into the ferromagnetic resonance (Kittel) mode at the second critical field H_{c2}. Figures 3.1**c** and **d** highlight an additional feature: the dipolar interaction induces a non-analytic dependence of the excitation spectrum on the wavevector $\mathbf{k}$, which cannot be captured within a purely local exchange framework. Furthermore, when a finite external magnetic field is applied, inversion symmetry along the helix axis is broken. This symmetry breaking gives rise to a non-reciprocal magnon dispersion for finite transverse momentum, such that

$$\omega(\mathbf{k}_\perp, -k_z) \neq \omega(\mathbf{k}_\perp, k_z) \quad \text{for} \quad |\mathbf{k}_\perp| \neq 0, \mathrm{H} \neq 0. \tag{3.31}$$

This non-reciprocity can be observed by probing the magnon excitations at finite momentum, for example via Brillouin light scattering [73].

3.3 Magnon excitations in the SkL phase

In this Section we focus on the calculation of spinwave excitations within the skyrmion lattice phase. Our aim is to solve the lossless Landau–Lifshitz equation in linear approximation. To this end, the magnetization field is decomposed into its static equilibrium part and a small fluctuation,

$$\mathbf{M}(\mathbf{r},t) = \mathbf{M}_{\mathrm{eq}}(\mathbf{r}) + \delta\mathbf{M}(\mathbf{r},t)\,, \tag{3.32}$$

where $\mathbf{M}_{\mathrm{eq}}(\mathbf{r})$ denotes the mean-field solution corresponding to the skyrmion lattice configuration, as obtained numerically in the previous Chapter. The fluctuation $\delta\mathbf{M}(\mathbf{r},t)$ describes the spinwave amplitude and is assumed to be small compared to the equilibrium magnetization. To derive the linearized dynamics, we expand the Ginzburg–Landau free energy functional in powers of $\delta\mathbf{M}$:

$$F[\mathbf{M}] = F[\mathbf{M}_{\mathrm{mf}}] + \left.\frac{\delta F[\mathbf{M}]}{\delta \mathbf{M}_i}\right|_{\mathbf{M}_{\mathrm{mf}}} \delta\mathbf{M}_i + \frac{1}{2}\delta\mathbf{M}_i \left.\frac{\delta^2 F[\mathbf{M}]}{\delta\mathbf{M}_i \delta\mathbf{M}_j}\right|_{\mathbf{M}_{\mathrm{mf}}} \delta\mathbf{M}_j + \mathscr{O}(\delta\mathbf{M}^3)\,. \tag{3.33}$$

Since $\mathbf{M}_{\mathrm{eq}}$ minimizes the free energy within mean-field theory, the first-order variation vanishes. Consequently, the expansion can be expressed as

$$F[\mathbf{M}] \simeq F[\mathbf{M}_{\mathrm{eq}}] + \frac{1}{2}\int d\mathbf{r}\, d\mathbf{r}'\, \delta M_i(\mathbf{r})\, \chi_{ij}(\mathbf{r},\mathbf{r}')\, \delta M_j(\mathbf{r}')\,, \tag{3.34}$$

where we have introduced the kernel

$$\chi_{ij}(\mathbf{r},\mathbf{r}') = \left.\frac{\delta^2 F}{\delta M_i(\mathbf{r}) \delta M_j(\mathbf{r}')}\right|_{\mathbf{M}_{\mathrm{eq}}}\,. \tag{3.35}$$

Substituting this expression into the Landau–Lifshitz equation (3.5) and retaining only linear terms in $\delta\mathbf{M}$ yields

$$\partial_t \delta M_i(\mathbf{r},t) = \gamma \varepsilon_{ijk} M_{\mathrm{eq},j}(\mathbf{r}) \int d\mathbf{r}'\, \chi_{kl}(\mathbf{r},\mathbf{r}')\, \delta M_l(\mathbf{r}',t)\,, \tag{3.36}$$

where ε_{ijk} is the Levi-Civita tensor. At this order, only the equilibrium magnetization enters the precession term, while higher-order corrections are consistently neglected. This linearized Landau–Lifshitz equation forms the basis for the spinwave analysis in the skyrmion lattice, as it governs the dynamics of small-amplitude fluctuations on top of the static, noncollinear background [39, 78].

Here we limit the discussion to the linear response regime of a time-independent system, where the Hamiltonian has no explicit dependence on time. In this case, the fluctuations of the magnetization can

be expressed in terms of plane-wave modes with well-defined frequency and wavevector. We therefore adopt the ansatz

$$\delta\mathbf{M}(\mathbf{r},t) = \delta\mathbf{M}(\mathbf{r})\, e^{-i\omega t}\,, \tag{3.37}$$

where $\delta\mathbf{M}$ denotes the spatial profile of the fluctuation. Inserting this ansatz into Eq. (3.36) leads to the eigenvalue problem

$$-i\omega\, \delta M_i(\mathbf{r}) = \gamma \varepsilon_{ijk} M_{\mathrm{eq},j}(\mathbf{r}) \int d\mathbf{r}'\, \chi_{kl}(\mathbf{r},\mathbf{r}')\, \delta M_l(\mathbf{r}')\,. \tag{3.38}$$

The spinwave spectrum is obtained from the eigenvalues ω of this linear operator, while the corresponding eigenfunctions $\delta\mathbf{M}(\mathbf{r})$ describe the spatial structure of the magnon modes. These excitations form the magnon band structure characteristic of the skyrmion lattice phase, reflecting the noncollinear and periodic nature of the equilibrium magnetic texture.

3.3.1 Momentum space formulation

The determination of the magnon band structure in the skyrmion lattice phase requires solving the eigenvalue problem given in Eq. (3.38). Due to the presence of dipolar interaction in the system, the calculation is considerably simplified in reciprocal space, as was already the case for the equilibrium configuration discussed in the previous Chapter. According to Bloch's theorem, the spinwave spectrum inherits the lattice periodicity of the skyrmion crystal, such that

$$\omega(\mathbf{k}+\mathbf{Q}) = \omega(\mathbf{k}) \tag{3.39}$$

for any reciprocal lattice vector $\mathbf{Q} = \mathbf{G}_\mathbf{n}$, with $\mathbf{n} \in Z \times Z$ and $\mathbf{G}_\mathbf{n}$ defined in Eq. (6.28). It is therefore natural to decompose a generic wavevector as $\mathbf{k} = \mathbf{Q}+\mathbf{q}$, where $\mathbf{q}$ lies inside the first Brillouin zone (BZ). Accordingly, the spinwave amplitudes can be written as $\delta\mathbf{m}(\mathbf{k}) = \delta\mathbf{m}_\mathbf{Q}(\mathbf{q})$, with Fourier transforms defined as

$$\delta\mathbf{m}(\mathbf{k}) = \int d\boldsymbol{\rho}\, dt\, \delta\mathbf{M}(\boldsymbol{\rho},t) e^{-i(\mathbf{k}\cdot\boldsymbol{\rho}-\omega t)}\,, \quad \delta\mathbf{M}(\boldsymbol{\rho},t) = \int \frac{d\mathbf{k}}{(2\pi)^3}\frac{d\omega}{2\pi}\, \delta\mathbf{m}(\mathbf{k}) e^{i(\mathbf{k}\cdot\boldsymbol{\rho}-\omega t)}\,. \tag{3.40}$$

To proceed, we analyse the Hessian of the free energy functional [Eq. (2.27)], which in Fourier space takes the form [78]

$$\begin{aligned}\left.\frac{\delta^2 F}{\delta m^i(-\mathbf{k})\delta m^j(\mathbf{k}')}\right|_{\mathbf{m}_\mathrm{eq}} &= \Big[\delta(\mathbf{q}-\mathbf{q}')\delta_{\mathbf{Q},\mathbf{Q}'} r^{ij}(\mathbf{Q}+\mathbf{q}) + \delta(\mathbf{q}-\mathbf{q}')\delta_{\mathbf{Q},\mathbf{Q}'} D^{ij}(\mathbf{Q}+\mathbf{q}) \\ &\qquad + 2\delta^{ij}\sum_{\mathbf{Q}''} \mathbf{m}_{-\mathbf{Q}''}\cdot\mathbf{m}_{\mathbf{Q}-\mathbf{Q}'+\mathbf{Q}''}\delta(\mathbf{q}-\mathbf{q}') + 4\sum_{\mathbf{Q}''} m^i_{-\mathbf{Q}''} m^j_{\mathbf{Q}-\mathbf{Q}'+\mathbf{Q}''}\delta(\mathbf{q}-\mathbf{q}')\Big] \\ &= \left(\chi_0^{-1}\right)^{ij}_{\mathbf{Q}\mathbf{Q}'}(\mathbf{q})\delta(\mathbf{q}-\mathbf{q}')\end{aligned} \tag{3.41}$$

where we used the notation $\mathbf{m}_{\mathbf{Q}} = \mathbf{m}_{\mathrm{eq}}(\mathbf{Q})$, and defined the matrices

$$\mathbf{r}^{ij}(\mathbf{k}) = (1 + t + |\mathbf{k}|^2)\delta^{ij} - 2i\varepsilon^{ijl}k^l\,, \tag{3.42}$$

$$D^{ij}(\mathbf{k}) = \frac{1}{2}\mu_0 \begin{cases} \frac{\mathbf{k}^i\mathbf{k}^j}{|\mathbf{k}|^2} & \text{for} \quad |\mathbf{k}| \gg 1/\mathrm{L} \\ N^{ij} & \text{for} \quad |\mathbf{k}| \ll 1/\mathrm{L} \end{cases}\,. \tag{3.43}$$

Here we introduced the matrix notation $\chi_0^{-1} = \frac{\delta^2 F}{\delta \mathbf{M}^2}\Big|_{\mathbf{M}_{\mathrm{eq}}}$, which makes the dependence on both discrete ($\mathbf{Q}$) and continuous ($\mathbf{q}$) momenta explicit. Substituting Eq. (3.41) into the Fourier expression of the effective magnetic field yields

$$\begin{aligned} \mu_0 H^{\mathrm{eff},i}(\mathbf{k}) = \mu_0 H^{\mathrm{eff},i}_{\mathbf{Q}}(\mathbf{q}) &= -\sum_{\mathbf{k}'} \frac{\delta^2 F}{\delta m^i(-\mathbf{k})\delta m^j(\mathbf{k}')}\delta m^j(\mathbf{k}') \\ &= -\sum_{\mathbf{Q}'} \left(\chi_0^{-1}\right)^{ij}_{\mathbf{Q}\mathbf{Q}'}(\mathbf{q})\delta m^j_{\mathbf{Q}'}(\mathbf{q}),. \end{aligned} \tag{3.44}$$

Finally, the linearised Landau–Lifshitz equation (3.36) can be expressed in Fourier space by combining the skyrmion lattice Fourier decomposition [Eq. (2.47)] with Eq. (3.40). This leads to

$$\begin{aligned} -i\omega\delta m^i_{\mathbf{Q}}(\mathbf{q}) &= \gamma\mu_0 \sum_{\mathbf{Q}'\mathbf{Q}''} \varepsilon^{ijl} m^j_{\mathbf{Q}'} H^{\mathrm{eff},l}_{\mathbf{Q}''}(\mathbf{q})\delta_{\mathbf{Q}'+\mathbf{Q}'',\mathbf{Q}} \\ &= -\gamma \sum_{\mathbf{Q}''} \left(\sum_{\mathbf{Q}'} \varepsilon^{ijl} m^j_{\mathbf{Q}'} \delta_{\mathbf{Q}'+\mathbf{Q}'',\mathbf{Q}} \right) \left(\mu_0 H^{\mathrm{eff},l}_{\mathbf{Q}''}(\mathbf{q}) \right) \\ &= \gamma \sum_{\mathbf{Q}''\mathbf{Q}'''} (\mathbf{m}_{\mathrm{eq}}\times)^{il}_{\mathbf{Q}\mathbf{Q}''} \left(\chi_0^{-1}\right)^{lb}_{\mathbf{Q}''\mathbf{Q}'''}(\mathbf{q})\delta m^b_{\mathbf{Q}'''}(q)\,, \end{aligned} \tag{3.45}$$

where we defined the operator

$$(\mathbf{m}_{\mathrm{eq}}\times)^{il}_{\mathbf{Q}\mathbf{Q}''} = \sum_{\mathbf{Q}'} \varepsilon^{ijl} m^j_{\mathbf{Q}'} \delta_{\mathbf{Q}'+\mathbf{Q}'',\mathbf{Q}}\,. \tag{3.46}$$

In principle, the sums in Eqs. (3.45) and (3.46) run over infinitely many reciprocal lattice vectors. For numerical implementation, a cutoff $|\mathbf{Q}| < \Lambda$ is introduced, as already discussed in the previous Chapter. This truncation is justified since the free energy converges with a finite number of Fourier components in the skyrmion lattice phase. Nevertheless, the approximation becomes less accurate for higher-energy magnon modes. Therefore, reliable results are only obtained in the low-energy regime, while quantitative predictions at larger energies require including an increasingly large number of Fourier components.

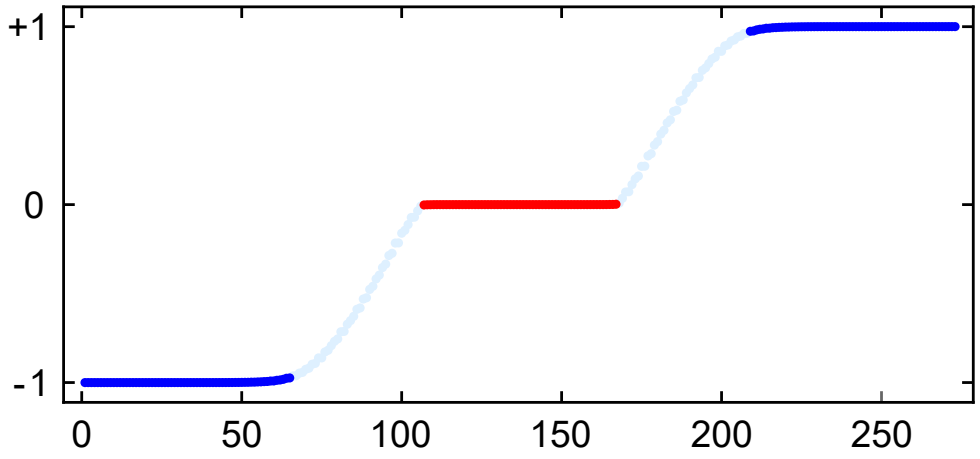

Figure 3.2.: **Eigenvalues of $\left(\mathbf{m}_{\mathrm{eq}}\times\right)$.** Typical distribution of the eigenvalues λ_n introduced in Eq. (3.47), computed for $N = 5$ shells in reciprocal space. The blue dots correspond to the physical subspace, the red dots represent the orthogonal basis, and the light-blue dots indicate intermediate eigenvalues that are projected to zero.

Projection onto the dynamical subspace

A direct manifestation of the cutoff introduced in reciprocal space appears when analysing the operator $(\mathbf{m}_{\mathrm{eq}}\times)$ defined in Eq. (3.46). This operator can be expressed in terms of its eigenbasis $\mathbf{v}_n$ as

$$(\mathbf{m}_{\mathrm{eq}}\times)^{il}_{\mathbf{Q}\mathbf{Q}''} = \sum_n \lambda_n \mathbf{v}_n \otimes \mathbf{v}_n^* \in M_{m\times m}(\mathbb{C})\,, \tag{3.47}$$

where λ_n are the corresponding eigenvalues and $\otimes$ denotes the outer product. The size of the matrix, $m \times m$, is set by the number of Fourier components retained within the cutoff Λ. For the hexagonal lattice of Fig. 2.8, this dimension is

$$m = 3\left(1 + 6\sum_{j=1}^{N} j\right)\,, \tag{3.48}$$

where N counts the number of reciprocal-space shells. In the limit of an infinite cutoff $\Lambda \to \infty$ and for a normalized magnetization $|\mathbf{M}_{\mathrm{eq}}(\mathbf{r})| = M_s$, the spectrum of eigenvalues would reduce to the discrete set $\lambda_n = \{0, \pm 1\}$. However, within the linear σ-model the magnetization is allowed to vary in magnitude, thus the eigenvalues fluctuate around these ideal values. Physically, $\lambda_n = \pm 1$ correspond to transverse oscillations, while $\lambda_n = 0$ would represent purely longitudinal modes. Since the Landau–Lifshitz equation does not capture longitudinal fluctuations, the problem must be consistently restricted to the subspace spanned by eigenvectors with $\lambda_n \simeq \pm 1$.

Figure 3.2 illustrates the typical distribution of eigenvalues for $N = 5$ rings. Because the reciprocal-space cutoff truncates the Fourier basis, a significant fraction of the eigenvalues fall into an intermediate regime (shown in light blue), where they cannot be uniquely identified as either longitudinal ($\lambda_n = 0$) or transverse ($\lambda_n = \pm 1$) modes. These spurious modes predominantly arise from the boundaries in

momentum space. To ensure consistency, we project out these ambiguous states by retaining only those eigenvalues sufficiently close to ± 1 [78]. In practice, this amounts to defining a projected operator

$$(\mathbf{m}_{\mathrm{eq}}\times)^P = \sum_n{}' \lambda_n \mathbf{v}_n \otimes \mathbf{v}_n^*, \tag{3.49}$$

where the sum is restricted to eigenvectors with $|\lambda_n| > \Lambda_P$. A typical choice for the projection threshold is $\Lambda_P \simeq 0.97$. For the sake of readability, we have omitted explicit indices in Eq. (3.49). With this projection, the Landau-Lifshitz equation takes the form

$$-i\omega_\alpha \delta\mathbf{m}_\alpha(\mathbf{q}) = \gamma(\mathbf{m}_{\mathrm{eq}}\times)^P \chi_0^{-1}(\mathbf{q})\, \delta\mathbf{m}_\alpha(\mathbf{q}) \tag{3.50}$$

where the index α labels the magnon modes.

This projection step has an important physical meaning: it enforces the fact that spin dynamics in the Landau-Lifshitz framework is purely transversal, i.e. magnetization precesses around the equilibrium configuration without changing its magnitude. The spurious eigenvalues introduced by the cutoff would otherwise mix transverse and unphysical longitudinal components, leading to artificial contributions to the magnon spectrum. By keeping only the eigenvalues close to ± 1, we effectively isolate the physical subspace of transverse spin precession, ensuring that the calculated modes correspond to genuine magnons. The price to pay is a loss of accuracy at high energies, where the truncated Fourier expansion becomes less reliable, whereas the low-energy spectrum remains robust.

Bogoliubov–de Gennes orthogonality

In contrast to ordinary Hermitian eigenvalue problems, the Bogoliubov–de Gennes structure of the Landau–Lifshitz equation implies that the spinwave eigenfunctions do not obey the standard Euclidean orthogonality relation. Instead, they form an orthogonal basis only with respect to a suitably defined scalar product. To make this explicit, let us examine the Hermitian conjugate of Eq. (3.50), which reads

$$\delta\mathbf{m}_\alpha^\dagger \mathscr{H}_{\mathrm{BdG}}^\dagger \left(\left(i\mathbf{m}_{\mathrm{eq}} \times \right)^P \right)^\dagger = \delta\mathbf{m}_\alpha^\dagger \mathscr{H}_{\mathrm{BdG}} \left(i\mathbf{m}_{\mathrm{eq}} \times \right)^P = \omega_\alpha \delta\mathbf{m}_\alpha^\dagger, \tag{3.51}$$

where we used that both $\mathscr{H}_{\mathrm{BdG}}$ and $\left(i\mathbf{m}_{\mathrm{eq}} \times \right)^P$ are Hermitian operators, and that the magnon eigenfrequencies ω_α are real. From this, it follows that the Landau-Lifshitz equation can be expressed in two equivalent forms:

$$\mathscr{H}_{\mathrm{BdG}} \delta\mathbf{m}_\alpha = \omega_\alpha \left(\left(i\mathbf{m}_{\mathrm{eq}} \times \right)^P \right)^{-1} \delta\mathbf{m}_\alpha, \tag{3.52}$$

and

$$\delta\mathbf{m}_\alpha^\dagger \mathscr{H}_{\mathrm{BdG}} = \omega_\alpha \delta\mathbf{m}_\alpha^\dagger \left(\left(i\mathbf{m}_{\mathrm{eq}} \times \right)^P \right)^{-1}. \tag{3.53}$$

Therefore, by comparing these two expressions one obtains the relation

$$\delta\mathbf{m}_\beta^\dagger \mathscr{H}_{\mathrm{BdG}} \delta\mathbf{m}_\alpha = \omega_\alpha \delta\mathbf{m}_\beta^\dagger \left(\left(i\mathbf{m}_{\mathrm{eq}} \times \right)^P \right)^{-1} \delta\mathbf{m}_\alpha = \omega_\beta \delta\mathbf{m}_\beta^\dagger \left(\left(i\mathbf{m}_{\mathrm{eq}} \times \right)^P \right)^{-1} \delta\mathbf{m}_\alpha \,. \tag{3.54}$$

For two distinct, non-degenerate eigenmodes with $\omega_\alpha \neq \omega_\beta$, this equality is satisfied if and only if

$$\delta\mathbf{m}_\beta^\dagger \left(\left(i\mathbf{m}_{\mathrm{eq}} \times \right)^P \right)^{-1} \delta\mathbf{m}_\alpha = 0 \,. \tag{3.55}$$

In other words, the spinwave functions form an orthogonal basis with respect to the scalar product defined by the operator $\left(\left(i\mathbf{m}_{\mathrm{eq}} \times \right)^P \right)^{-1}$. This generalised scalar product also provides a natural normalisation condition for the magnon modes. Indeed, each eigenvector can be rescaled as

$$\delta\mathbf{m}_\alpha \to \frac{1}{\sqrt{n_\alpha}} \delta\mathbf{m}_\alpha \quad \text{with} \quad n_\alpha = \delta\mathbf{m}_\alpha^\dagger \left(\left(i\mathbf{m}_{\mathrm{eq}} \times \right)^P \right)^{-1} \delta\mathbf{m}_\alpha \,, \tag{3.56}$$

ensuring a consistent normalization across all modes. The inverse operator appearing here can be explicitly constructed in the projected transverse subspace introduced earlier, which yields

$$\left(\left(i\mathbf{m}_{\mathrm{eq}} \times \right)^P \right)^{-1} = \sum_n{}' \frac{1}{\lambda_n} \mathbf{v}_n \otimes \mathbf{v}_n^* \,, \tag{3.57}$$

where the sum is restricted to the eigenstates with finite eigenvalues λ_n.

3.3.2 Mode characterisation

Before analysing the full magnon band structure, it is instructive to examine the lowest-energy excitations at zero wavevector $\mathbf{q} = \mathbf{0}$. In this case, Eq. (3.50) reduces to an eigenvalue problem that yields the collective modes of the skyrmion lattice, i.e., coherent oscillations of the entire texture. Studying these excitations provides an insightful intuition on the different excitation modes, and allows us to introduce a characterisation of the magnon bands. Figure 3.3 shows the out-of-plane component of the magnon eigenfunctions $\delta\mathbf{M}_\alpha(\mathbf{r},t)$ corresponding to the twelve lowest excited modes, evaluated for the equilibrium configuration in Fig. 2.8**b** with parameters $h = 0.5$, $\xi\mathrm{ms} = 0.88$ and $\lambda = 500$. Each panel illustrates the fluctuation pattern at a fixed time t, i.e., the instantaneous deviation from the equilibrium magnetisation $\mathbf{M}_{\mathrm{eq}}(\mathbf{r})$. Snapshots of the time evolution for each excitation mode are shown in the Appendix. The skyrmion lattice hosts a large variety of collective modes, many of which are highly intricate due to the nontrivial topology and periodic arrangement of skyrmions. Here we highlights some of their important features, and explain the different nomenclature used in the picture.

In the literature, the three most prominent low-energy excitations that dominate both theoretical and experimental studies are the counter-clockwise (CCW), breathing and clockwise (CW) mode [45]. These

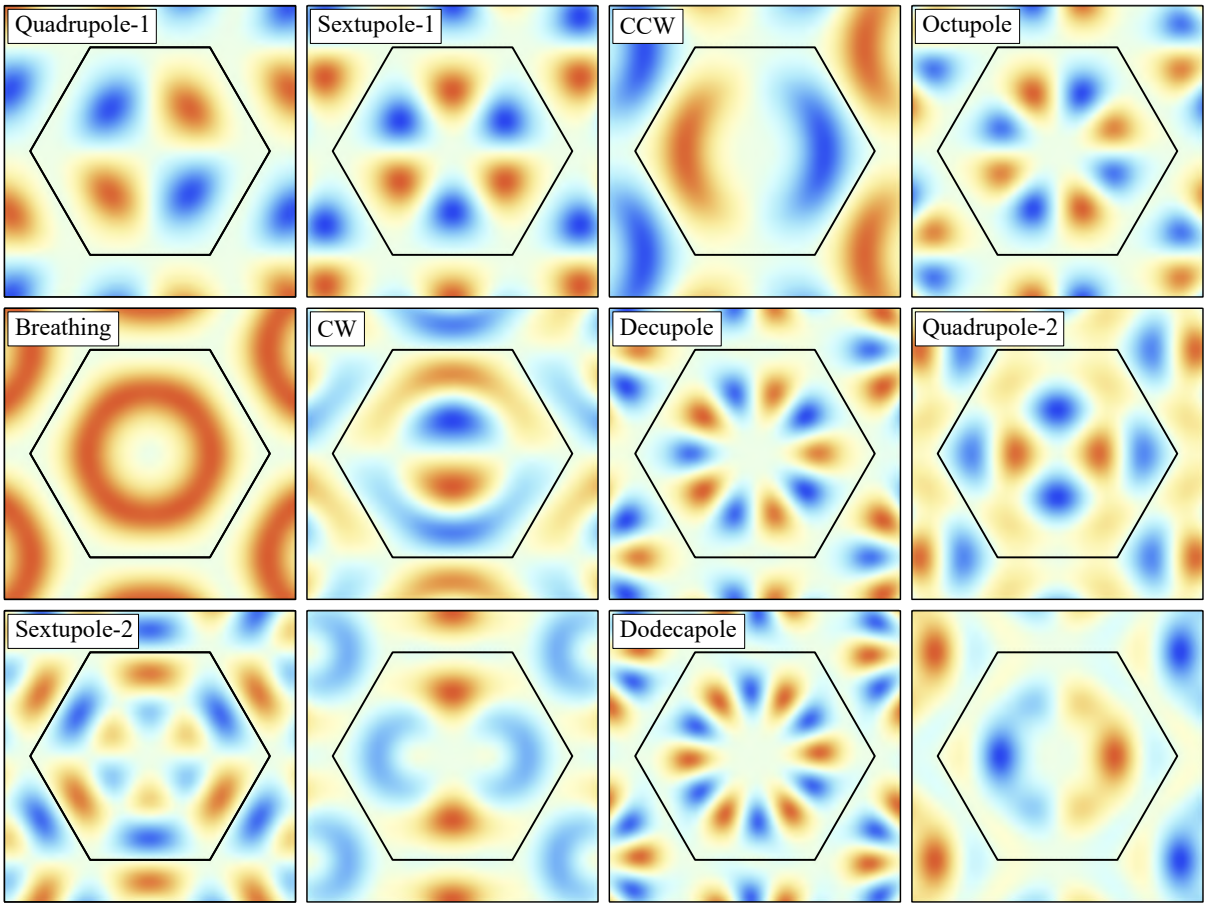

Figure 3.3.: **Spatial profile of the SkL spinwave functions.** Snapshots at a fixed time of the spatial profile of the out-of-plane component δM_z. The solutions are calculated at the Γ-point of the Brillouin zone, with colours indicating that the spinwave points parallel (red) or anti-parallel (blue) to the applied magnetic field. The hexagon in each panel is the Wigner-Seitz cell, whose extension is given by the skyrmion lattice constant a_{SkL}.

three fundamental modes have been the subject of extensive research because they can be directly excited by applying a spatially uniform, time-dependent magnetic field. In fact, they yield a finite oscillating homogeneous magnetisation, $\delta\mathbf{m}_{\alpha,\mathbf{Q}=\mathbf{0}}(\mathbf{q}=\mathbf{0}) \neq \mathbf{0}$, therefore they possess a macroscopic alternating current (AC) magnetic dipole moment. Consequently, they couple efficiently to microwave fields, making them visible in microwave spectroscopy [46–51] and other experimental probes like resonant elastic x-ray scattering [52] and time-resolved magneto-optics [53, 54]. Other modes generically do not yield a microwave response, and their characteristics as well as functionalities are mostly unexplored. Only for specific values of the magnetic field, the cubic crystalline environment hybridized the CCW and the breathing resonance, respectively, with a sextupole-1 and octupole mode such that these otherwise dark modes left a characteristic frequency gap in the microwave response [50]. These three modes get their names from the corresponding time evolution of the total magnetisation $\mathbf{M}(\mathbf{r},t)$. In particular, the CCW mode corresponds to a collective gyration of skyrmions around their equilibrium positions in a counterclockwise sense. Locally, each skyrmion core undergoes a circular trajectory, while the surrounding spin

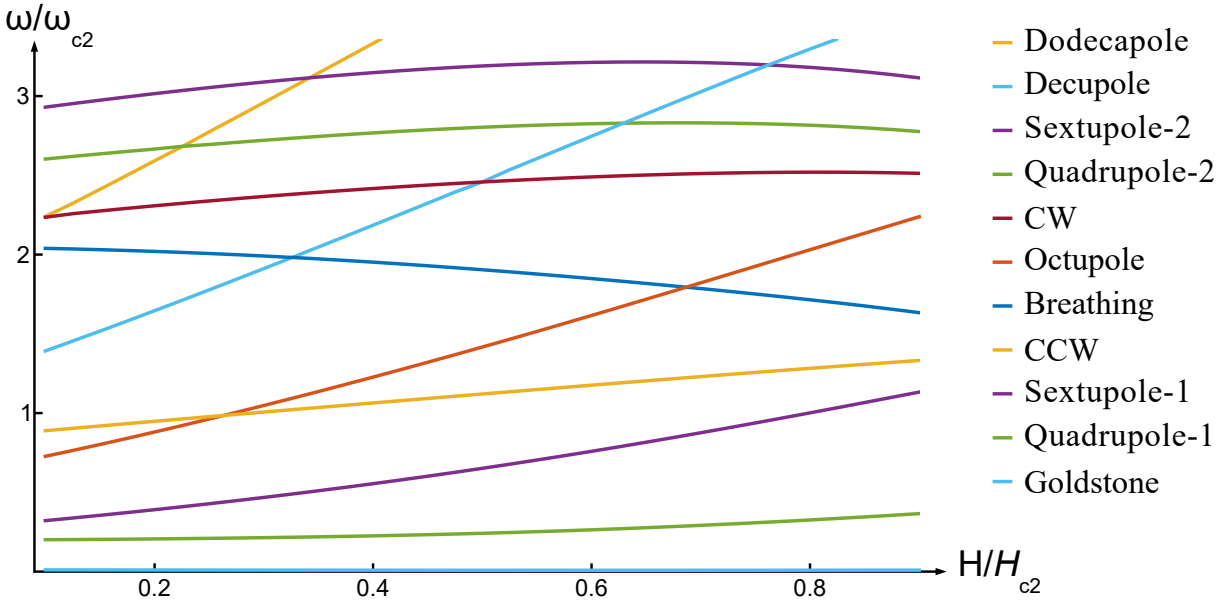

Figure 3.4.: **Resonance frequencies of the skyrmion lattice.** The low-energy resonance frequencies have been calculated at the Γ-point for $\xi_{ms} = 0.88$, $\lambda = 500$, and frequencies in the range $0 \leq \omega/2\pi \leq 3.2$. The identification of each mode is determined by the wavefunction analysis shown in Fig. 3.3.

texture follows coherently. The breathing mode represents a radial oscillation of each skyrmion core. During this excitation, the skyrmion periodically expands and contracts, while its centre remains fixed. Finally, in contrast to the CCW gyration, the CW mode describes a collective clockwise rotation of the skyrmion cores. This excitation is not simply the time-reversed partner of the CCW mode: the two are split in frequency, with the CW mode appearing at higher energies due to the gyroscopic force described in Section 3.1.

In Fig. 3.3, we introduce an additional classification of the lowest excitation modes of the skyrmion lattice. This scheme is based on the multipolar character and radial structure of the corresponding spinwave eigenfunctions. For instance, the mode labelled quadrupole-1 refers to the eigenfunction $\delta\mathbf{M}_{\alpha=1}(\mathbf{r},t)$ that exhibits a quadrupolar symmetry within the unit cell, with no radial nodes. In contrast, quadrupole-2 is distinguished by the presence of a radial node at a finite distance from the skyrmion core, dividing the eigenfunction into an inner and an outer oscillating ring inside the magnetic unit cell. Within this framework, the familiar CCW, breathing, and CW excitations correspond to dipole-1, monopole, and dipole-2, respectively. Nevertheless, in the following we adopt the conventional nomenclature for these three modes, since it is widely used in the literature and more directly conveys their dynamical character. In fact, the purely multipolar classification captures the spatial symmetry of the eigenfunctions, but does not account for essential dynamical features, such as the sense of rotation of the oscillation. This limitation becomes particularly evident for more complex excitations: for example, in the sextupole-2 mode the inner and outer rings rotate in opposite directions, a feature that cannot be inferred from multipolar symmetry alone. A detailed visualization of the time evolution of all the modes shown in Fig. 3.3 is

provided in the Appendix. Moreover, the multipolar classification fails to capture the character of the higher–energy excitations, such as the two highest modes displayed here. We do not attempt to refine the classification at this stage, since these modes play no role in the experimental observations reported in this Thesis. Nonetheless, it is important to note that the excitation spectrum of the skyrmion lattice can exhibit a remarkably intricate band structure, whose full description requires a more elaborate framework. Fig. 3.4 displays the magnetic field dependence of the spinwave eigenfrequencies at zero wavevector. While most modes exhibit only a weak variation with field, certain excitations, such as the octupole and decupole modes, show a pronounced field sensitivity. The different behaviour enables the hybridisation between specific modes, which can be induced, for example, by magneto-crystalline anisotropy [50] or via magneto-optic coupling [74].

3.3.3 Spectrum

In this Section we finally present the spinwave spectra of the hexagonal skyrmion lattice configuration. Figure 3.5 shows the calculated magnon bands for an in-plane wavevector, restricted to the first Brillouin zone, i.e., $\mathbf{q} \perp \mathbf{H}$ with $\mathbf{q} \in 1^{\text{st}}$ BZ. We see the emergence of a low-energy excitation with quadratic dispersion, $\omega \sim |\mathbf{q}|^2$, at small wavevectors. This mode is the Goldstone mode of the skyrmion lattice [113]. Its origin can be traced back to the spontaneous breaking of continuous translational symmetry: the underlying Hamiltonian is invariant under arbitrary translations in the plane, but the formation of a periodic magnetic lattice fixes a discrete set of lattice positions. According to Goldstone's theorem, this broken symmetry implies the existence of a gapless mode. Physically, it corresponds to the translational motion of the entire skyrmion lattice, analogous to phonons in a crystal. The quadratic dispersion reflects the fact that the skyrmion lattice is a two-dimensional object without restoring forces against rigid translations, leading to a particularly soft mode at long wavelengths. Some branches remain almost dispersionless (flat bands), such as the sextupole-1 mode. In contrast, other modes, such as the the CCW and breathing modes, display strong dispersions within the magnetic BZ. This indicates that their excitation energy at finite wavevector can vary significantly from the zero-momentum case typically probed in experiments.

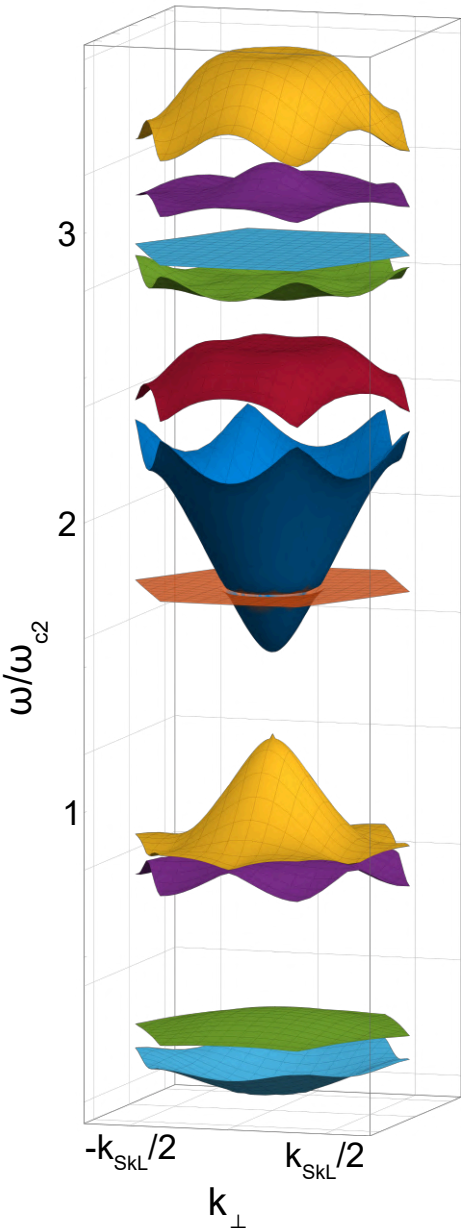

Figure 3.5.: **Magnon band structure.** Magnon band structure calculated for in-plane wavevectors $\mathbf{k} \perp \mathbf{H}$ within the first magnetic Brillouin zone. The first 11 excitation modes are shown here, calculated for $H/H_{c2} = 0.5$, $\xi_{ms} = 0.88$ and $\lambda = 500$. The modes can be identified according to the colour coding reported in Fig. 3.4 and Fig. 3.6.

Figure 3.6 presents the magnon spectra for propagation along the applied magnetic field direction, i.e., parallel to the skyrmion tubes. Here we restrict to the case $|\mathbf{q}_\perp| = 0$, such that the wavevector is purely longitudinal. As expected, the gapless Goldstone mode continuously approaches zero energy in the long-wavelength limit $q_\parallel \to 0$. Moreover, the spectra are dominated by a pronounced non-reciprocity: the dispersion at $+q_\parallel$ differs significantly from that at $-q_\parallel$.

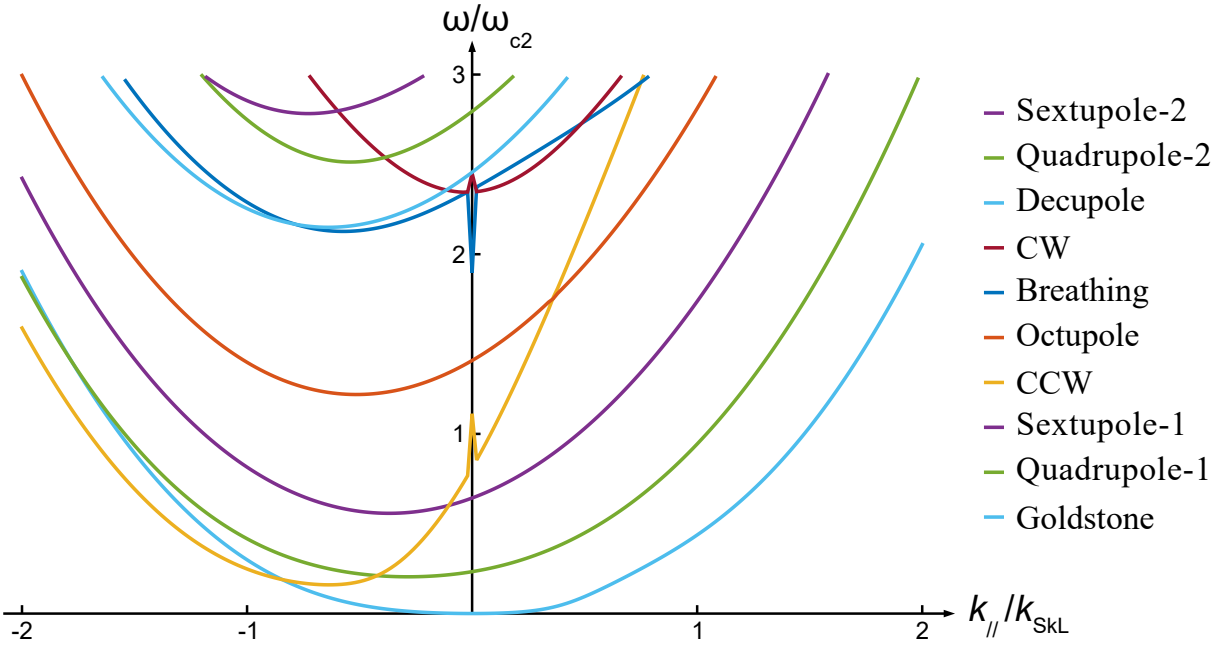

Figure 3.6.: **Magnon dispersion for longitudinal wavevectors.** Theoretically calculated dispersion for $|\mathbf{k}_\perp| = 0$, $H/H_{c2} = 0.5$, $\xi_{ms} = 0.88$ and $\lambda = 500$. The dipole active modes are discontinuous for $\mathbf{k}_\parallel \to 0$ due to approximations of the dipolar interaction. Among all the low-energy excitations, the CCW mode shows the strongest non-reciprocity.

This asymmetry is a direct consequence of broken inversion symmetry in the chiral magnetic texture, enhanced by the dipolar interaction. Among the various branches, the CCW mode exhibits the most striking non-reciprocity. Combined with its dipolar nature and resonance frequency lying in the experimentally accessible GHz range, this makes it the most relevant excitation for studying directional spinwave propagation in skyrmion lattices [76]. Interestingly, several modes display an apparent discontinuity as $q_\parallel \to 0$. This behaviour originates from the approximations used in treating the dipolar interaction. In our energy functional, the dipolar term was expanded only in the asymptotic limits $|\mathbf{k}| \gg 1/L$ and $|\mathbf{k}| \ll 1/L$, where L denotes the system size. The intermediate regime, however, is not captured within this approximation, leading to an artificial mismatch at small wavevectors. A more accurate treatment of the dipolar kernel would likely resolve this discrepancy, but lies beyond the scope of the present work.

3.3.4 Experimental observations

Over the past decade, substantial efforts have been made to probing the dynamical properties of the skyrmion lattice phase. To date, two complementary classes of experimental techniques have been most widely employed: homogeneous excitation methods, such as wave-guide microwave spectroscopy [46–51], resonant elastic x-ray scattering [52] and time-resolved magneto-optic Kerr effect (TR-MOKE) [53, 54], and momentum-resolved probes, most notably inelastic neutron scattering [43]. These approaches differ not only in the type of information they yield, but also in the aspects of the magnon spectrum that

they are naturally sensitive to.

Homogeneous excitation techniques probe the system's response to spatially uniform time-dependent magnetic fields. As such, they selectively couple to modes at zero momentum, $\mathbf{q} = 0$, corresponding to oscillations that are spatially coherent over the entire sample. Experiments of this kind were able to investigate the properties of dipole-active modes, i.e., the counter-clockwise, clockwise and breathing modes. These modes appear as sharp absorption resonances in the gigahertz range and constitute clear dynamical fingerprints of the SkL phase. Importantly, their frequencies and relative spectral weights provide valuable insight into the stability and internal structure of skyrmions. However, by construction, homogeneous excitation experiments are blind to the momentum dependence of the excitations. They cannot resolve how the magnon modes disperse throughout the Brillouin zone, nor can they access directly higher-order internal modes whose dipole matrix elements vanish for uniform driving.

In contrast, inelastic neutron scattering provides a direct window into the full magnon band structure. By measuring the energy and momentum transfer associated with neutron spin-flip processes, this technique resolves excitations much beyond the first magnetic Brillouin zone. A recent neutron scattering study has confirmed the existence of dispersing Goldstone modes arising from the broken translational symmetry of the SkL [43], as well as the coexistence of flat and strongly dispersive branches at finite wavevector. These results complement the picture obtained from homogeneous driving by providing a momentum-resolved map of the spinwave spectrum. At the same time, this neutron scattering experiment was only able to explore the convoluted signal of a manifold of spinwave excitations without resolving individual magnon bands.

Taken together, these two classes of experiments provide a valuable, though still incomplete, picture of the skyrmion lattice spinwave dynamics in bulk chiral magnets. In particular, the intermediate regime of wavevectors $|\mathbf{q}| \sim k_{\mathrm{SkL}}$ remains largely unexplored, despite its crucial relevance for signal-processing and computational schemes based on propagating magnons. In the following Chapters, we take a step toward addressing this gap by presenting two complementary projects that extend beyond the current state of the art. In the first project, magneto-optic coupling is exploited to probe spinwave dynamics with wavelengths comparable to the inter-skyrmion distance. Through micro-focused Brillouin light scattering, we resolve several multipole excitation modes across a wide magnetic-field range. In addition to the dipolar counterclockwise, breathing, and clockwise modes, a quantitative comparison between experimental spectra and theoretical predictions enabled the identification of the quadrupole-2 and, possibly, the sextupole-2 modes [74]. The second project investigates the role of magneto-elastic coupling within the skyrmion lattice phase. Here, spinwaves and acoustic phonons interact at finite wavevector, giving rise to magnon–phonon hybrid modes. Ultrasonic measurements of the phonon velocity reveal clear signatures of this coupling, allowing the indirect identification of the low-energy quadrupole-1 magnon

mode [114]. Together, these studies extend our understanding of skyrmion lattice dynamics into previously unexplored regimes, thereby bridging the gap between traditional experimental probes and future applications in magnonics.

4 Theoretical description of Brillouin light scattering

In this Chapter, we introduce the experimental technique of micro-focused Brillouin light scattering (BLS) spectroscopy, which serves as a powerful tool for probing finite momentum spinwave dynamics with frequency resolution. We first present the theoretical foundations of BLS in its most general framework, emphasizing how magneto-optic coupling enables the detection of spinwave spectra. This interaction is conveniently described in terms of the photon–magnon scattering process, which provides a clear picture of how incident light couples to collective magnetic excitations. Finally, we discuss the specific implementation of the micro-focused setup, deriving the general expression for the corresponding BLS cross section.

4.1 Magneto-optic coupling

Brillouin scattering describes the interaction between an electromagnetic field, typically provided by a monochromatic laser, and low-energy excitations in a crystalline medium. Depending on the nature of

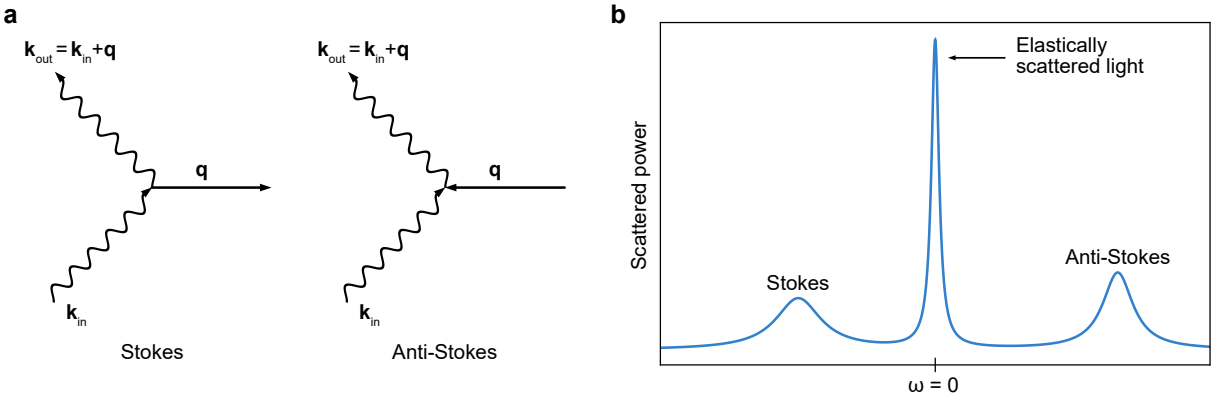

Figure 4.1.: **Schematic diagram of inelastic Brillouin light scattering.** **(a)** Emission (Stokes) and absorption (anti-Stokes) diagrams of a quasiparticle with wavevector **q** induced by the incident light. **(b)** Typical BLS spectra which measures the frequency shift of the scattered photons with respect to the elastically scattered light.

the excitation, the scattered light can couple to acoustic vibrations (phonons), charge-density fluctuations (polarons), or spin oscillations (magnons). In this dissertation, our focus is exclusively on the magnonic case. Nevertheless, the scattering geometry and theoretical framework developed here can be readily adapted to describe the other types of interactions as well [115–117].

Fig. 4.1**a** shows the fundamental mechanism underlying inelastic Brillouin light scattering. In this process, an incoming photon with wavevector $\mathbf{k}_{\text{in}}$ interacts with the magnetic medium and either emits or absorbs a quasiparticle of wavevector $\mathbf{q}$. As a result, the photon is scattered with momentum $\mathbf{k}_{\text{out}} = \mathbf{k}_{\text{in}} + \mathbf{q}$. Energy-momentum conservation law implies that the scattered quasiparticle possesses energy $\hbar\omega = \hbar c'(|\mathbf{k}_{\text{in}}| - |\mathbf{k}_{\text{out}}|)$, where c' is the speed of light within the magnetic sample. Depending on whether the magnon is created or annihilated in the scattering event, the process corresponds to a Stokes or anti-Stokes transition, respectively. This frequency shift produces the characteristic BLS spectrum shown in Fig. 4.1**b**, which provides direct access to the spinwave dynamics of the system [117]. In particular, BLS can reveal non-reciprocity of spinwaves, manifested as asymmetries in the spectral peaks of the Stokes and anti-Stokes lines. Since these processes probe magnons propagating in opposite directions, such differences are especially pronounced in chiral magnets, where broken inversion symmetry plays a key role [73, 118, 119]. It is also worth to compare BLS with inelastic Raman scattering: while both rely on light–matter interactions, BLS probes much lower excitation energies and correspondingly smaller wavevectors. This makes it particularly well suited for investigating magnetic excitations over mesoscopic length scales, such as those found in skyrmion lattices. These advantages, together with its non-destructive character and high spectral sensitivity, explain why BLS has become an increasingly powerful and widely adopted technique in modern magnonics [14, 15, 19, 120–124].

4.1.1 Differential scattering cross section

According to Landau and Lifshitz's formulation of electrodynamics, the photon–magnon differential scattering cross section can be expressed in terms of the dielectric permittivity tensor, $\varepsilon_{\mu\nu}(\mathbf{r},t)$, and the polarization vectors of the incoming and outgoing photons, $\mathbf{e}_{\text{in/out}}$. In its general form, it reads [125]

$$\frac{d\sigma_{\text{out,in}}(\mathbf{q},\omega)}{d\Omega'_{\text{out}}} \propto \mathbf{e}_{\text{out},\mu}\, \mathbf{e}^*_{\text{in},\nu}\, \mathbf{e}^*_{\text{out},\lambda}\, \mathbf{e}_{\text{in},\delta}\, \langle \delta\varepsilon^*_{\mu\nu}(\mathbf{r},t)\delta\varepsilon_{\lambda\delta}(\mathbf{r}',t')\rangle_{\mathbf{q},\omega}\,, \tag{4.1}$$

up to a prefactor that depends on the optical frequency. This expression shows explicitly that the photon scattering probability is governed by the correlation function of the fluctuations of the dielectric tensor. In other words, the magneto-optic coupling enters the cross section through the dependence of $\varepsilon_{\mu\nu}$ on the magnetization $\mathbf{M}(\mathbf{r},t)$. During inelastic scattering, part of the spinwave angular momentum is transferred to the photon, leading to a characteristic 90° rotation of the scattered polarization vector $\mathbf{e}_{\text{out}}$ relative to the incident one $\mathbf{e}_{\text{in}}$ [126, 127]. The derivation of Eq. (4.1) further assumes that the frequency shift is small compared to the photon frequency, i.e., $\omega/(c'|\mathbf{k}_{\text{in}}|) \ll 1$. This condition is naturally fulfilled in

standard BLS, which focuses on the detection of low-energy excitations compared to other experimental techniques based on inelastic light scattering such as Raman spectroscopy.

In noncentrosymmetric helimagnets, continuous translational invariance is in general broken, hence the correlation function of dielectric fluctuations can be expressed as

$$\langle \delta\varepsilon^*_{\mu\nu}(\mathbf{r},t)\delta\varepsilon_{\lambda\delta}(\mathbf{r}',t')\rangle_{\mathbf{q},\omega} = \frac{1}{V}\int d\mathbf{r}d\mathbf{r}'dt\, e^{-i\mathbf{q}\cdot(\mathbf{r}-\mathbf{r}')+i\omega t}\,\langle \delta\varepsilon^*_{\mu\nu}(\mathbf{r},t)\delta\varepsilon_{\lambda\delta}(\mathbf{r}',0)\rangle\,, \tag{4.2}$$

where V is the volume of the system. Here, we are only interested in the magnetic contribution of the dielectric permittivity tensor, which can be expressed as a series expansion in the magnetisation. Up to second order in $\mathbf{M}(\mathbf{r},t)$, this tensor reduces to [118]

$$\varepsilon_{\mu\nu}(\mathbf{r},t) = K_{\mu\nu\lambda}\mathbf{M}_\lambda(\mathbf{r},t) + G_{\mu\nu\lambda\delta}\mathbf{M}_\lambda(\mathbf{r},t)\mathbf{M}_\delta(\mathbf{r},t)\,, \tag{4.3}$$

where K and G are the magneto-optic coupling tensors of first and second order, respectively. Their structure is constrained by the crystal symmetry class. For instance, in cubic magnets such as Cu_2OSeO_3, one finds $K_{\mu\nu\lambda} = K\varepsilon_{\mu\nu\lambda}$, where $\varepsilon_{\mu\nu\lambda}$ is the anti-symmetric Levi-Civita tensor, while the quartic term $G_{\mu\nu\lambda\delta}$ reduces to just three independent parameters: G_{11}, G_{12}, and G_{44}. In particular, we get $G_{xxxx} = G_{yyyy} = G_{zzzz} = G_{11}$, $G_{xxyy} = G_{xxzz} = G_{yyzz} = G_{12}$, and $G_{xyxy} = G_{xzxz} = G_{yzyz} = G_{44}$ [128, 129]. Within linear spinwave theory, the magnetization can be expanded around the equilibrium profile, $\mathbf{M}(\mathbf{r},t) = \mathbf{M}_{\rm eq}(\mathbf{r}) + \delta\mathbf{M}(\mathbf{r},t)$, where $\delta\mathbf{M}$ represents the magnon excitations. Substituting this into the expression for $\varepsilon_{\mu\nu}$ and retaining only linear terms in $\delta\mathbf{M}$ gives

$$\delta\varepsilon_{\mu\nu}(\mathbf{r},t) = K_{\mu\nu\lambda}\delta\mathbf{M}_\lambda(\mathbf{r},t) + 2G_{\mu\nu\lambda\delta}\mathbf{M}_{{\rm eq},\lambda}(\mathbf{r})\delta\mathbf{M}_\delta(\mathbf{r},t) + \mathscr{O}(\delta\mathbf{M}^2)\,. \tag{4.4}$$

Consequently, magnon excitations generate time-dependent fluctuations of the dielectric tensor, which directly enter the scattering cross section in Eq. (4.1). Explicitly, the correlation function can be expressed as

$$\langle \delta\varepsilon^*_{\mu\nu}(\mathbf{r},t)\delta\varepsilon_{\lambda\delta}(\mathbf{r}',0)\rangle = \left(K^*_{\mu\nu\xi} + G^*_{\mu\nu\rho\xi}\mathbf{M}_{{\rm eq},\rho}(\mathbf{r})\right)\left(K_{\lambda\delta\xi'} + G_{\lambda\delta\rho'\xi'}\mathbf{M}_{{\rm eq},\rho'}\right)\langle \delta\mathbf{M}_\xi(t,\mathbf{r})\delta\mathbf{M}_{\xi'}(0,\mathbf{r}')\rangle\,. \tag{4.5}$$

This result shows how the BLS differential cross section depends both on the magnetic equilibrium configuration, as well as the corresponding spinwave solutions. Through magneto-optic coupling, we are able to describe how magnons produce fluctuations of the dielectric tensor, which modulate the optical field inside the material. This leads to inelastic scattering of photons that exchange their energy and momentum with spinwave excitations. In other words, the BLS signal provides an optical fingerprint of the magnon spectrum, with the intensity and symmetry of the peaks directly reflecting the underlying spinwave dynamics and crystal symmetries.

4.1.2 Fluctuation-dissipation theorem

In this Section, we employ the fluctuation–dissipation theorem to draw the connection between the magnetic correlation function and the dissipative part of the magnetic susceptibility. We begin by assuming that the system responds linearly to a weak perturbing source, $\phi_j(t)$. In this case, the change in the expectation value of an operator $\mathscr{O}_i(t)$ is linear in the perturbation,

$$\delta\langle\mathscr{O}_i(t)\rangle = \int dt'\,\chi_{ij}(t;t')\phi_j(t')\,, \tag{4.6}$$

where $\chi_{ij}(t;t')$ is known as the linear response function. We further assume that the system is invariant under time translation, thus $\chi_{ij}(t;t') = \chi_{ij}(t-t')$ only depends on the time difference, and the Fourier transform of Eq. (4.6) reduces to

$$\delta\langle\mathscr{O}_i(\omega)\rangle = \int dt'dt\, e^{i\omega t}\chi_{ij}(t-t')\phi_j(t') = \int dt'dt\, e^{i\omega(t-t')}\chi_{ij}(t-t')e^{i\omega t'}\phi_j(t') = \chi_{ij}(\omega)\phi_j(\omega)\,. \tag{4.7}$$

In particular, we are interested in the imaginary part of the response function, $\chi''_{ij}(\omega)$, which is associated with dissipative processes in the system. This can be understood from the lack of time-reversal invariance:

$$\chi''(\omega) = -\frac{i}{2}\Big(\chi(\omega)-\chi^*(\omega)\Big) = -\frac{i}{2}\int dt\,\chi(t)\left(e^{i\omega t}-e^{-i\omega t}\right) = -\frac{i}{2}\int dt\, e^{i\omega t}\Big(\chi(t)-\chi(-t)\Big)\,, \tag{4.8}$$

which vanishes only if $\chi(t)$ is invariant under $t \to -t$. Another key ingredient is the Kubo formula, which expresses the response function in terms of commutators of operators,

$$\chi_{ij}(t-t') = -i\theta(t-t')\langle[\mathscr{O}_i(t),\mathscr{O}_j(t')]\rangle\,, \tag{4.9}$$

where the expectation value is calculated in the canonical ensemble. The density matrix $\rho = e^{\beta H}$ allows us to write the expectation value of an operator as

$$\langle\mathscr{O}_i(t)\rangle = \mathrm{Tr}\Big[\rho\,\mathscr{O}_i(t)\Big]\,. \tag{4.10}$$

The Kubo formula shows how the system's response is fundamentally linked to two-point quantum correlation functions.

To proceed, we evaluate the dissipative part of the response function. Using Eq. (4.9), one obtains

$$\begin{aligned}\chi''_{ij}(t) &= -\frac{i}{2}\Big(\chi_{ij}(t)-\chi_{ji}(-t)\Big) \\ &= -\frac{1}{2}\theta(t)\Big(\langle\mathscr{O}_i(t)\mathscr{O}_j(0)\rangle - \langle\mathscr{O}_j(0)\mathscr{O}_i(t)\rangle\Big) + \frac{1}{2}\theta(-t)\Big(\langle\mathscr{O}_j(-t)\mathscr{O}_i(0)\rangle - \langle\mathscr{O}_i(0)\mathscr{O}_j(-t)\rangle\Big)\,,\end{aligned} \tag{4.11}$$

where we used the time translational invariance to set $t' = 0$. Under the same assumption, we get $\langle \mathscr{O}_j(0)\mathscr{O}_i(t)\rangle = \langle \mathscr{O}_j(-t)\mathscr{O}_i(0)\rangle$, which then leads to

$$\chi''_{ij}(t) = -\frac{1}{2}\langle \mathscr{O}_i(t)\mathscr{O}_j(0)\rangle + \frac{1}{2}\langle \mathscr{O}_j(-t)\mathscr{O}_i(0)\rangle\,. \tag{4.12}$$

The second correlation function can be rewritten using the cyclic property of the trace in the canonical ensemble,

$$\langle \mathscr{O}_j(-t)\mathscr{O}_i(0)\rangle = \mathrm{Tr}\left[e^{-\beta H}\mathscr{O}_j(-t)e^{\beta H}e^{-\beta H}\mathscr{O}_i(0)\right] = \mathrm{Tr}\left[e^{-\beta H}\mathscr{O}_i(0)\mathscr{O}_j(-t+i\beta)\right] = \langle \mathscr{O}_i(t-i\beta)\mathscr{O}_j(0)\rangle\,, \tag{4.13}$$

which connects real-time and imaginary-time correlations. Finally, Fourier transforming Eq. (4.12) yields the fluctuation–dissipation theorem:

$$\chi''_{ij}(\omega) = -\frac{1}{2}\left(1 - e^{-\beta\omega}\right)\int dt\, e^{i\omega t}\langle \mathscr{O}_i(t)\mathscr{O}_j(0)\rangle \tag{4.14}$$

which relates the fluctuation in frequency space, captured by the time integral, to the dissipation, represented by $\chi''_{ij}(\omega)$. This fundamental relation shows that fluctuations of observables in thermal equilibrium are directly tied to the dissipative response of the system.

This expression can be used to rewrite the magnon correlation function that appears in Eq. (4.5) by identifying the operator $\mathscr{O}_\xi(t) \to \delta\mathbf{M}_\xi(\mathbf{r},t)$. In this case the fluctuation-dissipation theorem reads

$$\langle \delta\mathbf{M}_\xi(\mathbf{r},t)\delta\mathbf{M}_{\xi'}(\mathbf{r}',0)\rangle_\omega = -\frac{2\hbar}{1-e^{-\beta\hbar\omega}}\,\chi''_{\xi\xi'}(\mathbf{r},\mathbf{r}';\omega)\,, \tag{4.15}$$

where $\chi''_{\xi\xi'}(\mathbf{r},\mathbf{r}';\omega)$ denotes the magnetic susceptibility. In the low-energy limit, i.e., for $\beta\hbar\omega \ll 1$, the BLS differential scattering cross section from Eq. (4.1) simplifies to [73]

$$\frac{d\sigma_{\mathrm{out,in}}(\mathbf{q},\omega)}{d\Omega'_{\mathrm{out}}} \propto \frac{2}{\beta\omega}\frac{1}{V}\int d\mathbf{r}d\mathbf{r}'\, e^{-i\mathbf{q}\cdot(\mathbf{r}-\mathbf{r}')}\upsilon^*_\xi(\mathbf{r})\,\chi''_{\xi\xi'}(\mathbf{r},\mathbf{r}';\omega)\,\upsilon_{\xi'}(\mathbf{r}')\,, \tag{4.16}$$

where we defined the auxiliary vector

$$\upsilon_{\xi'}(\mathbf{r}') = \mathbf{e}^*_{\mathrm{out},\lambda}\,\mathbf{e}_{\mathrm{in},\delta}\left(K_{\lambda\delta\xi'} + G_{\lambda\delta\rho'\xi'}\mathbf{M}_{\mathrm{eq},\rho'}(\mathbf{r}')\right). \tag{4.17}$$

Equation (4.16) provides the general expression for the differential BLS cross section in the case of scattering between monochromatic plane waves and magnons.

4.1.3 Spectral weights

In order to evaluate the BLS scattering cross section in Eq. (4.16), one needs to compute the magnetic susceptibility $\chi''_{\xi\xi'}(\mathbf{r},\mathbf{r}';\omega)$ for the different ordered phases of a chiral magnet. According to the fluctuation–dissipation theorem [Eq. (4.15)], the imaginary part of the magnetic susceptibility reduces to

$$\chi''_{\xi\xi'}(\mathbf{r},\mathbf{r}';\omega) \simeq \frac{\omega}{2k_{\mathrm{B}}T}\left\langle \delta\mathbf{M}_{\xi}(\mathbf{r},t)\delta\mathbf{M}_{\xi'}(\mathbf{r}',0)\right\rangle_{\omega} \tag{4.18}$$

in the limit of $\beta\hbar\omega \ll 1$, which applies to standard BLS experiments. Substituting the Holstein–Primakoff representation of the spinwave excitations introduced in Eq. (3.8), the right-hand side of this expression takes the form

$$\chi''_{\xi\xi'}(\mathbf{r},\mathbf{r}';\omega) = -\frac{g\mu_B M_s}{2i}\Big(\hat{e}_{+,\xi}(\mathbf{r}),\hat{e}_{-,\xi}(\mathbf{r})\Big)\left[g^{\mathrm{R}}(\mathbf{r},\mathbf{r}';\omega)-g^{\mathrm{A}}(\mathbf{r},\mathbf{r}';\omega)\right]\begin{pmatrix}\hat{e}_{-,\xi'}(\mathbf{r}')\\ \hat{e}_{+,\xi'}(\mathbf{r}')\end{pmatrix}, \tag{4.19}$$

where $\hat{e}_{\pm} = (\hat{e}_x \pm i\hat{e}_y)/\sqrt{2}$ is defined with respect to the locally orthogonal frame $\{\hat{e}_x,\hat{e}_y,\hat{e}_z\}$. The retarded Green's function is naturally defined as

$$g^{\mathrm{R}}_{ij}(\mathbf{r},\mathbf{r}';\omega) = -\frac{i}{\hbar}\int_0^{\infty} dt\, e^{i\omega t}\left\langle\Big[\mathbf{\Psi}_i(\mathbf{r},t),\mathbf{\Psi}^{\dagger}_j(\mathbf{r}',0)\Big]\right\rangle, \tag{4.20}$$

where $i,j=1,2$, and $\mathbf{\Psi}^T=(\psi,\psi^*)$ is the bosonic spinor field introduced in the previous Chapter. The advanced Green's function follows from the complex conjugation of Eq. (4.20)

$$g^{\mathrm{A}}_{ij}(\mathbf{r},\mathbf{r}';\omega) = \left(g^{\mathrm{R}}_{ij}(\mathbf{r}',\mathbf{r};\omega)\right)^{\dagger}. \tag{4.21}$$

Therefore, the entire problem of determining the BLS response reduces to computing the retarded Green's function for the different magnetic textures across the phase diagram of chiral magnets.

In the field-polarised phase, the retarded Green's function in reciprocal space is obtained from the Dyson equation

$$\Big(\hbar(\omega+i0^+)\tau_z-\mathscr{H}\Big)g^{\mathrm{R}}(\mathbf{q},\omega)=\mathbb{I}, \tag{4.22}$$

where $\mathscr{H}$ denotes the BdG Hamiltonian introduced in Eq. (3.15). Here, we consider the case of bulk magnetic samples and laser wavelengths in the visible range, hence the finite photon momentum transfer

selects the regime $|\mathbf{q}| \gg 1/L$ for the dipolar interaction. Therefore, we find an explicit solution that reads [73]

$$g^{\mathrm{R}}(\mathbf{q},\omega) = \frac{1}{\Big(\hbar\omega + i0^{+} - \hbar\omega^{\mathrm{r}}(\mathbf{q})\Big)\Big(\hbar\omega + i0^{+} + \hbar\omega^{\mathrm{r}}(-\mathbf{q})\Big)} \times \left[\hbar\omega\tau_z + \mathscr{D}\Big(|\mathbf{q}|^2\mathbb{I} - 2Qq_z\tau_z\Big) + g\mu_B\mu_0 H_{\mathrm{int}}\mathbb{I} + \frac{g\mu_B\mu_0 M_s}{2|\mathbf{q}|^2}\begin{pmatrix} q_+q_- & q_-^2 \\ q_+^2 & q_+q_- \end{pmatrix}\right], \tag{4.23}$$

where $\omega^{\mathrm{r}}(\mathbf{q})$ denotes the resonance frequency of the spinwave excitations derived in Eq. (3.16). At fixed momentum $\mathbf{q}$, the Green's function contains only simple poles, corresponding to delta-function contributions in the spectral density. This reflects the fact that, according to the lossless Landau–Lifshitz equation of motion, magnons are perfectly sharp quasiparticles and scattering can only occur exactly at the resonance frequency $\omega^{\mathrm{r}}(\mathbf{q})$.

A similar procedure applies to the conical and skyrmion lattice phases. In these cases, the retarded Green's function is again obtained from the Dyson equation, but the inversion of the corresponding operator is no longer analytically tractable, unlike in the simple field-polarised phase. Instead, one must rely on numerical methods, which can be constructed using the magnon eigenmodes $\delta\mathbf{M}$ derived in the previous Chapter. These numerical Green's functions provide the basis for evaluating the BLS response in non-collinear magnetic phases. The results of this analysis will be presented in the next Chapter, in the context of micro-focused BLS spectroscopy.

4.2 Theory of micro-focused BLS

In this Section, we present the theoretical model developed to describe micro-focused Brillouin light scattering. We begin by outlining the experimental setup, highlighting the key features that characterise the micro-focused configuration. We then calculate the spatial distribution of the electric field resulting from the focusing of the BLS laser onto the magnetic sample. Finally, we derive the scattering cross section for the general case of incoherent magnon-photon scattering, based on the coupling between the spinwave excitations and the electric field. This derivation constitutes one of the main contributions of this dissertation, as it provides a general analytical framework for interpreting a broad class of micro-focused BLS experiments, thus filling an important gap in the literature.

4.2.1 Experimental setup

The experimental setup for the cryogenic micro-focused BLS measurements is illustrated in Fig. 4.2 [117]. A monochromatic continuous-wave laser with wavelength λ_{in} is focused onto the top surface of the magnetic sample using an objective lens. This generates an electric field distribution that interacts with spinwave excitations during the inelastic scattering processes, which will be examined in detail in the

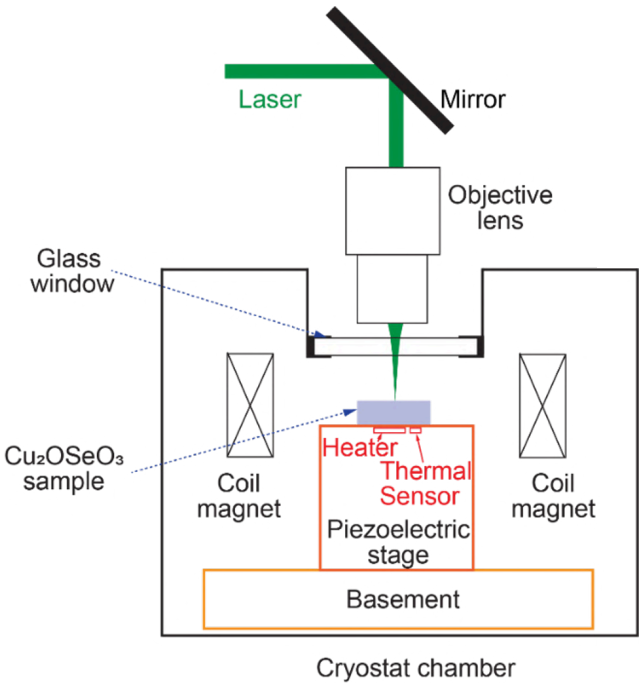

Figure 4.2.: **Micro-focused BLS experimental setup.** Schematic diagram of the experimental setup for the micro-focused BLS used in the Chapter 5 to map the magnon spectra in Cu_2OSeO_3. The picture is adapted from [133].

following Section. In general, the setup may include a magnon source, such as a microwave antenna, to generate coherent spinwave excitations inside the magnetic sample. Here, we exclusively consider incoherent, thermally excited magnons that are present in the sample. A polarising filter ensures that the laser beam reaches the objective lens with a defined linear polarisation. A second polarising element, oriented at 90 degrees with respect to the incident beam, selectively transmits only those photons that have undergone a change in polarisation due to light-matter interaction, thereby isolating the scattered signal. The reflected light is then analysed using a Fabry–Perot interferometer, which measures the frequency shift relative to the reference laser peak.

This experimental setup can be employed to perform various types of measurements, such as time-resolved or spatially resolved studies [123, 124, 130–132]. In this work, however, we focus exclusively on the indirect measurement of magnon spectra at fixed magnetic field. During each measurement run, the applied magnetic field, laser position, and temperature are kept constant. Meanwhile, the Fabry–Perot interferometer collects all photons resulting from magnon–photon scattering events, thereby enabling the sampling of the frequency positions of individual magnon bands along with their relative intensities. By subsequently varying the applied magnetic field across the entire phase diagram, the full magnon spectrum can be reconstructed.

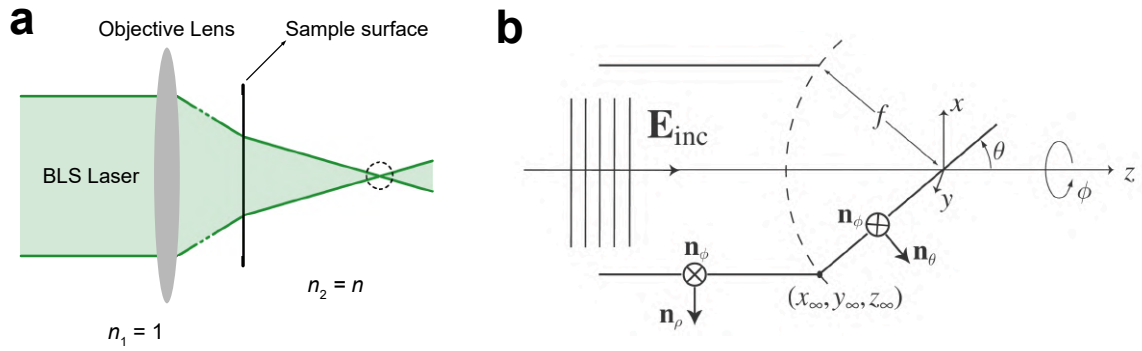

Figure 4.3.: **Focused electric field.** (**a**) Schematic representation of the focusing process in micro-focused BLS. The collimated laser beam is tilted by the objective lens and refracted at the sample surface according to Snell's law. (**b**) Schematic illustration of the aplanatic optical system. The electric field is refracted at the surface of a reference sphere with radius f, and its components are decomposed along the local polarisation directions to describe the focused field distribution.

4.2.2 Electric field distribution

In Section 4.1, we derived the differential scattering cross section for the case of a plane electromagnetic wave interacting with a single magnon. Here, the focused BLS laser generates a more intricate electric field distribution inside the magnetic sample. This can be expressed using the angular spectrum representation, which consists of a superposition of plane waves propagating in all directions, originating from a single source point. In the case of a focused beam, the source point corresponds to the focal point of the optical system, where all light rays converge. This standard problem is discussed in several textbooks; here, we follow the formulation presented in Ref. [134].

In the micro-focused BLS geometry, a collimated light beam is focused by the objective lens, producing a conical distribution of incident angles around the optical axis (see Fig. 4.3**a**). The maximum cone angle, θ_{max}, is determined by the numerical aperture (NA) of the lens by

$$\text{NA} = n_1 \sin\theta_{\text{max}}\,, \tag{4.24}$$

where n_1 is the refractive index of the medium in which the lens works. At the sample surface, the light is refracted according to Snell's law,

$$\frac{|\mathbf{k}_{\text{in/out}}|}{|\mathbf{k}'_{\text{in/out}}|} = \frac{\sin\theta'_{\text{in/out}}}{\sin\theta_{\text{in/out}}} = \frac{n_1}{n_2}\,, \tag{4.25}$$

where $|\mathbf{k}_{\text{in}}| = 2\pi/\lambda_{\text{in}}$, n_2 is the material refractive index, and the prime identifies the quantities within the sample. As a result, the focused laser beam inside the medium forms a conical distribution with cone angle θ'_{max} determined by $\sin\theta'_{\text{max}} = \text{NA}/n_2$. The combined effect of the objective lens and the refraction at the sample interface can be effectively represented by an equivalent aplanatic optical system, in which the collimated beam is mapped onto a spherical surface of radius equal to the focal length f and

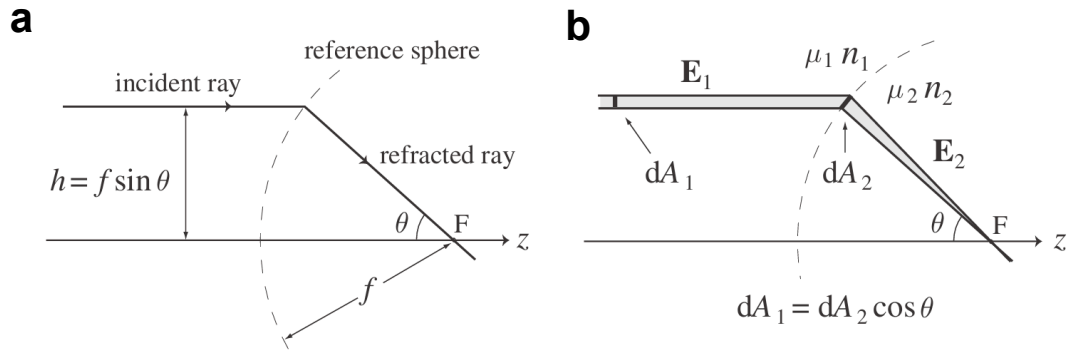

Figure 4.4.: **Geometrical optics at an aplanatic lens.** (**a**) Illustration of the sine condition in geometrical optics. The refraction of light rays at an aplanatic lens is governed by a spherical surface of radius f. (**b**) Illustration of the intensity law in geometrical optics. The energy transported along a ray remains constant during refraction, ensuring conservation of energy flux.

refractive index n_2 (see Fig. 4.3**b**).

The aplanatic system is characterised by two principles: the *sine condition* and the *intensity law*, see Fig. 4.4. The *sine condition* specifies that any optical ray either emerging from or directed toward the focal point F of an aplanatic lens intersects its corresponding conjugate ray on the surface of a sphere with radius f, where f is the focal length of the lens. The conjugate ray refers to the incident or refracted ray that travels parallel to the optical axis, which is determined by the direction of propagation of the collimated beam. The radial distance ρ between this ray and the optical axis is given by

$$\rho = f \sin\theta\,, \tag{4.26}$$

where θ represents the divergence angle of the conjugate ray. The *intensity law* states that the energy flux along each optical ray must be preserved. We can express this condition in terms of the power conservation through the infinitesimal cross-section dA, namely $dP = \frac{1}{2} Z_{\mu\varepsilon}^{-1} |\mathbf{E}|^2 dA$, where $Z_{\mu\varepsilon} = \sqrt{\frac{\varepsilon_0 \varepsilon_r}{\mu_0 \mu_r}}$ is the wave impedance with ε_r and μ_r being the relative permittivity and permeability, respectively. Thus, as indicated in Fig. 4.4**b**, the electric fields before and after refraction must satisfy

$$|\mathbf{E}_2| = |\mathbf{E}_1| \sqrt{\frac{n_1}{n_2}} \sqrt{\frac{\mu_2}{\mu_1}} \sqrt{\cos\theta}\,, \tag{4.27}$$

with $n_r = \sqrt{\varepsilon_r \mu_r}$ being the refractive index of the media, and $dA_1 = dA_2 \cos\theta$. Most materials exhibit a magnetic permeability close to unity at optical frequencies, i.e., $\mu_1 \approx \mu_2 \approx 1$, therefore we omit this term in subsequent expressions to simplify the notation.

Finally, we can derive the electric field distribution using the angular spectrum representation for the laser beam focused by the aplanatic lens. We assume that the laser is initially propagating along the

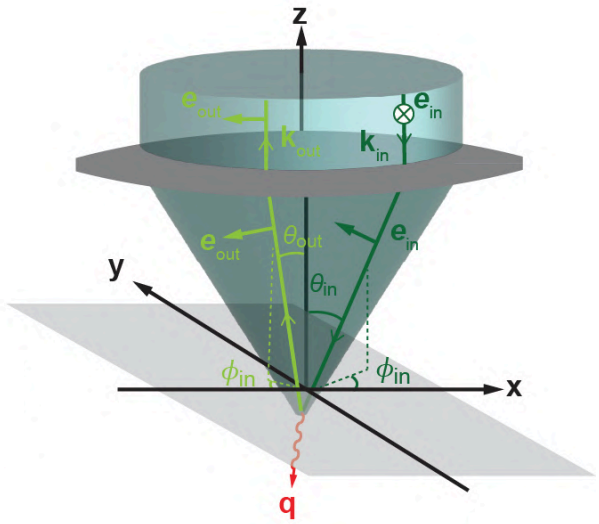

Figure 4.5.: **Polarisation vectors.** The lens focuses the incoming laser light (dark green) with polarization $\mathbf{e}_{\text{in}}$ which leads to a distribution of polarizations that depend on the wavevector of the focused light. The light green arrow represents a photon that is scattered after emitting a magnon (red arrow) in the sample and detected with a polarization filter $\mathbf{e}_{\text{out}}$.

$\hat{z}$-direction and linearly polarised in the $\hat{y}$-direction, see Fig. 4.3**b**. In order to describe the refraction on the reference sphere surface, it is convenient to decompose the incident electric field into its parallel, $\mathbf{E}^{(\text{s})}_{\infty,\text{in}}$, and orthogonal, $\mathbf{E}^{(\text{p})}_{\infty,\text{in}}$, components, where (s) and (p) stands for s- and p-polarisation, respectively. We introduce the unit vectors $\hat{n}_\phi$ and $\hat{n}_\rho$ such that

$$\mathbf{E}^{(\text{s})}_{\infty,\text{in}} = \Big[\mathbf{E}_{\infty,\text{in}} \cdot \hat{n}_\phi\Big]\hat{n}_\phi\,, \quad \mathbf{E}^{(\text{p})}_{\infty,\text{in}} = \Big[\mathbf{E}_{\infty,\text{in}} \cdot \hat{n}_\rho\Big]\hat{n}_\rho\,, \tag{4.28}$$

where $\mathbf{E}_{\infty,\text{in}}$ indicates the electric field inside the collimated laser beam. These unit vectors can be expressed using the spherical coordinates $\{\theta,\phi\}$ introduced in Fig. 4.3**b**, namely $\hat{n}_\phi = -\sin\phi\,\hat{x} + \cos\phi\,\hat{y}$ and $\hat{n}_\rho = \cos\phi\,\hat{x} + \sin\phi\,\hat{y}$. After refraction, the vector $\hat{n}_\phi$ remains unaffected, while $\hat{n}_\rho$ is mapped according to the sine condition to $\hat{n}_\theta = \cos\theta\cos\phi\,\hat{x} + \cos\theta\sin\phi\,\hat{y} + \sin\theta\,\hat{z}$. Finally, we use the angular spectrum representation to write the electric field distribution generated by the focused laser within the material

$$\mathbf{E}_{\text{in}}(\mathbf{r}) = \int_0^{\theta'_{\text{max}}} d\theta'_{\text{in}} \sin\theta'_{\text{in}} \int_0^{2\pi} d\phi'_{\text{in}}\, \mathbf{E}_{\infty,\text{in}}\, e^{i\mathbf{k}'_{\text{in}}\cdot\mathbf{r}} \tag{4.29}$$

where the origin, $\mathbf{r} = \mathbf{0}$, is identified with the focal point, F, of the optical system. The refracted incoming wavevector expressed in spherical coordinates results

$$\mathbf{k}'_{\text{in}} = |\mathbf{k}'_{\text{in}}|(\hat{x}\sin\theta'_{\text{in}}\cos\phi'_{\text{in}} + \hat{y}\sin\theta'_{\text{in}}\sin\phi'_{\text{in}} - \hat{z}\cos\theta'_{\text{in}})\,, \tag{4.30}$$

as sketched in Fig. 4.5, and the amplitude distribution is given by

$$\mathbf{E}_{\infty,\mathrm{in}} = \varepsilon_{\mathrm{in}}(\theta'_{\mathrm{in}}) \left[t^s(\theta'_{\mathrm{in}}) \cos\phi'_{\mathrm{in}} \hat{n}'_\phi + t^p(\theta'_{\mathrm{in}}) \sin\phi'_{\mathrm{in}} \hat{n}'_\theta \right] \sqrt{\frac{n_1}{n_2}} \sqrt{\cos\theta'_{\mathrm{in}}}\,, \tag{4.31}$$

where we assumed that $\mathbf{E}_{\infty,\mathrm{in}} \parallel \hat{y}$. The function $\varepsilon_{\mathrm{in}}(\theta_{\mathrm{in}})$ describes the intensity profile of the collimated laser, and its angular dependence reflects the cylindrical symmetry of the beam shape. A monochromatic laser beam is typically modelled by a Gaussian profile. However, when the lens aperture is much smaller than the beam diameter, only a small fraction of the light is transmitted, and its intensity can be approximated by a uniform distribution. The Fresnel amplitudes $t^{s/p}$ account for the light transmission through the surface of the material for the s- and p-polarised components, respectively. We can express these coefficients as a function of the longitudinal wavenumber, $k_{\mathrm{z,in}} = |\mathbf{k}_{\mathrm{in}}| \cos\theta_{\mathrm{in}}$ and $k'_{\mathrm{z,in}} = |\mathbf{k}'_{\mathrm{in}}| \cos\theta'_{\mathrm{in}}$,

$$t^s(\theta_{\mathrm{in}}) = \frac{2\mu_2 k_{\mathrm{z,in}}}{\mu_2 k_{\mathrm{z,in}} + \mu_1 k'_{\mathrm{z,in}}}\,, \tag{4.32}$$

$$t^p(\theta_{\mathrm{in}}) = \frac{2\varepsilon_2 k_{\mathrm{z,in}}}{\varepsilon_2 k_{\mathrm{z,in}} + \varepsilon_1 k'_{\mathrm{z,in}}}\,. \tag{4.33}$$

It is worth noticing that in the limit of small incident angles θ_{in}, the Fresnel transmission coefficients in first order approximation reduces to $t^s(0) = t^p(0) = \frac{1}{1+n_2/n_1}$.

4.2.3 Micro-focused BLS cross section

Now that we determined the electric field distribution inside the sample, we need to introduce its coupling to the magnetic spinwave excitations in order to compute the micro-focused BLS cross section. This can be formulated starting from an effective light–matter interaction action, which includes magneto-optic terms up to second order in spin–orbit coupling:

$$S_{\mathrm{int}} = \int dt d\mathbf{r}\, \frac{1}{2} \left(\tilde{K}(\mathbf{E} \times \partial_t \mathbf{E}) \cdot \mathbf{M} + G_{\mu\nu\lambda\kappa} E_\mu E_\nu M_\lambda M_\kappa \right), \tag{4.34}$$

where $\mathbf{E}$ is the electric field from Eq. (4.31), and the coefficients $\tilde{K}$ and $G_{\mu\nu\lambda\kappa}$ parametrize the magneto-optic interaction. Expanding the magnetization in lowest-order spinwave theory, the action becomes linear in the spinwave fluctuation:

$$S^{(1)}_{\mathrm{int}} = \int dt d\mathbf{r}\, \frac{1}{2} \left(\tilde{K}(\mathbf{E} \times \partial_t \mathbf{E}) \cdot \delta\mathbf{M} + 2 G_{\mu\nu\lambda\kappa} E_\mu E_\nu M_{\mathrm{eq},\lambda}\, \delta M_\kappa \right). \tag{4.35}$$

Light polarisation

When deriving the electric field distribution, we assumed that the incoming laser is linearly polarized along $\hat{y}$. Inside the magnetic sample, the transmitted polarization becomes

$$\mathbf{e}'_{\mathrm{in}} = t^s(\theta'_{\mathrm{in}}) \cos\phi'_{\mathrm{in}}\, \hat{n}_{\phi',\mathrm{in}} + t^p(\theta'_{\mathrm{in}}) \sin\phi'_{\mathrm{in}}\, \hat{n}_{\theta',\mathrm{in}}\,, \tag{4.36}$$

where t^s and t^p are Fresnel transmission coefficients, and $\hat{n}_{\phi',\text{in}}$, $\hat{n}_{\theta',\text{in}}$ denote unit vectors describing s– and p–polarized light inside the sample. The total light polarisation $\hat{e}'_{\text{in}}$ is no longer a unit vector due to the Fresnel transmission coefficients, which weights the s- and p-polarised components differently. However, in the limit of small incident angles, this effect reduces to a uniform rescaling with $t^s = t^p = t$. The experimental setup is only sensitive to out-going light that is linearly polarized along the $\hat{x}$-direction, which is rotated by 90° with respect to the incident laser beam. Accordingly, the polarization vector of the detected light inside the sample is

$$\mathbf{e}'_{\text{out}} = -t^s(\theta'_{\text{out}}) \sin\phi'_{\text{out}}\, \hat{n}_{\phi',\text{out}} + t^p(\theta'_{\text{out}}) \cos\phi'_{\text{out}}\, \hat{n}_{\theta',\text{out}}\,, \tag{4.37}$$

where $\hat{n}_{\phi',\text{out}}$ and $\hat{n}_{\theta',\text{out}}$ are defined analogously to the incoming case.

Transition probability

From Eq. (4.35), the BLS scattering amplitude for a focused beam scattering into an outgoing plane wave $(\mathbf{k}'_{\text{out}}, \omega_{\text{out}})$ is proportional to

$$\int dt d\mathbf{r} \int_{\theta'_{\text{max}}} d\Omega'_{\text{in}} \sqrt{\cos\theta'_{\text{in}}}\, e^{i(\mathbf{k}'_{\text{in}} - \mathbf{k}'_{\text{out}})\cdot\mathbf{r}} e^{-i(\omega_{\text{in}} - \omega_{\text{out}})t}\, e'^{*}_{\text{out},\mu}\, \delta\varepsilon_{\mu\nu}(\mathbf{r},t)\, e'_{\text{in},\nu}\,. \tag{4.38}$$

Here we used the fluctuating part of the dielectric permittivity already introduced in Eq. (4.4) with $K_{\lambda\mu\nu} = K\varepsilon_{\mu\nu\lambda}$ where $\varepsilon_{\mu\nu\lambda}$ is the anti-symmetric Levi-Civita tensor. Note that the time derivative in the effective action leads to a complex-valued permittivity that depends on the center-of-mass frequency of the in- and out-going light which is absorbed in the coefficient $K = -i\tilde{K}(\omega_{\text{out}} + \omega_{\text{in}})/2$. We use Fermi's golden rule to describe the transition probability between two photon states mediated by the magnon-photon coupling. Moreover, we consider the thermal average over the initial states, and summing over the final states of the magnetic subsystem we obtain

$$\begin{aligned} P \propto \int dt\, e^{i(\omega_{\text{in}} - \omega_{\text{out}})t} \int d\mathbf{r}_1 d\mathbf{r}_2 \int_{\theta'_{\text{max}}} d\Omega'_{\text{in},1} d\Omega'_{\text{in},2} \sqrt{\cos\theta'_{\text{in},1} \cos\theta'_{\text{in},2}} \\ \times e^{i(\mathbf{k}'_{\text{in},1} - \mathbf{k}'_{\text{out}})\cdot\mathbf{r}_1} e^{-i(\mathbf{k}'_{\text{in},2} - \mathbf{k}'_{\text{out}})\cdot\mathbf{r}_2} e'_{\text{out},\mu} e'^{*}_{\text{in},2,\nu} e'^{*}_{\text{out},\rho} e'_{\text{in},1,\delta} \langle \delta\varepsilon^{*}_{\mu\nu}(\mathbf{r}_2,t) \delta\varepsilon_{\rho\delta}(\mathbf{r}_1,0)\rangle\,, \end{aligned} \tag{4.39}$$

where the brackets $\langle . \rangle$ denote the thermal averaging explained in the previous Section. The incoming polarization vectors $\mathbf{e}'_{\text{in},1}$ and $\mathbf{e}'_{\text{in},2}$ are understood to be parametrized with angles related to the two integrations over solid angles $d\Omega'_{\text{in},1}$ and $d\Omega'_{\text{in},2}$, with the abbreviation $\int_{\theta'_{\text{max}}} d\Omega'_{\text{in}} = \int_0^{2\pi} d\theta'_{\text{in}} \sin\theta'_{\text{in}} \int_0^{2\pi} d\phi'_{\text{in}}$. Now, consider the spatial integrals

$$\begin{aligned} &\int d\mathbf{r}_1 d\mathbf{r}_2\, e^{i(\mathbf{k}'_{\text{in},1} - \mathbf{k}'_{\text{out}})\cdot\mathbf{r}_1} e^{-i(\mathbf{k}'_{\text{in},2} - \mathbf{k}'_{\text{out}})\cdot\mathbf{r}_2} \langle \delta\varepsilon^{*}_{\mu\nu}(\mathbf{r}_2,t) \delta\varepsilon_{\rho\delta}(\mathbf{r}_1,0)\rangle = \\ &= \int d\mathbf{r} e^{i\left(\mathbf{k}'_{\text{out}} - \frac{\mathbf{k}'_{\text{in},1} + \mathbf{k}'_{\text{in},2}}{2}\right)\cdot\mathbf{r}} \int d\mathbf{R}\, e^{i(\mathbf{k}'_{\text{in},1} - \mathbf{k}'_{\text{in},2})\cdot\mathbf{R}} \langle \delta\varepsilon^{*}_{\mu\nu}(\mathbf{r}_2,t) \delta\varepsilon_{\rho\delta}(\mathbf{r}_1,0)\rangle\,, \end{aligned} \tag{4.40}$$

that can be decomposed into an integral over the distance, $\mathbf{r} = \mathbf{r}_2 - \mathbf{r}_1$, and the center-of-mass coordinate, $\mathbf{R} = (\mathbf{r}_1 + \mathbf{r}_2)/2$. For a translationally invariant system, the correlation function $\langle \delta\varepsilon^*_{\mu\nu}(\mathbf{r}_2,t)\delta\varepsilon_{\rho\delta}(\mathbf{r}_1,0)\rangle$ is independent of $\mathbf{R}$ and its integral fixes the two incoming wavevectors to be identical, i.e., $\mathbf{k}'_{\mathrm{in},1} = \mathbf{k}'_{\mathrm{in},2}$. However, in the presence of a spatial dependent magnetisation texture, such as the conical or the skyrmion lattice phases, the correlation function is determined by the spinwave fluctuations of the magnetic structure. For example, the skyrmion crystal breaks translational invariance such that the correlation function in fact depends periodically on the center-of-mass coordinate $\mathbf{R}$ with Fourier components given by the reciprocal lattice vectors of the skyrmion crystal k_{SkL}. However, the spread of the incoming wavevectors within the focused beam is at most $|\Delta\mathbf{k}_{\mathrm{in}}| = |\mathbf{k}'_{\mathrm{in},1} - \mathbf{k}'_{\mathrm{in},2}| \leq \sqrt{2}n|\mathbf{k}_{\mathrm{in}}|\sqrt{1-\cos(2\theta'_{\mathrm{max}})}$, which depends on the laser wavelength and the numerical aperture of the lens. In the example of the magnetic skyrmion texture, this number must be compared with the lowest reciprocal lattice vector k_{SkL}. Here, we only consider the case $|\Delta\mathbf{k}_{\mathrm{in}}| \ll k_{\mathrm{SkL}}$, which applies to the experimental observations presented in the next Chapter. Consequently, the spatial integral over $\mathbf{R}$ can only pick up the zero-wavevector component of the correlation function similar to a translationally invariant system. The transition probability in this case reduces to

$$P \propto \int_{\theta'_{\mathrm{max}}} d\Omega'_{\mathrm{in}} \cos\theta'_{\mathrm{in}}\, e'_{\mathrm{out},\mu} e'^{*}_{\mathrm{in},\nu} e'^{*}_{\mathrm{out},\rho} e'_{\mathrm{in},\delta}\, \langle \delta\varepsilon^*_{\mu\nu}(\mathbf{r}_2,t)\delta\varepsilon_{\rho\delta}(\mathbf{r}_1,0)\rangle_{\mathbf{q},\omega}\,, \tag{4.41}$$

where the wavevector and frequency transferred from the light beam to the sample are $\mathbf{q} = \mathbf{k}'_{\mathrm{in}} - \mathbf{k}'_{\mathrm{out}}$ and $\omega = \omega_{\mathrm{in}} - \omega_{\mathrm{out}}$, respectively, and the Fourier transform of the correlation function is given by Eq. (4.2). The angle-dependent contribution, $\cos\theta'_{\mathrm{in}}$, follows from assuming that the intensity distribution of the incoming laser beam is homogeneous throughout the entire profile. This applies to the experimental setup that was used in the measurements we present in the next Chapter, where the beam passes through a narrow pinhole before reaching the objective lens. A different intensity distribution, such as a Gaussian profile, would simply lead to a different factor in Eq. (4.41).

Cross section

The transition probability can be understood as the incoherent sum of the intensities of individual scattering processes, where each incoming wavevector $\mathbf{k}'_{\mathrm{in}}$ within the focused beam is scattered into an outgoing wavevector $\mathbf{k}'_{\mathrm{out}}$. Interference between amplitudes corresponding to different $\mathbf{k}'_{\mathrm{in}}$ does not occur, since the spread of wavevectors in the focused beam is too small to resolve the periodicity of the magnetic lattice. This assumption is not a fundamental limitation of micro-focused BLS in general, but it is appropriate for the specific experiment analysed in the next Chapter. Finally, by summing over all outgoing wavevectors, one obtains the BLS scattering cross section

$$\sigma(\omega) \propto \int_0^{2\pi} d\phi'_{\mathrm{out}} \int_{\pi-\theta'_{\mathrm{max}}}^{\pi} d\theta'_{\mathrm{out}} \sin\theta'_{\mathrm{out}} \int_0^{2\pi} d\phi'_{\mathrm{in}} \int_0^{\theta'_{\mathrm{max}}} d\theta'_{\mathrm{in}} \sin\theta'_{\mathrm{in}} \cos\theta'_{\mathrm{in}} \frac{d\sigma_{\mathrm{out,in}}(\mathbf{q},\omega)}{d\Omega'_{\mathrm{out}}}\,, \tag{4.42}$$

with the differential cross section introduced in Eq. (4.1). In principle, this expression could be evaluated numerically by constructing a sufficiently dense mesh of incoming and outgoing wavevectors, and calculating the differential cross section for each point, as outlined in the previous Section. However, such a brute-force approach is computationally very demanding, since it requires recalculating both the light polarization and the magnon dynamics at every integration step.

In order to calculate the micro-focused BLS spectral weights, it is convenient to rewrite the scattering cross section in the form

$$\sigma(\omega) \propto \int d\mathbf{q}\, F_{\mu\nu\rho\delta}(\mathbf{q}) \langle \delta\varepsilon^*_{\mu\nu}(\mathbf{r},t)\delta\varepsilon_{\rho\delta}(\mathbf{r}',0)\rangle_{\mathbf{q},\omega} \tag{4.43}$$

with the auxiliary tensorial function

$$\begin{aligned} F_{\mu\nu\rho\delta}(\mathbf{q}) = &\left(\int_0^{2\pi} d\phi'_{\text{in}} \int_0^{\theta'_{\max}} d\theta'_{\text{in}} \sin\theta'_{\text{in}} \cos\theta'_{\text{in}} e'^*_{\text{in},\nu} e'_{\text{in},\delta}\right) \\ &\times \left(\int_0^{2\pi} d\phi'_{\text{out}} \int_{\pi-\theta'_{\max}}^{\pi} d\theta'_{\text{out}} \sin\theta'_{\text{out}} e'_{\text{out},\mu} e'^*_{\text{out},\rho}\right) \delta(\mathbf{q} - (\mathbf{k}'_{\text{in}} - \mathbf{k}'_{\text{out}})), \end{aligned} \tag{4.44}$$

where the two integrals are convoluted via the delta function. This formulation naturally separates the problem into two independent steps. On one hand, we compute the auxiliary function, which depends exclusively on the experimental geometry and polarization conditions, and it is completely independent of the magnetic background. On the other hand, we calculate the correlation function of the dielectric permittivity as a function of the magnon wavevector $\mathbf{q}$, which does not require any knowledge of the experimental setup.

4.2.4 Micro-focused BLS spectra

The formulation of the scattering cross section in Eq. (4.43) already highlights several distinctive features of the micro-focused technique. To appreciate these differences, it is instructive to compare them with those of the k-resolved BLS setup. In the latter, the incident light is not focused, and measurements are typically conducted in the back-scattering geometry, i.e., for $\mathbf{k}_{\text{out}} = -\mathbf{k}_{\text{in}}$. This fixes the magnon wavevector to $\mathbf{q} = 2\mathbf{k}'_{\text{in}}$, thus allowing the spinwave dispersion to be mapped out by varying the angle of incidence with respect to the sample orientation and applied magnetic field. From a theoretical perspective, this technique can be analysed using the differential scattering cross section presented in Section 4.1.1. When damping is neglected in the Landau-Lifshitz equation, i.e., effectively assuming an infinite magnon lifetime, the resulting magnon-photon scattering process yields delta function-like spectral peaks in the BLS signal. As a result, k-resolved BLS is ideally suited for probing spinwave non-reciprocity, which manifests as asymmetries in the position and intensity of the Stokes and anti-Stokes peaks [73]. In contrast, the micro-focused BLS geometry naturally averages out such non-reciprocity. This follows directly from the structure of the auxiliary function in Eq. (4.44), which is even in the

magnon wavevector due to the cylindrical symmetry of the focused laser beam: $F_{\mu\nu\rho\delta}(-\mathbf{q}) = F_{\mu\nu\rho\delta}(\mathbf{q})$. Moreover, the auxiliary function determines an intrinsic broadening of the spectral lines, even in the absence of damping in the magnon dynamics. In fact, the resulting peak shape arises from both the spinwave contribution, introduced by the correlation function in Eq. 4.43, and the integration over the auxiliary function, which is fully determined by the experimental setup configuration.

Another important consequence of employing a focused laser beam concerns the spatial profile of the electric field intensity within the magnetic sample. In traditional k-resolved BLS configurations, the laser beam typically exhibits a plane-wave character and penetrates the entire depth of the sample. As a result, magnon-photon scattering events are uniformly distributed throughout the illuminated volume, enabling a spatially averaged measurement of the spinwave spectrum. In contrast, the micro-focused BLS technique introduces a significant spatial confinement of the probing field distribution, which is localised around the focal point. This localisation is governed by the *intensity law* associated with the aplanatic lens system, which, under the assumption of spherical wavefronts, determines that the electric field amplitude scales as $1/r$, where r denotes the distance from the focal point. This confinement defines an effective interaction volume where the vast majority of magnon-photon scattering events occur. This region is typically on the order of a few cubic micrometres, depending on the numerical aperture of the objective lens and the optical properties of the sample. Such spatial resolution enhances the quality of the measurement by isolating single magnetic domain, hence reducing the noise associated with averaging over domains with differing spin configurations. As a result, the micro-focused BLS configuration provides a significantly improved signal-to-noise ratio and a clearer interpretation of the observed spinwave spectra. This capability is particularly advantageous in systems with complex magnetic textures, such as chiral magnets or multilayers, where spatial inhomogeneities can otherwise obscure key features of the magnonic response.

5 Cryogenic micro-focused BLS in Cu_2OSeO_3

In this Chapter, we report measurements of the finite wavevector spinwave spectroscopy across various magnetic phases of Cu_2OSeO_3, obtained using micro-focused Brillouin light scattering. We begin by analysing the field-polarised and conical phases, which serve as a benchmark for the theoretical formulation presented in the previous Chapter. These magnetic phases provide a well-understood context in which key parameters of the system can be extracted, facilitating both quantitative comparisons and the validation of our theoretical model. Additionally, this analysis highlights several features intrinsic to the micro-focused BLS technique, including its spectral resolution and wavevector selectivity. Subsequently, we focus on the measurement of topological magnon bands associated with the metastable skyrmion lattice phase. The ability of BLS to access finite magnon wavevectors, **q**, through the light-matter coupling mechanism proves crucial in this context. In particular, the theoretical model developed herein enables the identification of additional magnonic branches that, to the best of our knowledge, have not been observed previously using alternative experimental methods. These findings underscore the power of micro-focused BLS as a tool for exploring complex magnetic excitations and topological spin textures. The experimental data presented in this part were acquired by Dr. Ping Che and Prof. Dirk Grundler at the Swiss Federal Institute of Technology in Lausanne (EPFL).

5.1 Experimental setup

The experiment was performed on a bulk single crystal of Cu_2OSeO_3, mounted within a magneto-optical cryostat equipped with superconducting coils for the application of an external magnetic field. The crystal was grown with approximate dimensions of 4mm$\times$3mm$\times$0.5mm, oriented along the crystallographic directions $[001] \times [110] \times [1\bar{1}0]$, respectively. The orientation of the sample with respect to the incident laser and the applied magnetic field is illustrated in Fig. 5.1**a**. The BLS laser is focused on the polished top $(1\bar{1}0)$ surface, while the magnetic field **H** is applied along the $[001]$ axis. The direction of the applied magnetic field plays a crucial role in determining the magnetic texture within the sample. In the field-

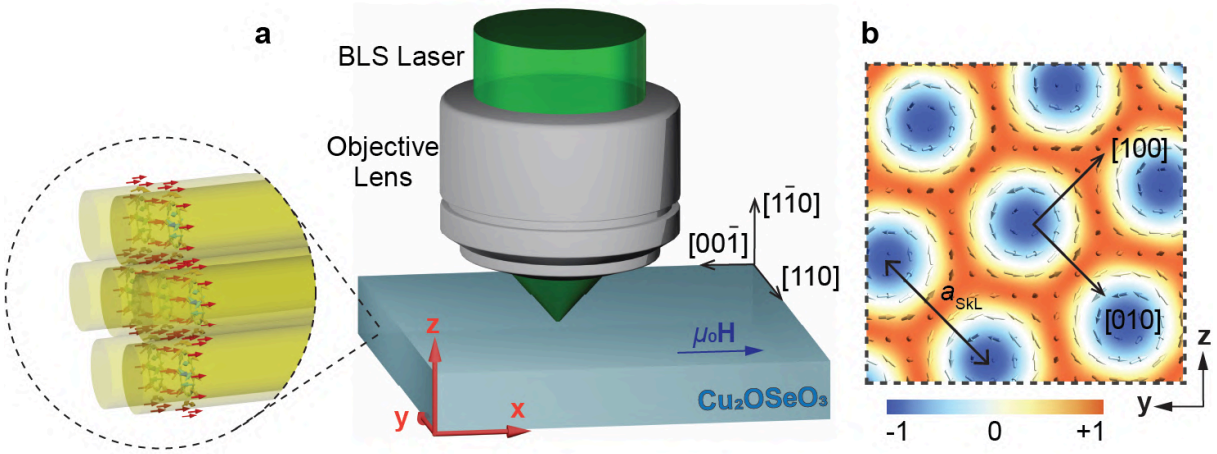

Figure 5.1.: **Experimental setup for BLS of magnons in the skyrmion lattice.** (**a**) Sketch of the BLS laser focused on the $(1\bar{1}0)$ surface of Cu_2OSeO_3. The external magnetic field **H** is applied along [001], i.e., the **x** axis. Skyrmion tubes align with the magnetic field and form a hexagonal lattice within the **y**-**z** plane. (**b**) Plane of the skyrmion lattice shown in panel (**a**). The arrows depict the in-plane magnetization and the color coding represent its out-of-plane component. One skyrmion lattice vector connecting two skyrmion centers is assumed to point along [010]. The lattice constant depends weakly on the external magnetic field, and it is on the order of $a_{\mathrm{SkL}} \approx 72\,\mathrm{nm}$.

polarised phase, it sets the direction of the uniform magnetisation, while in the conical phase, it defines the axis along which the helical modulation of the spins develops. Furthermore, in the skyrmion lattice phase, the external field direction stabilises skyrmion tubes aligned parallelly, as illustrated in the inset of Fig. 5.1**a**. For consistency with the theoretical formulation presented in the previous Chapters, the Cartesian unit vectors are expressed in the crystallographic basis as follows: $\hat{x}^{\mathrm{T}} = (0,0,1)$, $\hat{y}^{\mathrm{T}} = -\frac{1}{\sqrt{2}}(1,1,0)$, and $\hat{z}^{\mathrm{T}} = \frac{1}{\sqrt{2}}(1,-1,0)$. According to this choice, the incident BLS laser propagates along the $\hat{z}$-axis and is initially linearly polarised along the $\hat{y}$-direction, as shown in Fig. 4.5.

We use a monochromatic continuous-wave solid-state laser with a wavelength of $\lambda_{\mathrm{in}} = 532$ nm. This specific wavelength lies within the optical absorption window of Cu_2OSeO_3, where the material exhibits a local minimum in its absorption spectrum near 2.2eV [73]. Therefore, it enables efficient probing of bulk spinwave excitations in this material. Initially, a polariser is used to ensure the incident collimated beam is linearly polarised along the $\hat{y}$-direction. Then, a narrow pinhole is placed before the objective lens, effectively matching the beam profile to the aperture of the lens. Consequently, we assume a uniform intensity distribution across the collimated beam, corresponding to a constant function $\varepsilon_{\mathrm{in}}(\theta'_{\mathrm{in}}) \simeq \varepsilon_{\mathrm{in}}(0)$ in the electric field representation given in Eq. (4.31). This approximation is further justified by the relatively small incident angle $0 \leq \theta'_{\mathrm{in}} \leq \theta'_{\mathrm{max}}$. In fact, the light passes through an objective lens, with numerical aperture NA$= 0.55$, and is finally refracted at the sample surface, with refractive index $n = 2.03$. Therefore, the maximum cone angle inside the magnetic sample is $\theta'_{\mathrm{max}} = 16^{\circ}$. This small angle

approximation also allows us to simplify the Fresnel amplitudes by $t_{s/p}(\theta'_{\text{in}}) \simeq t_{s/p}(0) = \frac{1}{1+n}$. Therefore, the electric field amplitude distribution inside the sample reduces to

$$\mathbf{E}_{\infty,\text{in}} = \frac{\varepsilon_{\text{in}}(0)}{1+n}\sqrt{\frac{\cos\theta'_{\text{in}}}{n}}\,\mathbf{e}'_{\text{in}}\,, \tag{5.1}$$

with incoming polarisation vector defined by

$$\mathbf{e}'_{\text{in}} = \cos\phi'_{\text{in}}\hat{n}'_{\phi,\text{in}} + \sin\phi'_{\text{in}}\hat{n}'_{\theta,\text{in}}\,. \tag{5.2}$$

Here, $\hat{n}'_{\phi,\text{in}}$ and $\hat{n}'_{\theta,\text{in}}$ represent the unit vectors expressed in spherical coordinates that were introduced in the previous Chapter, namely

$$\hat{n}'_{\phi,\text{in}} = -\sin\phi'\,\hat{x} + \cos\phi'\,\hat{y} \tag{5.3}$$

$$\hat{n}'_{\theta,\text{in}} = \cos\theta'\cos\phi'\,\hat{x} + \cos\theta'\sin\phi'\,\hat{y} + \sin\theta'\,\hat{z}\,, \tag{5.4}$$

where $\{\theta_{\text{in}}, \phi_{\text{in}}\}$ are shown in Fig. 4.5. The laser beam is focused to a spot size of approximately $4\,\mu$m on the sample surface, indicating that the focal point is located roughly $7.2\,\mu$m beneath the surface. This length is much larger than the typical magnetic length scale of Cu_2OSeO_3, which is on the order of $2\pi/Q \simeq 60$ nm. Thus, surface-induced effects on the magnetic texture can be neglected, and the system can be treated in the bulk limit.

Finally, the scattered photons are analysed using a six-pass Fabry–Perot interferometer equipped with a polarisation filter that transmits only the $\hat{x}$-polarised component of the scattered light. This filtering process suppresses phonon contributions and enhances the signal-to-noise ratio for magnon detection in the BLS measurements.

5.1.1 Magnon wavevectors domain

The transferred magnon wavevector $\mathbf{q}$ is defined as the difference between the internal wavevectors of the incoming and scattered photons, $\mathbf{q} = \mathbf{k}'_{\text{in}} - \mathbf{k}'_{\text{out}}$. The magnitude of the transferred wavevector $\mathbf{q}$ can be approximated as

$$|\mathbf{q}| = \sqrt{\left(\mathbf{k}'_{\text{in}} - \mathbf{k}'_{\text{out}}\right)^2} \approx \sqrt{2}n|\mathbf{k}_{\text{in}}|\sqrt{1 - \frac{\mathbf{k}'_{\text{in}}\cdot\mathbf{k}'_{\text{out}}}{|\mathbf{k}'_{\text{in}}||\mathbf{k}'_{\text{out}}|}} \tag{5.5}$$

where we neglected corrections on the order of 10^{-6} due to the transferred frequency

$$\omega = c'(|\mathbf{k}'_{\text{in}}| - |\mathbf{k}'_{\text{out}}|) = c(|\mathbf{k}_{\text{in}}| - |\mathbf{k}_{\text{out}}|)\,, \tag{5.6}$$

where $c' = c/n$ denotes the speed of light within the material. The accessible range of $|\mathbf{q}|$ is determined by the refractive index n, the laser wavelength $\lambda_{\text{in}} = 2\pi/|\mathbf{k}_{\text{in}}|$, and the numerical aperture of the objective

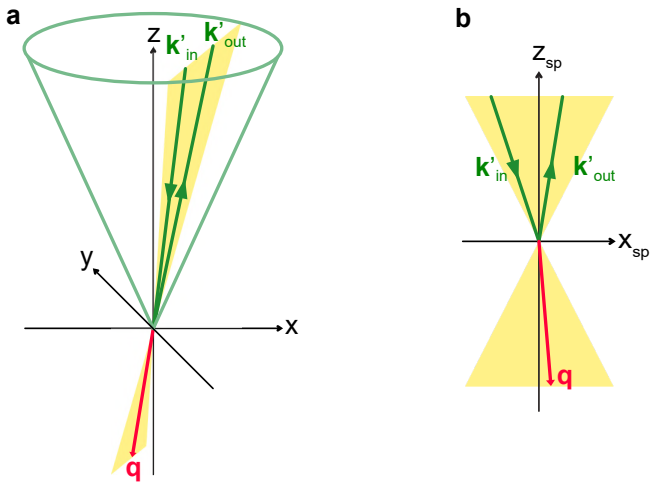

Figure 5.2.: **Scattering plane.** (**a**) Example of a generic scattering event taking place in the experimental setup close to the objective lens' focal point. The opening angle θ'_{max} of the green cone is determined by the aperture of the lens. The wavevectors of the incoming photon, $\mathbf{k}'_{\text{in}}$, the scattered magnon, $\mathbf{q}$, and the outgoing photon, $\mathbf{k}'_{\text{out}}$, are all located within the same scattering plane indicated by the yellow surface. Panel (**b**) shows the same scattering event in the corresponding scattering plane; whereas the $\mathbf{x}_{\text{sp}}$-axis is located within the **xy**-plane, the $\mathbf{z}_{\text{sp}}$-axis is generally tilted away from the **z**-axis of panel (**a**).

lens, which defines the maximum cone angle θ'_{max}. The largest possible wavevector transfer occurs in the backscattering geometry, where $\mathbf{k}'_{\text{out}} = -\mathbf{k}'_{\text{in}}$, yielding $|\mathbf{q}| = 2n|\mathbf{k}_{\text{in}}| \simeq 48.0\ \text{rad}/\mu\text{m}$. The minimal value for $|\mathbf{q}|$ is obtained if the angle enclosed between in- and outgoing photon wavevectors is minimal, that is $\pi - 2\theta'_{\text{max}}$ for which $|\mathbf{q}| \simeq 46.2\ \text{rad}/\mu\text{m}$.

It is useful to decompose the magnon wavevector into components parallel and perpendicular to the applied magnetic field: $\mathbf{q}_{\parallel} = \hat{x} q_{\parallel}$ and $\mathbf{q}_{\perp}$, respectively. The magnitude of these components depends on the orientation of the scattering plane relative to the external magnetic field, and it can be understood with the help of Fig. 5.2. In particular, the photon wavevectors, $\mathbf{k}'_{\text{in}}$ and $\mathbf{k}'_{\text{out}}$, determine the scattering plane (yellow region) where the magnon wavevector lies. When this plane is perpendicular to the applied field, then $q_{\parallel} = 0$ and the entire transferred wavevector lies in the transverse direction, $|\mathbf{q}| = |\mathbf{q}_{\perp}|$, covering the full range between 46.2 and 48.0 $\text{rad}/\mu\text{m}$. The longitudinal component $q_{\parallel}$ reaches its maximum when the magnetic field lies within the scattering plane and the photon wavevectors $\mathbf{k}'_{\text{in}}$ and $\mathbf{k}'_{\text{out}}$ are anti-parallel. In that case, $|q_{\parallel}| = 2n|\mathbf{k}_{\text{in}}| \sin\theta'_{\text{max}} \simeq 12.9\ \text{rad}/\mu\text{m}$. This wavevector range determines the region of the spinwave spectrum that is accessible in the experiment.

As the focused laser beam enters the sample, it experiences the magneto-optical Faraday effect. In this process, the linearly polarised light decomposes into two circularly polarised contributions, which propagate at different speeds inside the magnetic sample. This effect results in a net rotation of the linear polarisation axis, which strength is usually expressed as the rotation angle per unit length. For Cu_2OSeO_3, Versteeg *et al.* [135] measured the Faraday rotation angle θ_{F} as a function of temperature and

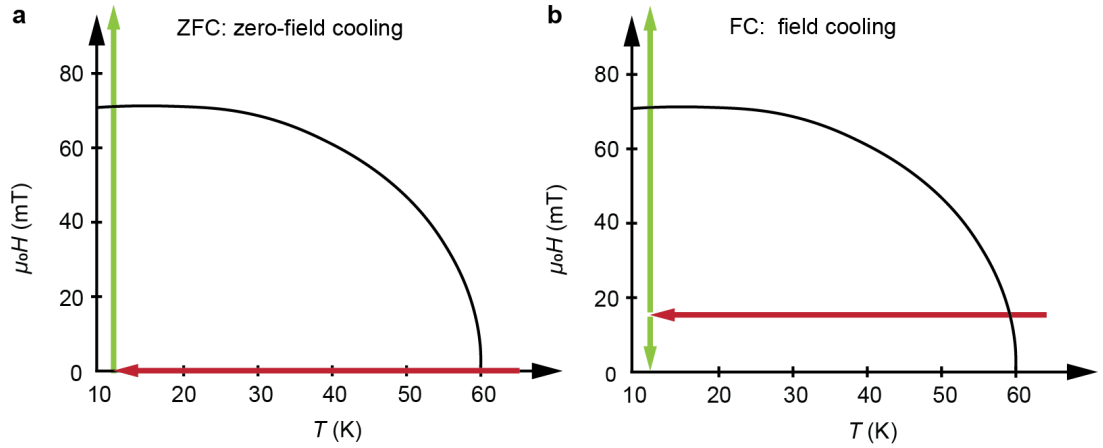

Figure 5.3.: **Sketch of temperature-versus-field histories.** (**a**) Zero-field cooling (ZFC) at $\mu_0 H_{FC}$ = 0 mT. (**b**) Field cooling (FC) at $\mu_0 H_{FC}$ = 16 mT. Red arrow indicates the cooling field and green arrow indicate the field scanning direction.

applied magnetic field. At $T = 15$ K, they reported a maximum rotation of $\theta_F = 0.003$ rad/μm. When compared to the typical magnon wavevectors probed in our experimental setup, this effect amounts to a correction that is four orders of magnitude smaller, and can therefore be safely neglected in our analysis.

5.1.2 Cooling procedure

Fig. 5.3 show the temperature versus magnetic field history of the experimental scan. The procedure is divided into two steps: the field cooling (red arrow), which serves as a preparation of the sample, and the field swap (green arrow), when the magnon spectra are collected. In the first step the applied magnetic field, $\mu_0 H_{FC}$, is kept constant while the temperature decreases down to $T = 12K$. This low temperature allows to improve the signal-to-noise ratio, which proves crucial to resolve the individual magnon bands of the skyrmion lattice phase. Meanwhile, the cooling field allows to enter the phase diagram for different magnetic textures. Here we analyse two examples of this procedure, namely the zero-field cooling (ZFC) and the field cooling (FC) for 10mT$< \mu_0 H_{FC} <$16mT.

In the first case, the system enters the conical phase from the paramagnetic phase at around $T_c \simeq 57K$. Then, once the temperature of $T = 12K$ is reached, the magnetic field is gradually increased (green arrow), and the magnon spectra are collected at regular intervals. At the critical field $\mu_0 H_{c2}$ the system undergoes a phase transition between the conical and the field polarised phase.

In the FC protocol, instead, the applied cooling field $\mu_0 H_{FC}$ is selected such that the magnetic sample enters the stable skyrmion lattice pocket near $T_c \simeq 57K$. After this, the system is cooled down to $T = 12K$ at a rate of $25K$ per minute. This rapid quench enables the skyrmion lattice to persist in a meta-stable state, protected by its topological nature [76, 87–89]. The metastable SkL phase is known to display long lifetimes, making it accessible to experiments. Moreover, this metastable phase survives for a

wider range of applied magnetic fields thanks to the low temperature of the system, thus enabling to reconstruct a richer field-dependent map of the magnon band structures. Once this state is established, magnon spectra are measured during the subsequent field sweep (green arrow) while the temperature is held constant at 12 K.

5.2 Zero-field cooling

Fig. 5.4**a** shows the intensity map of the experimental BLS spectra obtained using the zero-field cooling protocol (red arrow). Only the anti-Stokes component, corresponding to magnon absorption, is reported here. After stabilizing the temperature at $T = 12$ K, the external field was increased from 0 mT to 70 mT as indicated by the green arrow. In the field range from 0 mT to 38 mT, two modes are clearly resolved: a strong-intensity mode and a weaker, lower-frequency mode, which we attribute to the +Q and –Q modes of the conical helix phase, respectively. At around 40 mT, the slope of the frequency-versus-field dependence of the resonance reverses from negative to positive, which indicates a phase transition. In this regime, an intermediate phase X_1 may exist, attributed either to a tilted-conical state or to a low-temperature skyrmion lattice phase. Both phases are known to be metastable or stable, respectively, due to magnetocrystalline anisotropies in Cu_2OSeO_3 at low temperatures for the present field orientation [80, 83–87]. For larger fields above 48 mT, the resonance exhibits a field dependency typically attributed to the Kittel mode. This behaviour indicates that the field polarised phase is reached.

In this Section, we restrict the discussion to a comparison between the experimental spectra and the theoretical model for the helical and field-polarised phases of the chiral magnet. This approach enables us to extract several parameters characteristic of the Cu_2OSeO_3 sample used in the measurements. The detailed derivation of the theoretical BLS intensity map is presented in the following paragraphs. Fig. 5.4**b** illustrates the result of this calculation for the same range of applied field and frequency, expressed in dimensionless units.

5.2.1 Field polarised phase

In order to evaluate the micro-focused BLS spectra in the field-polarized phase, we calculate the scattering cross section [Eq. (4.43)], where the correlation function is constructed analytically from the Green's function given in Eq. (4.23). The most demanding computational step involves evaluating the auxiliary function $F_{\mu\nu\rho\delta}(\mathbf{q})$ defined in Eq. (4.44). For this purpose, we discretize the angular domain of integration into a dense mesh that samples the full solid angle allowed by the numerical aperture of the optical setup. The integrand is then evaluated point-by-point on this mesh, and the result is obtained by summing over all angular contributions with appropriate quadrature weights. In practice, the accuracy of the calculation is controlled by the mesh resolution: a finer angular grid ensures convergence of the integral while capturing the detailed angular dependence of the scattering geometry. This procedure effectively accounts

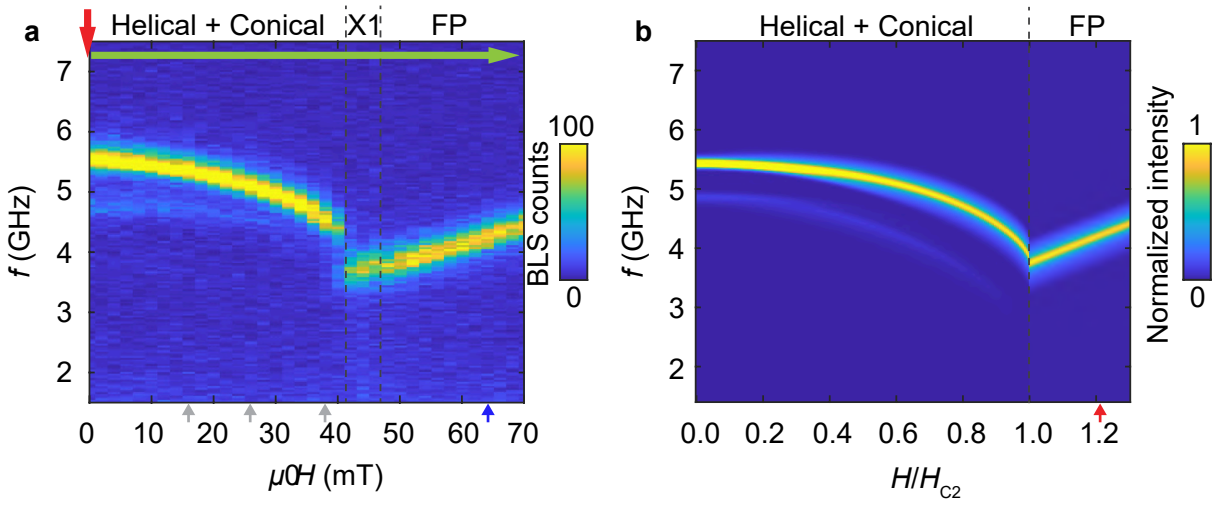

Figure 5.4.: **Zero field cooling (ZFC) BLS spectra.** **(a)** Anti-Stokes BLS intensities for zero-field cooling (red arrow) down to T=12K and a subsequent field scan (green arrow). Color bar represent the BLS counts. **(b)** Theoretical BLS spectra of the conical phase, $H < H_{c2}$, and field polarised phase, $H > H_{c2}$, with the same normalization as in (**a**).

for the averaging over the conical distribution of incoming and outgoing photon directions inherent to the micro-focused BLS setup.

The linear spinwave theory presented in Chapter 3 is characterized by three parameters only: a frequency scale $\omega_{c2} = \gamma_0 \mu_0 H_{c2}^{\text{int}}$, a wavevector scale $Q = D/J$ and the magnetic susceptibility within the conical phase $\chi_{\text{con}}^{\text{int}} = M_s/H_{c2}^{\text{int}}$, that quantifies the strength of the dipolar interaction. For the latter two parameters, we took values from the literature, i.e., $Q = 105$ rad/μm and $\chi_{\text{con}}^{\text{int}} = 1.76$ reported in Ref. [48]. The frequency scale can be extrapolated within the field polarised phase by taking advantage of the linear dispersion relation of the Kittel resonance mode. The central peak position corresponding to the uniform magnon dynamics in the micro-focused BLS geometry is approximated by a linear relationship

$$\frac{2\pi f_{\text{Kittel}}}{\omega_{c2}} = A_0 + B_0 \frac{H}{H_{c2}}, \tag{5.7}$$

with A_0 and B_0 depending on the experimental setup and sample properties, see Fig. 5.5**a**. Fitting Eq. (5.7) to the experimental data yields the parameters $\omega_{c2}/2\pi = 2.03$ GHz. The critical frequency agrees within our error bar with the value of 2.06 GHz found in Ref. [73] in the same material. We note that the value for the frequency scale fitted to the data in the field polarized phase implies for a g-factor of $g = 2.1$ an internal critical field $\mu_0 H_{c2}^{\text{int}} = 68$ mT. This overestimates the value found experimentally $\mu_0 H_{c2}^{\text{int}} = \mu_0 H_{c2}/(1 + N_x \chi_{\text{con}}^{\text{int}}) \approx 41$ mT where $\mu_0 H_{c2} \approx 50$ mT and the demagnetization factor $N_x \approx 0.13$. A similar discrepancy was found in the angle-resolved BLS experiments performed by Ogawa *et al.* [73]. The origin of this inconsistency is unclear but could be due to local heating by the laser or due to the so

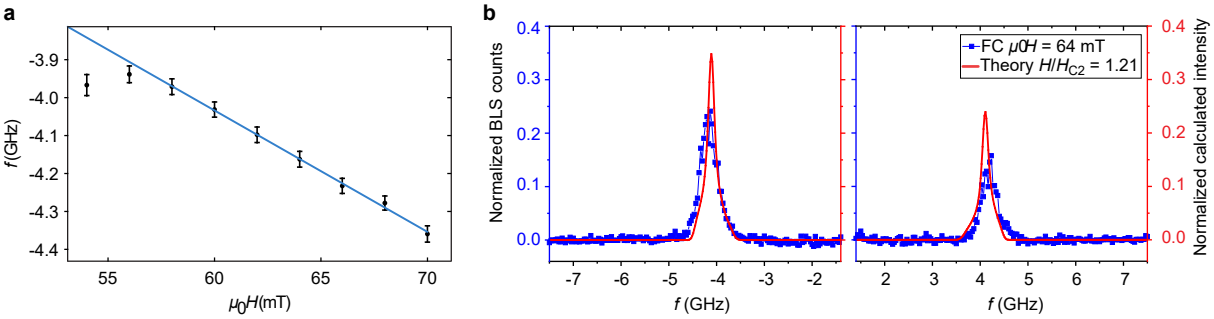

Figure 5.5.: **Field-polarised BLS spectra.** (**a**) Experimental frequency positions of the Anti-Stokes resonance in the field-polarised phase (black dots). The theoretical model gives a linear behaviour (orange line) that can be fitted in order to obtain the parameters $\mu_0 H_{c2} = 53$ mT and $\omega_{c2}/2\pi = 2.03$ GHz. Panel (**c**) (Stokes) and (**d**) (anti-Stokes) shows line cuts of the spectra obtained at fixed magnetic field $\mu_0 H$ = 64 mT (blue symbols) and comparison to theory with H/H_{c2} = 1.21 (red line). A frequency-independent background signal (dark counts) was removed from the raw BLS spectra to realize a baseline similar to the theoretical curves. Both the experimental and theoretical data have been normalized with respect to the total spectral weight integrated over the full frequency range from -7.5 GHz to -1.4 GHz and from 1.4 GHz to 7.5 GHz.

far neglected magnetocrystalline anisotropies.

In order to evaluate the BLS spectra, we need the magneto-optic constants introduced in Eq. (4.5). In a cubic material, the tensor $K_{\mu\nu\lambda} = K\varepsilon_{\mu\nu\lambda}$, with the Levi-Civita symbol $\varepsilon_{\mu\nu\lambda}$, is characterized by a single constant K that sets the overall intensity scale. The higher-order tensor $G_{\mu\nu\lambda\kappa}$ governs the asymmetry between Stokes and Anti-Stokes intensities. In the field-polarized phase, we obtained a satisfactory description of the data using $G_{11} = G_{12} = 0$ and $2iM_sG_{44}/K \approx 0.123$. However, the experimental data do not provide enough independent observables to uniquely determine all parameters of the tensor. As a result, the chosen values should be regarded as one possible consistent set that reproduces the measured spectra within the present analysis. Figure 5.5 shows the measured BLS spectra at $\mu_0 H = 64$ mT (blue symbols) compared with the theoretical prediction at $H/H_{c2} = 1.21$ (red line). The observed asymmetry between Stokes and Anti-Stokes signals provides the basis for fitting the magneto-optic constants $G_{\alpha\beta}$. Notably, the theory captures well the spectral line shape that arises from the geometric averaging of in- and out-going photon wavevectors in the micro-focused BLS setup and, in particular, it accounts for the observed full-width-at-half-maximum.

5.2.2 Conical phase

In the conical phase, we evaluate the micro-focused BLS spectra using exactly the same set of parameters that were extracted in the field polarized phase. Remarkably, no additional adjustments are required: the frequency scale ω_{c2}, the characteristic wavevector Q, the magnetic susceptibility $\chi^{\text{int}}_{\text{con}}$, and the magneto-optic tensor $G_{\mu\nu\lambda\kappa}$ determined in the FP analysis already provide an excellent description of the data in the conical state. This consistency demonstrates the robustness of the parameter extraction and highlights

the predictive power of the theoretical model presented in the previous Chapters.

The spectra obtained in the conical phase exhibit two distinct magnon branches, which we identify as the $+Q$ and $-Q$ resonances. In the experimental spectra, the $+Q$ branch appears as the dominant feature, carrying the largest spectral weight, while the $-Q$ branch is visible only as a much weaker signal. This hierarchy of intensities is a characteristic fingerprint of the conical magnon spectrum and directly reflects the different coupling strengths between the magnon modes and the probing light. The asymmetry between the two branches is not unique to our experiment but is a well-established feature of Cu_2OSeO_3, as confirmed by Ogawa *et al.* in their angle-resolved BLS measurements [73]. In those studies, performed with a well-collimated laser beam and a backscattering geometry, a similarly strong intensity imbalance was reported between the $+Q$ and $-Q$ modes. A key distinction, however, arises from the use of the micro-focused geometry in our experiment. In the k-resolved BLS configuration, the scattering condition selects a specific magnon wavevector for each beam incidence angle, which allows the non-reciprocal character of the conical magnon spectrum to be directly resolved. By contrast, in the micro-focused BLS setup, the finite numerical aperture of the objective lens introduces an intrinsic angular averaging over a distribution of photon wavevectors. As a result, the sharp non-reciprocity that is characteristic of the conical spectrum becomes effectively smeared out in our measurements. The auxiliary function $F_{\mu\nu\rho\delta}(\mathbf{q})$ introduced in Chapter 4 reflects this averaging explicitly, being an even function of $\mathbf{q}$ in the case of a focused beam. Consequently, the micro-focused BLS spectra no longer display the pronounced frequency splitting and directional asymmetry of the modes but rather yield a broadened, symmetric response that integrates over both directions of magnon propagation. Despite this difference, the observation of both $+Q$ and $-Q$ resonances in our data demonstrates that the micro-focused geometry still captures the essential features of the conical spinwave spectrum.

5.3 Field cooling

Figure 5.6 shows the BLS intensity map obtained after a field-cooling (FC) protocol carried out at a rate of 25 K per minute. In this procedure, the sample was cooled to 12 K while a finite magnetic field of $\mu_0 H_{\mathrm{FC}} = 16$ mT was applied (red arrow). The choice of this field ensures that the system crosses the high-temperature skyrmion lattice phase during cooling, thereby stabilizing a metastable skyrmion lattice at 12 K. Previous studies have demonstrated that this metastable phase can be remarkably robust at low temperatures when the field is aligned along the cubic axes. This is favoured by the topological charge associated with the magnetic texture, which protects the system against its annihilation. Upon increasing $\mu_0 H$ from 16 mT up to about 55 mT, the resulting BLS spectra display several resonances between 1.4 GHz and 7.5 GHz. These resonances are clearly distinct from those associated with the conical helix phase, as observed in the ZFC protocol. Both Stokes (negative frequency) and Anti-Stokes (positive frequency) signals are present, corresponding to the emission and absorption of magnons, respectively.

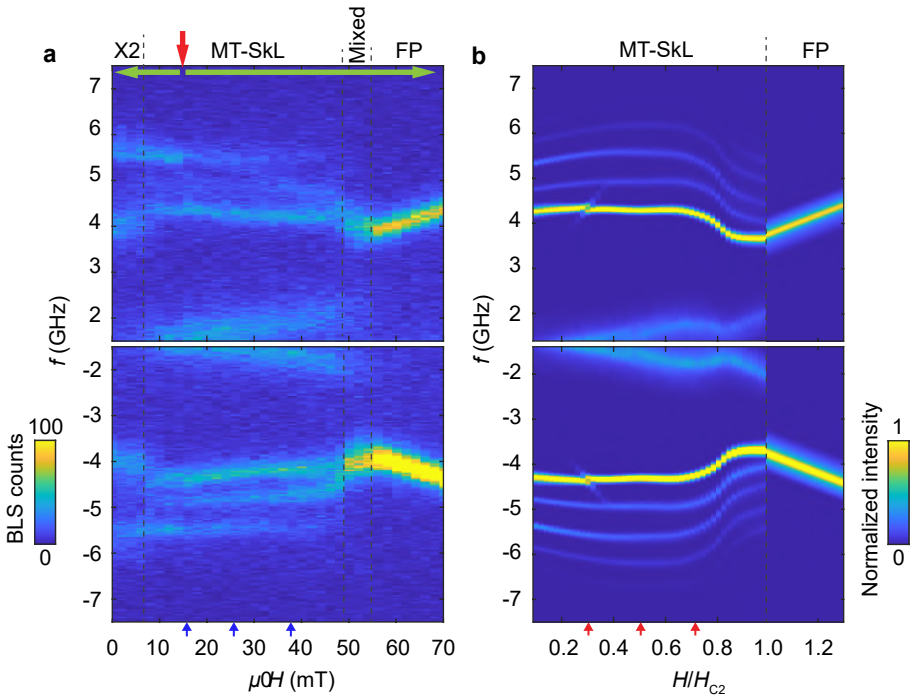

Figure 5.6.: **Field cooling (FC) BLS spectra.** (**a**) BLS intensities for field-cooling at $\mu_0 H_{\mathrm{FC}} = 16$ mT (red arrow) down to $T = 12$ K and subsequent field scans (green arrows). Colour bar represents the BLS counts. (**b**) Theoretical BLS spectra of the (metastable) skyrmion lattice (MT-SkL) phase, $H < H_{c2}$, and the field polarized (FP) phase, $H > H_{c2}$, with the same normalization as in (**a**). Line cuts of the spectra for three values of the magnetic field as indicated by the blue and red arrows at the bottom of panel (**a**) and (**b**), respectively, are shown in Fig. 5.8.

We find an asymmetry of intensity between the two signals with the Stokes component being enhanced compared to the Anti-Stokes one. At around 55 mT, the spectrum reconstructs in a single branch characterised by linear dispersion. This high-field signature is consistent with the Kittel mode appearing in the field polarized phase. For intermediate magnetic fields between 50 mT and 55 mT, the spectra exhibits a different behaviour characterised by a dominant magnon band with opposite slope compared to the Kittel mode. This is the signature of a different magnetic phase, that we denote here by *Mixed*, which is not found in our minimal model.

Subsequently, the sample was warmed to 100 K and subjected to the same field-cooling protocol, after which BLS spectra were collected for magnetic fields smaller than $\mu_0 H_{\mathrm{FC}}$, i.e., $\mu_0 H < 16$ mT. Notably, the branches at low field connect smoothly to those detected above 16 mT, confirming the reliability and reproducibility of the FC preparation. However, for $\mu_0 H \leq 5$ mT, certain branches either change slope or disappear altogether, signaling a phase transition near zero field, marked as X2 in the figure. In this low-field regime, the metastable skyrmion lattice is likely subject to an oblique distortion, producing an elongated lattice configuration, as previously reported in Refs. 24 and 37. Such distortions are attributed to the influence of magnetocrystalline anisotropies in the material.

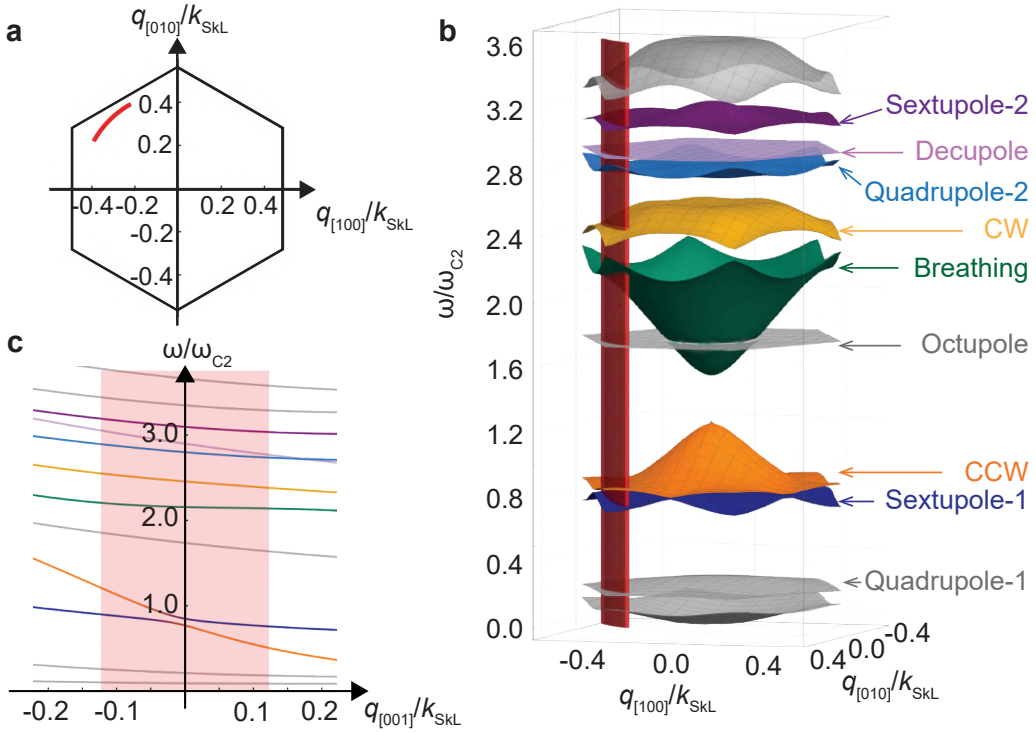

Figure 5.7.: **Theoretically calculated magnon band structure of the skyrmion lattice for $H = 0.5H_{c2}$.** (**a**) First Brillouin zone of the skyrmion lattice with one of the reciprocal lattice vectors, k_{SkL}, oriented along [100] [81]. (**b**) Magnon band structure for wavevectors within the plane of the skyrmion lattice, as presented in Fig. 3.5. The same colouring of relevant modes applies throughout this entire Chapter. (**c**) Dispersion of the magnon modes as a function of wavevector along the skyrmion tubes at fixed in-plane wavevector $|\mathbf{q}_\perp| = 47$ rad μm^{-1} pointing along $\hat{z} \parallel [1\bar{1}0]$. The red annulus segments in panel (**a**) and (**b**) as well as the red shaded regime in **c** indicate the range of magnon wavevectors accessible with the BLS setup of this work.

In what follows, we restrict our analysis to the metastable SkL phase in the field range $\mu_0 H > 5$ mT. Extending the analysis to lower fields would require including corrections to the standard theory introduced in Chapter 2. Although such corrections can, in principle, be incorporated systematically as higher-order contributions from spin–orbit coupling, they also introduce a large number of additional unknown parameters. This would substantially reduce the predictive power of the theoretical calculation and is therefore beyond the scope of the present work.

5.3.1 Magnon bands structure

The external magnetic field is applied along the [001] crystallographic axis. Consequently, the hexagonal skyrmion lattice forms within the (001) plane, i.e., perpendicular to the field direction. For this field orientation, it has been shown [81] that one of the reciprocal lattice vectors of the skyrmion lattice aligns with the [100] direction, implying that one of its primitive lattice vectors lies along [010], as illustrated in Fig. 5.7**a**. According to Fig. 2.9, the characteristic reciprocal lattice vector k_{SkL} is of the same order of magnitude as the helical pitch $Q = 105$ rad/μm, and only weakly depends on the applied magnetic field. Consequently, the transferred magnon wavevector $|\mathbf{q}|$ probed in the experiment is comparable in

magnitude to k_{SkL}. In this regime, inelastic light scattering involving the emission or absorption of single magnons provides direct access to the magnon dispersion near the boundary of the first magnetic Brillouin zone, as illustrated by the red region in Fig. 5.7**a**.

The theoretically expected magnon band structure for the skyrmion lattice phase of cubic chiral magnets is displayed in Fig. 5.7 for a field strength $H = 0.5H_{\mathrm{c2}}$, using parameters relevant to Cu_2OSeO_3 [39]. Panel **a** sketches the hexagonal magnetic Brillouin zone, with the red arc indicating the range of transverse wavevectors $\mathbf{q} \perp$ sampled in the experiment. Panel **b** shows the corresponding dispersion of low-energy spinwave modes for in-plane wavevectors $\mathbf{q}_\perp$. The color coding highlights the modes most relevant to the present BLS measurements, with corresponding names identifying the excitations according to Section 3.3.2. In particular, the counterclockwise (orange), breathing (green), and clockwise (yellow) modes are the only dipole-active excitations at the Γ-point. Notably, due to their strong dispersion, the frequencies of the CCW and breathing modes within the experimentally accessible $\mathbf{q}_\perp$ range differ significantly from their values at the Γ-point. Panel **c** displays the magnon dispersion along the skyrmion tube axis, i.e., as a function of $\mathbf{q}_\parallel$ at a fixed $|\mathbf{q}_\perp| = 47$ rad/μm directed along the $\hat{z}$-axis. The red-shaded region marks the experimentally accessible $\mathbf{q}_\parallel$ range. The CCW mode, in particular, exhibits a pronounced non-reciprocity, consistent with previous observations reported in Ref. [76].

5.3.2 Mode identification

Similarly to the conical phase, the theoretical calculations of the micro-focused BLS spectra in the skyrmion lattice phase were performed independently of the experimental measurements. The model parameters used here were determined by the comparison between the measurements and the theoretically evaluated BLS intensity in the field-polarized phase. Figure 5.8 presents line cuts of the calculated spectral weights for three representative magnetic fields, 16, 26, and 38 mT, as indicated by the arrows at the bottom of Figs. 5.6**a** and **b**. The blue symbols correspond to the experimental data obtained in the metastable skyrmion lattice phase, Fig. 5.6**a**, while the grey symbols show, for reference, the corresponding spectra in the conical phase, Fig. 5.4**a**. The red solid lines represent the theoretical BLS spectra. The colored bars at the bottom of each panel identify the various modes following the color scheme introduced in Fig. 5.7.

At the lowest frequencies, the CCW mode (orange) exhibits the largest spectral weight. Around 26 mT, it hybridizes with the sextupole-1 mode (dark blue), resulting in two branches that are not clearly distinguishable in the spectra. The breathing mode (green) gives rise to a prominent spectral peak between 4 and 4.5 GHz. At 16 mT, it hybridizes with the decupole mode (pink), as illustrated in the inset of Fig. 5.7**b**. The experimental spectra possess features that are reminiscent of this hybridization both at positive (Anti-Stokes) and negative (Stokes) frequencies. The CW mode (yellow) is predicted to possess a relatively small spectral weight, and it is more clearly resolved in the Stokes spectrum. At the

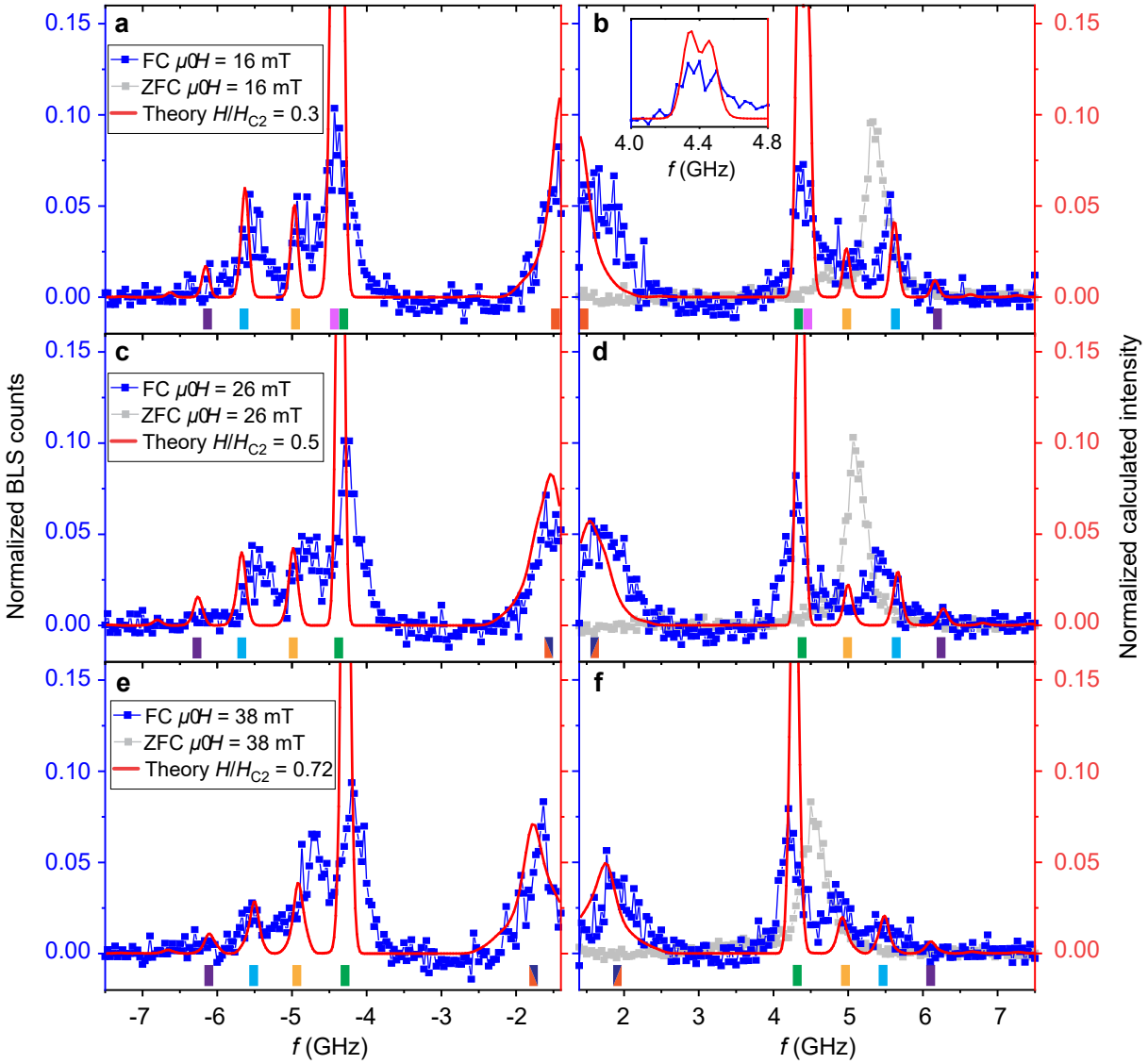

Figure 5.8.: **Normalized line cuts of experimental and theoretical BLS spectra.** Line cuts of the spectra in 5.6**a** (blue symbols) and Fig. 5.4**a** (grey symbols) for three magnetic field values $\mu_0 H$ = 16 mT, 26 mT and 38 mT with Stokes signals shown in panels (**a**), (**c**), and (**e**) and Anti-Stokes signals shown in panels (**b**), (**d**), and (**f**). The blue (grey) symbols are obtained in the metastable skyrmion phase (conical phase). The frequency-independent background signal (dark counts) found in the field-polarized phase was removed from the raw BLS spectra to realize a baseline similar to the theoretical curves (red lines). Negative counts in the experimental data (blue symbols) result from the background-signal subtraction. Red solid lines are theoretical BLS spectra for H/H_{c2} = 0.3, 0.5, 0.72. Coloured bars at the bottom of each panel indicate positions of theoretical skyrmion lattice resonances using the same colour coding as in Fig. 5.7. Both the experimental and theoretical data have been normalized with respect to the total spectral weight integrated over the full frequency range from -7.5 GHz to -1.4 GHz and from 1.4 GHz to 7.5 GHz. Inset of (**b**) shows the hybridization between the breathing and decupole modes.

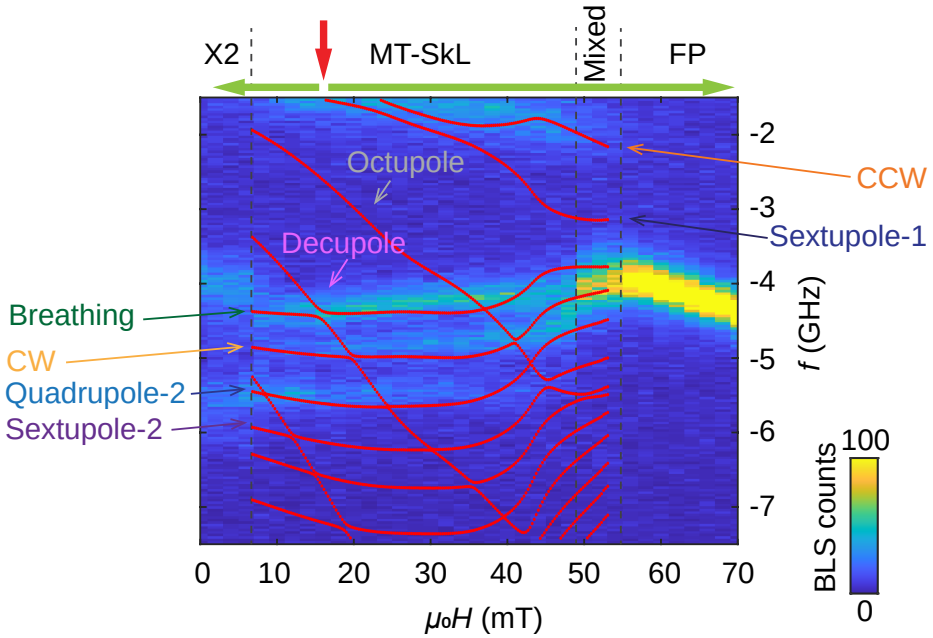

Figure 5.9.: **Magnon mode identification.** Stokes spectrum of Fig. 5.6**a** overlaid with magnon frequencies of the metastable skyrmion lattice phase calculated for a backscattering event with angle of incidence $\theta_{\text{in}} = \theta_{\text{out}} = 0$.

finite wavevectors probed in the experiment, the quadrupole-2 mode (light blue) is expected to exhibit a stronger signal than the CW mode especially at low field, consistent with the experimental data. In contrast, the sextupole-2 mode (purple) shows only very weak theoretical intensity. At 16 mT, the experimental spectra still reveal a finite signal above the noise level in the corresponding frequency range, whereas with increasing field H the signal becomes weaker and is no longer resolved.

For comparison, the Anti-Stokes spectra obtained in the conical phase using the zero-field-cooling (ZFC) protocol are shown in light gray. The clear discrepancies in both peak positions and field dependence between the two data sets demonstrate that the spectral features of the metastable skyrmion lattice phase (blue) are distinct from those of the conical phase (gray). In particular, the high-frequency peaks, i.e., for $f > 4.5$ GHz, can be unambiguously attributed to the CW and quadrupole-2 modes, respectively.

Figure 5.9 compares the experimental Stokes spectra with the theoretically calculated magnon branches for a fixed wavevector $\mathbf{q} = \hat{z}48$ rad μm^{-1}, corresponding to an incidence angle $\theta_{\text{in}} = \theta_{\text{out}} = 0$ in the present setup. At low frequencies, most of the spectral weight is carried by the CCW mode. As the BLS experiment probes magnons with a finite wavevector, a hybridization between the CCW and sextupole-1 modes is expected, even in the absence of magnetocrystalline anisotropies (see also Fig. 5.6**b**). The measured CCW mode appears broadened over a wide frequency range, consistent with its strong dispersion for out-of-plane wavevectors and the finite wavevector range collected by the focused BLS setup shown in Fig. 5.7**c**. This broadening, together with the limited signal-to-noise ratio, likely prevents the experi-

mental resolution of the hybridization with the sextupole-1 mode.

The narrow and intense branch between 4 and 4.5 GHz corresponds to the breathing mode, whose absolute frequency decreases with increasing field in contrast to the CCW mode. The frequency separation between the CCW and breathing modes is considerably larger than that observed in microwave spectroscopy, reflecting their opposite dispersion $f(q)$ as a function of in-plane wavevector, as shown in Fig. 5.7**b**. Although the predicted frequency gap associated with the avoided crossing with the decupole mode is not experimentally resolved, the breathing branch exhibits a small blue shift towards lower fields, in line with theoretical expectations.

The intensity around 5 GHz is attributed to the CW mode, whereas the nearly field-independent branch at approximately 5.5 GHz corresponds to the quadrupole-2 mode. Its characteristic weak field dependence distinguishes it from the $+Q$ mode of the conical phase, whose frequency decreases substantially with increasing H. In both the theoretical spectra, Fig. 5.6**b**, and the experiment, Fig. 5.9, the sextupole-2 and octupole modes display negligible BLS spectral weight and are not clearly resolved in the measured intensity maps.

5.3.3 Conclusions

In this work, we demonstrated that micro-focused BLS can resolve higher-order magnon modes of the skyrmion lattice phase that have not been accessible through previous experimental techniques such as microwave spectroscopy [47–51] or neutron scattering [43] in the chiral magnet Cu_2OSeO_3. In the backscattering geometry, BLS probes spin waves with relatively large wavevectors, $|\mathbf{q}| \sim k_{\mathrm{SkL}}$, comparable to the reciprocal lattice vector of the periodic magnetic texture. As a result, this technique provides access to the intermediate wavevector regime of the magnon dispersion $f(q)$, which bridges the gap between long-wavelength, $q \ll k_{\mathrm{SkL}}$ and short-wavelength, $q \gg k_{\mathrm{SkL}}$, excitations. This regime is of particular relevance for the design and implementation of future nanomagnonic circuits, where such intermediate wavevectors naturally emerge.

The good agreement between the experimental data and theoretical predictions, both in terms of eigenfrequencies and spectral weights, enabled the unambiguous identification of several magnon modes. We observed clear evidence of the wavevector-dependent eigenfrequencies of the CCW, breathing, and CW modes, previously characterized only at the Γ-point ($q = 0$). In addition, our measurements revealed higher-order excitations that had not been experimentally reported before. In particular, a mode with quadrupole character (quadrupole-2) is distinctly resolved across a broad magnetic field range. For the sextupole-2 mode, theory predicts very small spectral weights, consistent with the weak signatures observed in our BLS spectra at 16 mT, which vanish at higher magnetic fields. The complex nodal structure of these higher-order modes within the Wigner–Seitz cell [Fig. 3.3] implies pronounced anti-phase pre-

cession of neighboring spins within each skyrmion. At the finite wavevector probed by BLS, this leads to a strongly reduced net spin precession per skyrmion, and hence a weak coupling to light through the dynamic permittivity tensor — accounting for the low experimental visibility of such modes. Similarly, the decupole mode exhibits a small BLS spectral weight, but its hybridization with the breathing mode around 16 mT leaves subtle signatures that are consistent with our observations.

Overall, our study establishes focused BLS as a powerful tool for probing spin dynamics in skyrmion lattice systems with high spectral resolution. When combined with a quantitative theoretical model of the scattering process, which captures the distribution of transferred wavevectors, this technique enables the experimental exploration of magnon minibands within the first magnetic Brillouin zone. The resulting quantitative understanding of these magnonic bands represents a key step toward the control and engineering of magnonic crystals with topologically nontrivial band structures operating at microwave frequencies.

Looking ahead, the combination of a tightly focused laser spot and the ability to separately detect oppositely propagating magnons through Stokes and anti-Stokes scattering offers a promising route to identify magnon edge modes with topological character at the boundaries of skyrmion lattice domains [40–42]. The nontrivial magnon bands uncovered here further enrich the perspective of unconventional computing architectures based on wavevector-dependent spectral weights [22, 136–138]. These findings highlight the essential role of cryogenic BLS as a versatile and sensitive probe for advancing the experimental study of topological spin excitations in complex magnetic textures.

6 Theory of magneto-elastic coupling

In this part of the Thesis, we shift our focus to a different coupling mechanism in chiral magnets: the coupling between their magnetic textures and the underlying crystal lattice. In the previous Chapters, the discussion was centered on inelastic light scattering processes that were described starting from magneto-optic coupling. In contrast, our aim here is to develop a theoretical description of how the magnetic and mechanical properties of the system influence one another and to derive the collective magneto-elastic excitation dynamics.

The physical picture is the following: magnetic textures can distort the crystal lattice through spin–orbit interactions, while elastic deformations of the lattice can in turn affect the stability and dynamics of the magnetic states. This bidirectional coupling, known as magneto-elastic coupling, plays an essential role in determining both the static and dynamic properties of the material. A central goal of this part of the Thesis is to formulate a model that captures this interplay and allows us to investigate the resulting collective excitations of the coupled magnons and phonons dynamics. Understanding these hybrid modes provides a theoretical foundation for exploring the phonon magneto-chiral effect where spin and lattice vibrations cannot be treated independently. Our attention will be directed especially toward the skyrmion lattice phase. While skyrmions are now well established as topologically non-trivial magnetic textures, their coupling to lattice degrees of freedom remains largely unexplored, both theoretically and experimentally. This makes the problem particularly appealing, as it opens the possibility of identifying novel mechanisms of stability and collective excitations.

The structure of this Chapter is as follows. We begin by introducing the framework of linear elasticity theory, which provides a baseline description of the mechanical response of the crystal in the absence of magnetism. Next, we incorporate the contribution of magneto-elastic coupling arising from spin–orbit interactions, thereby linking the elastic strain field to the magnetic order parameter. This is done via a mean-field approach, similar to what was presented in Chapter 3, which allows us to determine the stable configurations of the coupled system. In particular, we put our focus on the skyrmion lattice phase by providing a formulation of its energy density, and the relative minimisation techniques.

6.1 Linear elasticity theory

This Section serves as an introduction for the linear theory of elasticity. This theory describes the mechanical properties of solid bodies when regarded as continuous media that are weakly deformed under the action of external forces. The formulation is well established in the literature, and here we closely follow the derivation presented by Landau and Lifshitz in their book *Theory of elasticity* [139], as well as Refs. [55, 56, 140].

At the microscopic level, deformations of a crystal can, in principle, be described by calculating the energy cost associated with displacing individual atoms from their equilibrium positions. However, this approach is generally very complex, as it requires accounting for multiple energy contributions and carefully taking the thermodynamic limit. The classical theory of elasticity takes a different route: it describes the energy required to deform a solid body under the assumption that the wavelength of the deformation is much larger than the atomic lattice spacing. In the case of magneto-elastic coupling in bulk chiral magnets, this assumption is well justified. The relevant magnetic textures are governed by the characteristic wavevector $Q = D/J$, which typically corresponds to length scales ranging from tens to hundreds of nanometers — much larger than the underlying atomic lattice spacing. Consequently, lattice displacements induced by the magnetic texture through spin–orbit coupling inherit the same long wavelength. This validates the use of the classical continuum description, where the crystal is modelled as a continuous medium. A key strength of this approach is its reliance on symmetry principles. Rather than requiring a detailed microscopic description, the theory builds on symmetry arguments to derive the governing equations. As a result, one arrives at a minimal model that captures the essential physics using only a small set of phenomenological parameters.

6.1.1 Strain tensor

When a solid is subjected to external forces, it deforms with respect to its equilibrium configuration. In this case, each material point originally located at position $\mathbf{r}$ is displaced to a new position $\mathbf{r}' = \mathbf{r} + \mathbf{u}(\mathbf{r})$, where $\mathbf{u}(\mathbf{r})$ denotes the displacement field, defined as

$$\mathbf{u}(\mathbf{r}) = \mathbf{r}' - \mathbf{r}\,. \tag{6.1}$$

This definition of the displacement field allows us to quantify how the distance between two nearby points changes during deformation. Initially, the vector connecting the two points is $d\mathbf{l}$; after deformation, it becomes $d\mathbf{l}' = d\mathbf{l} + d\mathbf{u}$. Since $\mathbf{u}(\mathbf{r})$ is assumed to be a continuous and differentiable function everywhere, the new distance between the two points reduces to

$$d\mathbf{l}'^2 = (dr_1 + du_1)^2 + (dr_3 + du_3)^2 + (dr_3 + du_3)^2 = d\mathbf{l}^2 + 2\frac{\partial u_i}{\partial r_j} dr_i dr_j + \frac{\partial u_i}{\partial r_j}\frac{\partial u_i}{\partial r_k} dr_j dr_k\,, \tag{6.2}$$

where we used that $du_i = (\partial u_i/\partial r_j)dr_j$. This expression can be written in an equivalent, more compact form as

$$d\mathbf{l}'^2 = d\mathbf{l}^2 + 2\varepsilon_{ij}dr_i dr_j\,, \tag{6.3}$$

where we introduced the symmetric rank-2 tensor ε_{ij}, which is known as the strain tensor and is defined as

$$\varepsilon_{ij} = \frac{1}{2}\left(\frac{\partial u_i}{\partial r_j} + \frac{\partial u_j}{\partial r_i} + \frac{\partial u_k}{\partial r_i}\frac{\partial u_k}{\partial r_j}\right). \tag{6.4}$$

Physically, the diagonal components ε_{ii} describe normal strains, i.e., relative elongations or compressions along coordinate axes, while the off-diagonal components ε_{ij} represent shear strains, i.e., changes in the angle between initially perpendicular directions. Within the framework of linear elasticity, we assume that body deformations, i.e., changes in distances, are always small compared with the distances themselves. If this condition is satisfied, then all components of the strain tensor must be small. This enables us to neglect the quadratic term in Eq. (6.4).

So far, the discussion has been restricted to local deformations. However, in addition to these, a body may also undergo some global transformations, such as dilatation or shear deformation. These deformations affect all points in the body equally and thus have a global character, in contrast with the local variations of the displacement field. We describe such contributions by a space-independent, rank-2 tensor E_{ij}, referred to here as the global strain. Combining both contributions together, the strain tensor within the lineal elasticity theory can be expressed as

$$\varepsilon_{ij} = \frac{1}{2}\left(\frac{\partial u_i}{\partial r_j} + \frac{\partial u_j}{\partial r_i}\right) + E_{ij}\,. \tag{6.5}$$

This element represents the fundamental building block of elasticity theory, as it fully characterizes the deformation of a solid under external forces, such as the magneto-elastic coupling that we present later.

6.1.2 Free energy functional

When the body is not deformed, each atom occupies its equilibrium position and the system as a whole is in thermal equilibrium. In this case, the strain tensor vanishes. Once a force is applied, however, the system relaxes into a new equilibrium in which the atomic arrangement is modified. Each atom then experiences restoring forces that attempt to bring the body back to its original configuration. These interatomic forces are inherently short-ranged compared to the characteristic length scales entering magneto-elastic coupling interactions in chiral magnets, which are determined by the ratio $2\pi/Q$. Since our interest lies in macroscopic behaviour, we do not need to consider the detailed microscopic force fields. Instead, the symmetric strain tensor [Eq. (6.5)] provides the essential information: whenever it is nonzero, a deformation has taken place, which implies that finite restoring forces act within the material. From an energetic viewpoint, this corresponds to an increase in the internal energy of the system, balanced by the

work done by the external field.

Mathematically, this is captured by introducing a harmonic free energy functional of the strain tensor:

$$\mathscr{F}_{\text{ela}}[\varepsilon] = \frac{1}{V}\int d\mathbf{r}\,\frac{1}{2}\varepsilon_{ij}C_{ijkl}\varepsilon_{kl}\,. \tag{6.6}$$

Eq. (6.6) represents the most general quadratic expression for the elastic energy in terms of the strain tensor ε_{ij}. From this formulation, it follows immediately that the undistorted solid, i.e., $\varepsilon_{ij} = 0$, corresponds to the equilibrium configuration in the absence of external forces. The rank-4 tensor C_{ijkl}, known as the stiffness tensor, governs the response of the material to deformations. Due to the symmetry of the strain tensor, C_{ijkl} itself satisfies the following index symmetries:

$$C_{ijkl} = C_{jilk} = C_{klij}\,. \tag{6.7}$$

Physically, one may think of C_{ijkl} as a generalized spring constant for the crystal: just as a spring resists stretching with a restoring force proportional to the applied displacement, the stiffness tensor quantifies how strongly the crystal resists different types of deformation, such as compression, shear, or combinations of these.

Symmetry classes

The rank of the stiffness tensor reflects the fact that, in a crystalline solid, the material response depends on both the direction of the applied force and the direction of the resulting deformation. In principle, the stiffness tensor C_{ijkl} is a fourth-rank tensor with $3^4 = 81$ components. However, many of these components are not independent due to the intrinsic symmetries of the strain tensor and the requirement that the elastic energy must remain invariant under rotations consistent with the crystal symmetry. The index symmetries ($C_{ijkl} = C_{jikl} = C_{ijlk} = C_{klij}$) already reduce the number of independent entries to 21 in the most general case of a fully anisotropic solid. This maximal anisotropy corresponds to the triclinic crystal system. Higher crystal symmetries constrain the elastic response further, thereby lowering the number of independent elastic constants [139]. For example, orthorhombic crystals possess 9, tetragonal crystals 6 or 7, and hexagonal crystals 5 independent constants. Of particular relevance here are cubic crystals, which exhibit very high symmetry that imposes strong constraints on C_{ijkl}, leaving only 3 independent elastic constants, typically denoted C_{11}, C_{12}, and C_{44}. Physically, these correspond to the elastic response under uniaxial compression (C_{11}), under shear (C_{44}), and the coupling between orthogonal directions (C_{12}).

Voigt notation

To simplify the formulation of elasticity, it is convenient to adopt Voigt notation, which provides a compact way of writing the strain and stiffness tensors by exploiting their index symmetries. Since the

strain tensor ε_{ij} is symmetric, it contains only six independent components which can be expressed as a six-dimensional vector,

$$\varepsilon = \begin{bmatrix} \varepsilon_{11} \\ \varepsilon_{22} \\ \varepsilon_{33} \\ 2\varepsilon_{23} \\ 2\varepsilon_{13} \\ 2\varepsilon_{12} \end{bmatrix} = \begin{bmatrix} \varepsilon_1 \\ \varepsilon_2 \\ \varepsilon_3 \\ \varepsilon_4 \\ \varepsilon_5 \\ \varepsilon_6 \end{bmatrix} . \tag{6.8}$$

In the same spirit, the stiffness tensor C_{ijkl}, which in full form is a fourth-rank tensor with up to 21 independent entries, can be expressed as a symmetric 6×6 matrix $C_{\alpha\beta}$ in Voigt notation. For example, in the case of cubic crystals, which is of particular interest for the following discussion, this takes the form

$$C = \begin{bmatrix} C_{11} & C_{12} & C_{12} & 0 & 0 & 0 \\ C_{12} & C_{11} & C_{12} & 0 & 0 & 0 \\ C_{12} & C_{12} & C_{11} & 0 & 0 & 0 \\ 0 & 0 & 0 & C_{44} & 0 & 0 \\ 0 & 0 & 0 & 0 & C_{44} & 0 \\ 0 & 0 & 0 & 0 & 0 & C_{44} \end{bmatrix} . \tag{6.9}$$

With these definitions, the quadratic elastic energy density that follows from Eq. (6.6) reduces to

$$f = \frac{1}{2} \sum_{i,j,k,l} \varepsilon_{ij} C_{ijkl} \varepsilon_{kl} = \frac{1}{2} \sum_{\alpha,\beta=1}^{6} \varepsilon_\alpha C_{\alpha\beta} \varepsilon_\beta \, . \tag{6.10}$$

This notation is widely used in elasticity theory because it reduces the complexity of tensorial equations and makes the symmetry constraints on the elastic constants transparent.

6.2 Magneto-elastic coupling

The physical origin of magneto-elastic coupling lies in the mutual interplay between the lattice vibrational degrees of freedom and the spin configuration. On one hand, the arrangement of spins can modify the equilibrium positions of atoms by exerting forces on the lattice. On the other hand, deformations of the crystal lattice alter the energy landscape that governs the magnetic configuration. This feedback mechanism provides a natural route for spin and lattice degrees of freedom to become strongly intertwined. Here, we are interested in effects characterised by long wavelength modulations. Therefore, the building blocks of our theory are naturally provided by the local magnetisation $\mathbf{M}(\mathbf{r}) = M_s \mathbf{m}(\mathbf{r})$ and the strain tensor $\varepsilon_{ij}(\mathbf{r})$.

The coupling can be systematically classified according to its order in spin–orbit interaction. The leading contribution is given by

$$\mathscr{F}_{\mathrm{mec}}[\varepsilon, \mathbf{m}] = \frac{1}{V} \int d\mathbf{r}\, \varepsilon_{ij}(\mathbf{r}) \lambda_{ijkl} m_k(\mathbf{r}) m_l(\mathbf{r}) \,, \tag{6.11}$$

which represents the lowest-order magneto-elastic free energy functional containing both strain and magnetisation fields. The coupling tensor λ_{ijkl} is fully constrained by the symmetry class of the underlying crystal, analogous to the stiffness tensor in linear elasticity. Physically, Eq. (6.11) can be interpreted as an elastically-induced magnetic anisotropy, where lattice deformations effectively generate an additional single-ion anisotropy term for the spins [141].

Chiral coupling

Higher-order contributions to the magneto-elastic interaction are also possible. A relevant example is

$$\mathscr{F}_{\mathrm{mec}}[\varepsilon, \mathbf{m}] = \frac{1}{V} \int d\mathbf{r}\, \varepsilon_{ij}(\mathbf{r}) \mu_{ijkl} w_{kl}(\mathbf{r}) \,, \tag{6.12}$$

with the Lifshitz invariant

$$w_{kl}(\mathbf{r}) = \varepsilon_{ksp} m_s(\mathbf{r}) \partial_l m_p(\mathbf{r}) \,. \tag{6.13}$$

This term describes how strain can modulate the DM interaction, and is typically considered as a higher-order effect compared to the anisotropic coupling in Eq. (6.11). However, it can become the dominant mechanism in specific situations. For instance, in the field polarised phase the leading anisotropic contribution is suppressed, and the strain-induced modulation of the DM interaction provides the primary source of magneto-elastic coupling. In this regime, the lattice deformation tilts the otherwise collinear spin order, significantly affecting the collective magnon–phonon dynamics [142].

6.2.1 Coupling tensor

The magneto-elastic coupling tensor λ_{ijkl} can be conveniently written using Voigt notation, in direct analogy with the stiffness tensor introduced earlier. As in the case of linear elasticity, the specific form of λ_{ijkl} is fully determined by the symmetry of the underlying crystal lattice [141, 143, 144]. However, since this tensor now couples the strain field to the magnetization, the index contraction differs from that of the stiffness tensor. As a result, the magneto-elastic coupling generally contains a larger number of independent components, reflecting the additional degrees of freedom associated with the spin variables. In the following, we focus on the case of cubic crystals, where symmetry considerations significantly

reduce the number of independent terms. In this case, the most general form of the coupling tensor can be written as

$$\lambda = \begin{bmatrix} \lambda_{11} & \lambda_{21} & \lambda_{12} & 0 & 0 & 0 \\ \lambda_{12} & \lambda_{11} & \lambda_{21} & 0 & 0 & 0 \\ \lambda_{21} & \lambda_{12} & \lambda_{11} & 0 & 0 & 0 \\ 0 & 0 & 0 & \lambda_{44} & 0 & 0 \\ 0 & 0 & 0 & 0 & \lambda_{44} & 0 \\ 0 & 0 & 0 & 0 & 0 & \lambda_{44} \end{bmatrix} . \tag{6.14}$$

The individual components $C_{\alpha\beta}$ of the stiffness tensor can be directly determined from the phonon dispersion, as will be discussed in the following Chapter. In contrast, there exists no straightforward experimental procedure to determine the exact form of the magneto-elastic coupling tensor $\lambda_{\alpha\beta}$. This situation is analogous to that encountered for the magneto-optic coupling tensor G_{ijkl} discussed previously. Here, we want to employ symmetry arguments to constrain the possible tensor components. For this reason, the present discussion will be limited to a few representative cases in which we impose additional restrictions on the number of independent elements of $\lambda_{\alpha\beta}$. In order to achieve this, it is convenient to introduce the following combinations

$$\lambda_{\pm} = \lambda_{12} \pm \lambda_{21} \,, \tag{6.15}$$

which link the off-diagonal contributions of the coupling tensor. In centrosymmetric cubic magnets, the system's symmetry imposes that the anti-symmetric contribution must vanish, i.e, $\lambda_{-} = 0$. This is not the case for noncentrosymmetric materials, where the chiral structure relaxes this condition.

Isotropic coupling

The isotropic coupling tensor represents the simplest case compatible with the cubic symmetry of the crystal. In this configuration, the magneto-elastic interaction is invariant under spatial rotations, implying that no magneto-crystalline anisotropies can arise in the system. The symmetry constraints lead to the relations

$$\lambda_{11} - \frac{1}{2}\lambda_{+} = 2\lambda_{44} \quad \text{and} \quad \lambda_{-} = 0 \,, \tag{6.16}$$

thus reducing the number of independent parameters. In this limit, the strain field couples uniformly to the magnetisation, producing an isotropic modulation of the magnetic free energy that is independent of the specific orientation of the deformation.

Chiral coupling

A more general form of the coupling tensor arises in the case of chiral cubic crystals, where the absence of inversion symmetry allows for antisymmetric components in $\lambda_{\alpha\beta}$ [143, 144]. This can be quantified

by the combination $\lambda_{-} = \lambda_{12} - \lambda_{21}$ introduced earlier. Hence, the magneto-elastic coupling tensor in this case reads

$$\lambda_{11} - \frac{1}{2}\lambda_{+} = 2\lambda_{44} \quad \text{and} \quad \lambda_{-} \neq 0\,, \tag{6.17}$$

where the second relation lowers the overall symmetry of the system and introduces a chiral contribution to the magneto-elastic coupling. This form reflects the handedness inherent to the underlying crystal structure and may result in asymmetric magneto-elastic responses.

Anisotropic coupling

The magneto-elastic coupling tensor can also be used to effectively introduce magneto-crystalline anisotropies in the system. In general, this can be done by lowering the symmetry constraint in the first relationship, that is,

$$\lambda_{11} - \frac{1}{2}\lambda_{+} \neq 2\lambda_{44} \quad \text{and} \quad \lambda_{-} = 0\,. \tag{6.18}$$

The first inequality breaks the full rotational invariance of the coupling contribution, giving rise to a directional dependence in the magneto-elastic interaction. As a consequence, the strain field may favour specific magnetisation orientations or distortions, thereby influencing the equilibrium magnetic configuration and the associated collective excitations.

In the following Chapters, the consequences of these three representative coupling cases will be analysed, with particular emphasis on their impact on the equilibrium configuration and collective dynamics within the magnetic skyrmion lattice phase.

6.2.2 Free energy analysis

The complete theoretical description of the system includes three main contributions: the magnetic free energy derived in Chapter 2, the elastic term associated with lattice deformations, and the magneto-elastic coupling that links the two subsystems. The total free energy functional can therefore be written as

$$\mathscr{F}[\mathbf{m}, \boldsymbol{\varepsilon}] = \mathscr{F}_0[\mathbf{m}] + \mathscr{F}_{\text{dip}}[\mathbf{m}] + \mathscr{F}_{\text{ela}}[\boldsymbol{\varepsilon}] + \mathscr{F}_{\text{mec}}[\mathbf{m}, \boldsymbol{\varepsilon}]\,, \tag{6.19}$$

where $\mathscr{F}_0$ and $\mathscr{F}_{\text{dip}}$ are given by Eq. (2.43) and Eq. (2.44), respectively. The first two terms describe the purely magnetic contribution, including exchange, Dzyaloshinskii–Moriya, Zeeman, and dipolar interactions, while the last two encode the elastic and magneto-elastic energies associated with lattice strain and spin–lattice coupling.

Since the magnetic subsystem already defines a natural energy scale set by the ratio D^2/J, it is convenient to express the elastic and magneto-elastic coefficients in dimensionless form as

$$\tilde{C}_{ijkl} = \frac{1}{D^2/J} C_{ijkl} \quad \text{and} \quad \tilde{\lambda}_{ijkl} = \frac{1}{D^2/J} \lambda_{ijkl}\,. \tag{6.20}$$

This rescaling enables a direct comparison between magnetic and elastic energy contributions. The components of the stiffness tensor C_{ijkl} are typically determined experimentally from measurements of the phonon velocities along different crystallographic directions, as will be discussed in the next Chapter. For most crystals, these components range from tens to hundreds of gigapascals, several orders of magnitude larger than the characteristic magnetic energy scale D^2/J. This difference in magnitude reflects their distinct microscopic origins: the elastic energy arises from interatomic bonding forces that maintain the crystal structure, whereas the magnetic energy originates from much weaker spin–spin exchange interactions. As a consequence, magnetically induced lattice distortions lead to only small variations in the displacement field $\mathbf{u}(\mathbf{r})$, typically well within the linear elasticity regime.

In contrast, the strength of the magneto-elastic coupling tensor is far more difficult to determine experimentally. In the next Chapter, we will infer its strength based on measurements of the phonon velocity in the presence of an ordered magnetic phase. Typical values range from a few kilopascals to several megapascals, and they often show a strong temperature dependence, reflecting the underlying spin–orbit interaction strength. These values are fully consistent with the weak-coupling approximation $\lambda/C \ll 1$, which underlies the validity of our linearised theory.

6.3 Skyrmion lattice phase

In the following, we focus exclusively on deriving the equilibrium configuration of the coupled magneto-elastic system starting from the magnetic skyrmion lattice phase. To exploit the periodic nature of this state, we first express the total energy density in reciprocal space, following the same approach introduced in Chapter 2. We then present the numerical solutions for both the magnetic configuration and the corresponding displacement field $\mathbf{u}(\mathbf{r})$, obtained from the minimisation of the total free energy. These equilibrium configurations will serve as the foundation for the next Chapter, where we investigate the collective magnon–phonon dynamics emerging from these non-trivial coupled textures.

6.3.1 Formulation in reciprocal space

In Chapter 2, we analysed the periodic structure of the magnetic skyrmion lattice phase starting from the Bravais lattice vector $\mathbf{R_n}$. Here, the local displacement field $\mathbf{u}(\mathbf{r})$ is modulated by the magnetic texture through the magneto-elastic coupling. Consequently, we assume that the displacement field inherits the same periodicity within the magnetic lattice plane, namely

$$\mathbf{u}(\boldsymbol{\rho} + \mathbf{R_n}) = \mathbf{u}(\boldsymbol{\rho})\,. \tag{6.21}$$

This periodicity condition further implies that the displacement field is uniform along the out-of-plane direction, i.e., $\partial_z \mathbf{u}(\mathbf{r}) = 0$, where $\hat{z}$ denotes the axis perpendicular to the skyrmion lattice plane. Eq. (6.21) allows us to express the displacement field as a Fourier series over the reciprocal lattice vectors $\mathbf{G}_{\boldsymbol{\nu}}$:

$$\mathbf{u}(\boldsymbol{\rho}) = \sum_{\mathbf{G}_{\boldsymbol{\nu}}} \mathbf{u}(\mathbf{G}_{\boldsymbol{\nu}}) e^{i\boldsymbol{\rho}\cdot\mathbf{G}_{\boldsymbol{\nu}}} \,. \tag{6.22}$$

The Fourier coefficients $\mathbf{u}(\mathbf{G}_{\boldsymbol{\nu}})$ are obtained by integrating over the magnetic unit cell,

$$\mathbf{u}(\mathbf{G}_{\boldsymbol{\nu}}) = \frac{1}{A^{\mathrm{puc}}} \int_{\mathrm{uc}} \mathbf{u}(\boldsymbol{\rho}) e^{-i\boldsymbol{\rho}\cdot\mathbf{G}_{\boldsymbol{\nu}}} \, d\boldsymbol{\rho} \,, \tag{6.23}$$

where A^{puc} denotes the area of the primitive magnetic unit cell.

Lattice distortion

In the absence of magneto-elastic coupling, the magnetic skyrmion lattice is assumed to form a perfect hexagonal structure. Its Bravais lattice vectors are given in Eq. (2.49), defined in terms of the hexagonal covariant basis $\mathbf{g}_i$ given in Eq. (2.50). When the magneto-elastic coupling is introduced, however, the displacement field $\mathbf{u}(\mathbf{r})$ deforms the underlying atomic lattice. Consequently, the magnetic skyrmion lattice undergoes a corresponding distortion. To account for this effect, we generalize the original hexagonal basis by introducing two additional degrees of freedom that parametrize its deformation:

$$\mathbf{g}_1 = \begin{pmatrix} \cos\left(\frac{\pi}{6}+\frac{\phi}{2}\right) \\ -\sin\left(\frac{\pi}{6}+\frac{\phi}{2}\right) \\ 0 \end{pmatrix}, \quad \mathbf{g}_2 = \eta \begin{pmatrix} \cos\left(\frac{\pi}{6}+\frac{\phi}{2}\right) \\ \sin\left(\frac{\pi}{6}+\frac{\phi}{2}\right) \\ 0 \end{pmatrix}, \quad \mathbf{g}_3 = \begin{pmatrix} 0 \\ 0 \\ 1 \end{pmatrix}. \tag{6.24}$$

Here, the parameter ϕ quantifies the change in the relative angle between the in-plane basis vectors $\mathbf{g}_1$ and $\mathbf{g}_2$, while η describes an oblique distortion of the lattice. However, this parametrization alone does not account for the overall in-plane rotation of the skyrmion lattice relative to the crystallographic axes. Since magnetoelastic coupling breaks rotational invariance, the magnetic lattice may reorient itself to minimize the total free energy. To describe this effect, we introduce an in-plane rotation matrix

$$R_\theta = \begin{pmatrix} \cos\theta & -\sin\theta & 0 \\ \sin\theta & \cos\theta & 0 \\ 0 & 0 & 1 \end{pmatrix}, \tag{6.25}$$

where θ denotes the rotation angle of the magnetic lattice with respect to the crystal axes. The distorted Bravais lattice vectors can therefore be expressed as

$$\mathbf{R}_{\mathbf{n}} = a_{\mathrm{SkL}} R_\theta \Big(n_1 \mathbf{g}_1 + n_2 \mathbf{g}_2 \Big), \quad \mathbf{n} = (n_1, n_2) \in \mathscr{Z} \times \mathscr{Z} \,. \tag{6.26}$$

The area of the primitive unit cell now depends on the distortion parameters η and ϕ, and is given by

$$A^{\mathrm{puc}} = \frac{1}{2}\eta\sqrt{2+\cos(2\phi)+\sqrt{3}\sin(2\phi)}\,a_{\mathrm{SkL}}^2\,. \tag{6.27}$$

Naturally, the reciprocal lattice vectors deform correspondingly. They can be written as

$$\mathbf{G}_{\boldsymbol{\nu}} = \frac{2\pi}{a_{\mathrm{SkL}}} R_\theta \left(\nu_1 \mathbf{g}^1 + \nu_2 \mathbf{g}^2\right), \quad \text{with } \boldsymbol{\nu} = (\nu_1, \nu_2) \in \mathscr{Z} \times \mathscr{Z}\,, \tag{6.28}$$

where $\mathbf{g}^i$ are the contravariant basis vectors dual to $\mathbf{g}_i$, defined such that $\mathbf{g}^i \cdot \mathbf{g}_j = \delta^i_j$. Explicitly, they read

$$\mathbf{g}^1 = \gamma \begin{pmatrix} \sin\left(\frac{\pi}{6}+\frac{\phi}{2}\right) \\ -\cos\left(\frac{\pi}{6}+\frac{\phi}{2}\right) \\ 0 \end{pmatrix}, \quad \mathbf{g}^2 = \gamma\frac{1}{\eta} \begin{pmatrix} \sin\left(\frac{\pi}{6}+\frac{\phi}{2}\right) \\ \cos\left(\frac{\pi}{6}+\frac{\phi}{2}\right) \\ 0 \end{pmatrix}, \quad \mathbf{g}^3 = \begin{pmatrix} 0 \\ 0 \\ 1 \end{pmatrix}, \tag{6.29}$$

with prefactor

$$\gamma = \frac{1}{2\cos\left(\frac{\pi}{6}+\frac{\phi}{2}\right)\sin\left(\frac{\pi}{6}+\frac{\phi}{2}\right)}\,. \tag{6.30}$$

Energy density

The reciprocal-space formulation of the dimensionless free energy density per unit cell is obtained by substituting the Fourier expansion of the magnetisation and displacement fields into the total free energy functional [Eq. (6.19)]. The magnetic contribution was previously derived in Eq. (2.56). In the present case, however, the reciprocal lattice vectors $\mathbf{G}_{\boldsymbol{\nu}}$ now incorporate the additional degrees of freedom $\{\eta, \phi, \theta\}$ that characterize the distortion of the skyrmion lattice, as introduced in Eq. (6.28). The elastic contribution to the total energy density can be expressed as

$$\frac{\varepsilon_{\mathrm{ela}}^{\mathrm{puc}}}{D^2/J} = \frac{1}{2}E_{ij}C_{ijkl}E_{kl} + \frac{1}{2}\sum_{\mathbf{G}_{\boldsymbol{\nu}}}(\mathbf{G}_{\boldsymbol{\nu}})_i u_j(\mathbf{G}_{\boldsymbol{\nu}})C_{ijkl}(\mathbf{G}_{\boldsymbol{\nu}})_k u_l(-\mathbf{G}_{\boldsymbol{\nu}})\,, \tag{6.31}$$

where we have omitted the tilde notation introduced in Eq. (6.20) for the sake of readability. The first term represents the homogeneous elastic energy, which depends on the macroscopic strain tensor E_{ij}, while the second term accounts for the periodic elastic modulations in reciprocal space, expressed through the Fourier amplitudes of the displacement field $u_j(\mathbf{G}_{\boldsymbol{\nu}})$.

The magneto-elastic contribution presented in Eq. (6.11) takes the form

$$\frac{\varepsilon_{\mathrm{mec}}^{\mathrm{puc}}}{D^2/J} = \sum_{\mathbf{G}_{\boldsymbol{\nu}}} E_{ij}\lambda_{ijkl}m_k(-\mathbf{G}_{\boldsymbol{\nu}})m_l(\mathbf{G}_{\boldsymbol{\nu}}) - i\sum_{\mathbf{G}_{\boldsymbol{\nu}},\mathbf{G}_{\boldsymbol{\eta}}}(\mathbf{G}_{\boldsymbol{\nu}}+\mathbf{G}_{\boldsymbol{\eta}})_i u_j(-\mathbf{G}_{\boldsymbol{\nu}}-\mathbf{G}_{\boldsymbol{\eta}})\lambda_{ijkl}m_k(\mathbf{G}_{\boldsymbol{\nu}})m_l(\mathbf{G}_{\boldsymbol{\eta}})\,. \tag{6.32}$$

We present here also the chiral magneto-elastic coupling, introduced in Eq. (6.12), which be expressed in reciprocal space as

$$\begin{aligned}\frac{\varepsilon^{\text{puc}}_{\text{mec,chiral}}}{D^2/J} =& i\sum_{\mathbf{G_\nu}} E_{ij}\mu_{ijkl}\varepsilon_{ksp} m_s(-\mathbf{G_\nu})(\mathbf{G_\nu})_j m_p(\mathbf{G_\nu}) \\ &+ \sum_{\mathbf{G_\nu},\mathbf{G_\eta}} (\mathbf{G_\nu}+\mathbf{G_\eta})_i u_j(-\mathbf{G_\nu}-\mathbf{G_\eta})\mu_{ijkl}\varepsilon_{ksp} m_s(\mathbf{G_\nu})(\mathbf{G_\nu})_l m_p(\mathbf{G_\eta})\,.\end{aligned} \tag{6.33}$$

Numerical minimisation

In Chapter 2, we introduced the numerical procedure for minimizing the magnetic energy density by applying a cutoff Λ in reciprocal space, such that only modes with $|\mathbf{G_\nu}| < \Lambda$ were retained. The number of independent Fourier components, and therefore the dimensionality of the variational problem, was directly determined by this cutoff. In the present case, the introduction of magneto-elastic coupling significantly increases the number of degrees of freedom in the system. In addition to the magnetic Fourier components $\mathbf{m}(\mathbf{G_\nu})$, we now include the Fourier amplitudes of the displacement field

$$\mathbf{u}(\mathbf{G_\nu}) = \left(u'_x(\mathbf{G_\nu}) + iu''_x(\mathbf{G_\nu}),\, u'_y(\mathbf{G_\nu}) + iu''_y(\mathbf{G_\nu}),\, u'_z(\mathbf{G_\nu}) + iu''_z(\mathbf{G_\nu})\right)^T, \tag{6.34}$$

together with the global strain tensor E_{ij} and the lattice distortion parameters $\{\eta, \phi, \theta\}$. Consequently, the system's configuration space becomes substantially larger, leading to a higher-dimensional optimization problem.

We can reduce the number of independent components by exploiting additional constraints for the magnetic and displacement field. In particular, both these field are real-valued in real space, thus their Fourier components must satisfy

$$\begin{cases}\mathbf{m}(-\mathbf{G_\nu}) = \mathbf{m}(\mathbf{G_\nu})^* \\ \mathbf{u}(-\mathbf{G_\nu}) = \mathbf{u}(\mathbf{G_\nu})^*\end{cases}. \tag{6.35}$$

This condition ensures that only half of the Fourier coefficients are independent, effectively reducing the computational complexity. In Chapter 2, we further simplified the magnetic problem by imposing in-plane inversion symmetry on the skyrmion lattice, namely $m_{x,y}(-\boldsymbol{\rho}) = -m_{x,y}(\boldsymbol{\rho})$ and $m_z(-\boldsymbol{\rho}) = m_z(\boldsymbol{\rho})$. However, when the magneto-elastic coupling is included, the lattice distortion breaks the in-plane inversion symmetry, leading to an asymmetric deformation of both the magnetic and elastic textures. Therefore, this simplification is no longer valid in this case.

Magnetic lattice orientation

Up to this point, we have not explicitly distinguished between the Cartesian axes $\{\hat{x}, \hat{y}, \hat{z}\}$ used in our formulation and the crystallographic directions of the underlying lattice. In general, however, the magneto-elastic coupling breaks the rotational invariance of the isotropic chiral magnet free energy functional. As

a result, the orientation of the magnetic lattice relative to the crystal axes becomes relevant. In the following, we assume that the magnetic lattice always lies in the plane orthogonal to the applied magnetic field. This approximation is well justified for standard cubic chiral magnets, where magnetocrystalline anisotropies typically induce only small tilts on the order of a few degrees of the skyrmion plane [82].

When the magnetic field $\mu_0\mathbf{H}$ is applied along one of the principal crystallographic directions, for example $\mathbf{H} \parallel [001]$, the skyrmion lattice lies in the xy-plane, which corresponds to the $[100]$ and $[010]$ crystal directions for $\theta = 0$. In this case, the total free energy can be minimised with respect to the angle θ, which determines the in-plane relative orientation between the skyrmion lattice vectors, described in Cartesian coordinates, and the crystallographic axis. Therefore, the energy density formulation and reciprocal lattice definitions presented so far remain valid in this situation. However, when the magnetic field is tilted away from the principal crystallographic axes, we must account for the mismatch between the magnetic and crystallographic coordinate systems. Our goal is to preserve the previously derived expressions for the reciprocal lattice basis [Eq. (6.29)] and for the energy density per unit cell. To achieve this, we define the $\hat{z}$-axis of our working frame as the direction of the applied magnetic field, so that the skyrmion lattice always remains confined to the corresponding xy-plane.

While this convention simplifies the treatment of the magnetic structure, it introduces a subtlety: the stiffness and magneto-elastic coupling tensors, C_{ijkl} and λ_{ijkl}, are originally defined in the crystallographic coordinate system, where the indices $i = 1,2,3$ correspond to the $[100]$, $[010]$, and $[001]$ directions, respectively. Consequently, the tensor components must be rotated into the frame associated with the skyrmion lattice. This is achieved through a fourth-rank tensor transformation rule:

$$T'_{ijkl} = R_{in}R_{jm}R_{ks}R_{lp}T_{mnsp}\,, \tag{6.36}$$

where T_{ijkl} represents a generic rank-4 tensor in the crystallographic frame, and R is the rotation matrix that aligns the crystal axes with the new Cartesian frame defined by the magnetic field and lattice plane. This transformation also clarifies the notion of an isotropic tensor, as introduced previously. A tensor is isotropic if it remains invariant under any arbitrary rotation, i.e., if $T'_{ijkl} = T_{ijkl}$ for all R. In the case of a cubic crystal, this condition is satisfied when the stiffness and coupling tensor components obey the proportionality relations

$$C_{11} - C_{12} = 2C_{44} \quad \text{and} \quad \lambda_{11} - \frac{1}{2}\lambda_{+} = 2\lambda_{44}\,,\ \ \lambda_{-} = 0\,, \tag{6.37}$$

respectively.

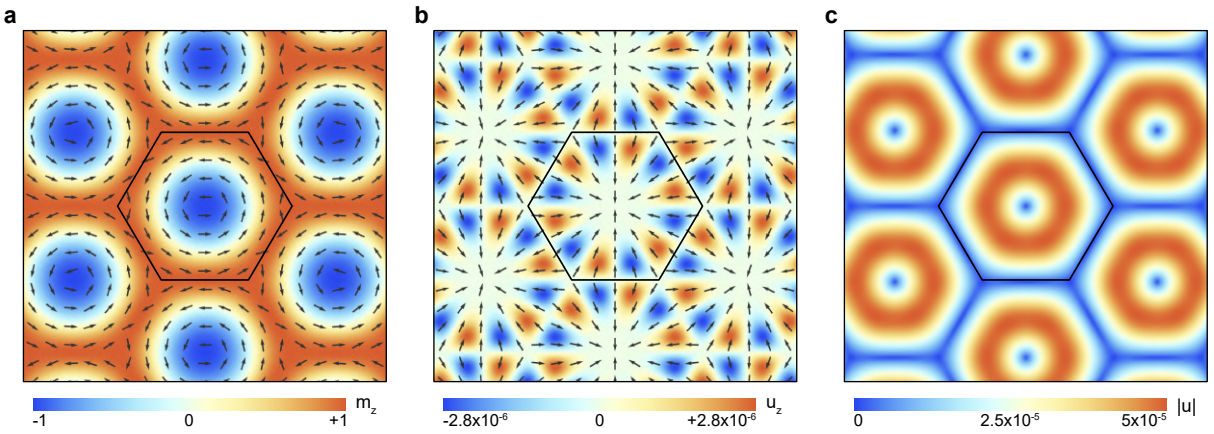

Figure 6.1.: **Equilibrium configuration for isotropic magneto-elastic coupling. (a-b)** Real-space equilibrium configuration of the magnetisation and displacement field, respectively. The colour indicates the out-of-plane component, parallel to the applied magnetic field, while arrows denote the in-plane directions. (**c**) Real-space elastic deformation magnitude, which becomes maximal at the skyrmions edge where the magnetisation varies most rapidly in space. The black hexagons denote the Wigner–Seitz cell, whose size is given by the skyrmion lattice constant a_{SkL}. The configurations are calculated for $H = 0.5H_{\mathrm{c2}}$ and $\xi_{ms} = 0.88$.

6.3.2 Equilibrium configurations

Figure 6.1 illustrates the equilibrium configuration for the fully isotropic case, corresponding to the tensor components defined in Eq. (6.37). In the small magneto-elastic coupling regime, the distortion of the magnetic lattice is minimal, so the resulting skyrmion lattice closely resembles the configuration discussed in Chapter 1. The out-of-plane component of the displacement field exhibits a sixfold symmetry within the magnetic unit cell. This pattern directly reflects the underlying hexagonal symmetry of the skyrmion lattice, which dominates when both the stiffness and magneto-elastic coupling tensors are isotropic.

Fig 6.1**c** shows the real-space displacement magnitude $|\mathbf{u}_{\mathrm{eq}}(\mathbf{r})|$, which remains rotationally invariant within the unit cell due to the isotropic structure of the coupling tensor. The deformation vanishes in regions where the magnetization $\mathbf{m}_{\mathrm{eq}}(\mathbf{r})$ is perpendicular to the lattice plane. This occurs at the center and edges of each magnetic unit cell, where the magnetization is aligned antiparallel and parallel to the external magnetic field, respectively. In contrast, the deformation reaches its maximum along the skyrmion edge, where the magnetization direction varies most rapidly in space. In this fully isotropic configuration, the primary effect of the magneto-elastic coupling is a local contraction of the crystal lattice toward each skyrmion core.

Elastic deformation

In this Section, we present the equilibrium configurations obtained in the limit of weak magneto-elastic coupling for a cubic chiral magnet. To establish a quantitative comparison, we employ here the experi-

mental parameters corresponding to a bulk sample of Cu_2OSeO_3, which will be further investigated in Chapter 8. The elastic parameters read [114]

$$C_{11} = 77\text{GPa} \quad C_{12} = 25\text{GPa} \quad C_{44} = 31\text{GPa}\,, \tag{6.38}$$

where $C_{\alpha\beta}$ denote the independent components of the cubic stiffness tensor in Voigt notation. For the magneto-elastic coupling tensor, we analyse three representative cases based on the discussion presented in Section 6.2.1. In particular, we consider: $\lambda_{11} = 3\lambda_{12} = 3\lambda_{12} = 3\lambda_{44}$ (isotropic), $\lambda_{11} = 3\lambda_{12} = -3\lambda_{12} = 3\lambda_{44}$ (chiral), and $\lambda_{11} = 3\lambda_{12} = 3\lambda_{12} = 1.2\lambda_{44}$ (anisotropic). It is worth noticing that the chiral example represents an extreme case where $\lambda_{-} = 2\lambda_{12}$ and $\lambda_{+} = 0$, which is chosen here in order to maximise the effects of chirality in the system. Moreover, this coupling tensor violates the condition $\lambda_{11} - \lambda_{+}/2 = 2\lambda_{44}$, hence introducing cubic anisotropy in the system. Here, we are interested in the regime of small magneto-elastic coupling, where the induced lattice deformations are weak and do not significantly modify the magnetic equilibrium texture. For this reason, we restrict the following discussion to the resulting displacement field configurations. Figure 6.2 shows the equilibrium configurations of the displacement field for two different orientations of the applied magnetic field: along a principal crystallographic axis (top rows) and along the cubic diagonal, $\mathbf{H} \parallel [111]$ (bottom rows).

For the isotropic magneto-elastic tensor with $\mathbf{H} \parallel [001]$, the displacement field closely resembles the configuration discussed previously. However, when the symmetry of the coupling tensor is lowered, the equilibrium configuration becomes more intricate. In particular, the total deformation magnitude $|\mathbf{u}_{\text{eq}}(\mathbf{r})|$ acquires a two-fold symmetry within the magnetic unit cell. This behaviour reflects the underlying symmetry of the cubic crystal in the plane perpendicular to the applied field. In this geometry, the skyrmion lattice lies in a plane containing two principal crystallographic axes, and the corresponding anisotropy in the magneto-elastic coupling selectively enhances certain deformation channels over others. As a consequence, the continuous rotational symmetry present in the isotropic case is explicitly broken, giving rise to the observed two-fold pattern.

When the magnetic field is applied along the cubic diagonal, $\mathbf{H} \parallel [111]$, both the stiffness and coupling tensors must be rotated according to Eq. (6.36). The corresponding rotation matrix is obtained by first rotating by $\pi/4$ around the $\hat{z}$-axis, followed by a rotation by $\arccos(1/\sqrt{3})$ around the new $\hat{y}$-axis:

$$R = R_y\left(\arccos\left(1/\sqrt{3}\right)\right).R_z\left(\frac{\pi}{4}\right) = \frac{1}{\sqrt{6}}\begin{pmatrix} 1 & -1 & 2 \\ \sqrt{3} & \sqrt{3} & 0 \\ -\sqrt{2} & \sqrt{2} & \sqrt{2} \end{pmatrix}, \tag{6.39}$$

where $R_j(\theta)$ denotes a rotation by an angle θ about the j-axis. For the isotropic magneto-elastic tensor, the total deformation strength remains rotationally invariant within the magnetic unit cell. Nevertheless,

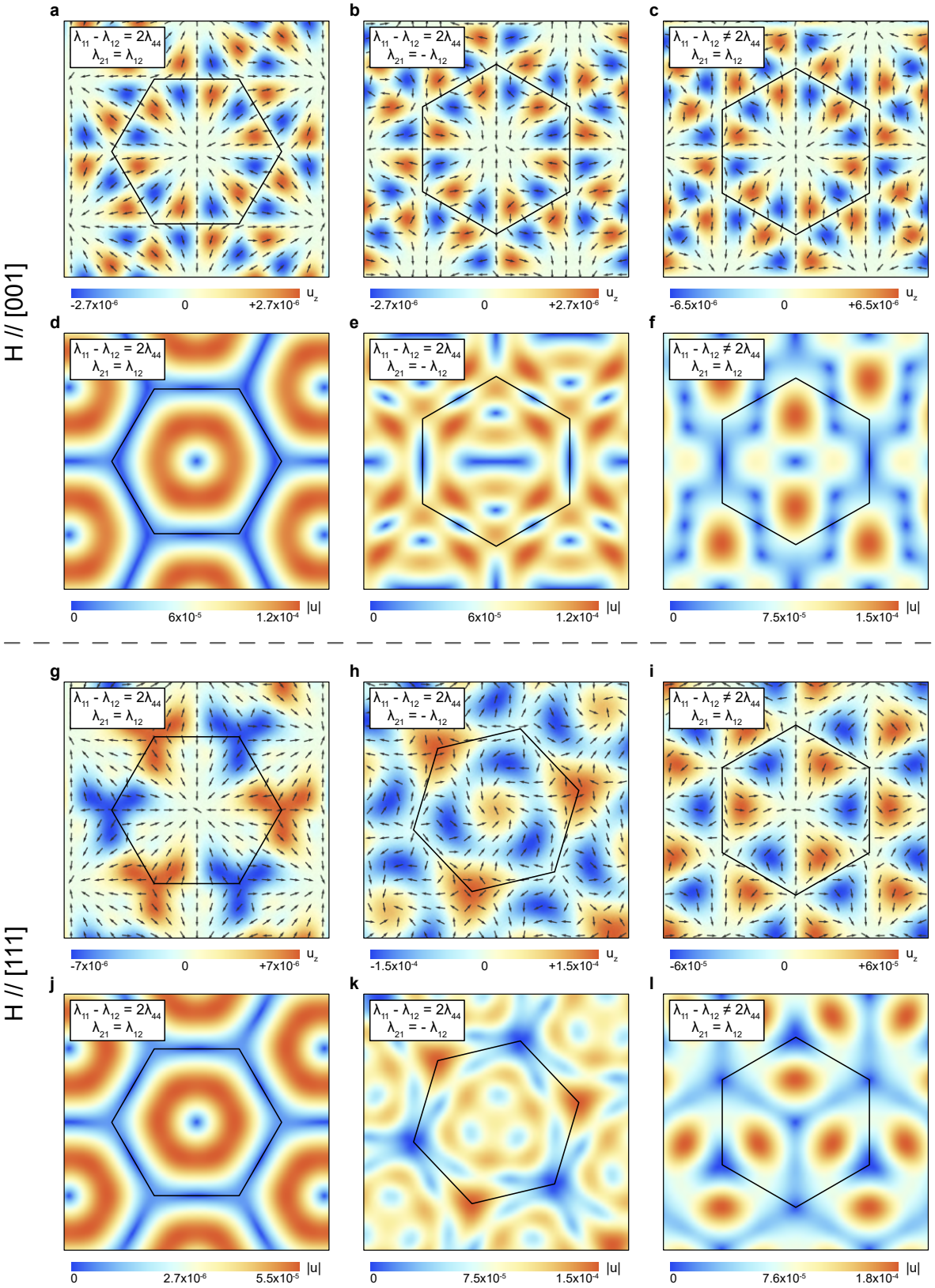

Figure 6.2.: **Displacement field configurations.** The figure shows different equilibrium configurations of the displacement field corresponding to $\mathbf{H} \parallel [001]$ (top 6 panels) and $\mathbf{H} \parallel [111]$ (bottom 6 panels). The three columns correspond to isotropic, chiral and anisotropic coupling tensor, respectively. The black hexagons denote the Wigner–Seitz cell, whose orientation is determined by the angle θ. The configurations are calculated for $H = 0.5H_{c2}$ and $\xi_{ms} = 0.88$. The magneto-elastic coupling strength is set by $\lambda_{11} = 0.22$ MPa, which value is compatible with the high-temperature skyrmion lattice in Cu_2OSeO_3 for $T \lesssim T_c = 57$ K (*see Chapter 8*).

the out-of-plane component of the displacement field $\mathbf{u}_{\mathrm{eq}}(\mathbf{r})$ now exhibits a distinct three-fold symmetry. The same feature is also observed for the chiral and anisotropic coupling tensors, highlighting that the symmetry of the deformation is now governed by the projection of the cubic lattice onto the plane perpendicular to the $[111]$ direction. In this orientation, the underlying crystal exhibits a three-fold rotational symmetry, which is imprinted onto the equilibrium deformation pattern through the magneto-elastic interaction.

Physically, this behaviour can be interpreted as the selection of symmetry-allowed coupling channels between the magnetic and elastic subsystems. The orientation of the magnetic field determines the skyrmion lattice plane, while the crystal anisotropy constrains the form of the elastic response. Depending on the relative alignment between these two symmetry frameworks, the magneto-elastic coupling can either preserve or break rotational invariance, leading to distinct deformation textures such as the two-fold or three-fold patterns observed here. In other words, the symmetry of both the stiffness and magneto-elastic tensors plays a decisive role in shaping the local equilibrium displacement field within the magnetic unit cell. The observed deformation patterns reflect how crystal anisotropy and magnetic order intertwine to define the symmetry and magnitude of the magneto-elastic response. In the following Chapter, we present a unified theoretical formulation to describe the collective excitation dynamics emerging on top of these equilibrium configurations.

7 Collective magneto-elastic dynamics in the skyrmion lattice phase

In this Chapter, we investigate the collective magneto-elastic excitations emerging in the skyrmion lattice phase of chiral magnets. Our aim is to establish a unified theoretical framework describing the interplay between spin dynamics and elastic deformations mediated by magneto-elastic coupling.

We derive a linearized theory for the coupled dynamics by combining the Landau–Lifshitz equation for the magnetization with the elastic wave equation for the lattice displacement field. Both are obtained self-consistently from the complete free energy functional developed in the previous Chapter, which includes magnetic, elastic, and magneto-elastic contributions. Linearization around the skyrmion lattice equilibrium configuration then allows us to study the collective excitation spectrum of the coupled system.

This framework enables us to explore the hybrid excitation modes that arise from the coupling mechanism. In particular, we analyse the role of symmetries within the magneto-elastic coupling tensor λ_{ijkl}, which impose specific selection rules governing the interaction between magnetic and elastic modes. Finally, we demonstrate that this coupling can give rise to non-reciprocal propagation of acoustic phonons along the magnetic skyrmion tubes.

7.1 Phonon dynamics

To describe the propagation of elastic waves in the presence of magneto-elastic coupling, we begin by formulating the equation of motion for the displacement field $\mathbf{u}(\mathbf{r},t)$. Any time-dependent deformation of the crystal lattice carries a kinetic energy contribution, given by [139]

$$\mathscr{T} = \int d\mathbf{r}\, \frac{1}{2}\rho_0 \Big(\partial_t \mathbf{u}(\mathbf{r},t)\Big)^2, \tag{7.1}$$

where ρ_0 denotes the mass density of the crystal. The corresponding Lagrangian functional of the elastic medium is then

$$\mathscr{L} = \mathscr{T} - \mathscr{F}_{\text{ela}} = \frac{1}{2}\int d\mathbf{r}\left[\rho_0\Big(\partial_t \mathbf{u}(\mathbf{r},t)\Big)^2 - \varepsilon_{ij}(\mathbf{r},t)C_{ijkl}\varepsilon_{kl}(\mathbf{r},t)\right], \tag{7.2}$$

where the time dependent strain tensor reads

$$\varepsilon_{ij}(\mathbf{r},t) = E_{ij} + \frac{1}{2}\Big(\partial_i u_j(\mathbf{r},t) + \partial_j u_i(\mathbf{r},t)\Big). \tag{7.3}$$

The total displacement field can be decomposed into an equilibrium contribution and a small time-dependent deviation,

$$\mathbf{u}(\mathbf{r},t) = \mathbf{u}_{\text{eq}}(\mathbf{r}) + \delta\mathbf{u}(\mathbf{r},t), \tag{7.4}$$

where $\mathbf{u}_{\text{eq}}(\mathbf{r})$ represents the static distortion induced by magneto-elastic coupling, and $\delta\mathbf{u}(\mathbf{r},t)$ describes the dynamic lattice vibration around equilibrium. It is worth noticing that the time-dependent contribution is not necessarily small compared to the equilibrium configuration. In fact, $\mathbf{u}_{\text{eq}}(\mathbf{r})$ vanishes in the limit of zero magneto-elastic coupling, while dynamical perturbations are still allowed. In this context, $\delta\mathbf{u}$ must remain small enough for the linear approximation to hold, i.e., quadratic terms in the strain tensor definition [Eq. (6.5)] can be neglected.

Applying Hamilton's principle to the Lagrangian (7.2) yields the linearized equation of motion for the elastic displacement:

$$\rho_0\partial_t^2 u_i(\mathbf{r},t) = -\frac{\delta\mathscr{F}_{\text{ela}}}{\delta u_i} = C_{ijkl}\partial_j\partial_k\delta u_l(\mathbf{r},t). \tag{7.5}$$

This equation describes the propagation of small-amplitude elastic waves in an anisotropic medium characterized by the tensor C_{ijkl}. To analyse these excitations in reciprocal space, we perform a space-time Fourier transform:

$$\delta\mathbf{u}(\mathbf{r},t) = \int \frac{d\mathbf{k}}{(2\pi)^3}\frac{d\omega}{2\pi}\,\delta\mathbf{u}(\mathbf{k})e^{i(\mathbf{k}\cdot\mathbf{r}-\omega t)}, \tag{7.6}$$

with amplitudes determined by

$$\delta\mathbf{u}(\mathbf{k}) = \int d\mathbf{r}dt\,\delta\mathbf{u}(\mathbf{r},t)e^{-i(\mathbf{k}\cdot\mathbf{r}-\omega t)}. \tag{7.7}$$

Substituting this form into the equation of motion gives the elastic wave equation in reciprocal space,

$$\rho_0\omega^2\delta\mathbf{u}(\mathbf{k}) = D(\mathbf{k})\delta\mathbf{u}(\mathbf{k}) \tag{7.8}$$

where $D_{il}(\mathbf{k}) = C_{ijkl}k_jk_k$ is known as the dynamical matrix. Its eigenvalues determine the allowed phonon frequencies $\omega(\mathbf{k})$, while the eigenvectors describe the corresponding polarization modes of lattice vibrations.

7.2 Unified magneto-elastic dynamics

The collective dynamics of the coupled magneto-elastic system arise from the simultaneous time evolution of the magnetic and elastic subsystems. These two degrees of freedom are described, respectively, by the Landau–Lifshitz equation for the magnetization dynamics and by the elastic wave equation for the displacement field. Combining the two yields a unified description of the coupled system:

$$\begin{cases} \partial_t \mathbf{m} = \frac{\gamma_0}{M_s} \mathbf{m} \times \frac{\delta \mathscr{F}}{\delta \mathbf{m}} \\ \rho_0 \partial_t^2 \mathbf{u} = -\frac{\delta \mathscr{F}}{\delta \mathbf{u}} \end{cases} , \tag{7.9}$$

where $\mathscr{F}$ is the total free energy functional introduced in Eq. (6.19), which includes the magnetic, elastic, and magneto-elastic coupling contributions. To study the collective excitations, we express the dynamical variables in frequency space, where Eq. (7.9) becomes

$$\begin{cases} \omega \delta \mathbf{m} = i \frac{\gamma_0}{M_s} \mathbf{m} \times \frac{\delta \mathscr{F}}{\delta \mathbf{m}} \\ \omega^2 \rho_0 \delta \mathbf{u} = \frac{\delta \mathscr{F}}{\delta \mathbf{u}} \end{cases} . \tag{7.10}$$

The two equations differ in the order of time derivatives: the magnetic subsystem is first order in time according to the processional motion of magnetic moments, while the elastic subsystem is second order due to its inertial character. Consequently, the frequency ω enters the problem with different powers, complicating the formulation of a unified eigenvalue problem. To overcome this, we introduce an auxiliary field $\delta \boldsymbol{\xi}$ defined by

$$\omega \delta \mathbf{u} = \omega_0 \delta \boldsymbol{\xi} , \tag{7.11}$$

where ω_0 is an arbitrary scaling frequency to be fixed later. Physically, $\delta \boldsymbol{\xi}$ is proportional to the velocity field of the lattice displacements. Substituting this definition, Eq. (7.10) can be rewritten as a set of first-order equations:

$$\begin{cases} \omega \delta \mathbf{m} = i \frac{\gamma_0}{M_s} \mathbf{m} \times \frac{\delta \mathscr{F}}{\delta \mathbf{m}} \\ \omega \delta \mathbf{u} = \omega_0 \delta \boldsymbol{\xi} \\ \omega \delta \boldsymbol{\xi} = \frac{1}{\rho_0 \omega_0} \frac{\delta \mathscr{F}}{\delta \mathbf{u}} \end{cases} . \tag{7.12}$$

This transformation recasts the coupled magneto-elastic problem into a linear eigenvalue system in ω, suitable for numerical and analytical analysis of the hybridized excitation spectrum.

7.2.1 Linearisation

To study small oscillations around the equilibrium configuration, we expand the total free energy functional to second order in the small deviations $\delta\mathbf{m}$ and $\delta\mathbf{u}$:

$$\begin{aligned}\mathscr{F}[\mathbf{m},\mathbf{u}] \simeq \mathscr{F}[\mathbf{m}_{\mathrm{eq}},\mathbf{u}_{\mathrm{eq}}] &+ \frac{\delta\mathscr{F}[\mathbf{m},\mathbf{u}]}{\delta m_i}\bigg|_{\mathbf{m}_{\mathrm{eq}},\mathbf{u}_{\mathrm{eq}}}\delta m_i + \frac{\delta\mathscr{F}[\mathbf{m},\mathbf{u}]}{\delta u_i}\bigg|_{\mathbf{m}_{\mathrm{eq}},\mathbf{u}_{\mathrm{eq}}}\delta u_i + \frac{1}{2}\delta m_i\frac{\delta^2\mathscr{F}[\mathbf{m},\mathbf{u}]}{\delta m_i\delta m_j}\bigg|_{\mathbf{m}_{\mathrm{eq}},\mathbf{u}_{\mathrm{eq}}}\delta m_j \\ &+ \frac{1}{2}\delta u_i\frac{\delta^2\mathscr{F}[\mathbf{m},\mathbf{u}]}{\delta u_i\delta u_j}\bigg|_{\mathbf{m}_{\mathrm{eq}},\mathbf{u}_{\mathrm{eq}}}\delta u_j + \frac{1}{2}\delta m_i\frac{\delta^2\mathscr{F}[\mathbf{m},\mathbf{u}]}{\delta m_i\delta u_j}\bigg|_{\mathbf{m}_{\mathrm{eq}},\mathbf{u}_{\mathrm{eq}}}\delta u_j\,. \end{aligned} \tag{7.13}$$

The linear terms vanish because the equilibrium configuration is obtained from the mean-field theory as the solution that minimises the free energy functional. Substituting this expansion into the linearized equations of motion yields the compact matrix form:

$$\omega\begin{pmatrix}\delta\mathbf{m}\\ \delta\mathbf{u}\\ \delta\boldsymbol{\xi}\end{pmatrix} = \begin{pmatrix} i\mathbf{m}_{\mathrm{eq}}\times & 0 & 0\\ 0 & \mathbf{I} & 0\\ 0 & 0 & \mathbf{I}\end{pmatrix}\begin{pmatrix} \frac{\gamma_0}{M_s}\frac{\delta^2\mathscr{F}}{\delta\mathbf{m}\delta\mathbf{m}} & \frac{\gamma_0}{2M_s}\frac{\delta^2\mathscr{F}}{\delta\mathbf{m}\delta\mathbf{u}} & 0\\ 0 & 0 & \omega_0\mathbf{I}\\ \frac{1}{2\rho_0\omega_0}\frac{\delta^2\mathscr{F}}{\delta\mathbf{u}\delta\mathbf{m}} & \frac{1}{\rho_0\omega_0}\frac{\delta^2\mathscr{F}}{\delta\mathbf{u}\delta\mathbf{u}} & 0\end{pmatrix}\begin{pmatrix}\delta\mathbf{m}\\ \delta\mathbf{u}\\ \delta\boldsymbol{\xi}\end{pmatrix}, \tag{7.14}$$

where the factor $1/2$ in the off-diagonal contributions comes from the linear expansion of the free energy density. The next step consists of deriving a dimensionless formulation for this expression. First of all, the problem contains a natural energy scale set by the ratio D^2/J, which defines the characteristic frequency $\omega_{\mathrm{c2}} = \frac{\gamma_0}{M_s}\frac{D^2}{J}$, introduced in Chapter 3. Moreover, we introduce the dimensionless quantities

$$\mathbf{u}' = \frac{\mathbf{u}}{a_{\mathrm{SkL}}} \quad \text{and} \quad \delta\boldsymbol{\xi}' = \frac{\delta\boldsymbol{\xi}}{a_{\mathrm{SkL}}}\,, \tag{7.15}$$

where a_{SkL} provides the natural length scale within the skyrmion lattice phase. The resulting dimensionless equation of motion reads:

$$\frac{\omega}{\omega_{\mathrm{c2}}}\begin{pmatrix}\delta\mathbf{m}\\ \delta\mathbf{u}'\\ \delta\boldsymbol{\xi}'\end{pmatrix} = \begin{pmatrix} i\mathbf{m}_{\mathrm{eq}}\times & 0 & 0\\ 0 & \mathbf{I} & 0\\ 0 & 0 & \mathbf{I}\end{pmatrix}\begin{pmatrix} \frac{\delta^2\mathscr{F}}{\delta\mathbf{m}\delta\mathbf{m}} & \frac{1}{2}\frac{\delta^2\mathscr{F}}{\delta\mathbf{m}\delta\mathbf{u}'} & 0\\ 0 & 0 & \frac{J}{D^2a_{\mathrm{SkL}}^2\rho_0}\mathbf{I}\\ \frac{1}{2}\frac{\delta^2\mathscr{F}}{\delta\mathbf{u}'\delta\mathbf{m}} & \frac{\delta^2\mathscr{F}}{\delta\mathbf{u}'\delta\mathbf{u}'} & 0\end{pmatrix}\begin{pmatrix}\delta\mathbf{m}\\ \delta\mathbf{u}'\\ \delta\boldsymbol{\xi}'\end{pmatrix}. \tag{7.16}$$

where we set $\omega_0 = \frac{\gamma_0}{M_s a_{\mathrm{SkL}}^2\rho_0}$. This compact dimensionless formulation establishes the eigenvalue problem for the collective magneto-elastic excitations. The corresponding eigenfrequencies describe the hybridized magnon–phonon modes, while the eigenvectors encode the relative magnetic and elastic character of each excitation. A detailed discussion of these hybrid modes is presented later in this Section.

7.2.2 Excitations in the SkL phase

In order to determine the excitation spectrum in the magnetic skyrmion lattice phase, we follow a procedure analogous to that presented in Section 3.3.1 for the pure magnetic case. The coupled magneto-elastic system retains the periodicity of the distorted magnetic lattice. Consequently, Bloch's theorem applies, and the excitation frequencies satisfy

$$\omega(\mathbf{k}+\mathbf{Q}) = \omega(\mathbf{k}), \tag{7.17}$$

for any reciprocal lattice vector $\mathbf{Q} = \mathbf{G}_{\boldsymbol{\nu}}$. It is convenient to decompose the total wavevector as $\mathbf{k} = \mathbf{Q}+\mathbf{q}$, where $\mathbf{q}$ lies within the first Brillouin zone of the magnetic lattice. This allows us to label the excitation amplitudes by their reciprocal lattice index,

$$\delta\mathbf{m}(\mathbf{k}) = \delta\mathbf{m}_{\mathbf{Q}}(\mathbf{q}), \quad \delta\mathbf{u}(\mathbf{k}) = \delta\mathbf{u}_{\mathbf{Q}}(\mathbf{q}), \quad \delta\boldsymbol{\xi}(\mathbf{k}) = \delta\boldsymbol{\xi}_{\mathbf{Q}}(\mathbf{q}). \tag{7.18}$$

For the sake of readability, in what follows we omit the primes on the displacement and velocity fields, even though they remain dimensionless quantities.

We now analyse the individual Hessian contributions entering the collective equation of motion (7.16). Recall that the magneto-elastic coupling in the total free energy is quadratic in the magnetization and linear in the displacement field, so the mixed derivatives naturally connect the two subsystems. The purely magnetic contribution reads

$$\begin{aligned}\left.\frac{\delta^2\mathscr{F}}{\delta m^i(-\mathbf{k})\delta m^j(\mathbf{k}')}\right|_{\mathrm{eq}} &= \left.\frac{\delta^2\mathscr{F}_{\mathrm{mag}}}{\delta m^i(-\mathbf{k})\delta m^j(\mathbf{k}')}\right|_{\mathrm{eq}} + \delta(\mathbf{q}-\mathbf{q}')\left[\delta_{\mathbf{Q},\mathbf{Q}'}E_{kl}\lambda_{klij} + i\Big(\mathbf{Q}-\mathbf{Q}'\Big)_k u_{\mathbf{Q}-\mathbf{Q}',l}\lambda_{klij}\right] \\ &= \Big(\chi_0^{-1}\Big)^{ij}_{\mathbf{QQ}'}(\mathbf{q})\delta(\mathbf{q}-\mathbf{q}'),\end{aligned} \tag{7.19}$$

where the the first term corresponds to the magnetic Hessian derived in Eq. (3.41). The notation $\mathbf{u}_{\mathbf{Q}} = \mathbf{u}_{\mathrm{eq}}(\mathbf{Q})$ refers to the Fourier components of the equilibrium displacement field. Even though this term originates from the magnetic sector, it already includes corrections due to the magneto-elastic coupling, reflecting the feedback of the lattice distortion on the magnetic stiffness. The purely elastic contribution has the standard form

$$\left.\frac{\delta^2\mathscr{F}}{\delta u^i(-\mathbf{k})\delta u^j(\mathbf{k}')}\right|_{\mathrm{eq}} = \delta(\mathbf{q}-\mathbf{q}')D^{ij}_{\mathbf{QQ}'}(\mathbf{q}), \tag{7.20}$$

where the matrix

$$D^{ij}_{\mathbf{QQ}'}(\mathbf{q}) = \delta_{\mathbf{Q},\mathbf{Q}'}C_{iklj}\Big(\mathbf{Q}+\mathbf{q}\Big)_k\Big(\mathbf{Q}+\mathbf{q}\Big)_l \tag{7.21}$$

plays the role of a dynamical matrix for the phonon modes, analogous to the one obtained in the derivation of the elastic wave dispersion. Finally, the off-diagonal contribution associated with the magneto-elastic coupling energy density reads

$$\left.\frac{\delta^2\mathscr{F}}{\delta m^i(-\mathbf{k})\delta u^j(\mathbf{k}')}\right|_{\mathrm{eq}} = -2i\delta(\mathbf{q}-\mathbf{q}')\Big(\mathbf{Q}+\mathbf{q}\Big)_k \lambda_{ikl\,j} m_{\mathbf{Q}-\mathbf{Q}',l} = (\mathscr{S}_{\mathrm{mec}})^{ij}_{\mathbf{Q}\mathbf{Q}'}(\mathbf{q})\delta(\mathbf{q}-\mathbf{q}')\,. \tag{7.22}$$

This term explicitly couples the phonon wavevector $\mathbf{k}$ to the spatially modulated magnetization through the magneto-elastic tensor $\lambda_{ikl\,j}$. Its Hermitian conjugate provides the reverse coupling:

$$\left.\frac{\delta^2\mathscr{F}}{\delta u^i(-\mathbf{k})\delta m^j(\mathbf{k}')}\right|_{\mathrm{eq}} = \left(\left.\frac{\delta^2\mathscr{F}}{\delta m^i(-\mathbf{k})\delta u^j(\mathbf{k}')}\right|_{\mathrm{eq}}\right)^{\dagger}. \tag{7.23}$$

All the above contributions can now be inserted into the collective magneto-elastic equation of motion (7.16). In the numerical implementation, a momentum cutoff is applied in order to determine a finite subset of Fourier components. Therefore, the operator $(\mathbf{m}_{\mathrm{eq}}\times)$ is replaced by $(\mathbf{m}_{\mathrm{eq}}\times)^P$, representing its projection onto the dynamical subspace as defined in Eq. (3.49). The resulting eigenvalue problem for the coupled magneto-elastic excitations takes the compact form

$$\frac{\omega_\alpha}{\omega_{\mathrm{c}2}}\begin{pmatrix}\delta\mathbf{m}_\alpha(\mathbf{q})\\ \delta\mathbf{u}_\alpha(\mathbf{q})\\ \delta\boldsymbol{\xi}_\alpha(\mathbf{q})\end{pmatrix} = \begin{pmatrix} i(\mathbf{m}_{\mathrm{eq}}\times)^P & 0 & 0\\ 0 & \mathbf{I} & 0\\ 0 & 0 & \mathbf{I}\end{pmatrix}\begin{pmatrix}\chi_0^{-1}(\mathbf{q}) & \frac{1}{2}\mathscr{S}_{\mathrm{mec}}(\mathbf{q}) & 0\\ 0 & 0 & \frac{J}{D^2a_{\mathrm{SkL}}^2\rho_0}\mathbf{I}\\ \frac{1}{2}\mathscr{S}^{\dagger}_{\mathrm{mec}}(\mathbf{q}) & D(\mathbf{q}) & 0\end{pmatrix}\begin{pmatrix}\delta\mathbf{m}_\alpha(\mathbf{q})\\ \delta\mathbf{u}_\alpha(\mathbf{q})\\ \delta\boldsymbol{\xi}_\alpha(\mathbf{q})\end{pmatrix}, \tag{7.24}$$

where the index α labels the excitation modes. Here, we omitted the implicit contraction of all the reciprocal lattice vectors, as well as the matrix indices. The resulting resonance frequencies $\omega_\alpha(\mathbf{q})$ define the hybrid magnon–phonon band structure within the skyrmion lattice phase.

Eigenmodes

The eigenfunctions obtained from the collective equation of motion (7.24) describe the full set of excitation modes in the skyrmion lattice phase. Each eigenmode is represented by a vector that contains both the magnetic and elastic components of the excitation,

$$\mathbf{v}_\alpha(\mathbf{q}) = \begin{pmatrix}\delta\mathbf{m}_\alpha(\mathbf{q})\\ \delta\mathbf{u}_\alpha(\mathbf{q})\\ \delta\boldsymbol{\xi}_\alpha(\mathbf{q})\end{pmatrix}, \tag{7.25}$$

where the index α labels the mode and $\mathbf{q}$ is the wavevector within the first Brillouin zone. In principle, each eigenvector $\mathbf{v}_\alpha(\mathbf{q})$ contains $3\times 3\times N$ independent components, where N is the number of points composing the reciprocal space. However, the displacement $\delta\mathbf{u}$ and velocity $\delta\boldsymbol{\xi}$ components are not

independent, due to the trivial relationship between them. Consequently, the physically relevant information is contained in a reduced subspace of the full vector.

Because the eigenmodes describe coupled magneto-elastic excitations, their orthogonality condition must properly account for both the magnetic and elastic contributions. The magnon part follows the Bogoliubov–de Gennes orthogonality relation defined in Eq. (3.55), reflecting the non-Hermitian structure of the Landau–Lifshitz dynamics. In contrast, the phonon part satisfies the standard Euclidean orthogonality condition associated with real, Hermitian wave equations. To combine these two subparts consistently, we define the collective scalar product as

$$\begin{pmatrix} \delta\mathbf{m}_\alpha^\dagger(\mathbf{q}) \\ \delta\mathbf{u}_\alpha^\dagger(\mathbf{q}) \\ \delta\boldsymbol{\xi}_\alpha^\dagger(\mathbf{q}) \end{pmatrix} \begin{pmatrix} \left(i(\mathbf{m}_{\mathrm{eq}}\times)^P\right)^{-1} & 0 & 0 \\ 0 & \mathbf{I} & 0 \\ 0 & 0 & \mathbf{I} \end{pmatrix} \begin{pmatrix} \delta\mathbf{m}_\beta(\mathbf{q}) \\ \delta\mathbf{u}_\beta(\mathbf{q}) \\ \delta\boldsymbol{\xi}_\beta(\mathbf{q}) \end{pmatrix} = \mathbf{v}_\alpha^\dagger(\mathbf{q})\mathscr{P}\mathbf{v}_\beta(\mathbf{q}) = 0 \quad \text{for} \quad \alpha \neq \beta\,, \tag{7.26}$$

where the matrix $\mathscr{P}$ defines the appropriate metric for the hybrid excitations space. Based on this scalar product, the normalisation of each eigenmode is defined as

$$\mathbf{v}_\alpha(\mathbf{q}) \to \frac{1}{\sqrt{n_\alpha}}\mathbf{v}_\alpha(\mathbf{q}) \quad \text{with} \quad n_\alpha = \mathbf{v}_\alpha^\dagger(\mathbf{q})\mathscr{P}\mathbf{v}_\alpha(\mathbf{q})\,, \tag{7.27}$$

which ensures a consistent amplitude definition across all magneto-elastic excitation modes.

In the limit of vanishing magneto-elastic coupling, the system supports two independent types of excitations: magnons, with nonzero magnetic components $\delta\mathbf{m}_\alpha$ and vanishing elastic part; and phonons, characterised solely by $\delta\mathbf{u}_\alpha$ and $\delta\boldsymbol{\xi}_\alpha$. In this regime, each eigenfunction is purely of one type, and the hybrid nature disappears. However, when the magneto-elastic coupling is finite, these two branches hybridise, resulting in modes that carry both magnetic and elastic character. The degree of this hybridisation depends strongly on the wavevector and on the details of the coupling tensor λ_{ijkl}. In the following Section, we analyse these normalised eigenvectors to determine the dominant character of each excitation and to identify the regions in reciprocal space where the magnon–phonon hybridisation becomes most pronounced.

7.3 Spectrum

In this Section, we analyse the low-energy excitation spectrum of the skyrmion lattice phase in the presence of magneto-elastic coupling. These collective excitations in the system are characterised by two distinct energy scales. On one hand, the magnons are typically described by a characteristic frequency scale $\omega_{\mathrm{c}2}$, which is set by the strength of magnetic interactions. In contract, the acoustic phonon modes are determined by the elastic stiffness tensor and the crystal mass density, as expressed in Eq. (7.8). Typ-

ically, these energy scales differ by order of magnitudes in standard chiral magnets, as as explained in the previous Chapter.

To establish a quantitative comparison, we employ here the experimental parameters corresponding to Cu_2OSeO_3 [114]

$$C_{11} = 77\text{GPa} \quad C_{12} = 25\text{GPa} \quad C_{44} = 31\text{GPa} \quad \rho_0 = 5.05\text{g/cm}^3\,, \tag{7.28}$$

which will be further investigated in Chapter 8. Our main objective here is to characterise the hybridisation features that emerge in noncentrosymmetric cubic magnets, particularly the selection rules governing the coupling between magnon and phonon excitations. These features are primarily dictated by the symmetries of the magneto-elastic coupling tensor. For this tensor, however, direct experimental determinations of its components are not available. In the next Chapter, we will extract an effective estimate by fitting the measured phonon phase velocities. Typical values of the coupling coefficients $\lambda_{\alpha\beta}$ lie in the range of a few hundred kilopascals to several tens of megapascals.

7.3.1 Zero magneto-elastic coupling

Fig. 7.1 shows the excitation spectra in the absence of magneto-elastic coupling. In this case, the low-energy excitations consist of the magnon modes already presented in Chapter 3 and the acoustic phonon branches. As expected from their distinct physical origins, the elastic waves exhibit a much steeper dispersion: their energy increases rapidly with wavevector magnitude. Since the magnetic and elastic subsystems are decoupled, no signatures of hybridisation are observed in this case. The linear dispersion of these acoustic modes,

$$\omega_{\text{ph}} \propto v_{\text{ph}}|\mathbf{q}|\,, \tag{7.29}$$

stems from the fact that their restoring force is elastic and proportional to the gradient of the displacement field. This contrasts with magnon excitations, whose dynamics are governed by the spin precession, leading to a quadratic low-energy dispersion in the long-wavelength limit.

The phonon branches can be identified from their corresponding eigenfunctions. These excitations originate from the spontaneous breaking of continuous translational symmetry in the crystal. When atoms condense into a periodic lattice, the continuous translational invariance of space is reduced to a discrete subgroup. According to Goldstone's theorem, each spontaneously broken continuous symmetry gives rise to a gapless collective mode. Consequently, the crystal hosts three acoustic phonon modes, corresponding to translations along the three spatial directions. These modes have zero energy at the Brillouin zone center $\mathbf{k} = \mathbf{0}$, reflecting their Goldstone nature. Physically, these modes represent coherent oscillations of the lattice displacement field $\delta\mathbf{u}$. One of them corresponds to displacements parallel to the propagation direction and is known as the longitudinal acoustic (LA) mode. The other two correspond

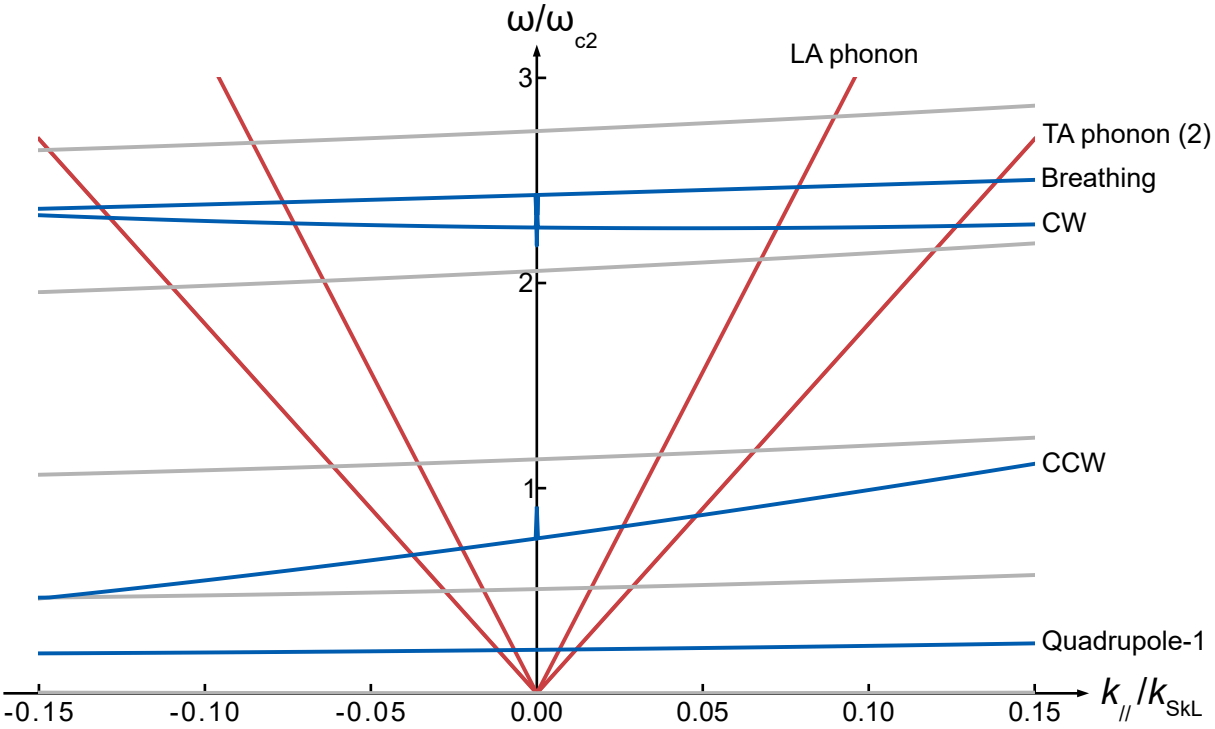

Figure 7.1.: **Excitation spectra in the absence of magneto-elastic coupling.** Collective mode dispersions calculated without magneto-elastic coupling for wavevectors parallel to the applied magnetic field, $\mathbf{k} \| \mathbf{H}$, at $H = 0.5H_{c2}$ and $\xi_{ms} = 0.88$. The acoustic phonon branches (red) exhibit linear dispersion, with one longitudinal (LA) and two degenerate transverse (TA) modes, the latter displaying a smaller group velocity. The blue and gray lines indicate the low-energy magnon excitations of the skyrmion lattice. The magnon branches shown in blue correspond to the modes that will hybridise with the acoustic phonons once magneto-elastic coupling is introduced.

to displacements perpendicular to the propagation direction and form two degenerate transverse acoustic (TA) modes. These are homogeneous solutions of the collective equations of motion, such that the corresponding eigenfunctions are non-zero only for $\delta\mathbf{u}_{\mathbf{Q}=\mathbf{0}}(\mathbf{q})$.

Each phonon branch is associated with a polarisation vector. For the longitudinal mode, the polarisation reads

$$\mathbf{p}^{\mathrm{LA}} = \delta\mathbf{u}^{\mathrm{LA}}_{\mathbf{Q}=\mathbf{0}}(\mathbf{q})\sqrt{1+\left(\frac{\omega}{\omega_{c2}}\frac{D^2 a_{\mathrm{SkL}}^2 \rho_0}{J}\right)^2} = \begin{pmatrix}0\\0\\1\end{pmatrix}, \tag{7.30}$$

where $\delta\mathbf{u}$ denotes the phonon component of the normalised eigenvector, while the square-root prefactor accounts for the trivial contribution from the auxiliary velocity field. In the absence of coupling, the two TA modes are degenerate and can be represented by any pair of orthogonal unit vectors in the xy-plane.

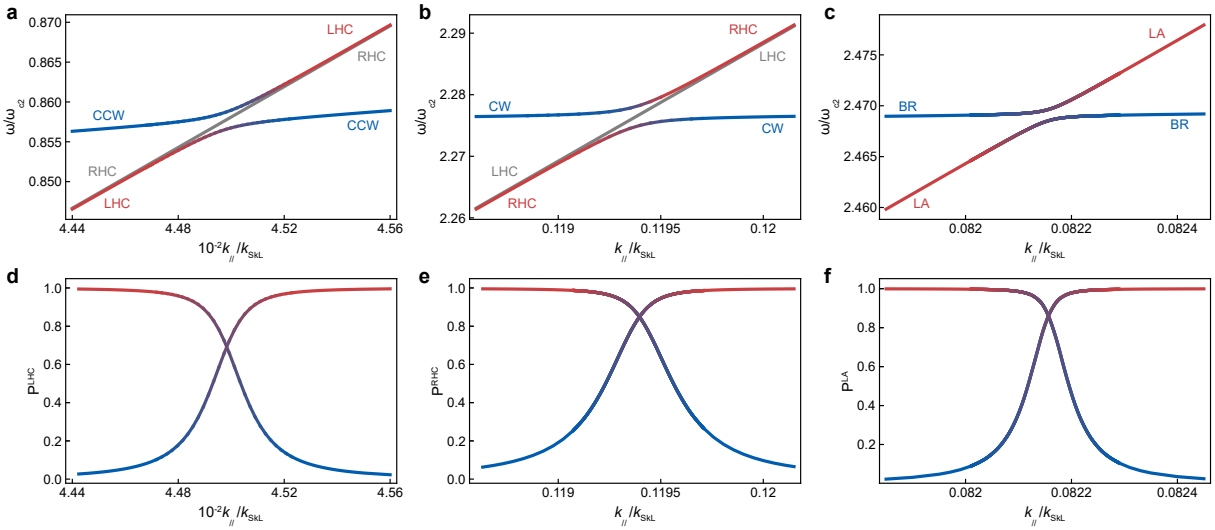

Figure 7.2.: **Hybridisation with dipole modes.** Hybridisation gaps opening between (**a**) the counterclockwise (CCW) magnon mode and the left-handed circularly (LHC) polarised transverse phonon, (**b**) the clockwise (CW) magnon mode and the right-handed circularly (RHC) polarised transverse phonon, and (**c**) the breathing (BR) mode and the longitudinal (LA) phonon. The results are calculated for isotropic magneto-elastic coupling with $\lambda_{11} = 0.22$ MPa and $\mathbf{k} \parallel \mathbf{H} \parallel [001]$. Panels (**d**)–(**f**) show the corresponding phonon polarisation weight, defined in Eq. (7.32), which quantifies how the phonon character is continuously transferred between excitation branches within the hybridisation regime.

A particularly convenient basis, especially once magneto-elastic coupling is included, is that of circularly polarised phonons, defined as

$$\mathbf{p}^{\mathrm{TA}}_{\mathrm{R/L}} = \frac{1}{\sqrt{2}} \begin{pmatrix} 1 \\ \pm i \\ 0 \end{pmatrix} , \tag{7.31}$$

where $\mathbf{p}^{\mathrm{TA}}_{\mathrm{R}}$ and $\mathbf{p}^{\mathrm{TA}}_{\mathrm{L}}$ denotes the right- and left-handed circularly polarised state, respectively.

7.3.2 Hybridisation with dipole modes

Once the magneto-elastic coupling is turned on, hybridisation gaps may open between different magnon and phonon branches. Figures 7.2**a**–**c** show the characteristic anti-crossing behaviour between the three acoustic phonon modes and the dipolar magnon excitations. The results are calculated for the isotropic magneto-elastic coupling with $\lambda_{11} = 0.22$ MPa and $\mathbf{H} \parallel [001]$. The corresponding equilibrium configuration of the displacement field is displayed in Fig. 6.2**a** and **d**. Figure 7.2**a** and **b** show how the magneto-elastic coupling lifts the degeneracy of the two transverse acoustic phonon modes. In particular, away from the crossing regions, the transverse mode solutions correspond to right- and left-handed circularly polarised phonons, whose polarisation can be expressed as in Eq. (7.31). The figure does not include calculations for negative wavevectors, where the coupling effects are analogous. However, due to the intrinsic non-reciprocity of the magnon modes in chiral magnets, the acoustic phonon branches acquire a similar feature. This is known as phonon magneto-chiral effect, which arises due to the simul-

taneous mirror and time-reversal symmetry breaking. This phenomena has already been observed for photons [145–149], electrons [150–153] and magnons [154–156]. Moreover, the magneto-chiral effect has also been observed for phonon excitations in the form of non-reciprocal propagation of surface-acoustic waves [157, 158] and, more recently, acoustic waves in bulk media [142, 159].

In the hybridisation region, however, the eigenmodes no longer represent purely elastic or magnetic excitations. Each mode acquires mixed character, containing both phononic and magnonic components. To quantify this mixing, we identify the homogeneous elastic polarisation $\delta\mathbf{u}_{\mathbf{Q}=\mathbf{0}}$ associated with each collective excitation, and evaluate its projection onto a chosen polarisation basis. This is illustrated in Fig. 7.2**d**–**f**, where we plot the polarisation weight

$$P^{\alpha} = \left| \delta\mathbf{u}^{\dagger}_{\mathbf{Q}=\mathbf{0}}(\mathbf{q}) \cdot \mathbf{p}^{\alpha} \right| \sqrt{1 + \left(\frac{\omega}{\omega_{\mathrm{c2}}} \frac{D^2 a_{\mathrm{SkL}}^2 \rho_0}{J} \right)^2}\,, \tag{7.32}$$

where $\mathbf{p}^{\alpha}$ denotes either the longitudinal or one of the two circular polarisations directions. This analysis reveals a clear mode selectivity: the left-handed circularly polarised transverse phonon couples to the counterclockwise magnon mode, the longitudinal phonon to the breathing mode, and the right-handed circularly polarised transverse phonon to the clockwise mode.

The origin of this mode selectivity can be directly understood from the collective excitation dynamics [Eq. (7.24)]. Since the relevant coupling occurs at small wavevectors, i.e., for $|\mathbf{k}| \ll k_{\mathrm{SkL}}$, we can expand the off-diagonal magneto-elastic term around $\mathbf{Q} = \mathbf{0}$. For small $\mathbf{q}$ along the magnetic field direction, one obtains

$$\delta u^{i}_{\mathbf{Q}=\mathbf{0}}(q_z) \propto q_z \lambda_{izzj} m^{z}_{\mathrm{eq},\mathbf{Q}=\mathbf{0}} \delta m^{j}_{\mathbf{Q}=\mathbf{0}}(q_z)\,. \tag{7.33}$$

The right-hand side is nonzero only for the magnetic dipole modes, as discussed in Chapter 3. Furthermore, the symmetry of the isotropic coupling tensor ensures that $i = j$, which naturally explains the selection rules observed in Fig. 7.2.

This selective hybridisation mechanism is quite general. We find similar behaviour in all configurations where the magneto-elastic coupling preserves the same symmetry. In particular, the same selection rules apply to cubic materials whenever the magnetic field is applied along the principal crystallographic axes for a generic coupling tensor, or in the isotropic coupling case for any field direction.

Finally, since the coupled excitations involve non-reciprocal magnon modes, the hybridised phonon branches inherit their non-reciprocity. This effect, which will be examined in more detail in the next Chapter implies that the propagation velocity of sound waves becomes direction-dependent with respect

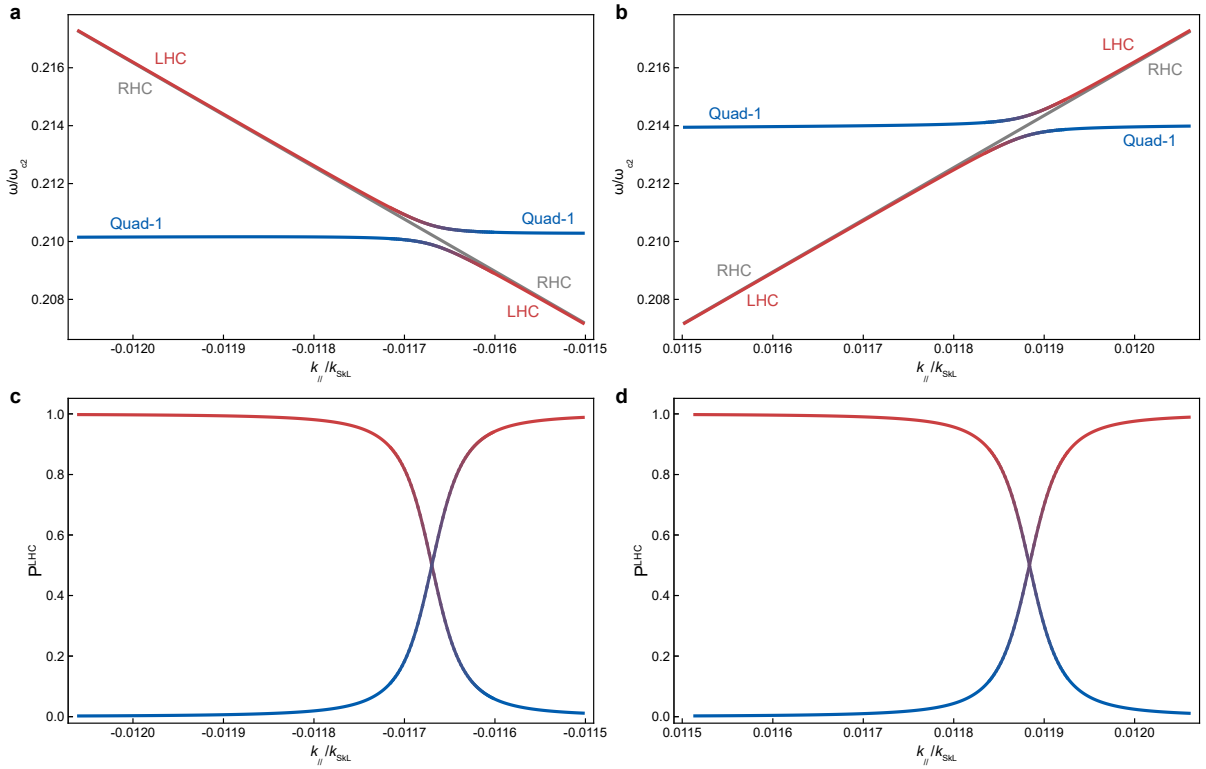

Figure 7.3.: **Hybridisation with quadrupolar mode.** Hybridisation gap opening between the quadrupole-1 magnon mode and the LHC polarised phonon branch at (**a**) negative and (**b**) positive wavevectors, respectively. The results are calculated for the anisotropic magneto-elastic coupling tensor with $\lambda_{11} = 0.22$ MPa and $\mathbf{k} \parallel \mathbf{H} \parallel [001]$. Panels (**c**) and (**d**) show the corresponding phonon polarisation weight, defined in Eq. (7.32), which quantifies how the phonon character is continuously transferred between the two excitation branches.

to the applied magnetic field. Such behaviour provides a direct manifestation of the magneto-elastic coupling in chiral magnets and offers a mechanism to control acoustic transport via magnetic fields.

7.3.3 Hybridisation with quadrupole mode

Upon lowering the system symmetry, we enable the coupling between additional magneto-elastic excitations. Here, we consider the anisotropic coupling tensor with $\lambda_{11} = 3\lambda_{12} = 3\lambda_{21} = 1.2\lambda_{44} = 0.22$ MPa, and magnetic field applied along the cubic diagonal $\mathbf{H} \parallel [111]$. The corresponding equilibrium configuration for the displacement field is shown in Fig. 6.2**i** and **l**. Fig. 7.3**a** and **b** show the anti-crossing behaviour between the LHC polarised transversal phonon and the quadrupole-1 magnon mode at negative and positive wavevectors, respectively. This coupling is allowed by the lowered symmetry of the magneto-elastic tensor. However, the overall symmetry of the system still prevents coupling with magnon modes with higher multipolar character, such as the sextupole-1 excitation. The coupling with the dipole magnon modes at higher frequency is still preserved, and it is usually characterised by larger energy gaps. The comparison between Fig. 7.3**a** and **b** illustrates how magneto-elastic coupling induces non-reciprocal phonon propagation in the system. Fig. 7.3**c** and **d** show the projection of the phonon polarisation onto

the LHC polarised basis. Similar selection rules are obtained for the chiral coupling tensor and magnetic field applied along the cubic diagonal.

8 Non-reciprocal phonon propagation along skyrmion strings

In this Chapter, we present experimental evidence of the magneto-chiral effect for bulk acoustic waves in the skyrmion lattice phase of the noncentrosymmetric helimagnet Cu_2OSeO_3. The measurements were obtained using the ultrasonic pulse-echo technique applied to a bulk sample. This technique probes variations in the phonon phase velocity by tracking how an ultrasonic pulse propagates through a magnetised sample. Among the various magnetic phases, the skyrmion lattice exhibits the most pronounced effect, showing a clear reconfiguration of the sound velocity and a distinct hybridisation with the quadrupole-1 magnon mode. The theoretical interpretation of these observations is based on the collective magneto-elastic framework developed in the previous two Chapters. The experimental data presented in this part were acquired by Dr. Naofumi Matsuyama at the Helmholtz-Zentrum Dresden-Rossendorf with the help of Prof. Sergei Zherlitsyn and collaborators from the University of Tokyo.

In addition, we investigate the influence of magneto-elastic interactions on the incommensurate state that emerges from the coupling between the atomic and magnetic lattices. We study the phason excitation that emerges from the collective oscillation of the relative phase between these two spatial modulations. In particular, we find that the phason mode acquires a gap in the presence of a magneto-elastic coupling, which drives the incommensurate-commensurate phase transition in the system. Furthermore, we predict a hybridisation between the acoustic phonon and the phason mode, which opens the possibility for future experimental observation of this effect.

8.1 Ultrasonic pulse-echo measurements

Ultrasonic pulse-echo technique is a powerful experimental method capable of detecting small changes in sound velocity in the presence of external fields. This well-established approach is described in detail in Ref. [160]. A schematic representation of the setup is shown in Fig. 8.1. In this method, the sample is mechanically excited by a short, polarised elastic pulse. The generated ultrasonic wave propagates

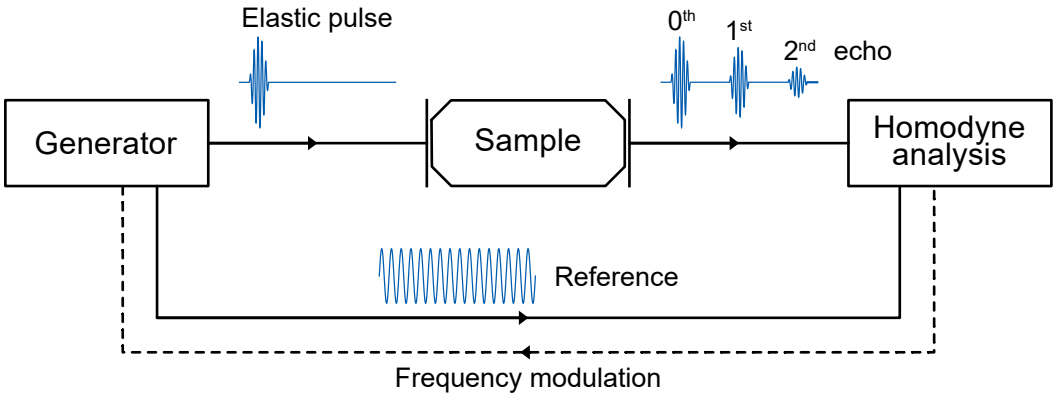

Figure 8.1.: **Ultrasonic pulse-echo setup.** Schematic diagram of the experimental setup for the ultrasonic pulse-echo measurements. The sample is excited on one side by a short, linearly polarised elastic pulse, and its echos are detected on the opposite side. The reference channel enables the phase locking procedure by modulations of the input frequency.

through the sample, and is reflected back and forth while gradually attenuating. Each time the wave reaches the opposite end, a fraction of its energy is converted back into an electrical signal and compared with a reference channel.

In the presence of magneto-elastic coupling, the propagation velocity of the sound wave is modified due to hybridisation with different magnon modes. The energy is conserved during this process, thus the velocity attenuation is attributed to a phase shift of the signal. However, a feedback loop can be employed to match the phase between the signal and the reference channel by adjusting the pulse frequency. This is known as ultrasound pulse-echo technique with constant-phase scheme. Within this framework, the relative change of sound velocity is attributed to the change of ultrasound frequency

$$\frac{\Delta \mathrm{v}}{\mathrm{v}_0} = \frac{\Delta \omega}{\omega_0}, \tag{8.1}$$

where v_0 and ω_0 denote the sound velocity and frequency in the absence of magneto-elastic coupling, respectively. It is important to note that this experimental technique is sensitive to the phase velocity of the pulse propagating through the sample. Moreover, because the feedback loop enforces phase locking, the frequency shift $\Delta\omega = \Big(\omega_0(\mathbf{k}) - \omega(\mathbf{k})\Big)$ is determined at a fixed wavevector $\mathbf{k}$.

8.1.1 Experimental setup

The experiment was performed on a bulk single crystal of Cu_2OSeO_3 with approximate dimensions of 4mm×3mm×1mm and a mass density of $\rho_0 = 5.05\mathrm{g/cm}^3$. The elastic constants were determined in the absence of an external magnetic field, yielding

$$C_{11} = 77\mathrm{GPa} \quad C_{12} = 25\mathrm{GPa} \quad C_{44} = 31\mathrm{GPa}\,. \tag{8.2}$$

During the measurements, the magnetic field was applied along the cubic diagonal, $\mathbf{H} \parallel [111]$, while the elastic waves propagated along the same direction. The crystal was excited by a linearly polarised elastic pulse, and the signal was detected along the same polarisation axis. Two configurations were investigated: longitudinal pulses, with the polarisation parallel to the propagation direction, and transverse pulses, with linear polarisation perpendicular to the propagation direction.

The experimental setup allows precise control over the temperature, magnetic field, and excitation frequency. For each measurement run, the temperature and frequency were kept constant while varying the magnetic field. This procedure enabled exploration of the elastic response across the different magnetic phases of Cu_2OSeO_3, presented in Chapter 2. In particular, we are interested in the signature attributed to the skyrmion lattice phase, which is stabilised for $T \lesssim T_c$, with $T_c \simeq 57K$, and magnetic field in the range 20 mT$\leq \mu_0 H \leq$ 40 mT. Measurements were conducted for temperatures between 50 K and 60 K, and for pulse frequencies between 65 MHz and 556 MHz.

When the system is excited by a transverse linearly polarised elastic pulse, the sound wave propagates as a superposition of the two circularly polarized eigenmodes that emerge in the presence of magneto-elastic coupling. These eigenmodes possess the same energy, $\hbar\omega$, as the incident pulse but differ in their wavevectors. The corresponding elastic displacement field can be written as

$$\delta\mathbf{u}(z,t) = \frac{1}{\sqrt{2}}\left(\mathbf{p}_{\mathrm{R}}^{\mathrm{TA}}\, \mathrm{e}^{\mathrm{i}(\mathrm{k_R z}-\omega \mathrm{t})} + \mathbf{p}_{\mathrm{L}}^{\mathrm{TA}}\, \mathrm{e}^{\mathrm{i}(\mathrm{k_L z}-\omega \mathrm{t})}\right), \tag{8.3}$$

where $\mathbf{p}_{\mathrm{R/L}}^{\mathrm{TA}}$ denote the polarisation vectors given in Eq. (7.31), $k_{\mathrm{R/L}}$ are the corresponding wavevectors, and the propagation direction is taken along the cubic diagonal $\hat{z} \parallel [111]$. We assume that both phonon modes contribute equally to the total elastic wave propagating in the medium. The detected signal is measured along the transverse direction $[1\bar{1}0]$, obtained by projecting $\delta\mathbf{u}(z,t)$ onto this axis. This yields a signal proportional to

$$\cos\left(\frac{k_{\mathrm{R}}-k_{\mathrm{L}}}{2}z\right)\sin\left(\frac{k_{\mathrm{R}}+k_{\mathrm{L}}}{2}z+\omega t\right). \tag{8.4}$$

The spatial modulation given by the beating term $\cos\Big((k_{\mathrm{R}}-k_{\mathrm{L}})z/2\Big)$ varies negligibly over the millimetre-scale sample length. In other words, the phase difference $(k_{\mathrm{R}}-k_{\mathrm{L}})L/2\pi$ remains small in the limit of weak magneto-elastic coupling, where L is the sample length. Consequently, the experimental setup effectively probes only the average wavevector $(k_{\mathrm{R}}+k_{\mathrm{L}})/2$, which is the quantity that enters the phase-locking procedure.

8.1.2 Results

Figure 8.2**a** presents the results for the linearly polarised transverse acoustic mode at $T = 56$ K for different excitation frequencies. The system's response in the conical and field-polarised phases, i.e., for

$\mu_0 H < 20.5$ mT and $\mu_0 H > 38.5$ mT, has been previously analysed in detail by T. Nomura *et al.* in Ref. [142]. In these magnetic phases, the phonon velocity is reduced as a result of the hybridisation between the transverse left-handed circularly polarised phonon and either the $+Q$ resonance mode (in the conical phase) or the Kittel mode (in the field-polarised configuration). These magnetic excitations are located at around 2 GHz, therefore the effect observed here is relatively weak. This hybridisation can be explained by the chiral magneto-elastic coupling introduced in Eq. (6.12), which induces a modulation of the Dzyaloshinskii–Moriya interaction by shear strain. It was shown that this contribution dominates over the standard magneto-elastic coupling considered in this Thesis, owing to the weak spatial modulations of the equilibrium magnetisation in these magnetic textures. The reduction in phonon velocity becomes most pronounced near the phase transition at $\mu_0 H_{c2} \simeq 62.5$ mT. The enhanced attenuation in this region can be traced back to the field dependence of the $+Q$ mode in the helical phase and of the Kittel resonance in the field-polarised phase, as shown in Refs. [39, 48] and in Fig. 5.4. The resonance frequencies of these modes exhibit a minimum near the critical field $\mu_0 H_{c2}$, such that the energy separation between the phonon and the magnetic excitation is smallest in this region, thereby enhancing the coupling and maximising the phonon velocity reduction.

At intermediate magnetic fields, 20.5 mT $< \mu_0 H <$ 38.5 mT, the skyrmion lattice phase is stabilised. Measurements of the phonon velocity in this regime reveal a distinct frequency dependence. In particular, for transverse phonon pulses at 286 MHz and 328 MHz, the phase velocity exceeds that of the reference signal. This behaviour indicates proximity to a magnon–phonon hybridisation region, where the characteristic anti-crossing between the two excitations can lead to an effective increase in the phase velocity. Measurements of the amplitude variation reveal a maximum reduction of about 1% in this field range. This signal reduction can be attributed to the phonon Faraday effect, which corresponds to a rotation of the polarisation plane caused by the different propagation velocities of the left- and right-handed circularly polarised phonons. From this small amplitude reduction, the Faraday rotation angle can be estimated to be less than 10° across the entire sample length.

Additional measurements were performed at a pulse frequency of 288 MHz. Figures 8.2**b** and **c** show the relative change in phonon velocity at $T = 56$ K for transverse and longitudinal excitations, respectively. Within the skyrmion lattice phase, the longitudinal phonon mode exhibits a nearly uniform velocity reduction. This reduction is more pronounced in the skyrmion lattice than in the conical or field-polarised phases. This can be understood in terms of the different coupling mechanisms that dominate in the respective magnetic states. In the skyrmion lattice, the standard magneto-elastic coupling introduced in Eq. (6.11) leads to an effective hybridisation between the acoustic longitudinal phonons and, for example, the breathing mode. This coupling, which is of lower order in the spin–orbit interaction compared to the chiral contribution dominating the other phases, leads to a stronger renormalisation of the phonon

velocity in the skyrmion phase.

In Fig. 8.2**b**, the transverse mode displays a distinct positive velocity shift, consistent with the anti-crossing behaviour characteristic of hybridised excitations. Furthermore, the data reveal a pronounced non-reciprocity, with elastic waves propagating faster along the direction of the applied magnetic field. This observation confirms the presence of a collective magnon mode with a resonance frequency around 300 MHz at small wavevectors, which couples strongly to transverse but not to longitudinal phonons. Importantly, this represents the first experimental observation of the phonon magneto-chiral effect within the skyrmion lattice phase.

Figures 8.2**a**–**c** correspond to measurements obtained while decreasing the applied magnetic field. Here, the sample was initially in the field-polarised phase, and the field was gradually reduced. In contrast, Figures 8.2**d** and **e** show data obtained under the opposite field history, where the field was increased from zero, starting in the helical configuration. The clear difference between the responses in Figs. 8.2**b** and **d** reveals a hysteretic behaviour of the system. The origin of this behaviour is not fully understood, but it may be related to the phase-locking mechanism employed in the experimental procedure. When the system is excited at frequencies close to the hybridisation gap, the left- and right-handed phonons propagate with significantly different wavevectors. Consequently, the phase difference $(k_{\mathrm{R}} - k_{\mathrm{L}})L/2\pi$ is no longer small, and the phase-locking procedure selectively detects one of the two wavevectors instead of their arithmetic average. According to this interpretation, the difference observed between Figs. 8.2**b** and **d** may arise from the selection of distinct transverse phonon eigenmodes, or from a non-trivial combination of these two.

8.1.3 Discussion

To compare the experimental results with the theoretical model presented in the previous Chapters, it is first necessary to determine the characteristic frequency ω_{c2}. This quantity is obtained by calculating the internal critical field at which the system transitions from the conical to the field polarised phase. Using the experimental data presented in the previous Section, we find

$$\mu_0 H_{c2}^{\mathrm{int}} = \frac{\mu_0 H_{c2}^{\mathrm{ext}}}{1 + N_z \chi_{\mathrm{con}}^{\mathrm{int}}} \simeq 31.5 \text{ mT}, \tag{8.5}$$

where we used $\mu_0 H_{c2}^{\mathrm{ext}} = 62.5$ mT and $N_z = 0.56$. According to Eq. (3.19), this corresponds to a characteristic frequency of $\omega_{c2}/2\pi = 0.93$ GHz. It is worth noticing that this value is considerably smaller than the one obtained for the same material in Chapter 5. The reason lies in the higher temperature at which the present measurements were obtained, i.e., just below the critical temperature T_c marking the transition to the paramagnetic phase. Consequently, the critical internal magnetic field is significantly

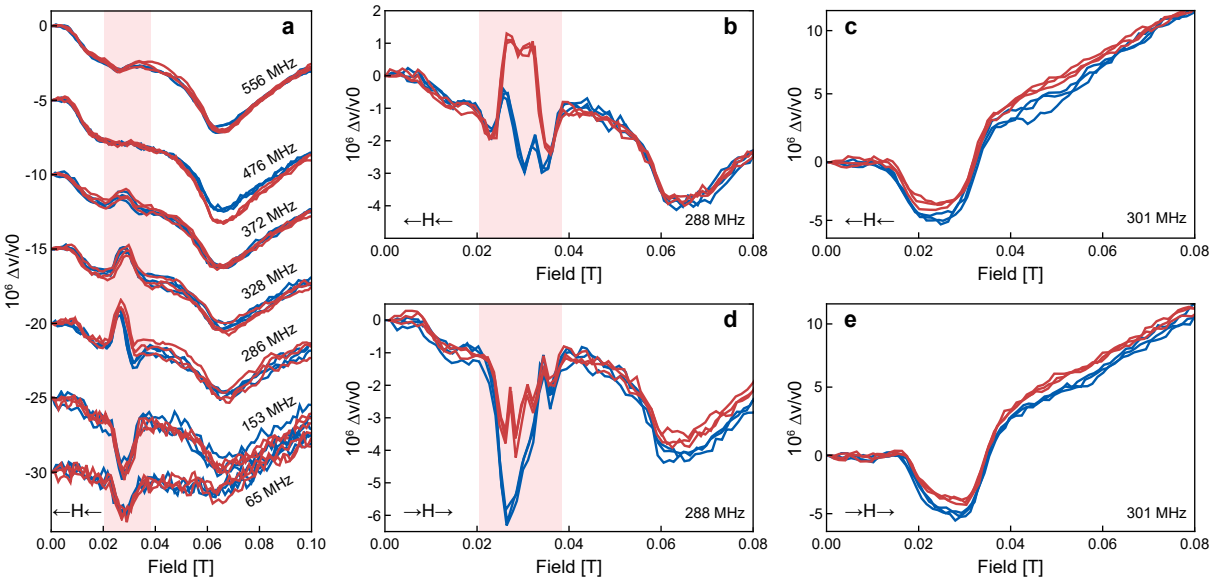

Figure 8.2.: **Measurements of the phonon phase velocity in Cu_2OSeO_3. (a)** Change in the phonon phase velocity for a transverse elastic pulse with $\delta\mathbf{u} \perp \mathbf{k} \parallel \mathbf{H}$, measured while decreasing the applied magnetic field. For each input frequency f_0, the measurement was repeated three times; red and blue lines indicate the velocity change for positive and negative field directions, respectively. **(b)–(c)** show measurements obtained under the same decreasing-field history for the transverse and longitudinal phonon polarisations, respectively. **(d)–(e)** correspond to measurements at the same frequency and temperature, but for increasing magnetic field. The shaded region marks the field range where the skyrmion lattice phase is stabilised in the range 20.5 mT $< \mu_0 H <$ 38.5 mT.

reduced, which directly modifies the characteristic frequency ω_{c2}.

The change in sound velocity obtained via the constant-phase scheme can be analysed starting from the spectra presented in the previous Chapter. In particular, one needs to compare the resonance frequencies of the phonon modes calculated with and without the magneto-elastic coupling. The relative change in phase velocity for a pulse frequency f_0 is therefore given by

$$\frac{\Delta v}{v_0} = \frac{\omega(\mathbf{k}) - \omega_0(\mathbf{k})}{\omega_0(\mathbf{k})}, \tag{8.6}$$

where both resonance frequencies correspond to the same wavevector $\mathbf{k}$, determined by $f_0 = \omega_0(\mathbf{k})/2\pi$.

Figure 8.3 shows the calculated velocity change for longitudinal elastic excitation in the low-energy region probed in the experiment. This has been calculated using parameters corresponding to Cu2OSeO3, with the applied magnetic field $H/Hc2 = 0.5$. Moreover, the magneto-elastic coupling tensor was set to

$$\lambda_{11} = 3\lambda_{12} = 3\lambda_{21} = 0.22 \text{ MPa} \quad \text{and} \quad \lambda_{44} = 0.18 \text{ MPa}. \tag{8.7}$$

For the longitudinal configuration, we find a nearly uniform reduction of the phonon velocity across the entire experimental frequency range. This behaviour arises from the hybridisation with the breathing

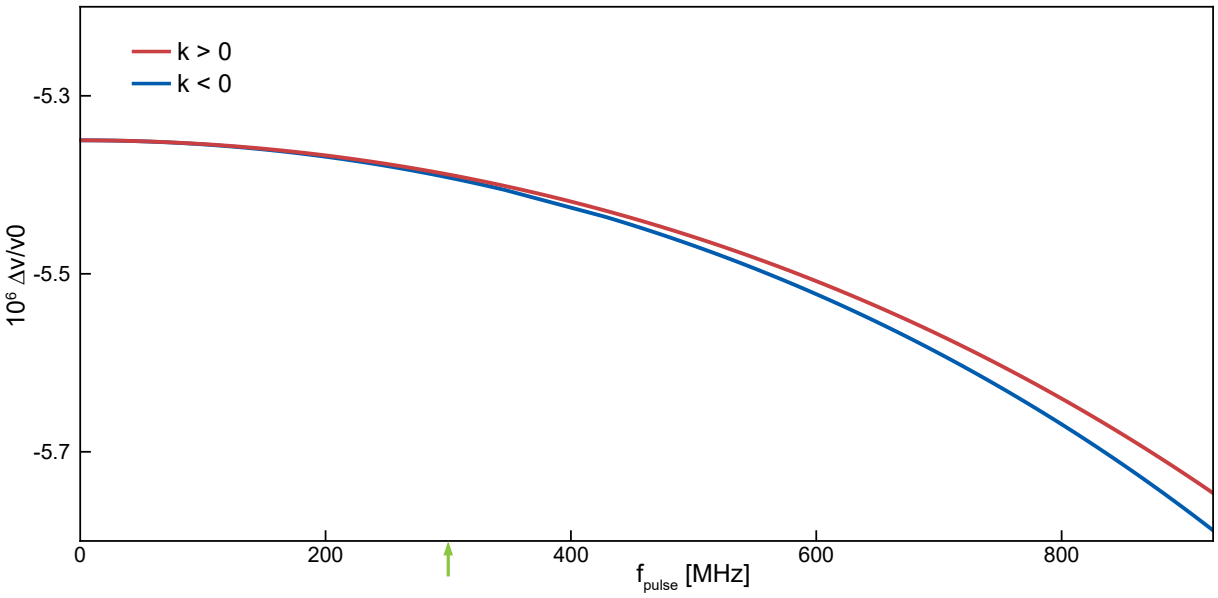

Figure 8.3.: **Theoretically calculated longitudinal phonon phase velocity.** Calculated phase velocity of the longitudinal phonon mode in the skyrmion lattice for $\delta\mathbf{u} \parallel \mathbf{k} \parallel \mathbf{H}$. The data are obtained by comparing the phase velocity with and without magneto-elastic coupling at $H = 0.5H_{c2}$ and $\xi_{ms} = 0.88$. The green arrow indicates the pulse frequency of 301 MHz used in the experiment. The red and blue curves correspond to positive and negative wavevectors, respectively.

mode, located around 3 GHz, which slows down the phonon propagation. The relative change in velocity, on the order of $|\Delta v/v_0| \sim 5 \times 10^{-6}$, is consistent with the experimental observations shown in Fig. 8.2**c** and **e**. This agreement indicates that the adopted coupling strength provides a quantitatively reliable description of the experimental response.

Mode identification

Figure 8.4 shows the calculated change in the phase velocity of the transverse phonon modes. The four solid lines correspond to the non-degenerate left- and right-handed circularly polarised phonons propagating parallel and antiparallel with respect to the applied magnetic field. As discussed in the previous Chapter, the left-handed (LHC) mode couples to the quadrupole-1 and counter-clockwise magnon excitations, giving rise to the characteristic anti-crossing behaviour observed near their resonance frequencies. The right-handed (RHC) mode, on the other hand, experiences a reduction in velocity due to hybridisation with the clockwise magnon mode, located around ~ 3 GHz.

In the experiment, the system only detects linearly polarised elastic waves. These excitations can be represented as a superposition of the two circularly polarised phonon states [Eq. (8.3)]. However, the experimental resolution is insufficient to distinguish the small frequency splitting between the LHC and RHC branches, as explained previously. The dashed lines in Fig. 8.4 illustrate the average response, obtained by taking the mean of the two chiral phonon branches at fixed energy $\hbar\omega$. This simplified treatment does not capture the finer details of the experimental data, such as the field dependence ob-

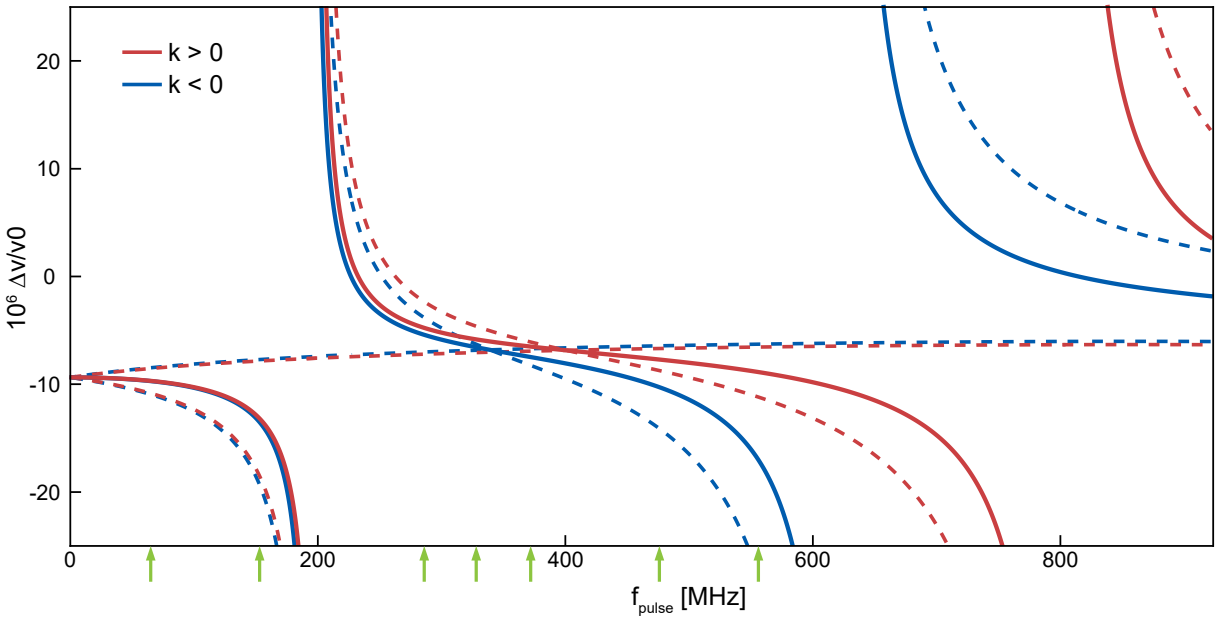

Figure 8.4.: **Theoretically calculated transverse phonon phase velocity.** Calculated phase velocity of the transverse phonon modes in the skyrmion lattice for $\delta\mathbf{u} \perp \mathbf{k} \parallel \mathbf{H}$. The data are obtained by comparing the phase velocity with and without magneto-elastic coupling at $H = 0.5H_{c2}$ and $\xi_{ms} = 0.88$. The red and blue curves correspond to positive and negative wavevectors, respectively. The dashed lines represent the right- and left-handed circularly polarised phonon modes, with the latter exhibiting clear anti-crossing behaviour near 200 MHz and 600–750 MHz. The solid lines denote the averaged signal obtained by combining the phase shifts of the right- and left-handed phonon eigenmodes at fixed frequency. The green arrows mark the pulse frequencies corresponding to Fig. 8.2**a**.

served within the skyrmion lattice phase in Fig. 8.2**b** and **d**, but it provides a qualitative understanding of the magnon–phonon hybridisation and identifies the nature of the collective excitation modes involved.

The calculation predicts a positive shift in the phonon phase velocity for frequencies between approximately 200 and 250 MHz, in agreement with the experimental observations in Fig. 8.2**a** and **b**. This feature can be attributed to the hybridisation with the quadrupole-1 magnon mode, whose profile is depicted in Fig. 3.3. Importantly, this observation represents the first experimental evidence of the quadrupole-1 excitation in the skyrmion lattice phase.

Finally, we note that the non-reciprocity between the two counter-propagating phonon branches primarily arises from their coupling to the CCW magnon mode, even at frequencies close to the quadrupole-1 resonance. In fact, this magnetic excitation exhibits a pronounced intrinsic non-reciprocity and couples strongly to the left-handed circularly polarised phonon, owing to its dipolar character at small wavevectors. Although the present experimental setup—limited by the accessible frequency range and the use of linearly polarised pulses—does not allow for a direct observation of this effect, the results strongly suggest that a more pronounced magneto-chiral effect could be achieved by exploiting the hybridisation with the CCW mode. Such coupling would enable low-energy, direction-dependent acoustic propagation along the skyrmion strings.

8.2 Phason mode in the skyrmion lattice phase

In the present system, the magnetic order forms a two-dimensional skyrmion lattice that develops on top of an underlying cubic atomic crystal. Commensurate skyrmion lattice phases have been reported, for instance, in the hcp-stacked Fe monolayer on Ir(111) [161] and in bulk centrosymmetric kagome magnets [162]. In these materials, the skyrmion textures exhibit characteristic length scales comparable to the atomic lattice spacing. Consequently, the coupling between the magnetic and atomic lattices is enhanced, and any incommensurate configuration carries a large energetic penalty. In contrast, skyrmion lattice phases that occur in noncentrosymmetric helimagnets are characterised by a large unit cell, and are generally incommensurate [162]. An incommensurate lattice arises when two periodic structures coexist in the same material but possess wavelengths whose ratios are irrational. In this case, the combined system lacks a common unit cell, and the superposition of the two modulations never exactly repeats in space. In bulk noncentrosymmetric helimagnets such as Cu_2OSeO_3, the magnetic modulation wavelength is several orders of magnitude larger than the atomic spacing, making the two periodicities effectively independent. When a weak magneto-elastic coupling is introduced, however, it links the magnetic and atomic subsystems, and the crystal can no longer be described by a single periodic lattice. The resulting configuration is an incommensurate state, in which both subsystems remain periodic individually but interact through the coupling field.

A distinctive feature of such incommensurate systems is the emergence of a gapless phason mode. This mode represents a collective oscillation of the relative phase between the two modulations: essentially a sliding motion of the magnetic superlattice with respect to the underlying atomic framework [163–165]. Unlike conventional phonons, which describe coherent atomic displacements in real space, phasons correspond to fluctuations of the phase of the modulation itself, leaving its amplitude essentially unchanged. The existence of this excitation stems from a continuous degeneracy: a uniform shift of the modulation phase does not alter the system's energy. Consequently, phasons are gapless excitations, analogous to Goldstone modes that appear whenever a continuous symmetry is spontaneously broken. Within this context, the magnetic Goldstone mode presented in Chapter 2 can be interpreted as a phason excitation of the incommensurate system formed by the magnetic and atomic lattices coupled via magneto-elastic interactions.

When the coupling between the two sublattices becomes sufficiently strong, a phase transition between the incommensurate and the commensurate state can occur. In this case, the ratio of the respective periodicities becomes rational, giving rise to a periodic superlattice. As a result, the sliding phason mode acquires an energy gap [166, 167], which reflects the finite energy cost of translating two commensurate, or quasi-commensurate, lattices relative to each other. In the present case, the distinct symmetries of the

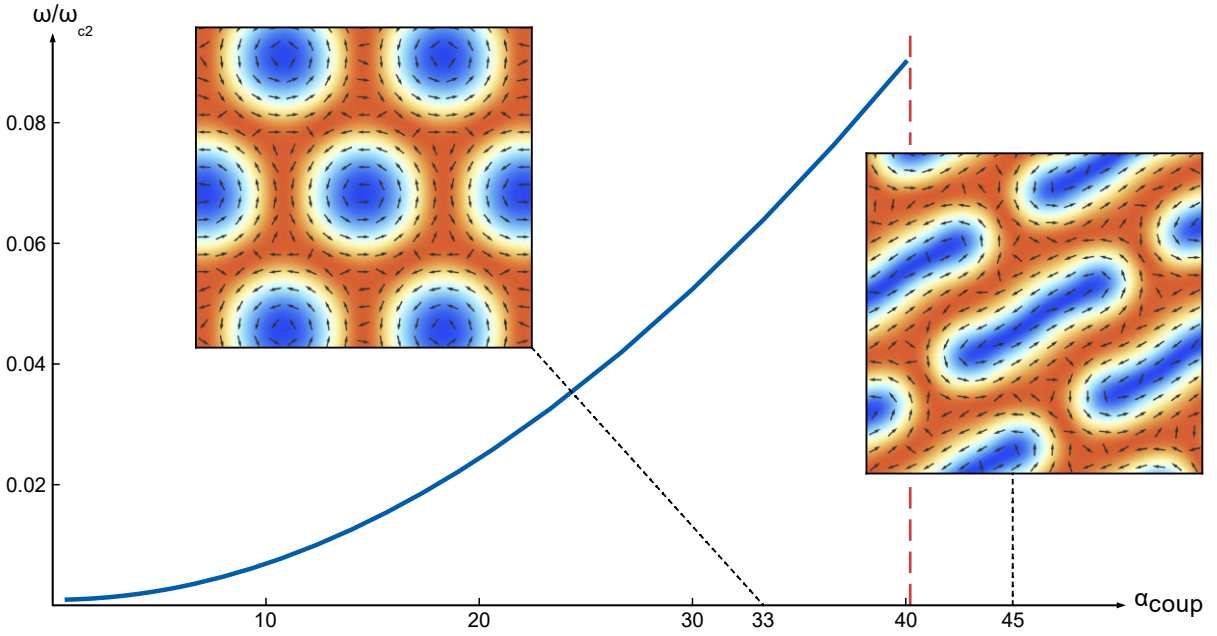

Figure 8.5.: **Phason gap and lattice distortion.** Calculated phason gap opening at the Γ-point as a function of the magneto-elastic coupling strength. The results correspond to $H = 0.5H_{c2}$ applied along the cubic diagonal [111], with $\xi_{ms} = 0.88$, and include the effects of the anisotropic coupling tensor. The insets display the magnetic ground state calculated for $\alpha_{coup} = 33$ and $\alpha_{coup} = 45$. For $\alpha_{coup} \gtrsim 40$, the skyrmion lattice undergoes an oblique distortion induced by the incommensurability between the hexagonal magnetic lattice and the underlying cubic atomic lattice.

cubic atomic lattice and the two-dimensional hexagonal magnetic lattice prevent perfect commensurability, thus preventing the realisation of a fully locked state.

8.2.1 Phason gap

In order to investigate the possible emergence of a phason gap, we need to increase the magneto-elastic coupling between the magnetic and atomic lattices. In Cu_2OSeO_3, this can be achieved by lowering the temperature within the magnetically ordered phase, thereby enhancing the spin–orbit contribution relative to the entropic energy [84]. Nomura *et al.* demonstrated this effect by mapping the phonon magneto-chiral effect as a function of temperature in the conical and field-polarised phases [142]. In particular, they observed a larger non-reciprocity in the phonon propagation for diminishing temperatures. Within the skyrmion lattice phase, the temperature can be lowered by quenching the sample and thus preserving the magnetic texture as discussed in Refs. [51, 76, 87–89], as well as in Chapter 5.

Fig. 8.5 shows the evolution of the phason gap, corresponding to the resonance frequency of the magnetic Goldstone mode at $|\mathbf{k}| = 0$, as a function of the coupling strength α_{coup}. The calculation was performed using the material parameters of Cu_2OSeO_3 introduced previously, with the magnetic field oriented along the cubic diagonal [111] at $H/H_{c2} = 0.5$. The magneto-elastic coupling tensor is parametrised as $\alpha_{coup}\lambda_{ij}$, where λ_{ij} are given by Eq. (8.7), and $\alpha_{coup} = 1$ corresponds to the configuration analysed

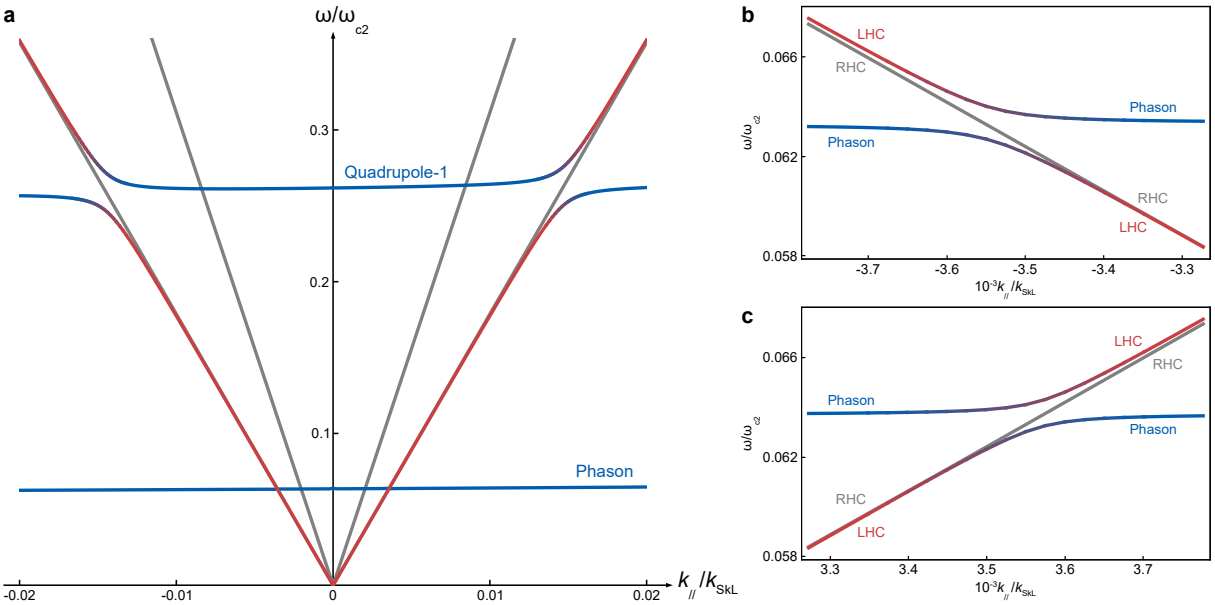

Figure 8.6.: **Hybridisation with the phason mode. (a)** Low-energy excitation spectra calculated for $H = 0.5H_{c2}$ applied along the cubic diagonal [111], with $\xi_{ms} = 0.88$ and anisotropic magneto-elastic coupling with $\lambda_{11} = 7.28$ MPa. A pronounced anti-crossing behaviour occurs between the left-handed circularly polarised (LHC) phonon and the quadrupole-1 magnon mode near $\omega/\omega_{c2} \simeq 0.25$. **(b)–(c)** Hybridisation gap opening between the acoustic LHC phonon and the phason mode, calculated for negative and positive wavevectors, respectively.

in Section 8.1. The resulting dependence reveals that the phason gap increases quadratically with α_{coup}. This behaviour reflects the fundamental effect of magneto-elastic coupling, which pins the relative phase between the magnetic and atomic lattices. As the coupling grows, a restoring force develops that resists their relative sliding. For weak magneto-elastic interaction, this force is proportional to the coupling strength, and the associated harmonic potential leads to an energy gap that scales quadratically. In Fig. 8.5, we also observe that the hexagonal skyrmion lattice becomes unstable for a certain value of the magneto-elastic coupling. The resulting deformations breaks both the rotational symmetry of individual skyrmions and the hexagonal order of the two-dimensional magnetic lattice. This is an indication that the system might undergo an incommensurate-commensurate phase transition.

The low-energy excitation spectra for $\alpha_{coup} = 33$ are shown in Fig. 8.6**a** for wavevectors $\mathbf{k} \parallel \mathbf{H}$, orthogonal to the skyrmion lattice plane. The corresponding coupling parameters, $\lambda_{11} = 7.28$ MPa and $\lambda_{44} = 6.06$ MPa, remain much smaller than the elastic stiffness components given in Eq. (8.2), indicating that the system can be described in the weak-coupling regime. These values are consistent with previous estimates for other noncentrosymmetric helimagnets and thus represent realistic conditions [168]. Under these parameters, the hybridisation gap between the transverse left-handed circularly polarised phonon and the magnetic quadrupole-1 excitation increases substantially. Such enhancement would strongly influence the phonon propagation dynamics, amplifying the magneto-chiral effect even in the presence of

weak non-reciprocity of the quadrupolar magnon mode at small wavevectors.

In this regime, the phason mode acquires a finite energy gap with eigenfrequency $\omega_{\mathrm{pha}}/\omega_{\mathrm{c2}} \simeq 0.06$. Plugging in the characteristic frequency $\omega_{\mathrm{c2}}/2\pi = 0.93$ GHz obtained in the previous Section, this corresponds to $\omega_{\mathrm{pha}}/2\pi \simeq 56$ MHz. In the quenched skyrmion lattice phase, this frequency is expected to increase further due to the higher critical field $\mu_0 H_{\mathrm{c2}}$ associated with reduced temperatures. The resulting energy scale lies near the detection limit of the ultrasonic pulse-echo technique presented in this Chapter. Nevertheless, for an experimental observation to be possible, the phason must hybridise with at least one acoustic phonon mode. Figures 8.6**b** and **c** illustrate the opening of a hybridisation gap between the phason and the left-handed circularly polarised transverse phonon. This produces a characteristic signature in the phase velocity of the acoustic signal, hence measurements of phonon dispersion using the present setup offer a direct route to probe the magneto-elastic coupling between the atomic and magnetic subsystems.

The emergence of a phason gap in the skyrmion lattice phase is particularly intriguing, as it represents a transition from a sliding incommensurate magnetic texture to a state partially locked to the atomic lattice. This behaviour is conceptually analogous to charge-density-wave or spin-density-wave systems [169, 170], where weak coupling to the underlying crystal leads to similar pinning effects and the appearance of a gap in the phason spectrum [166]. Detecting such a feature in Cu_2OSeO_3 would provide direct evidence of the magneto-elastic locking mechanism at play and offer valuable insight into the interplay between long-order chiral modulations of the spin texture, elasticity, and spin–orbit coupling in noncentrosymmetric helimagnets. We are currently planning a collaborative experimental effort to investigate this phenomenon using ultrasound spectroscopy, aiming to test the theoretical predictions presented in this Section.

9 Conclusions and Outlook

This Thesis has explored the spinwave dynamics of the skyrmion lattice in the chiral magnet Cu_2OSeO_3, focusing on the detection of magnon modes via magneto-optic and magneto-elastic coupling. Magnetic skyrmion lattices form self-organized, nanoscale periodic arrangements that act as natural magnonic crystals, providing an ideal platform for studying collective excitations in topologically nontrivial spin textures. Understanding the full magnonic spectrum of such systems is essential both for elucidating the fundamental physics of topological magnets and for realizing future magnon-based information technologies.

While previous experimental techniques, such as microwave spectroscopy and neutron scattering, have successfully probed, respectively, the long-wavelength and high-energy limits of the magnon dispersion, the intermediate wavevector regime remained experimentally inaccessible. This regime, in which the magnon wavelength is comparable to the skyrmion lattice constant, is crucial for describing wave propagation, interference, and hybridization in periodic magnetic structures. By combining theoretical modelling with complementary spectroscopic techniques, this Thesis has bridged this gap and extended the experimental access to the finite-wavevector dynamics of the skyrmion lattice phase.

Magneto-optic coupling and micro-focused BLS spectroscopy

In Chapter 4, a general theoretical formulation of micro-focused Brillouin light scattering (BLS) was developed, starting from the microscopic magneto-optic coupling between light and the dynamic magnetization. The derived framework accounts for the local electric field distribution within a tightly focused laser spot and couples it to the computed spinwave eigenmodes of the magnetic texture. This approach enabled the calculation of BLS spectra in a fully quantitative manner, including the influence of spatial focusing, selection rules, and the polarization dependence of the scattered light. The resulting model fills a gap in the existing literature by providing a comprehensive and versatile description of BLS scattering applicable to a broad range of magnetic systems.

In Chapter 5, this framework was applied to interpret experimental data obtained through a collaborative study using micro-focused BLS on the skyrmion lattice of Cu_2OSeO_3. The experiment probed spin waves with wavevectors on the order of the reciprocal lattice vector of the skyrmion lattice, $|\mathbf{q}| \sim k_{\mathrm{SkL}}$, thereby accessing the intermediate wavevector regime of the magnon dispersion. Analysis of the measured spectra revealed the three fundamental dipolar excitations, the counter-clockwise, breathing, and clockwise modes, whose field dependence matched theoretical predictions. Beyond these well-known modes, two additional higher-order magnon modes with quadrupolar and sextupolar character were identified for the first time. The agreement between calculated and measured eigenfrequencies, along with the corresponding spectral weights, confirmed the validity of the theoretical model and established micro-focused BLS as a powerful and selective probe of complex magnonic excitations in topological spin textures.

These findings demonstrate that focused BLS provides experimental access to magnon minibands within the first magnetic Brillouin zone, thereby opening a new route toward studying finite-wavevector dynamics and nontrivial topological effects in chiral magnets. The methodology developed in this Thesis paves the way for imaging magnon edge modes and nonreciprocal spinwave transport at domain boundaries of the skyrmion lattice using micro-focused BLS spectroscopy.

Magneto-elastic coupling and hybrid magnon–phonon excitations

In Chapters 6 and 7, the Thesis investigated the coupling between spin and lattice degrees of freedom and its consequences for the equilibrium and dynamical properties of the skyrmion lattice. Within the Ginzburg–Landau formalism, a mean-field description of the coupled magneto-elastic system was developed by minimizing the total free energy. This approach allowed the identification of strain-induced distortions of the skyrmion lattice and clarified the role of symmetries in the magneto-elastic coupling tensor components.

By solving the coupled equations of motion, the emergence of hybrid magnon–phonon modes was theoretically predicted. These collective excitations arise from the hybridization between low-energy spinwave modes and acoustic phonons at finite wavevector. The symmetry analysis clarified which magnetic excitations couple efficiently to longitudinal or transverse phonon polarizations, revealing selection rules determined by the underlying crystal symmetry. The model further predicted the opening of a phason gap, originating from the incommensurability between the magnetic and atomic lattices. This phenomenon represents a form of partial locking between the skyrmion lattice and the crystal, analogous to the pinning of charge-density or spin-density waves in correlated electronic systems.

Experimental observation of the phonon magneto-chiral effect

In Chapter 8, the theoretical predictions were tested through ultrasonic pulse-echo measurements of the phonon velocity along the skyrmion tubes in Cu_2OSeO_3. The experiment revealed clear anomalies in the phonon dispersion, evidencing magnon–phonon hybridization and a resulting phonon magneto-chiral effect, that is, nonreciprocal propagation of sound waves depending on their direction relative to the applied magnetic field. Comparison with theory confirmed that this behaviour originates from coupling to a low-energy quadrupolar magnon mode, previously undetected in any experiment. The identification of this mode provides compelling evidence for magneto-elastic coupling effects in the skyrmion lattice and highlights the potential of ultrasound spectroscopy as a sensitive probe of magnon–phonon hybrid excitations.

The combined theoretical and experimental results presented in this Thesis establish a consistent picture of spin–lattice hybridization in chiral magnets and uncover a new level of complexity in the dynamical behavior of skyrmion lattices. The detection of a quadrupolar mode and indications of a phason gap represent significant advances in our understanding of how noncollinear spin textures, spin dynamics, and elasticity intertwine in noncentrosymmetric magnetic materials.

Outlook

Building on the results presented in this Thesis, two main research directions naturally emerge for further investigation of the spin dynamics in chiral magnets. The first project focuses on the role of magneto-crystalline anisotropies in determining the equilibrium and dynamical properties of the skyrmion lattice, particularly in connection with its detection via magneto-elastic coupling. The experimental data discussed in Chapter 5 reveal indications of a magnetic phase transition at low magnetic fields within the metastable skyrmion lattice phase at low temperature. We attribute this behaviour to a transition toward an elongated skyrmion lattice configuration, stabilized by the cubic magneto-crystalline anisotropy. Understanding this transition and its signatures in the magnon spectra requires incorporating the fourth-order spin–orbit coupling term into the Ginzburg–Landau free-energy functional. Future work will therefore extend the theoretical description developed in this Thesis by including this anisotropy contribution and calculating its effect on the BLS spectra.

The second project aims to further explore the phonon magneto-chiral effect and its evolution at low temperatures. As discussed in Chapter 8, the observed nonreciprocity in the phonon velocity arises from hybridization between spinwave and acoustic phonon modes. Since the magneto-elastic coupling strength increases with decreasing temperature, the effect is expected to become more pronounced in the meta-stable phase obtained by quenching of the skyrmion lattice. Moreover, operating at lower temperatures would shift the phason gap predicted in this Thesis into an experimentally accessible frequency

range, providing an ideal platform to test the theoretical predictions of magneto-elastic locking between the magnetic and atomic lattices. Experimental access to this regime would not only confirm the existence of the phason gap but also allow quantitative assessment of its dependence on coupling strength, lattice symmetry, and magnetic field orientation.

A Appendix: Spinwave time evolution

In this Appendix we present the time evolution of the low-energy magnon modes of the skyrmion lattice discussed in Section 3.3. Each figure shows four snapshots within one oscillation period, calculated for $H = 0.5H_{c2}$, $\xi_{ms} = 0.88$, and $\lambda = 500$. The top row displays the out-of-plane component of the spin-wave function $\delta m_z(\mathbf{r}, T/T_0)$ at the Γ-point. The colour scale indicates whether the spinwave is parallel (red) or anti-parallel (blue) to the applied magnetic field.

The second row shows the out-of-plane component of the total magnetisation, calculated as

$$\mathbf{m}(\mathbf{r},t) = \mathbf{m}_{\mathrm{eq}}(\mathbf{r}) + \varepsilon\, \delta\mathbf{m}(\mathbf{r},t)\,, \tag{A.1}$$

where the equilibrium configuration $\mathbf{m}\mathrm{eq}(\mathbf{r})$ is shown in Fig. 2.8**b**. The parameter ε in Eq. (A.1) sets the relative weight between the ground-state magnetisation $\mathbf{m}_{\mathrm{eq}} = \mathbf{M}_{\mathrm{eq}}/M_s$ and the normalised spinwave eigenfunction. Here we use $\varepsilon = 0.3$, which does not correspond to a physical amplitude but serves to visualise the deformation of the ground-state configuration induced by the magnon eigenmodes. The colour code follows that of the top row, representing the out-of-plane component of the magnetisation.

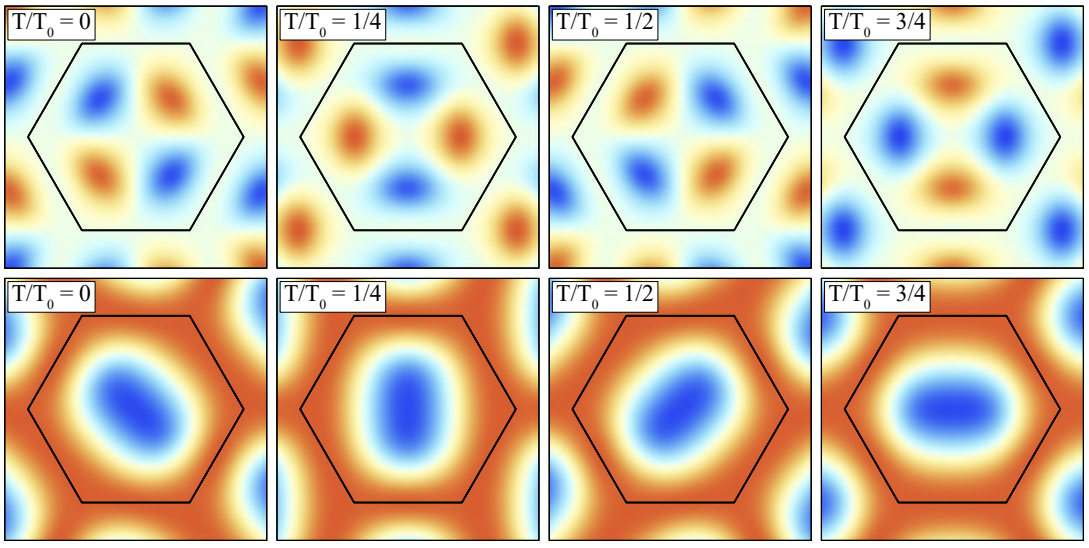

Figure A.1.: **Quadrupole-1.**

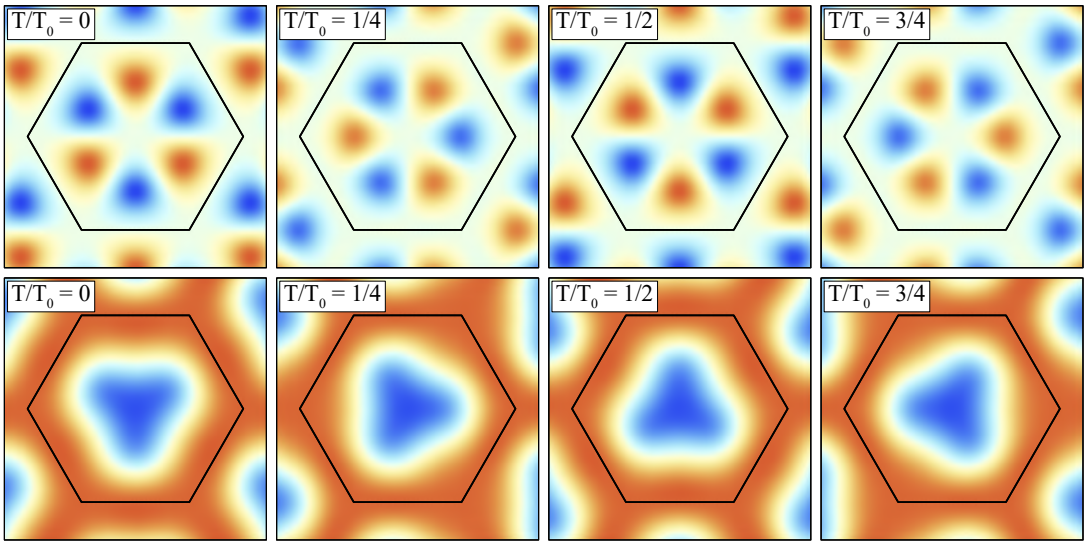

Figure A.2.: **Sextupole-1.**

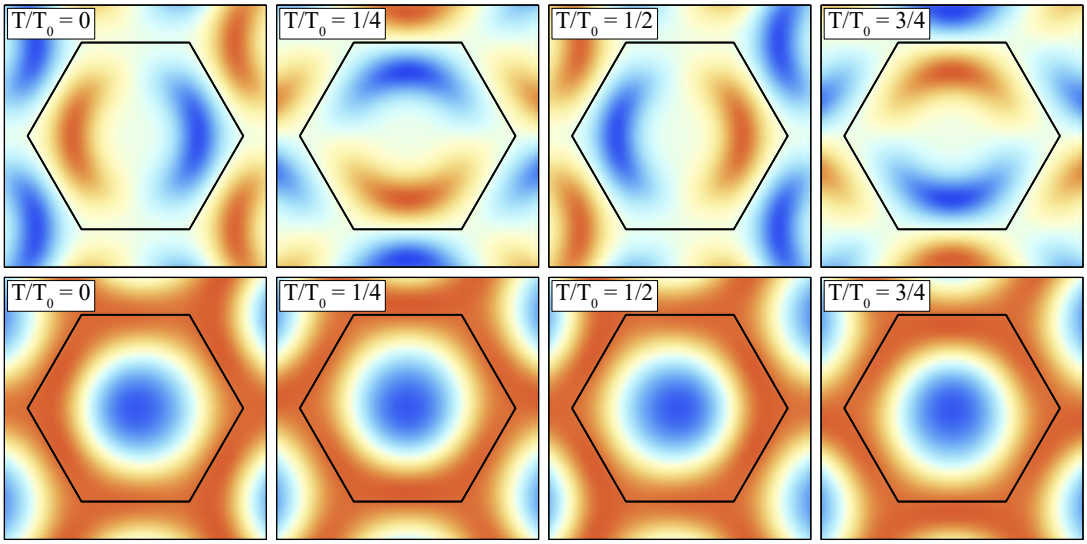

Figure A.3.: **Counter-clockwise (CCW)**

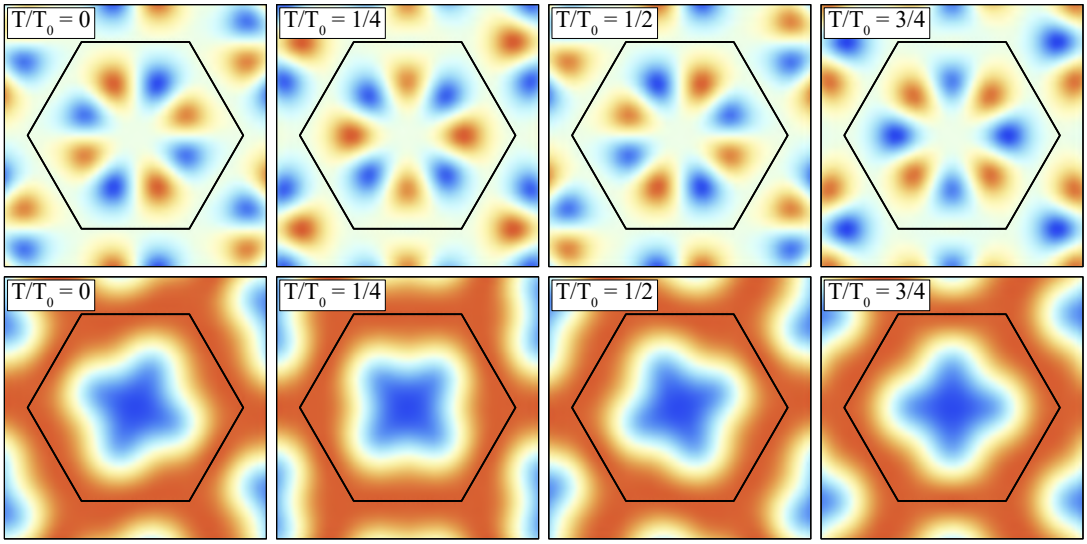

Figure A.4.: **Octupole**

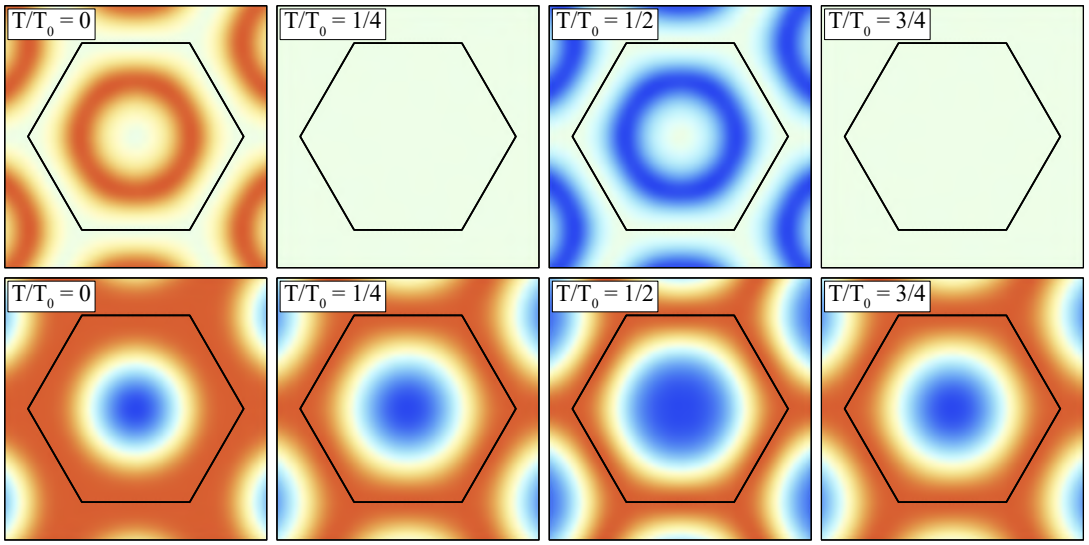

Figure A.5.: **Breathing.**

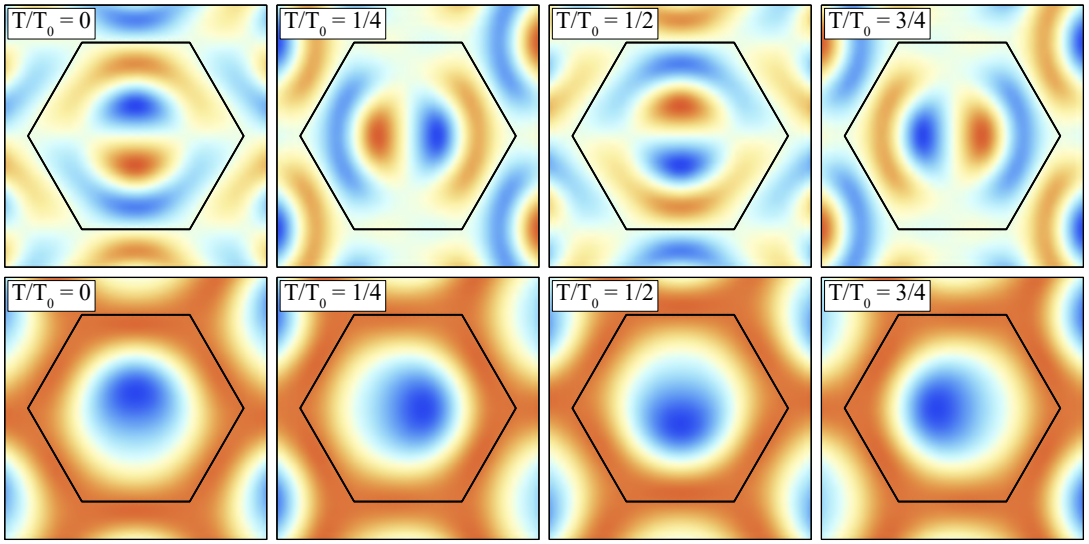

Figure A.6.: **Clockwise (CW)**

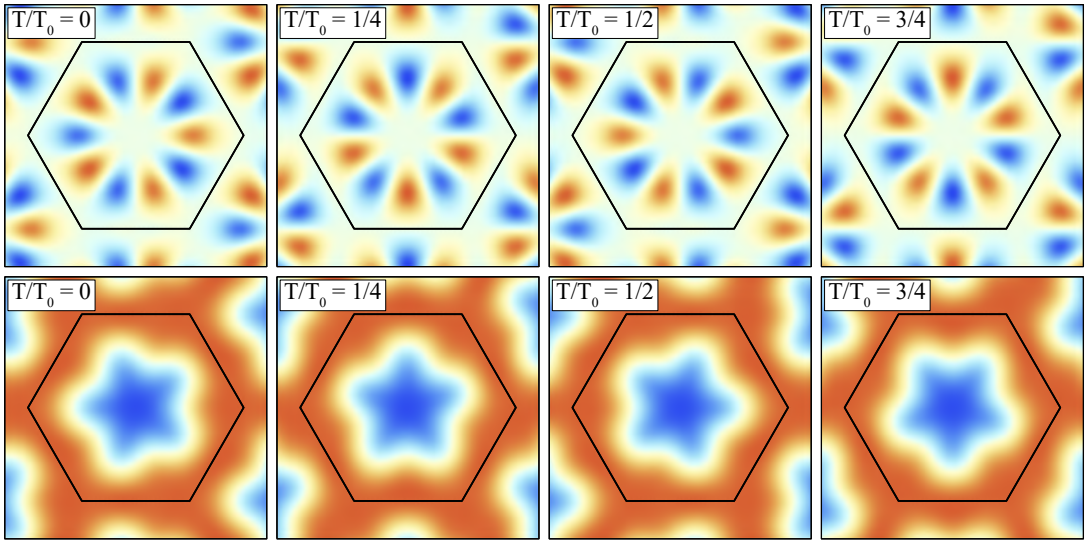

Figure A.7.: **Decupole**

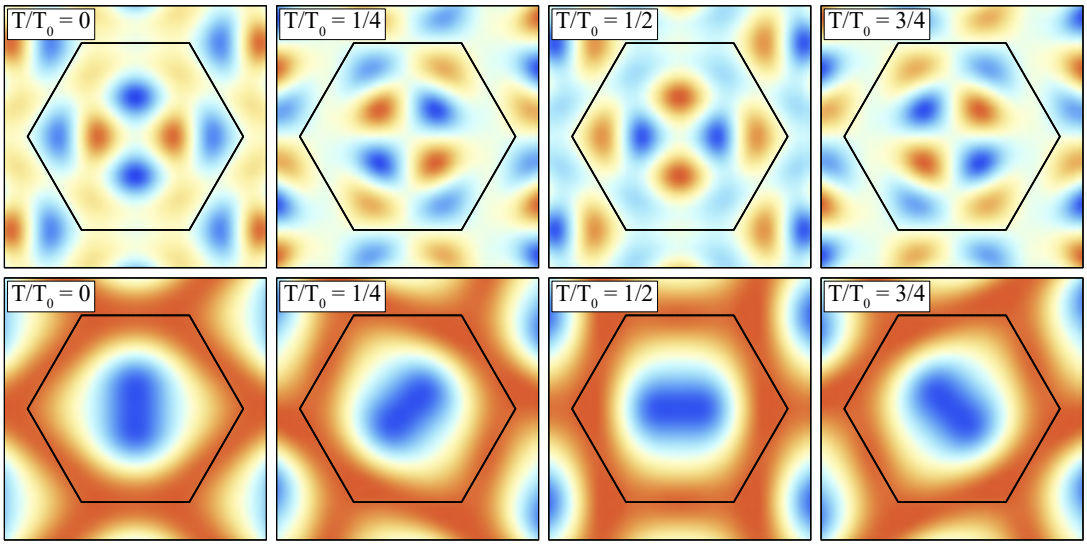

Figure A.8.: **Quadrupole-2.**

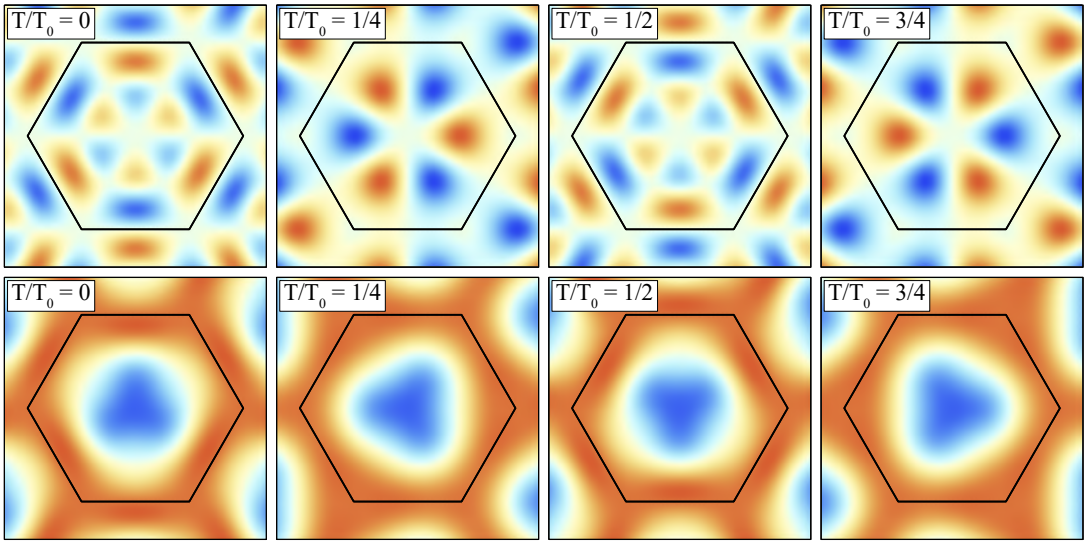

Figure A.9.: **Sextupole-2**

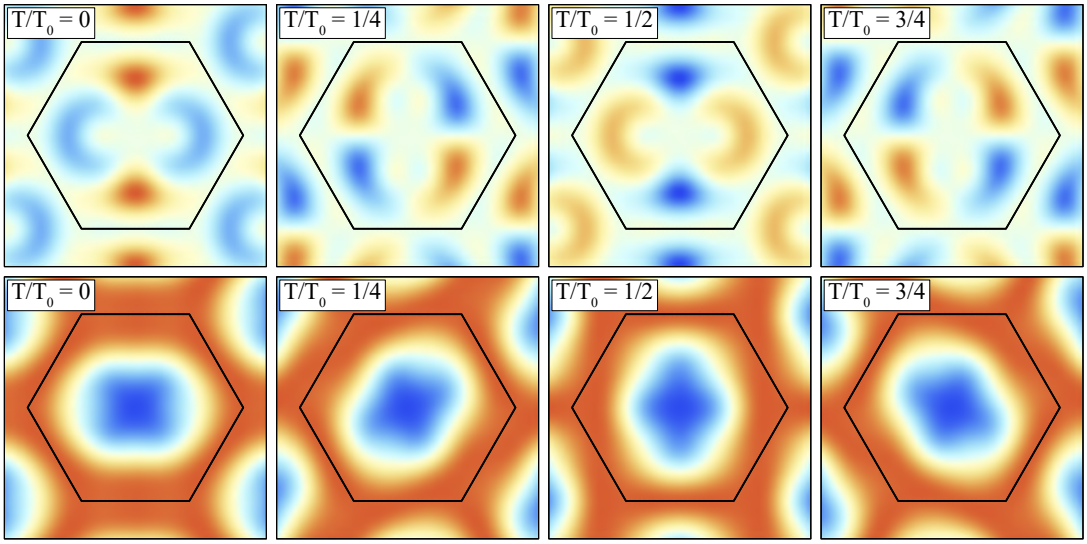

Figure A.10.: **Eight excitation**

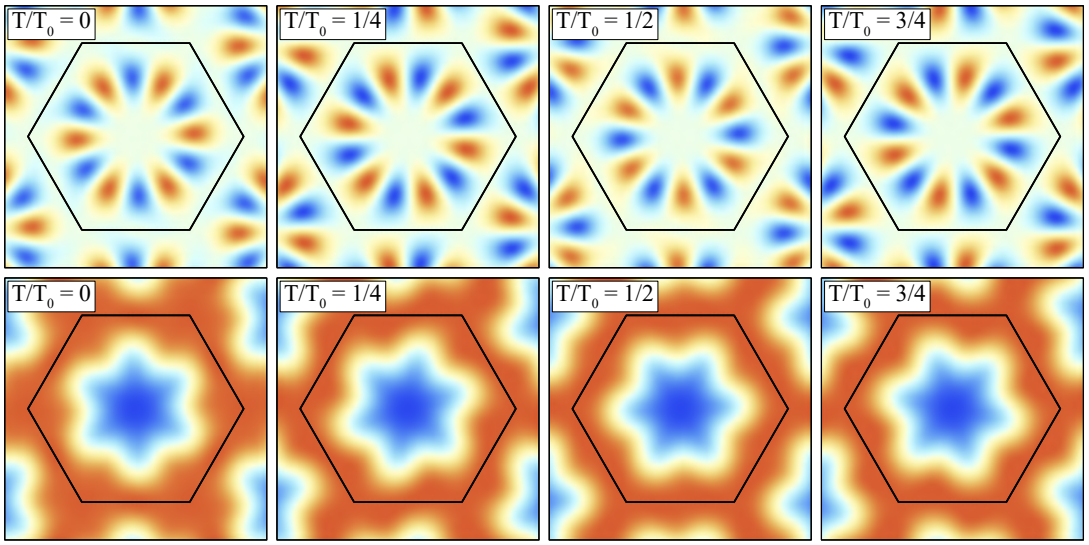

Figure A.11.: **Dodecapole.**

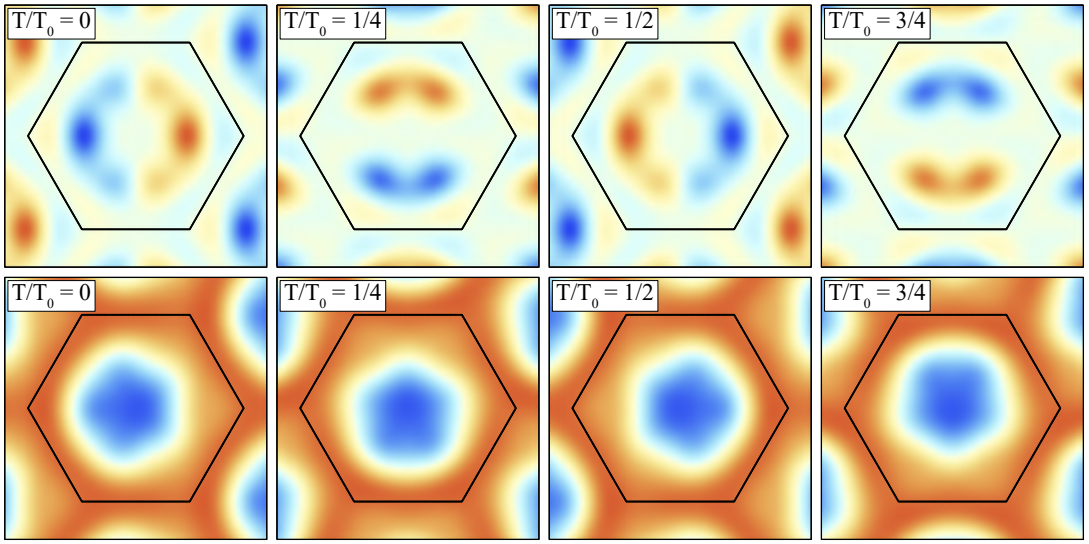

Figure A.12.: **Twelfth excitation**

B Bibliography

[1] F. Bloch. Zur theorie des ferromagnetismus. *Zeitschrift für Physik*, 61(206), 1930.

[2] F. Bloch. Zur theorie des austauschproblems und der remanenzerscheinung der ferromagnetika. *Z. Phys.*, 74(295), 1932.

[3] T. Holstein and H. Primakoff. Field dependence of the intrinsic domain magnetization of a ferromagnet. *Phys. Rev.*, 58(1098), 1940.

[4] F. J. Dyson. General theory of spin-wave interactions. *Phys. Rev.*, 102(1217), 1956.

[5] J. R. Eshbach. Spin-wave propagation and the magnetoelastic interaction in Yttrium Iron Garnet. *Phys. Rev. Lett.*, 8(357), 1962.

[6] F. Goedsche. Reflection and refraction of spin waves. *Phys. Status Solidi*, 39(K29), 1970.

[7] A. V. Vashkovskii, A. V. Stal'makhov, and D. G. Shakhnazaryan. Formation, reflection, and refraction of magnetostatic wave beams. *Sov. Phys. J.*, 31(908), 1988.

[8] J. Gouzerh, A. A. Stashkevich, N. G. Kovshikov, V. V. Matyushev, and J. M. Desvignes. Reflection of magnetostatic waves from a laser-annealed grating in a garnet film. *J. Magn. Magn. Mater.*, 101(189), 1991.

[9] V. K. Dugaev, P. Bruno, B. Canals, and C. Lacroix. Berry phase of magnons in textured ferromagnets. *Phys. Rev. B*, 72(024456), 2005.

[10] S. Yang, Z. Song, and C. P. Sun. Beam splitter for spin waves in quantum spin network. *Eur. Phys. J. B*, 52(377), 2006.

[11] S. Choi, K. S. Lee, and S. K. Kim. Spin-wave interference. *Appl. Phys. Lett.*, 89(62501), 2006.

[12] S. O. Demokritov, V. E. Demidov, O. Dzyapko, G. A. Melkov, A. A. Serga, B. Hillebrands, and A. N. Slavin. Bose˘Einstein condensation of quasi-equilibrium magnons at room temperature under pumping. *Nature*, 443(430-433), 2006.

[13] V. V. Kruglyak, S. O. Demokritov, and D. Grundler. Magnonics. *Journal of Physics D: Applied Physics*, 43(260301), 2010.

[14] A. Barman, G. Gubbiotti, S. Ladak, A. O. Adeyeye, M. Krawczyk, J. Gräfe, C. Adelmann, S. Cotofana, A. Naeemi, V. I. Vasyuchka, B. Hillebrands, S. A. Nikitov, H. Yu, D. Grundler, A. V. Sadovnikov, A. A. Grachev, S. E. Sheshukova, J-Y Duquesne, M. Marangolo, G. Csaba, W. Porod, V. E. Demidov, S. Urazhdin, S. O. Demokritov, E. Albisetti, D. Petti, R. Bertacco, H. Schultheiss, V. V. Kruglyak, V. D. Poimanov, S. Sahoo, J. Sinha, H. Yang, M. Münzenberg, T. Moriyama, S. Mizukami, P. Landeros, R. A. Gallardo, G. Carlotti, J-V Kim, R. L. Stamps, R. E. Camley, B. Rana, Y. Otani, W. Yu, T. Yu, G. E. W. Bauer, C. Back, G. S. Uhrig, O. V. Dobrovolskiy, B. Budinska, H. Qin, S. van Dijken, A. V. Chumak, A. Khitun, D. E. Nikonov, I. A. Young, B. W. Zingsem, and M. Winklhofer. The 2021 magnonics roadmap. *J. Phys.: Condens. Matter*, 33(413001), 2021.

[15] B. Flebus, D. Grundler, B. Rana, Y. Otani, I. Barsukov, A. Barman, G. Gubbiotti, P. Landeros, J. Akerman, U. Ebels, P. Pirro, V. E. Demidov, K. Schultheiss, G. Csaba, Q. Wang, F. Ciubotaru, D. E. Nikonov, P. Che, R. Hertel, T. Ono, D. Afanasiev, J. Mentink, T. Rasing, B. Hillebrands, S. V. Kusminskiy, W. Zhang, C. R. Du, A. Finco, T. van der Sar, Y. K. Luo, Y. Shiota, J. Sklenar, T. Yu, and J. Rao. The 2024 magnonics roadmap. *J. Phys.: Condens. Matter*, 36(363501), 2024.

[16] T. Chen, R. K. Dumas, A. Eklund, P. K. Muduli, A. Houshang, and A. A. Awad. Spin-torque and spin-Hall nano-oscillators. *Proc. IEEE*, 104(1919), 2016.

[17] B Divinskiy, S. Urazhdin, S. O. Demokritov, and V. E. Demidov. Controlled nonlinear magnetic damping in spin-Hall nano-devices. *Nat. Commun.*, 10(5211), 2019.

[18] N. Sato, K. Schultheiss, L. Körber, N. Puwenberg, T. Mühl, A. A. Awad, S. S. P. K. Arekapudi, O. Hellwig, J. Fassbender, and H. Schultheiss. Domain wall based spin-Hall nano-oscillators. *Phys. Rev. Lett.*, 123(057204), 2019.

[19] Q. Wang, M. Kewenig, M. Schneider, R. Verba, F. Kohl, B. Heinz, M. Geilen, M. Mohseni, B. Lägel, F. Ciubotaru, C. Adelmann, C. Dubs, S. D. Cotofana, O. V. Dobrovolskiy, T. Brächer, P. Pirro, and A. V. Chumak. A magnonic directional coupler for integrated magnonic half-adders. *Nature Electronics*, 3(765-774), 2020.

[20] M. Zahedinejad, A. A. Awad, S. Muralidhar, R. Khymyn, H. Fulara, H. Mazraati, M. Dvornik, and J. Åkerman. Two-dimensional mutually synchronized spin-Hall nano-oscillator arrays for neuromorphic computing. *Nat. Nanotechnol.*, 15(47-52), 2020.

[21] A. Papp, W. Porod, and G. Csaba. Nanoscale neural network using non-linear spin-wave interference. *Nat. Commun.*, 12(6422), 2021.

[22] O. Lee, T. Wei1, K. D. Stenning, J. C. Gartside, D. Prestwood, S. Seki, A. Aqeel, K. Karube, N. Kanazawa, Y. Taguchi, C. Back, Y. Tokura, W. R. Branford, and H. Kurebayashi. Task-adaptive physical reservoir computing. *Nature Materials*, 23(79-87), 2024.

[23] M. Krawczyk and D. Grundler. Review and prospects of magnonic crystals and devices with reprogrammable band structure. *J. Phys.: Condens. Matter*, 26(123202), 2014.

[24] A. N. Bogdanov and D. A. Yablonskii. Thermodynamically stable "vortices" in magnetically ordered crystals. The mixed state of magnets. *Sov. Phys. JETP*, 68(101), 1989.

[25] A. N. Bogdanov and A. Hubert. Thermodynamically stable magnetic vortex states in magnetic crystal. *J. Magn. Magn. Mater.*, 138(255), 1994.

[26] A. N. Bogdanov. New localized solutions of the nonlinear field-equations. *JETP Letters*, 62(231), 1995.

[27] S. Mühlbauer, B. Binz, F. Jonietz, C. Pfleiderer, A. Rosch, A. Neubauer, R. Georgii, and P. Böni. Skyrmion lattice in a chiral magnet. *Science*, 323(5916), 2009.

[28] X. Z. Yu, Y. Onose, N. Kanazawa, J. H. Park, J. H. Han, Y. Matsui, N. Nagaosa, and Y. Tokura. Real-space observation of a two-dimensional skyrmion crystal. *Nature*, 465(901-904), 2010.

[29] X. Z. Yu, N. Kanazawa, Y. Onose, K. Kimoto, W. Z. Zhang, S. Ishiwata, Y. Matsui, and Y. Tokura. Near room-temperature formation of a skyrmion crystal in thin-films of the helimagnet FeGe. *Nature Materials*, 10(106-109), 2011.

[30] T. Adams, A. Chacon, M. Wagner, A. Bauer, G. Brandl, B. Pedersen, H. Berger, P. Lemmens, and C. Pfleiderer. Long-wavelength helimagnetic order and skyrmion lattice phase in Cu_2OSeO_3. *Phys. Rev. Lett.*, 108(237204), 2012.

[31] S. Seki, X. Z. Yu, S. Ishiwata, and Y. Tokura. Observation of skyrmions in a multiferroic material. *Science*, 336(6078), 2012.

[32] A. Bauer and C. Pfleiderer. Magnetic phase diagram of MnSi inferred from magnetization and ac susceptibility. *Phys. Rev. B*, 85(214418), 2012.

[33] A. Tonomura, X. Yu, K. Yanagisawa, T. Matsuda, Y. Onose, N. Kanazawa, H. S. Park, and Y. Tokura. Real-space observation of skyrmion lattice in helimagnet MnSi thin samples. *Nano Lett.*, 12(3), 2012.

[34] P. Milde, D. Köhler, J. Seidel, L. M. Eng, A. Bauer, A. Chacon, J. Kindervater, S. Mühlbauer, C. Pfleiderer, S. Buhrandt, C. Schütte, and A. Rosch. Unwinding of a skyrmion lattice by magnetic monopoles. *Science*, 340(6136), 2013.

[35] Y. Tokunaga, X. Z. Yu, J. S. White, H. M. Rønnow, D. Morikawa, Y. Taguchi, and Y. Tokura. A new class of chiral materials hosting magnetic skyrmions beyond room temperature. *Nature Communications*, 6(7638), 2015.

[36] K. Karube, J. S. White, N. Reynolds, J. L. Gavilano, H. Oike, A. Kikkawa, F. Kagawa, Y. Tokunaga, H. M. Rønnow, Y. Tokura, and Y. Taguchi. Robust metastable skyrmions and their triangular–square lattice structural transition in a high-temperature chiral magnet. *Nature Materials*, 15(1237–1242), 2016.

[37] C. Back, V. Cros, H. Ebert, K. Everschor-Sitte, A. Fert, M. Garst, Tianping Ma, S. Mankovsky, T. L. Monchesky, M. Mostovoy, N. Nagaosa, S. S. P. Parkin, C. Pfleiderer, N. Reyren, A. Rosch, Y. Taguchi, Y. Tokura, K. von Bergmann, and J. Zang. The 2020 skyrmionics roadmap. *J. Phys. D: Appl. Phys.*, 53(363001), 2020.

[38] Z. Chen and F. Ma. Skyrmion based magnonic crystals. *J. Appl. Phys.*, 130(090901), 2021.

[39] M. Garst, J. Waizner, and D. Grundler. Collective spin excitations of helices and magnetic skyrmions: review and perspectives of magnonics in non-centrosymmetric magnets. *J. Phys. D: Appl. Phys.*, 50(293002), 2017.

[40] A. Roldán-Molina, A. S. Nunez, and J. Fernández-Rossier. Topological spin waves in the atomic-scale magnetic skyrmion crystal. *New J. Phys.*, 18(045015), 2016.

[41] S. A. Díaz, J. Klinovaja, and D. Loss. Topological magnons and edge states in antiferromagnetic skyrmion crystals. *Phys. Rev. Lett.*, 122(187203), 2019.

[42] S. A. Díaz, T. Hirosawa, J. Klinovaja, and D. Loss. Chiral magnonic edge states in ferromagnetic skyrmion crystals controlled by magnetic fields. *Phys. Rev. Research*, 2(013231), 2020.

[43] T. Weber, D. M. Fobes, J. Waizner, P. Steffens, G. S. Tucker, M. Böhm, L. Beddrich, C. Franz, H. Gabold, R. Bewley, D. Voneshen, M. Skoulatos, R. Georgii, G. Ehlers, A. Bauer, C. Pfleiderer, P. Böni, M. Janoschek, and M. Garst. Topological magnon band structure of emergent Landau levels in a skyrmion lattice. *Science*, 375(6584), 2022.

[44] K. Nakata, J. Klinovaja, and D. Loss. Magnonic quantum Hall effect and Wiedemann – Franz law. *Phys. Rev. B*, 95(125429), 2017.

[45] M. Mochizuki. Spin-wave modes and their intense excitation effects in skyrmion crystals. *Phys. Rev. Lett.*, 108(017601), 2012.

[46] Y. Onose, Y. Okamura, S. Seki, S. Ishiwata, and Y. Tokura. Observation of magnetic excitations of skyrmion crystal in a helimagnetic insulator Cu_2OSeO_3. *Phys. Rev. Lett.*, 109(037603), 2012.

[47] Y. Okamura, F. Kagawa, M. Mochizuki, M. Kubota, S. Seki, S. Ishiwata, M. Kawasaki, Y. Onose, and Y. Tokura. Microwave magnetoelectric effect via skyrmion resonance modes in a helimagnetic multiferroic. *Nature Communications*, 4(2391), 2013.

[48] T. Schwarze, J. Waizner, M. Garst, A. Bauer, I. Stasinopoulos, H. Berger, C. Pfleiderer, and D. Grundler. Universal helimagnon and skyrmion excitations in metallic, semiconducting and insulating chiral magnets. *Nature Materials*, 14(478–483), 2015.

[49] I. Stasinopoulos, S. Weichselbaumer, A. Bauer, J. Waizner, H. Berger, S. Maendl, M. Garst, C. Pfleiderer, and D. Grundler. Low spin wave damping in the insulating chiral magnet Cu_2OSeO_3. *Appl. Phys. Lett.*, 111(032408), 2017.

[50] R. Takagi, M. Garst, J. Sahliger, C. H. Back, Y. Tokura, and S. Seki. Hybridized magnon modes in the quenched skyrmion crystal. *Phys. Rev. B*, 104(144410), 2021.

[51] A. Aqeel, J. Sahliger, T. Taniguchi, S. Mändl, D. Mettus, H. Berger, A. Bauer, M. Garst, and C. Pfleiderer. Microwave spectroscopy of the low-temperature skyrmion state in Cu_2OSeO_3. *Phys. Rev. Lett.*, 126(017202), 2021.

[52] S. Pöllath, A. Aqeel, A. Bauer, C. Luo, H. Ryll, F. Radu, C. Pfleiderer, G. Woltersdorf, and C. H. Back. Ferromagnetic resonance with magnetic phase selectivity by means of resonant elastic X-ray scattering on a chiral magnet. *Phys. Rev. Lett.*, 123(167201), 2019.

[53] N. Ogawa, S. Seki, and Y. Tokura. Ultrafast optical excitation of magnetic skyrmions. *Scientific Reports*, 5(9552), 2015.

[54] J. Kalin, S. Sievers, H. Füser, H. W. Schumacher, M. Bieler, F. García-Sánchez, A. Bauer, and C. Pfleiderer. Optically excited spin dynamics of thermally metastable skyrmions in $Fe_{0.75}Co_{0.25}Si$. *Phys. Rev. B*, 106(054430), 2022.

[55] N. Ashcroft and D. Mermin. Solid state physics. *Harcourt College Publishers*, 1976.

[56] M. P. Marder. Condensed matter physics. *Wiley*, 2000.

[57] C. Herring. Direct exchange between well separated atoms. *Magnetism*, 2B, 1965.

[58] P. Bak and M. H. Jensen. Theory of helical magnetic structures and phase transitions in MnSi and FeGe. *J. Phys. C: Solid State Physics*, 13(L881), 1980.

[59] O. Nakanishi, A. Yanase, A. Hasegawa, and M. Kataoka. The origin of the helical spin density wave in MnSi. *Sol. St. Comm.*, 35(995), 1980.

[60] M. L. Plumer and M. B. Walker. Wavevector and spin reorientation in MnSi. *J. Phys. C: Solid State Physics*, 14(4689), 1981.

[61] M. Kataoka and O. Nakanishi. Helical spin density wave due to antisymmetric exchange interaction. *J. Phys. Soc. Jpn.*, 50(3888), 1981.

[62] I. Dzyaloshinskii. A thermodynamic theory of weak ferromagnetism of antiferromagnets. *J. Phys. Chem. Sol.*, 4(241), 1958.

[63] T. Moriya. Anisotropic superexchange interaction and weak ferromagnetism. *Physical Review*, 120(91), 1960.

[64] M. Tanaka, H. Takayoshi, M. Ishida, and Y. Endoh. Crystal chirality and helicity of the helical spin density wave in MnSi. I. Convergent-beam electron diraction. *J. Phys. Soc. Jpn.*, 54(2970), 1985.

[65] M. Ishida, Y. Endoh, S. Mitsuda, Y. Ishikawa, and M. Tanaka. Crystal chirality and helicity of the helical spin density wave in MnSi. II. polarized neutron diffraction. *J. Phys. Soc. Jpn.*, 54(2975), 1985.

[66] S. A. Siegfried, E. V. Altynbaev, N. M. Chubova, V. Dyadkin, D. Chernyshov, E. V. Moskvin, D. Menzel, A. Heinemann, A. Schreyer, and S. V. Grigoriev. Controlling the Dzyaloshinskii-Moriya interaction to alter the chiral link between structure and magnetism for $Fe_{1-x}Co_xSi$. *Phys. Rev. B*, 91(18), 2015.

[67] A. Hirohata and K. Takanashi. Future perspectives for spintronic devices. *J. Phys. D: Appl. Phys.*, 47(193001), 2014.

[68] A. Neubauer, C. Pfleiderer, B. Binz, A. Rosch, R. Ritz, P. G. Niklowitz, and P. Böni. Topological Hall effect in the A-phase of MnSi. *Phys. Rev. Lett.*, 102(186602), 2009.

[69] N. Nagaosa and Y. Tokura. Topological properties and dynamics of magnetic skyrmions. *Nature Nanotechnology*, 8(899-911), 2013.

[70] D. Shinoda and S. Asanabe. Magnetic properties of silicides of iron group transition elements. *J. Phys. Soc. Jpn.*, 21(555-555), 1966.

[71] S. Seki, J. H. Kim, D. S. Inosov, R. Georgii, B. Keimer, S. Ishiwata, and Y. Tokura. Formation and rotation of skyrmion crystal in the chiral-lattice insulator Cu_2OSeO_3. *Phys. Rev. B*, 85(22), 2012.

[72] H. Arnold. International tables for chrystallography. *Springer*, 2005.

[73] N. Ogawa, L. Köhler, M. Garst, S. Toyoda, S. Seki, and Y. Tokura. Nonreciprocity of spin waves in the conical helix state. *Proc. Natl Acad. Sci. Usa*, 118(e2022927118), 2021.

[74] P. Che, R. Ciola, M. Garst, V. Kravchuk, P. R. Baral, A. Magrez, H. Berger, T. Schönenberger, H. M. Rønnow, and D. Grundler. Short-wave magnons with multipole spin precession detected in the topological bands of a skyrmion lattice. *Communications Materials*, 6(139), 2025.

[75] P. Y. Portnichenko, J. Romhanyi, Y. A. Onykiienko, A. Henschel, M. Schmidt, A. S. Cameron, M. A. Surmach, J. A. Lim, J. T. Park, A. Schneidewind, D. L. Abernathy, H. Rosner, J. van den Brink, and D. S. Inosov. Magnon spectrum of the helimagnetic insulator Cu_2OSeO_3. *Nature Communications*, 7(10725), 2016.

[76] S. Seki, M. Garst, J. Waizner, R. Takagi, N. D. Khanh, Y. Okamura, K. Kondou, F. Kagawa, Y. Otani, and Y. Tokura. Propagation dynamics of spin excitations along skyrmion strings. *Nature Communications*, 11(256), 2020.

[77] C. Pfleiderer, T. Adams, A. Bauer, W. Biberacher, B. Binz, F. Birkelbach, P. Böni, C. Franz, R. Georgii, M. Janoschek, F. Jonietz, T. Keller, R. Ritz, S. Mühlbauer, W. Münzer, A. Neubauer, B. Pedersen, and A. Rosch. Skyrmion lattices in metallic and semiconducting B20 transition metal compounds. *J. Phys.: Condens. Matter*, 22(164207), 2010.

[78] J. Waizner. Spin wave excitations in magnetic helices and skyrmion lattices (Ph.D. thesis). *University of Cologne*, 2017.

[79] Y. Ishikawa, K. Tajima, D. Bloch, and M. Roth. Helical spin structure in manganese silicide MnSi. *Sol. St. Comm.*, 19(525), 1976.

[80] F. Qian, L. J. Bannenberg, H. Wilhelm, G. Chaboussant, L. M. Debeer-Schmitt, M. P. Schmidt, A. Aqeel, T. T. M. Palstra, E. Brück, A. J. E. Lefering, C. Pappas, M. Mostovoy, and A. O. Leonov. New magnetic phase of the chiral skyrmion material Cu_2OSeO_3. *Science Advances*, 4(9), 2018.

[81] S. L. Zhang, A. Bauer, D. M. Burn, P. Milde, E. Neuber, L.M. Eng, H. Berger, C. Pfleiderer, G. van der Laan, and T. Hesjedal. Multidomain skyrmion lattice state in Cu_2OSeO_3. *Nano Lett.*, 16(5), 2016.

[82] T. Adams, M. Garst, A. Bauer, R. Georgii, and C. Pfleiderer. Response of the skyrmion lattice in MnSi to cubic magnetocrystalline anisotropies. *Phys. Rev. Lett.*, 121(187205), 2018.

[83] A. Chacon, L. Heinen, M. Halder, A. Bauer, W. Simeth, S. Mühlbauer, H. Berger, M. Garst, A. Rosch, and C. Pfleiderer. Observation of two independent skyrmion phases in a chiral magnetic material. *Nature Physics*, 14(936-941), 2018.

[84] M. Halder, A. Chacon, A. Bauer, W. Simeth, S. Mühlbauer, H. Berger, L. Heinen, M. Garst, A. Rosch, and C. Pfleiderer. Thermodynamic evidence of a second skyrmion lattice phase and tilted conical phase in Cu_2OSeO_3. *Phys. Rev. B*, 98(144429), 2018.

[85] M. Crisanti, A. O. Leonov, R. Cubitt, A. Labh, H. Wilhelm, M. P. Schmidt, and C. Pappas. Tilted spirals and low-temperature skyrmions in Cu_2OSeO_3. *Phys. Rev. Research*, 5(033033), 2023.

[86] A. O. Leonov and C. Pappas. Skyrmion clusters and conical droplets in bulk helimagnets with cubic anisotropy. *Phys. Rev. B*, 99(144410), 2019.

[87] L. J. Bannenberg, H. Wilhelm, R. Cubitt, A. Labh, M. P. Schmidt, E. Lelièvre-Berna, C. Pappas, M. Mostovoy, and A. O. Leonov. Multiple low-temperature skyrmionic states in a bulk chiral magnet. *npj Quantum Materials*, 4(11), 2019.

[88] H. Oike, A. Kikkawa, N. Kanazawa, Y. Taguchi, M. Kawasaki, Y. Tokura, and F. Kagawa. Interplay between topological and thermodynamic stability in a metastable magnetic skyrmion lattice. *Nature Physics*, 12(62-66), 2016.

[89] R. Takagi, Y. Yamasaki, T. Yokouchi, V. Ukleev, Y. Yokoyama, H. Nakao, T. Arima, Y. Tokura, and S. Seki. Particle-size dependent structural transformation of skyrmion lattice. *Nature Communications*, 11(5685), 2020.

[90] T. H. R. Skyrme. A non-linear field theory. *Proc. R. Soc. A*, 260(127), 1961.

[91] T. H. R. Skyrme. A unified field theory of mesons and baryons. *Nucl. Phys.*, 31(556), 1962.

[92] I. Klebanov. Nuclear matter in the skyrme model. *Nucl. Phys. B*, 262(133), 1985.

[93] M. Kugler and S. Shtrikman. A new skyrmion crystal. *Phys. Lett. B*, 208(491), 1988.

[94] L. Castillejo. Dense skyrmion system. *Nucl. Phys. A*, 501(801), 1989.

[95] K. Everschor-Sitte, J. Masell, R. M. Reeve, and M. Kläui. Perspective: Magnetic skyrmions—overview of recent progress in an active research field. *J. Appl. Phys.*, 124(240901), 2018.

[96] S. Heinze, K. von Bergmann, M. Menzel, J. Brede, A. Kubetzka, R. Wiesendanger, G. Bihlmayer, and S. Blügel. Spontaneous atomic-scale magnetic skyrmion lattice in two dimensions. *Nature Physics*, 7(713–718), 2011.

[97] G. Chen. Skyrmion Hall effect. *Nature Physics*, 13(112-113), 2017.

[98] P. M. Chaikin and T. C. Lubensky. Principles of condensed matter physics. *Cambridge University Press*, 2006.

[99] A. Hubert and R. Schläfer. Magnetic domains. *Springer*, 1998.

[100] M. Gell-Mann and M. Lévy. The axial vector current in beta decay. *Il Nuovo Cimento*, 16(705), 1960.

[101] J. Jost. Geometry and physics. *Springer*, 2009.

[102] A. G. Gurevich and G. A. Melkov. Magnetization oscillations and waves. *CRC Press,*, 1996.

[103] L. D. Landau and E. Lifshitz. On the theory of the dispersion of magnetic permeability in ferromagnetic bodies. *Phys. Z. Sowjet.*, 8(153), 1935.

[104] D. D. Stancil and A. Prabhakar. Spin waves: Theory and applications. *Springer US*, 2009.

[105] T. L. Gilbert. A Lagrangian formulation of gyromagnetic equation of the magnetization field. *Phys. Rev.*, 100(1243), 1955.

[106] J. Bardeen, L. N. Cooper, and J. R. Schrieffer. Theory of superconductivity. *Phys. Rev.*, 108(1175), 1957.

[107] C. Kittel. Introduction to solid state physics. *Wiley and Sons.*, 1953.

[108] C. Herring and C. Kittel. On the theory of spin waves in ferromagnetic media. *Phys. Rev.*, 81(869), 1951.

[109] F. Bloch. Über die quantenmechanik der elektronen in kristallgittern. *Z. Phys.*, 52(7), 1929.

[110] D. Belitz, T. R. Kirkpatrick, and A. Rosch. Theory of helimagnons in itinerant quantum systems. *Phys. Rev. B*, 73(054431), 2006.

[111] M. Janoschek, F. Bernlochner, S. Dunsiger, C. Pfleiderer, P. Böni, B. Roessli, P. Link, and A. Rosch. Helimagnon bands as universal excitations of chiral magnets. *Phys. Rev. B*, 81(214436), 2010.

[112] K. Ho, T. R. Kirkpatrick, Y. Sang, and D. Belitz. Ordered phases of itinerant Dzyaloshinsky – Moriya magnets and their electronic properties. *Phys. Rev. B*, 82(134427), 2010.

[113] V. E. Timofeev and D. N. Aristov. Goldstone mode of skyrmion crystal. *JEPT Letters*, 118(448-454), 2023.

[114] N. Matsuyama, R. Ciola, M. Garst, L. Franke, T. Nomura, Y. Kohama, S. Zherlitsyn, and S. Seki. Manuscript in preparation.

[115] M. Cardona and G. Güntherodt. Light scattering in solids VII : Crystal-field and magnetic excitations. *Springer*, 2000.

[116] Y. Zhu. Modern techniques for characterizing magnetic materials. *Springer*, 2005.

[117] T. Sebastian, K. Schultheiss, B. Obry, B. Hillebrands, and H. Schultheiss. Micro-focused Brillouin light scattering: imaging spin waves at the nanoscale. *Front. Phys.*, 3(35), 2015.

[118] W. Wettling, M. G. Cottam, and J. R. Sandercock. The relation between one-magnon light scattering and the complex magneto-optic effects in YIG. *J. Phys. C: Solid State Phys.*, 8(211), 1975.

[119] P. Grünberg and F. Metawe. Light scattering from bulk and surface spin waves in EuO. *Phys. Rev. Lett.*, 39(1561-1565), 1977.

[120] S. Tacchi, J. Flores-Farías, D. Petti, F. Brevis, A. Cattoni, G. Scaramuzzi, D. Girardi, D. Cortés-Ortuño, R. A. Gallardo, E. Albisetti, G. Carlotti, and P. Landeros. Experimental observation of flat bands in one-dimensional chiral magnonic crystals. *Nano Lett.*, 23(14), 2023.

[121] M. Kuepferling, A. Casiraghi, G. Soares, G. Durin, F. Garcia-Sanchez, L. Chen, C. H. Back, C. H. Marrows, S. Tacchi, and G. Carlotti. Measuring interfacial Dzyaloshinskii – Moriya interaction in ultrathin magnetic films. *Rev. Mod. Phys.*, 95(015003), 2023.

[122] R. Cheenikundil, J. Bauer, M. Goharyan, M. d'Aquino, and R. Hertel. High-frequency modes in a magnetic buckyball nanoarchitecture. *APL Mater.*, 10(081106), 2022.

[123] K. Wagner, A. Kákay, K. Schultheiss, A. Henschke, T. Sebastian, and H. Schultheiss. Magnetic domain walls as reconfigurable spin-wave nanochannels. *Nature Nanotechnology*, 11(432-436), 2016.

[124] V. E. Demidov and S. O. Demokritov. Magnonic waveguides studied by microfocus Brillouin light scattering. *IEEE Trans. Magn.*, 51(0800215), 2015.

[125] L. D. Landau, E. M. Lifshitz, and L. P. Pitaevskij. Electrodynamics of continuous media: Ch. 119. *Elsevier Butterworth-Heinemann*, 2007.

[126] S. O. Demokritov, B. Hillebrands, and A. N. Slavin. Brillouin light scattering studies of confined spin waves: Linear and nonlinear confinement. *Phys. Rep.*, 348(441-489), 2001.

[127] S. O. Demokritov and V. E. Demidov. Micro-Brillouin light scattering spectroscopy of magnetic nanostructures. *IEEE Trans. Magn.*, 44(6-12), 2008.

[128] S. Bhagavantam. Crystal symmetry and physical properties. *Academic Press*, 1966.

[129] Š. Višňovský. Magneto-optical permittivity tensor in crystals. *Czechoslovak Journal of Physics B*, 36(1424-1433), 1986.

[130] J. Jersch, V. E. Demidov, H. Fuchs, K. Rott, P. Krzysteczko, J. Münchenberger, G. Reiss, and S. O. Demokritov. Mapping of localized spin-wave excitations by near-field Brillouin light scattering. *Appl. Phys. Lett.*, 97(152502), 2010.

[131] Z. K. Wang, V. L. Zhang, H. S. Lim, S. C. Ng, M. H. Kuok, S. Jain, and A. O. Adeyeye. Nanostructured magnonic crystals with size-tunable bandgaps. *ACS Nano*, 4(2), 2010.

[132] K. Lenz, R. Narkowicz, K. Wagner, C. F. Reiche, J. Körner, T. Schneider, A. Kákay, H. Schultheiss, U. Weissker, D. Wolf, D. Suter, B. Büchner, J. Fassbender, T. Mühl, and J. Lindner. Magnetization dynamics of an individual single-crystalline Fe-filled carbon nanotube. *Small*, 15(1904315), 2019.

[133] P. Che. Helimagnons and skyrmion dynamics in Cu_2OSeO_3 and Fe/Gd multilayers explored by Brillouin light scattering and $X-$ray microscopy (Ph.D. thesis). *Swiss Federal Technology Institute of Lausanne (EPFL)*, 2021.

[134] L. Novotny and B. Hecht. Principles of nano-optics. *Cambridge University Press*, 2012.

[135] R. B. Versteeg, I. Vergara, S. D. Schäfer, D. Bischoff, A. Aqeel, T. T. M. Palstra, M. Grüninger, and P. H. M. van Loosdrecht. Optically probed symmetry breaking in the chiral magnet Cu_2OSeO_3. *Phys. Rev. B*, 94(094409), 2016.

[136] B. Hetényi, A. Mook, J. Klinovaja, and D. Loss. Long-distance coupling of spin qubits via topological magnons. *Phys. Rev. B*, 106(1), 2022.

[137] L. Körber, C. Heins, T. Hula, J-V Kim, S. Thlang, H. Schultheiss, J. Fassbender, and K. Schultheiss. Pattern recognition in reciprocal space with a magnon-scattering reservoir. *Nature Communications*, 14(3954), 2023.

[138] T. Srivastava, H. Merbouche, I. N. Yemeli, N. Beaulieu, J. B. Youssef, M. Muñoz, P. Che, P. Bortolotti, V. Cros, O. Klein, S. Sangiao, J. M. De Teresa, S. O. Demokritov, V. E. Demidov, A. Anane, C. Serpico, M. d'Aquino, and G. de Loubens. Identification of a large number of spin-wave eigenmodes excited by parametric pumping in Yttrium Iron Garnet microdisks. *Phys. Rev. Appl.*, 19(1), 2023.

[139] L. D. Landau and E. M. Lifshitz. Theory of elasticity. *Pergamon Press*, 1959.

[140] J. F. Nye. Physical properties of crystals. *Oxford Science Publications*, 1957.

[141] E. Callen and H. B. Callen. Static magnetoelastic coupling in cubic crystals. *Phys. Rev.*, 129(578), 1963.

[142] T. Nomura, X.-X. Zhang, S. Zherlitsyn, J. Wosnitza, Y. Tokura, N. Nagaosa, and S. Seki. Phonon magnetochiral effect. *Phys. Rev. Lett.*, 122(145901), 2019.

[143] E. Callen and H. B. Callen. Magnetostriction, forced magnetostriction and anomalous thermal expansion in ferromagnets. *Phys. Rev.*, 139(A455), 1965.

[144] D. A. Kitchaev, I. J. Beyerlein, and A. Van der Ven. Phenomenology of chiral Dzyaloshinskii – Moriya interactions in strained materials. *Phys. Rev. B*, 98(214414), 2018.

[145] G. L. J. A. Rikken and E. Raupach. Observation of magneto-chiral dichroism. *Nature*, 390(493-494), 1997.

[146] M. Vallet, R. Ghosh, A. Le Floch, T. Ruchon, F. Bretenaker, and J.-Y. Thépot. Observation of magnetochiral birefringence. *Phys. Rev. Lett.*, 87(183003), 2001.

[147] C. Koerdt, G. Düchs, and G. L. J. A. Rikken. Magnetochiral anisotropy in Bragg scattering. *Phys. Rev. Lett.*, 91(073902), 2003.

[148] C. Train, R. Gheorghe, V. Krstic, L.-M. Chamoreau, N. S. Ovanesyan, G. L. J. A. Rikken, M. Gruselle, and M. Verdaguer. Strong magneto-chiral dichroism in enantiopure chiral ferromagnets. *Nature Materials*, 7(729-734), 2008.

[149] Y. Okamura, F. Kagawa, S. Seki, M. Kubota, M. Kawasaki, and Y. Tokura. Microwave magnetochiral dichroism in the chiral-lattice magnet Cu_2OSeO_3. *Phys. Rev. Lett.*, 114(197202), 2015.

[150] G. L. J. A. Rikken, J. Fölling, and P. Wyder. Electrical magnetochiral anisotropy. *Phys. Rev. Lett.*, 87(236602), 2001.

[151] V. Krstić, S. Roth, M. Burghard, K. Kern, and G. L. J. A. Rikken. Magneto-chiral anisotropy in charge transport through single-walled carbon nanotubes. *J. Chem. Phys.*, 117(11315-11319), 2002.

[152] F. Pop, P. Auban-Senzier, E. Canadell, G. L. J. A. Rikken, and N. Avarvari. Electrical magnetochiral anisotropy in a bulk chiral molecular conductor. *Nature Communications*, 5(3757), 2014.

[153] T. Yokouchi, N. Kanazawa, A. Kikkawa, D. Morikawa, K. Shibata, T. Arima, Y. Taguchi, F. Kagawa, and Y. Tokura. Electrical magnetochiral effect induced by chiral spin fluctuations. *Nature Communications*, 8(866), 2017.

[154] S. Seki, Y. Okamura, K. Kondou, K. Shibata, M. Kubota, R. Takagi, F. Kagawa, M. Kawasaki, G. Tatara, Y. Otani, and Y. Tokura. Magnetochiral nonreciprocity of volume spin wave propagation in chiral-lattice ferromagnets. *Phys. Rev. B*, 93(235131), 2016.

[155] R. Takagi, D. Morikawa, K. Karube, N. Kanazawa, K. Shibata, G. Tatara, Y. Tokunaga, T. Arima, Y. Taguchi, Y. Tokura, and S. Seki. Spin-wave spectroscopy of the Dzyaloshinskii – Moriya interaction in room-temperature chiral magnets hosting skyrmions. *Phys. Rev. B*, 95(220406(R)), 2017.

[156] Y. Iguchi, S. Uemura, K. Ueno, and Y. Onose. Nonreciprocal magnon propagation in a noncentrosymmetric ferromagnet $LiFe_5O_8$. *Phys. Rev. B*, 92(184419), 2015.

[157] J. Heil, B. Lüthi, and P. Thalmeier. Nonreciprocal surface-acoustic-wave propagation in aluminum. *Phys. Rev. B*, 25(6515(R)), 1982.

[158] R. Sasaki, Y. Nii, Y. Iguchi, and Y. Onose. Nonreciprocal propagation of surface acoustic wave in $Ni/LiNbO_3$. *Phys. Rev. B*, 95(020407(R)), 2017.

[159] T. Nomura, X.-X. Zhang, R. Takagi, K. Karube, A. Kikkawa, Y. Taguchi, Y. Tokura, S. Zherlitsyn, Y. Kohama, and S. Seki. Nonreciprocal phonon propagation in a metallic chiral magnet. *Phys. Rev. Lett.*, 130(176301), 2023.

[160] B. Wolf, B. Lüthi, S. Schmidt, H. Schwenk, M. Sieling, S. Zherlitsyn, and I. Kouroudis. New experimental techniques for pulsed magnetic fields – ESR and ultrasonics. *Physica B: Condensed Matter*, 294-295(612-617), 2001.

[161] K. von Bergmann, M. Menzel, A. Kubetzka, and R. Wiesendanger. Influence of the local atom configuration on a hexagonal skyrmion lattice. *Nano Lett.*, 15(3280), 2015.

[162] M. Hirschberger, B. G. Szigeti, M. Hemmida, M. M. Hirschmann, S. Esser, H. Ohsumi, Y. Tanaka, L. Spitz, S. Gao, K. K. Kolincio, H. Sagayama, H. Nakao, Y. Yamasaki, L. Forró, H.-A. K. von Nidda, I. Kezsmarki, T. Arima, and Y. Tokura. Lattice-commensurate skyrmion texture in a centrosymmetric breathing kagome magnet. *npj Quantum Materials*, 9(45), 2024.

[163] T. Fujiwara and Y. Ishii. Quasicrystals. *Elsevier*, 2008.

[164] A. W. Overhauser. Observability of charge-density waves by neutron diffraction. *Phys. Rev. B*, 3(3173–3182), 1971.

[165] R. Zeyher and W. Finger. Phason dynamics of incommensurate crystals. *Phys. Rev. Lett.*, 49(25), 1982.

[166] A. D. Bruce and R. A. Cowley. The theory of structurally incommensurate systems. *J. Phys. C: Solid State Phys.*, 11(3609–3630), 1978.

[167] H.-H. Yang, L. Desplat, V. P. Kravchuk, M. Hervé, T. Balashov, S. Gerber, M. Garst, B. Dupé, and W. Wulfhekel. Observation of the sliding phason mode of the incommensurate magnetic texture in $Fe/Ir(111)$. *npj Quantum Materials*, 9(54), 2024.

[168] E. A. Karhu, U. K. Rößler, A. N. Bogdanov, S. Kahwaji, B. J. Kirby, H. Fritzsche, M. D. Robertson, C. F. Majkrzak, and T. L. Monchesky. Chiral modulations and reorientation effects in MnSi thin films. *Phys. Rev. B*, 85(094429), 2012.

[169] G. Grüner. The dynamics of charge-density waves. *Rev. Mod. Phys.*, 60(1129–1181), 1988.

[170] G. Grüner. Density waves in solids. *CRC Press*, 1994.

C List of Figures

2.1 **Helix configuration.** The competition between Heisenberg and Dzyaloshinskii–Moriya interaction stabilises noncollinear spin textures. In the helical phase, the magnetization winds around **q**, the propagation vector denoted by the black arrow in the Figure, and is perpendicular to it. 6

2.2 **Qualitative magnetic phase diagram of the cubic chiral helimagnets.** Magnetic phase diagram as a function dimensionless temperature and applied magnetic field. T_c indicates the transition temperature between the disordered paramagnetic phase and the helical configuration in the absence of external fields. The critical field H_{c2} denotes the phase transition between the conical and the field-polarised states. The phase diagram is taken from Ref. [39]. 7

2.3 **Magnetically ordered phases in chiral magnets.** Picture taken from Ref. [78] 8

2.4 **Stereographic projection of (baby) skyrmions.** The south pole of the sphere is mapped onto the origin of $\mathbb{R}^2$, while the north pole corresponds to infinity. By introducing the transformation $\rho \mapsto \tan^{-1}(\rho)$, the infinite plane $\mathbb{R}^2$ can be compactly represented on a finite disk, where ρ denotes the radial distance from the origin. The configurations shown on the left and right correspond to Néel-type and Bloch-type skyrmions, respectively. The figure is adapted from Ref. [78]. 11

2.5 **Mean-field description of a ferromagnetic phase transition.** (**a**) Schematic temperature dependence of the homogeneous magnetisation **M**. (**b**) Sketch of the mean-field free energy functional around the second order phase transition. 15

2.6 **Triple helix configuration.** (**a**) Basis vectors of the spin order in the skyrmion lattice phase. (**b**) Skyrmion lattice configuration obtained using the triple-**Q** ansatz. The arrows depict the in-plane magnetisation and the colour coding represents its out-of-plane component. 22

2.7 **Mean-field phase diagram with thermal fluctuations.** Theoretical phase diagram as a function of the dimensionless magnetic field and the reduced parameter $t = r_0 J/D^2 - 1$. Inset: Energy difference between the skyrmion and conical phases as a function of the applied magnetic field for $t = -3.5$. The mean-field curve remains positive over the entire field range, indicating that the conical phase is the global minimum within mean-field theory. When thermal fluctuation corrections are included, the energy balance is reversed in a narrow region near the critical temperature T_c, stabilising the skyrmion lattice phase. The figure is taken from Ref. [27]. 24

2.8 **Skyrmion lattice configuration.** (**a**) Fourier components forming the reciprocal lattice up to the fourth shell. The gray arrows indicate the fundamental reciprocal lattice vectors $\mathbf{G}_{1,0}$ and $\mathbf{G}_{0,1}$, while the orange dots mark the independent Fourier components that remain after accounting for the system's symmetries. (**b**) Real-space skyrmion lattice configuration obtained by numerically minimizing the free energy density using the Fourier components shown in panel (a). The black hexagon denotes the Wigner–Seitz cell, whose size is given by the skyrmion lattice constant a_{SkL}. 30

2.9 **Reciprocal lattice vector.** Dependence of the skyrmion lattice reciprocal vector on (**a**) the applied magnetic field and (**b**) the magnetostatic parameter. The variation is relatively weak, and in general $k_{\mathrm{SkL}} \simeq Q$ within small deviations. The red arrows indicate the specific values of magnetic field and magnetostatic interaction used for the calculations shown in the opposite figure. In particular, $\xi_{\mathrm{ms}} = 0.88$ corresponds to the experimentally determined value for Cu_2OSeO_3. 31

3.1 **Magnon band structure of the helical phase.** Spinwave spectrum calculated for (**a**) longitudinal momenta $\mathbf{k}_{\parallel} \parallel \mathbf{Q}$ and (**b**) transverse momenta $\mathbf{k}_{\perp}$ in the absence of a applied magnetic field. (**c**-**d**) Non-analytical behaviour of the magnon dispersion of the bulk $\pm Q$ resonances for small wavevectors $|\mathbf{k}| \ll Q$. In zero field, the dispersion is reciprocal (**c**), whereas a finite magnetic field induces non-reciprocal propagation (**d**). 39

3.2 **Eigenvalues of $\left(\mathbf{m}_{\mathrm{eq}} \times\right)$.** Typical distribution of the eigenvalues λ_n introduced in Eq. (3.47), computed for $N = 5$ shells in reciprocal space. The blue dots correspond to the physical subspace, the red dots represent the orthogonal basis, and the light-blue dots indicate intermediate eigenvalues that are projected to zero. 44

3.3 **Spatial profile of the SkL spinwave functions.** Snapshots at a fixed time of the spatial profile of the out-of-plane component $\delta \mathrm{M_z}$. The solutions are calculated at the Γ-point of the Brillouin zone, with colours indicating that the spinwave points parallel (red) or anti-parallel (blue) to the applied magnetic field. The hexagon in each panel is the Wigner-Seitz cell, whose extension is given by the skyrmion lattice constant a_{SkL}. 47

3.4 **Resonance frequencies of the skyrmion lattice.** The low-energy resonance frequencies have been calculated at the Γ-point for $\xi_{ms} = 0.88$, $\lambda = 500$, and frequencies in the range $0 \leq \omega/2\pi \leq 3.2$. The identification of each mode is determined by the wavefunction analysis shown in Fig. 3.3. 48

3.5 **Magnon band structure.** Magnon band structure calculated for in-plane wavevectors $\mathbf{k} \perp \mathbf{H}$ within the first magnetic Brillouin zone. The first 11 excitation modes are shown here, calculated for $H/H_{c2} = 0.5$, $\xi_{ms} = 0.88$ and $\lambda = 500$. The modes can be identified according to the colour coding reported in Fig. 3.4 and Fig. 3.6. 50

3.6 **Magnon dispersion for longitudinal wavevectors.** Theoretically calculated dispersion for $|\mathbf{k}_{\perp}| = 0$, $H/H_{c2} = 0.5$, $\xi_{ms} = 0.88$ and $\lambda = 500$. The dipole active modes are discontinuous for $\mathbf{k}_{\parallel} \to 0$ due to approximations of the dipolar interaction. Among all the low-energy excitations, the CCW mode shows the strongest non-reciprocity. 51

4.1 **Schematic diagram of inelastic Brillouin light scattering. (a)** Emission (Stokes) and absorption (anti-Stokes) diagrams of a quasiparticle with wavevector **q** induced by the incident light. **(b)** Typical BLS spectra which measures the frequency shift of the scattered photons with respect to the elastically scattered light. 55

4.2 **Micro-focused BLS experimental setup.** Schematic diagram of the experimental setup for the micro-focused BLS used in the Chapter 5 to map the magnon spectra in Cu_2OSeO_3. The picture is adapted from [133]. 62

4.3 **Focused electric field.** (**a**) Schematic representation of the focusing process in micro-focused BLS. The collimated laser beam is tilted by the objective lens and refracted at the sample surface according to Snell's law. (**b**) Schematic illustration of the aplanatic optical system. The electric field is refracted at the surface of a reference sphere with radius f, and its components are decomposed along the local polarisation directions to describe the focused field distribution. 63

4.4 **Geometrical optics at an aplanatic lens.** (**a**) Illustration of the sine condition in geometrical optics. The refraction of light rays at an aplanatic lens is governed by a spherical surface of radius f. (**b**) Illustration of the intensity law in geometrical optics. The energy transported along a ray remains constant during refraction, ensuring conservation of energy flux. 64

4.5 **Polarisation vectors.** The lens focuses the incoming laser light (dark green) with polarization $\mathbf{e}_{\text{in}}$ which leads to a distribution of polarizations that depend on the wavevector of the focused light. The light green arrow represents a photon that is scattered after emitting a magnon (red arrow) in the sample and detected with a polarization filter $\mathbf{e}_{\text{out}}$. 65

5.1 **Experimental setup for BLS of magnons in the skyrmion lattice.** (**a**) Sketch of the BLS laser focused on the $(1\bar{1}0)$ surface of Cu_2OSeO_3. The external magnetic field **H** is applied along [001], i.e., the **x** axis. Skyrmion tubes align with the magnetic field and form a hexagonal lattice within the **y**-**z** plane. (**b**) Plane of the skyrmion lattice shown in panel (**a**). The arrows depict the in-plane magnetization and the color coding represent its out-of-plane component. One skyrmion lattice vector connecting two skyrmion centers is assumed to point along [010]. The lattice constant depends weakly on the external magnetic field, and it is on the order of $a_{\mathrm{SkL}} \approx 72\,\mathrm{nm}$. 72

5.2 **Scattering plane.** (**a**) Example of a generic scattering event taking place in the experimental setup close to the objective lens' focal point. The opening angle θ'_{max} of the green cone is determined by the aperture of the lens. The wavevectors of the incoming photon, $\mathbf{k}'_{\mathrm{in}}$, the scattered magnon, $\mathbf{q}$, and the outgoing photon, $\mathbf{k}'_{\mathrm{out}}$, are all located within the same scattering plane indicated by the yellow surface. Panel (**b**) shows the same scattering event in the corresponding scattering plane; whereas the $\mathbf{x}_{\mathrm{sp}}$-axis is located within the **xy**-plane, the $\mathbf{z}_{\mathrm{sp}}$-axis is generally tilted away from the **z**-axis of panel (**a**). 74

5.3 **Sketch of temperature-versus-field histories.** (**a**) Zero-field cooling (ZFC) at $\mu_0 H_{\mathrm{FC}}$ = 0 mT. (**b**) Field cooling (FC) at $\mu_0 H_{\mathrm{FC}}$ = 16 mT. Red arrow indicates the cooling field and green arrow indicate the field scanning direction. 75

5.4 **Zero field cooling (ZFC) BLS spectra. (a)** Anti-Stokes BLS intensities for zero-field cooling (red arrow) down to T=12K and a subsequent field scan (green arrow). Color bar represent the BLS counts. **(b)** Theoretical BLS spectra of the conical phase, $H < H_{\mathrm{c2}}$, and field polarised phase, $H > H_{\mathrm{c2}}$, with the same normalization as in (**a**). 77

5.5 **Field-polarised BLS spectra.** (**a**) Experimental frequency positions of the Anti-Stokes resonance in the field-polarised phase (black dots). The theoretical model gives a linear behaviour (orange line) that can be fitted in order to obtain the parameters $\mu_0 H_{c2} = 53$ mT and $\omega_{c2}/2\pi = 2.03$ GHz. Panel (**c**) (Stokes) and (**d**) (anti-Stokes) shows line cuts of the spectra obtained at fixed magnetic field $\mu_0 H$ = 64 mT (blue symbols) and comparison to theory with H/H_{c2} = 1.21 (red line). A frequency-independent background signal (dark counts) was removed from the raw BLS spectra to realize a baseline similar to the theoretical curves. Both the experimental and theoretical data have been normalized with respect to the total spectral weight integrated over the full frequency range from -7.5 GHz to -1.4 GHz and from 1.4 GHz to 7.5 GHz. 78

5.6 **Field cooling (FC) BLS spectra.** (**a**) BLS intensities for field-cooling at $\mu_0 H_{\mathrm{FC}}$ = 16 mT (red arrow) down to T = 12 K and subsequent field scans (green arrows). Colour bar represents the BLS counts. (**b**) Theoretical BLS spectra of the (metastable) skyrmion lattice (MT-SkL) phase, $H < H_{c2}$, and the field polarized (FP) phase, $H > H_{c2}$, with the same normalization as in (**a**). Line cuts of the spectra for three values of the magnetic field as indicated by the blue and red arrows at the bottom of panel (**a**) and (**b**), respectively, are shown in Fig. 5.8. 80

5.7 **Theoretically calculated magnon band structure of the skyrmion lattice for $H = 0.5H_{c2}$.** (**a**) First Brillouin zone of the skyrmion lattice with one of the reciprocal lattice vectors, k_{SkL}, oriented along [100] [81]. (**b**) Magnon band structure for wavevectors within the plane of the skyrmion lattice, as presented in Fig. 3.5. The same colouring of relevant modes applies throughout this entire Chapter. (**c**) Dispersion of the magnon modes as a function of wavevector along the skyrmion tubes at fixed in-plane wavevector $|\mathbf{q}_\perp| = 47$ rad μm^{-1} pointing along $\hat{z} \parallel [1\bar{1}0]$. The red annulus segments in panel (**a**) and (**b**) as well as the red shaded regime in **c** indicate the range of magnon wavevectors accessible with the BLS setup of this work. 81

5.8 **Normalized line cuts of experimental and theoretical BLS spectra.** Line cuts of the spectra in 5.6**a** (blue symbols) and Fig. 5.4**a** (grey symbols) for three magnetic field values $\mu_0 H$ = 16 mT, 26 mT and 38 mT with Stokes signals shown in panels (**a**), (**c**), and (**e**) and Anti-Stokes signals shown in panels (**b**), (**d**), and (**f**). The blue (grey) symbols are obtained in the metastable skyrmion phase (conical phase). The frequency-independent background signal (dark counts) found in the field-polarized phase was removed from the raw BLS spectra to realize a baseline similar to the theoretical curves (red lines). Negative counts in the experimental data (blue symbols) result from the background-signal subtraction. Red solid lines are theoretical BLS spectra for H/H_{c2} = 0.3, 0.5, 0.72. Coloured bars at the bottom of each panel indicate positions of theoretical skyrmion lattice resonances using the same colour coding as in Fig. 5.7. Both the experimental and theoretical data have been normalized with respect to the total spectral weight integrated over the full frequency range from -7.5 GHz to -1.4 GHz and from 1.4 GHz to 7.5 GHz. Inset of (**b**) shows the hybridization between the breathing and decupole modes. 83

5.9 **Magnon mode identification.** Stokes spectrum of Fig. 5.6**a** overlaid with magnon frequencies of the metastable skyrmion lattice phase calculated for a backscattering event with angle of incidence $\theta_{\mathrm{in}} = \theta_{\mathrm{out}} = 0$. 84

6.1 **Equilibrium configuration for isotropic magneto-elastic coupling. (a-b)** Real-space equilibrium configuration of the magnetisation and displacement field, respectively. The colour indicates the out-of-plane component, parallel to the applied magnetic field, while arrows denote the in-plane directions. (**c**) Real-space elastic deformation magnitude, which becomes maximal at the skyrmions edge where the magnetisation varies most rapidly in space. The black hexagons denote the Wigner–Seitz cell, whose size is given by the skyrmion lattice constant a_{SkL}. The configurations are calculated for $H = 0.5H_{\mathrm{c2}}$ and $\xi_{ms} = 0.88$. 100

6.2 **Displacement field configurations.** The figure shows different equilibrium configurations of the displacement field corresponding to $\mathbf{H} \parallel [001]$ (top 6 panels) and $\mathbf{H} \parallel [111]$ (bottom 6 panels). The three columns correspond to isotropic, chiral and anisotropic coupling tensor, respectively. The black hexagons denote the Wigner–Seitz cell, whose orientation is determined by the angle θ. The configurations are calculated for $H = 0.5H_{\mathrm{c2}}$ and $\xi_{\mathrm{ms}} = 0.88$. The magneto-elastic coupling strength is set by $\lambda_{11} = 0.22$ MPa, which value is compatible with the high-temperature skyrmion lattice in Cu_2OSeO_3 for $T \lesssim T_c = 57$ K (*see Chapter 8*). 102

7.1 **Excitation spectra in the absence of magneto-elastic coupling.** Collective mode dispersions calculated without magneto-elastic coupling for wavevectors parallel to the applied magnetic field, $\mathbf{k} \| \mathbf{H}$, at $H = 0.5H_{\mathrm{c2}}$ and $\xi_{\mathrm{ms}} = 0.88$. The acoustic phonon branches (red) exhibit linear dispersion, with one longitudinal (LA) and two degenerate transverse (TA) modes, the latter displaying a smaller group velocity. The blue and gray lines indicate the low-energy magnon excitations of the skyrmion lattice. The magnon branches shown in blue correspond to the modes that will hybridise with the acoustic phonons once magneto-elastic coupling is introduced. 113

7.2 **Hybridisation with dipole modes.** Hybridisation gaps opening between (**a**) the counter-clockwise (CCW) magnon mode and the left-handed circularly (LHC) polarised transverse phonon, (**b**) the clockwise (CW) magnon mode and the right-handed circularly (RHC) polarised transverse phonon, and (**c**) the breathing (BR) mode and the longitudinal (LA) phonon. The results are calculated for isotropic magneto-elastic coupling with $\lambda_{11} = 0.22$ MPa and $\mathbf{k} \| \mathbf{H} \| [001]$. Panels (**d**)–(**f**) show the corresponding phonon polarisation weight, defined in Eq. (7.32), which quantifies how the phonon character is continuously transferred between excitation branches within the hybridisation regime. . . 114

7.3 **Hybridisation with quadrupolar mode.** Hybridisation gap opening between the quadrupole-1 magnon mode and the LHC polarised phonon branch at (**a**) negative and (**b**) positive wavevectors, respectively. The results are calculated for the anisotropic magneto-elastic coupling tensor with $\lambda_{11} = 0.22$ MPa and $\mathbf{k} \parallel \mathbf{H} \parallel [001]$. Panels (**c**) and (**d**) show the corresponding phonon polarisation weight, defined in Eq. (7.32), which quantifies how the phonon character is continuously transferred between the two excitation branches. . . . 116

8.1 **Ultrasonic pulse-echo setup.** Schematic diagram of the experimental setup for the ultrasonic pulse-echo measurements. The sample is excited on one side by a short, linearly polarised elastic pulse, and its echos are detected on the opposite side. The reference channel enables the phase locking procedure by modulations of the input frequency. . . 120

8.2 **Measurements of the phonon phase velocity in Cu_2OSeO_3. (a)** Change in the phonon phase velocity for a transverse elastic pulse with $\delta\mathbf{u} \perp \mathbf{k} \parallel \mathbf{H}$, measured while decreasing the applied magnetic field. For each input frequency f_0, the measurement was repeated three times; red and blue lines indicate the velocity change for positive and negative field directions, respectively. **(b)–(c)** show measurements obtained under the same decreasing-field history for the transverse and longitudinal phonon polarisations, respectively. **(d)–(e)** correspond to measurements at the same frequency and temperature, but for increasing magnetic field. The shaded region marks the field range where the skyrmion lattice phase is stabilised in the range 20.5 mT $< \mu_0 H <$ 38.5 mT. 124

8.3 **Theoretically calculated longitudinal phonon phase velocity.** Calculated phase velocity of the longitudinal phonon mode in the skyrmion lattice for $\delta\mathbf{u} \parallel \mathbf{k} \parallel \mathbf{H}$. The data are obtained by comparing the phase velocity with and without magneto-elastic coupling at $H = 0.5H_{c2}$ and $\xi_{ms} = 0.88$. The green arrow indicates the pulse frequency of 301 MHz used in the experiment. The red and blue curves correspond to positive and negative wavevectors, respectively. 125

8.4 **Theoretically calculated transverse phonon phase velocity.** Calculated phase velocity of the transverse phonon modes in the skyrmion lattice for $\delta\mathbf{u} \perp \mathbf{k} \parallel \mathbf{H}$. The data are obtained by comparing the phase velocity with and without magneto-elastic coupling at $H = 0.5H_{c2}$ and $\xi_{ms} = 0.88$. The red and blue curves correspond to positive and negative wavevectors, respectively. The dashed lines represent the right- and left-handed circularly polarised phonon modes, with the latter exhibiting clear anti-crossing behaviour near 200 MHz and 600–750 MHz. The solid lines denote the averaged signal obtained by combining the phase shifts of the right- and left-handed phonon eigenmodes at fixed frequency. The green arrows mark the pulse frequencies corresponding to Fig. 8.2**a**. . . . 126

8.5 **Phason gap and lattice distortion.** Calculated phason gap opening at the Γ-point as a function of the magneto-elastic coupling strength. The results correspond to $H = 0.5H_{c2}$ applied along the cubic diagonal [111], with $\xi_{ms} = 0.88$, and include the effects of the anisotropic coupling tensor. The insets display the magnetic ground state calculated for $\alpha_{coup} = 33$ and $\alpha_{coup} = 45$. For $\alpha_{coup} \gtrsim 40$, the skyrmion lattice undergoes an oblique distortion induced by the incommensurability between the hexagonal magnetic lattice and the underlying cubic atomic lattice. 128

8.6 **Hybridisation with the phason mode. (a)** Low-energy excitation spectra calculated for $H = 0.5H_{c2}$ applied along the cubic diagonal [111], with $\xi_{ms} = 0.88$ and anisotropic magneto-elastic coupling with $\lambda_{11} = 7.28$ MPa. A pronounced anti-crossing behaviour occurs between the left-handed circularly polarised (LHC) phonon and the quadrupole-1 magnon mode near $\omega/\omega_{c2} \simeq 0.25$. **(b)–(c)** Hybridisation gap opening between the acoustic LHC phonon and the phason mode, calculated for negative and positive wavevectors, respectively. 129

A.1 **Quadrupole-1.** 136

A.2 **Sextupole-1.** 137

A.3 **Counter-clockwise (CCW)** 137

A.4 **Octupole** 137

A.5 **Breathing.** 138

A.6 **Clockwise (CW)** 138

A.7 **Decupole** 138

A.8 **Quadrupole-2.** 139

A.9 **Sextupole-2** 139

A.10 **Eight excitation** 139

A.11 **Dodecapole.** 140

A.12 **Twelfth excitation** 140